



Terms and Conditions of Use of Digitised Theses from Trinity College Library Dublin

Copyright statement

All material supplied by Trinity College Library is protected by copyright (under the Copyright and Related Rights Act, 2000 as amended) and other relevant Intellectual Property Rights. By accessing and using a Digitised Thesis from Trinity College Library you acknowledge that all Intellectual Property Rights in any Works supplied are the sole and exclusive property of the copyright and/or other IPR holder. Specific copyright holders may not be explicitly identified. Use of materials from other sources within a thesis should not be construed as a claim over them.

A non-exclusive, non-transferable licence is hereby granted to those using or reproducing, in whole or in part, the material for valid purposes, providing the copyright owners are acknowledged using the normal conventions. Where specific permission to use material is required, this is identified and such permission must be sought from the copyright holder or agency cited.

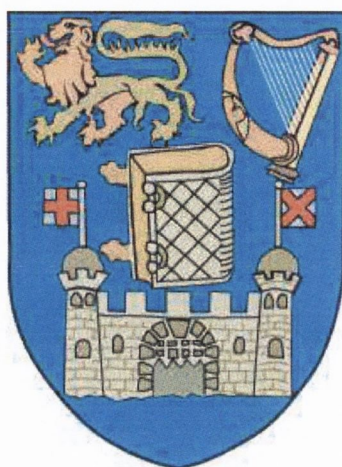
Liability statement

By using a Digitised Thesis, I accept that Trinity College Dublin bears no legal responsibility for the accuracy, legality or comprehensiveness of materials contained within the thesis, and that Trinity College Dublin accepts no liability for indirect, consequential, or incidental, damages or losses arising from use of the thesis for whatever reason. Information located in a thesis may be subject to specific use constraints, details of which may not be explicitly described. It is the responsibility of potential and actual users to be aware of such constraints and to abide by them. By making use of material from a digitised thesis, you accept these copyright and disclaimer provisions. Where it is brought to the attention of Trinity College Library that there may be a breach of copyright or other restraint, it is the policy to withdraw or take down access to a thesis while the issue is being resolved.

Access Agreement

By using a Digitised Thesis from Trinity College Library you are bound by the following Terms & Conditions. Please read them carefully.

I have read and I understand the following statement: All material supplied via a Digitised Thesis from Trinity College Library is protected by copyright and other intellectual property rights, and duplication or sale of all or part of any of a thesis is not permitted, except that material may be duplicated by you for your research use or for educational purposes in electronic or print form providing the copyright owners are acknowledged using the normal conventions. You must obtain permission for any other use. Electronic or print copies may not be offered, whether for sale or otherwise to anyone. This copy has been supplied on the understanding that it is copyright material and that no quotation from the thesis may be published without proper acknowledgement.



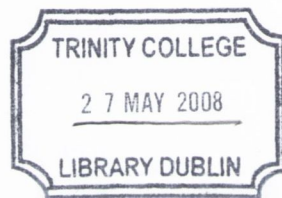
Implementation of Self Interaction Free Density Functional methods and applications to Dilute Magnetic Semiconductors

By

Sri Chaitanya Das Pemmaraju

A thesis submitted for the degree of
Doctor of Philosophy
School of Physics
Trinity College Dublin

October 2007



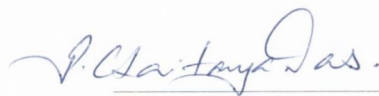
THESIS
8366

Declaration

I, Sri Chaitanya Das Pemmaraju, hereby declare that this dissertation has not been submitted as an exercise for a degree at this or any other University.

It comprises work performed entirely by myself during the course of my Ph.D. studies at Trinity College Dublin. I was involved in a number of collaborations, and where it is appropriate my collaborators are acknowledged for their contributions.

A copy of this thesis may be lent or copied by the Trinity College Library upon request by a third party provided it spans single copies made for study purposes only, subject to normal conditions of acknowledgement.



Sri Chaitanya Das Pemmaraju

Abstract

The present thesis mainly deals with the implementation of self interaction free density functional methods in a numerically efficient density functional theory code SIESTA and the application of the said methods in *ab-initio* electronic structure calculations. We present calculations on the polarizability of molecular chains using explicit orbital dependent density functional methods viz., exact exchange and self interaction corrected (SIC) functionals, which address some long standing issues in the field. We show that SIC functionals in fact perform better than the exact exchange functional at the KLI level of approximation. We discuss the ASIC method which is an approximate self interaction correction scheme that is computationally in-expensive. Results for finite systems as well as extended systems are discussed. We then discuss the electronic and magnetic structure of defective Hafnium Oxide systems where in we show that native Hafnium vacancies exhibit spin polarized ground states with ferromagnetic inter-defect coupling. An extensive study on Co doped ZnO is then presented mainly focusing on the possibility for intrinsic ferromagnetism in the material arising from native defect induced perturbations to the electronic structure of doped Co. We show that a defect-dopant complex center formed from a substitutional Co ion and an Oxygen vacancy can mediate long range ferromagnetic interactions. However we attribute the experimentally observed signatures of ferromagnetism to blocked superparamagnetic clusters. Finally we present *ab-initio* electronic transport calculations on Mn₁₂ based single molecule magnets in a two terminal device set up. The current-voltage (I-V) characteristics of the molecule for two different spin configurations of the Mn₁₂ center are studied. We show that a change in the local magnetic configuration on the molecule can lead to a detectable change in the I-V characteristics.

Acknowledgements

Over the last four years, I received a lot of help and support from a large number of people, without whom none of this research would have been possible.

First of all, I would like to thank my supervisor Prof. Stefano Sanvito. When I joined his group four years ago, he had two other students and one postdoc based in the arches underneath the Dart line that runs through Trinity college. Now, his group is one of the largest in the School of Physics, and he has established himself as one of the leaders in the field of computational materials science and molecular electronics. I have benefitted greatly from his advice and teaching during my time in his research group.

Secondly, I need to thank our external collaborators Prof. Kieron Burke, formerly of Rutgers in New Jersey and now based in University of California, Irvine, and Prof. Alessio Filippetti from the University of Cagliari, Italy. Without the assistance of both of these researchers the work described in this thesis could not have been performed. Alessio developed the pseudo-SIC approximation on which the ASIC method, used in calculations in this thesis, is based. We've had a number of useful discussions with Prof. Burke and the calculations on molecular polarizabilities presented in this thesis were carried out in collaboration with him.

As I mentioned above, Stefano's group has grown large, with a current total of ten postgraduate students and two postdocs, as well as two former poststudents and two former postdocs. However, there are a few former and current group members whose assistance was vital to the work performed in this thesis. Alex Rocha was Stefano's very first student, and he did the bulk of the work of developing SMEAGOL, in collaboration with groups in Lancaster, England and Oviedo, Spain. He has since graduated and is now a postdoctoral researcher in his native Brazil. I have to specially thank Alex for letting me be his housemate for about two years during which time we shared a great sea side house in Howth owned by a nice old lady Mrs. Thompson who rented the place to Alex at a very low rate. That was indeed a pleasant experience. I've had many a useful discussion with Cormac Toher in issues having to do with self interaction corrections and such. He is only slightly better than me at football so I've always enjoyed playing football with him. Miguel Afonso Oliveira was a postdoc in our group for the best part of three years, during which time he served as our system administrator, along with Tom Archer. They were both of great help in solving my computer related problems I've also had many useful discussions with Tom about density functional theory and on Dilute magnetic semiconductors. Ivan Rungger has also recently been promoted to the role of system administrator, and both

his help with computers and discussions about physics were very useful.

Other members of our group who have been here almost as long as myself include Maria Stamenova, Ruairi Hanafin, Will Lee and Akinlolu Akande. New members who have just joined in the last year include Nadjib Baadji, Durga Sankar Kusanakurthi, Andrea Droghetti and Nuala Caffrey. The former member of our group who has not yet been mentioned is Nicola Jean, who still returns to Dublin on occasion to visit us and to do some shopping.

It would not be possible to undertake research such as this without funding. The Science Foundation of Ireland (Grant SFI02/IN1/I175) paid my fees and maintenance, and also provided support for attending conferences. The calculations presented in this thesis were performed in the Trinity Centre for High Performance Computing (TCHPC) and the Irish Centre for High End Computing. The staff from TCHPC, particularly Jimmy Tang, Bob Crosbie, Dermot Frost, Geoff Bradley and Jose Redojo also provided technical assistance both on their cluster and visualisation suite, as well as on our own internal network.

Members from other groups who we've shared offices space with include Andy Wall and Dave Kirwan, Claudia Gomes Rocha, Andrew Rowan, and Eireann Cosgriff.

Finally, I should thank my family, who have always been supportive at every stage of my life.

Contents

Abstract	iii
Acknowledgements	v
1 General Introduction	1
1.1 Dilute magnetic semiconductors	2
1.2 Electron transport through magnetic molecules	6
1.3 Dissertation layout	8
I Theoretical tools	11
2 Theoretical and Numerical framework	13
2.1 The Quantum Many body problem	13
2.2 Wavefunction methods	15
2.3 Density Functional theory	17
2.3.1 The Hohenberg-Kohn theorem	18
2.3.2 The Kohn-Sham scheme	18
2.3.3 Approximate density functionals	21
2.3.4 Interpretation of Kohn Sham eigenvalues	23
2.4 Computational Methods	25
2.4.1 Basis sets	26
2.4.2 Pseudopotentials	27
2.4.3 The SIESTA code	29
2.4.4 Additions to SIESTA	35
2.5 Electronic transport at the nanoscale	36
2.5.1 NEGF and SMEAGOL	36
2.6 Conclusions	40
3 Orbital dependent functionals	41
3.1 Introduction	41
3.2 Orbital dependent functionals	42
3.3 The optimized effective potential	43

3.3.1	The exact exchange functional	46
3.3.2	The SIC functional	46
3.4	Implementation in SIESTA	49
3.5	Application: Polarizability of molecular chains	51
3.6	Conclusions	56
4	ASIC for molecules and solids	57
4.1	Introduction	57
4.2	Review of existing methods	60
4.3	Formalism and Implementation	64
4.3.1	The ASIC potential	65
4.3.2	Implementation	66
4.3.3	Total Energy	69
4.3.4	ASIC and LDA+ U	70
4.4	Results: Extended systems	72
4.4.1	Estimate of α for semiconductors	72
4.4.2	Wide-gap semiconductors: ZnO and GaN	75
4.4.3	Transition-metal oxide: MnO	77
4.5	Results: Molecules	79
4.5.1	Ionization potentials	79
4.5.2	Electron affinities	81
4.5.3	Vertical excitations	83
4.5.4	The HOMO-LUMO gap	85
4.5.5	Final Remarks	88
4.6	Conclusions	89
II	Materials simulations	91
5	Ferromagnetism in HfO₂	93
5.1	Introduction	93
5.2	Computational Details	95
5.3	Defect free HfO ₂	96
5.4	Oxygen Vacancies	98
5.5	Hafnium Vacancies	103
5.6	V_{Hf} in cubic and tetragonal Hafnia	108
5.7	Conclusions	112
6	ZnO:Co	115
6.1	Introduction	115
6.2	Computational setup	117
6.3	Defect free ZnO	119
6.4	Co in ZnO	121

6.5	Native defects	124
6.6	Donor-Co interactions	128
6.6.1	Zn _I -Co interaction	128
6.6.2	V _O -Co interaction	130
6.6.3	H _I -Co interaction	133
6.7	Magnetic coupling	135
6.7.1	<i>far</i> Configurations	136
6.7.2	<i>near</i> Configurations	138
6.8	Discussion on RTF	144
6.9	Conclusions	146
 III Electronic transport calculations		149
7	Transport through Mn₁₂ SMMs	151
7.1	Introduction	151
7.2	Structural properties	152
7.3	Computational setup	154
7.4	Ground state properties	155
7.4.1	Electronic structure of Mn ₁₂ f	156
7.4.2	Electronic structure of Mn ₁₂ TE	159
7.5	Transport properties	162
7.5.1	Zero bias transmission	162
7.5.2	I-V Characteristics	164
7.6	Conclusions	171
8	Conclusions and future work	173
A	Publications stemming from this work	199

List of Figures

2.1	All electron and pseudo wavefunctions	28
2.2	Device setup in SMEAGOL	37
3.1	Localized molecular orbitals	52
3.2	Response potentials	54
3.3	Slater potential plots	55
4.1	α and the band gaps of solids	73
4.2	Band structure of ZnO	76
4.3	Band structure of GaN	77
4.4	Band structure of MnO	78
4.5	HOMO eigenvalues and ionization potentials	81
4.6	HOMO eigenvalues and electron affinities	83
4.7	Charging of C_2H_4	85
5.1	Band structure and DOS for HfO_2	97
5.2	Local geometry at V_O	98
5.3	PDOS for V_O	99
5.4	V_O density iso-surfaces	100
5.5	DOS for V_O with extra doping	101
5.6	DOS for V_{Hf}	103
5.7	V_{Hf} hole density iso-surface	104
5.8	Magnetic moment localization plot	105
5.9	Magnetic moment on V_{Hf} against O ion distance	106
5.10	Spin states schematic	108
5.11	Hafnium Vacancy in tetragonal Hafnium	109
5.12	Hafnium Vacancy in cubic Hafnia	110
5.13	Magnetic moment decay with relaxation	111
6.1	Bands and PDOS for ZnO	120
6.2	PDOS for ZnO:Co	122
6.3	LDOS for V_O	125
6.4	Band structure of ZnO with native defects	126
6.5	Local geometry around Zn_I and H_I	127

6.6	Co and Zn _I interaction	129
6.7	Co and V _O interaction	131
6.8	LDOS for Co+V _O	132
6.9	Co and H _I interaction	133
6.10	supercells for first NN Co-Co coupling	137
6.11	<i>far</i> configurations summary	137
6.12	supercells for <i>near</i> configurations with Zn _I	138
6.13	supercells for <i>near</i> configurations with V _O and H _I	139
6.14	PDOS for two CoV centres	141
6.15	Schematic for CoV defect state	142
6.16	<i>near</i> configurations summary	143
6.17	phase diagram for ZnO:Co	145
7.1	The Mn ₁₂ TE molecule	153
7.2	PDOS for Mn ₁₂ f	157
7.3	Geometry of Mn ₁₂ f	158
7.4	PDOS for Mn ₁₂ TE	159
7.5	Mn ₁₂ TE Device Region	160
7.6	Mn ₁₂ TE Zero Bias	163
7.7	Mn ₁₂ TE Current-Voltage curves	165
7.8	Mn ₁₂ TE Transmission Vs Positive Bias	166
7.9	Mn ₁₂ TE Spatial charge distribution	168
7.10	Mn ₁₂ TE Transmission Vs Negative Bias	169

List of Tables

2.1	Scaling of <i>ab initio</i> methods	17
3.1	polarizabilities with local functionals	52
3.2	polarizabilities with SIC-DFT	53
3.3	polarizabilities with X-Only SIC-DFT	53
3.4	polarizabilities with the Slater potential	55
4.1	Comparison between KS and experimental gaps	74
4.2	Coparison of valence band widths	75
4.3	Ionization potentials and HOMO eigenvalues	80
4.4	Electron affinities and HOMO eigenvalues	82
4.5	Orbital energies -I	84
4.6	Orbital energies -II	84
4.7	HOMO-LUMO gaps in ASIC	87
5.1	Electronic configuration and basis set	96
5.2	Lattice parameters	98
5.3	Fix-spin energy differences	106
5.4	Magnetic coupling energies	107
5.5	Mülliken analysis of O ions	112
6.1	Electronic Configuration and Basis set	118
6.2	Cell parameters	119
6.3	Table of Magnetic coupling energies	135
7.1	Electronic Configuration and Basis set	154
7.2	Mülliken analysis of Mn ions	157

Chapter 1

General Introduction

Over the last two to three decades, the miniaturization of semiconductor based micro electronic devices achieved through advances in device fabrication technology has powered the growth of the information technology industry. Functional elements in state of the art silicon based microchips currently extend a few tens of nanometers in size and even smaller devices are envisaged for the near future. However the current trends in miniaturization cannot be sustained indefinitely. As devices get smaller, stochastic as well as quantum effects would inevitably start to have an increasing effect on the device properties making them less reliable. Problems such as leakage currents due to electron tunneling across ultra-thin SiO_2 layers in sub-10-nm metal-oxide-semiconductor transistors and the superparamagnetic limit in magnetic recording media are well known. While microelectronic devices will continue to improve into the immediate future, alternative paradigms such as *spintronics* [1, 2, 3] and *molecular electronics* [4, 5, 6] with the potential to replace conventional silicon based technologies are becoming increasingly more relevant.

The field of spintronics or spin-electronics is based on the idea of a new type of device that relies on the electron's intrinsic 'spin' degree of freedom to perform its function. More generally such devices would exploit both the charge and the spin states of electrons in conjunction to exhibit a whole range of exotic new functionalities. Since its inception in the late 1980s with the discovery of the Giant magnetoresistance(GMR) effect [7, 8], the field of spintronics has grown rapidly and is currently the single most active area of research in solid state physics. The first generation of spintronic devices were based on the giant magnetoresistance (GMR) effect which manifests as a significant change in the electrical resistance of the device in the presence of an applied magnetic field. These GMR based devices form the functional elements of modern hard drives and have revolutionized

the magnetic data storage industry. More sophisticated magnetoresistive random access memories (MRAMS) [3] are on the verge of mass production. However, both GMR devices and MRAMS are built from ferromagnetic metals and this class of spintronic devices would be restricted to applications in the data storage industry. On the other hand, if one could build a spintronic device from a semiconductor, the possibilities are endless. Semiconductor spintronic devices if integrated into currently existing semiconductor technologies would lead to a whole new breed of multi-functional devices controllable by a wide variety of external impulses such as optical, electrical and magnetic signals. Novel spintronic devices such as the *spin transistor* [3] with the ability to combine logic and memory function while being controlled either by electric or magnetic signals have been conceived. These devices also offer other advantages over conventional semiconductor devices such as non-volatility, lower power consumption, higher speeds and greater integration densities. Furthermore spintronic devices also hold the key to the practical implementation of futuristic quantum computing algorithms that might lead to a new era of quantum information.

1.1 Dilute magnetic semiconductors

In order to be able to realize the wide range of possible spin-dependent phenomena in semiconductor systems, effective and efficient means of electrically injecting strongly spin-polarized currents into semiconductors are needed [3]. *Dilute Magnetic Semiconductors* (DMS), in which a small percentage of magnetic transition metal atoms are introduced into a non-magnetic host semiconductor lattice, are in principle ideally suited as spin-polarized carrier sources for spin injection as they can be easily integrated into semiconductor devices. However, the search for the ideal DMS material that would exhibit a ferro-magnetic Curie temperature (T_c) above 300K while simultaneously preserving the desirable properties of the host semi-conductor is ongoing [9, 10, 11]. The prototypical (III-V) DMS material GaAs:Mn has been exhaustively studied, but the fact that the T_c in this material could not be pushed up above ~ 200 K [12, 13] has led physicists to look towards oxide DMS materials following theoretical predictions [14] that Mn doped p-type ZnO would exhibit a T_c above room temperature. A great amount of experimental and theoretical effort has since been put into studying a wide variety of transition metal (TM) doped oxide semiconductors such as ZnO, TiO₂, SnO₂, Cu₂O, In₂O₃ etc [11]. In particular, Co doped ZnO (ZnO:Co) has also been investigated actively over the past five to six years following early reports from Ueda *et al.* [15], of above 300K ferromagnetism in the ma-

terial. Unlike GaAs:Mn however, the Oxide based DMS have proven to be a lot more difficult to understand [11]. While signatures of ferromagnetic behaviour at and above 300K have been widely reported, the origin of ferromagnetism in these oxide based DMS is still actively debated. Conflicting reports of paramagnetic or even spinglass behavior in these materials are also abundant (see reviews [9], [10] and references therein). Issues such as in-homogeneity in the distribution of the magnetic dopants, the presence of secondary phases, contaminants and even experimental measurement artefacts have been discussed in this regard [11]. One of the fundamental problems with ferromagnetism in TM doped oxide DMS materials is that the well established models for ferromagnetism in conventional magnetic oxides such as $\alpha\text{Fe}_2\text{O}_3$, $\text{Y}_3\text{Fe}_5\text{O}_{12}$ or DMS materials such as GaAs:Mn or InMn:As cannot be invoked in their case. Within the traditional models for magnetism in solids, ferromagnetism can result via one of two broad mechanisms: (1) In insulating compounds, localized moments arising from partially filled d or f sub-shells of magnetic ions couple via short range super exchange [16] or double exchange [17] type interactions. High temperature magnetic order in this class of materials however requires a high concentration of magnetic ions with strong inter-ion magnetic coupling. (2) In metallic or semi-conducting systems, the interaction between localized spins and itinerant electrons can lead to the formation of narrow spin split bands with the carriers mediating the ferromagnetism as in the RKKY [18] or the mean-field Zener model [19, 14]. In particular, among the well established magnetic semi-conductors, two slightly different classes can be identified. In the *concentrated* magnetic semiconductors such as the Eu monochalcogenides [20] (EuO, EuS, EuSe), the exchange interaction between the localized 4f states and the empty 6s/5d conduction band states, produces an n-type semiconductor with a spin-split conduction band. Meanwhile, in the p-type III-V *dilute* magnetic semiconductor materials [21] such as GaAs:Mn and InAs:Mn, a spin-split valence band is formed because of the interaction between the 3d states of the Mn dopants and the semi-delocalized 4p-hole states at the top of the valence band. Crucially, one hole state is created at the top of the valence band for each Mn dopant and so the carrier concentrations in these materials are enormous by normal semiconductor standards. The dilute TM doped oxides differ from the III-V DMS systems in two aspects. Firstly, the oxides are usually strongly n-type which means the carriers are confined to the conduction band and secondly the introduction of TM dopants by itself does not create extra carriers. Therefore the carriers that interact with the magnetic dopant must be derived from other donor defects in the system. In this scenario the donor impurity band exchange (DIBE) [22] model relevant in highly defective systems was pro-

posed as a possible mechanism for ferromagnetism in the dilute magnetic oxides. Within this model, hydrogenic donor orbitals overlapping TM dopant cation sites are spin-split forming bound magnetic polarons. As the concentration of the donors is increased beyond a certain critical threshold x_d at which the overlapping polarons percolate throughout the sample, global ferromagnetism results [23]. However, the critical temperatures (T_c) predicted within this model for realistic parameters are in the range of $\sim 10\text{K}$ and therefore cannot account for the observed ferromagnetic signatures above 300K . Still, experimental trends accumulated over the years suggest a correlation between the presence of donor type defects and ferromagnetism in these systems. In particular, annealing in vacuum or oxygen deficient atmospheres [24] as well as exposing the samples to Zn vapours [25] or even Hydrogen [26] is seen to boost the ferromagnetism. In order to make sense of the various experimental observations in these dilute TM doped oxides, an in-depth investigation of the interaction between the dopant ions and the various donor defects in these oxides needs to be undertaken. If the TM doped oxides are to be established as genuine dilute magnetic semiconductors then a spin-split impurity band with carriers that mediate the ferromagnetism between the TM ions needs to be identified in these materials [11].

A different problem closely related to ferromagnetism in dilute TM doped oxides is that of ferromagnetism in semiconductors and insulators without any magnetic ions or dopants. This phenomenon dubbed d^0 ferromagnetism [27] or *phantom* ferromagnetism has received wide spread attention in the recent past following numerous reports of above room temperature ferromagnetic signals being detected in systems which should not be ferromagnetic. Materials such as irradiated graphite, nonstoichiometric CaB_6 and thin films of HfO_2 have been reported in this class of *phantom* ferromagnetic materials [27]. Observed experimental trends point to intrinsic defects in these materials as being responsible for the ferromagnetic signals. However these findings pose a challenge to our fundamental understanding of magnetism as several questions regarding the identity of the intrinsic defects and the mechanisms responsible for creating both the local magnetic moments on the defects as well as the inter defect coupling remain unanswered. In the case of HfO_2 , a mechanism similar to the DIBE model was proposed where by oxygen vacancies in HfO_2 would lead to the formation of partially occupied Hf-5d orbitals in the conduction band which would then spin-split due to inter ionic exchange interactions [28]. To date however, no direct experimental evidence of a spin-split conduction band in ferromagnetic HfO_2 has emerged. In the absence of any phenomenological model that can readily explain the ferromagnetism in these systems, one can approach the problem in a bottom-up manner within

the $m - J$ paradigm for ferromagnetism and look for the various individual contributing factors necessary for long range order. Thus defect centres which can give rise to local magnetic moments need to be identified. Then, the sign of the magnetic coupling as well as the variation of its strength with the distance between individual defect centres needs to be determined. Last but not least the concentration of the defect centres needed for the magnetic interactions to percolate through out the system needs to be established. In some cases the observed phenomena might arise solely from surface or interfacial regions at which the defect composition might be different from that in the bulk of the material. The fact that most instances of d^0 ferromagnetism occur in thin film samples [27] points to that possibility. Therefore surface sensitive characterization techniques need to be employed in studying these systems.

While careful experiments can indeed lead to a full understand of the materials discussed above, it is often difficult to control and characterize precisely the defect composition as well as the homogeneity of defect distribution in experimental samples. In such a scenario, theoretical first principles electronic structure calculations emerge as a valuable tool to investigate the electronic structure these materials at a very fundamental level. The availability of high speed computers and sophisticated theoretical tools such as Density functional theory (DFT) [29] make realistic simulations of Dilute magnetic semiconductors feasible. The GaAs:Mn DMS system was thoroughly investigated using theoretical DFT simulations and the mechanism for the observed ferromagnetism in GaAs:Mn is now relatively well established (c.f [30] and references therein). However the oxide DMS materials such as ZnO:Co have proven to be problematic even for theoretical studies using conventional Density functional methods. Approximate exchange-correlation (xc) functionals routinely employed in density functional calculations fail to describe the wide-gap transition metal oxides accurately often severely underestimating the band gap in these systems and in some cases even predicting metallic ground states [31]. One of the main reasons for the failure of approximate xc functionals in this regard is the presence of the spurious self interaction error (SIE) [32] which loosely described means that an electron feels part of its own electrostatic potential and repels itself. Thus the energy levels of localized d and f electrons for which the SIE is strongest, are too high resulting in an erroneous description of these systems. Therefore one must employ more sophisticated xc functionals that are free of the SIE in order to be able to adequately describe the oxide based DMS materials. Among the main objectives of the research work presented in this thesis is the investigation of density functional methods capable of describing these problematic DMS systems and

then to study the materials themselves in an effort to explain the observed behaviour.

1.2 Electron transport through magnetic molecules

The study of electronic transport through nanoscale devices is a fascinating new branch of modern solid state science. Initiated at the time when the first scanning tunneling microscopes (STMs) [33] appeared this field has seen rapid growth mainly because of its potential relevance to a multitude of technological disciplines such as nano-scale electronics, genetic medicine and chemical/biological detection and sensing. Because of the complexities one encounters at the nanoscale, molecular electronics presents its own set of challenges both from a fundamental theoretical perspective and a device engineering perspective. The rules of Ohmic transport valid in all metallic and semiconductor based devices breakdown at the nanoscopic level and transport across individual molecules or other atomic scale structures is strongly influenced by quantum mechanical effects. Also, device fabrication is only possible under extremely controlled conditions and most experimental setups of today come with a certain degree of uncertainty over the precise geometry of the device. The standard set up for a molecular electronics device is to sandwich either a single molecule or an organic monolayer between metallic electrodes. This setup was first proposed by Aviran and Ratner [4], but was accomplished experimentally only much later by Reed and co-workers [34]. Molecular devices have since been shown to exhibit a multitude of interesting features in their current-voltage characteristics such as negative differential resistance [35] and rectification [36]. Also fully functional molecular transistor type devices [37], logic gates [38, 39] and memories [40] have been realized in experiments and next generation computing and data storage technologies based on such nanoscale devices have been proposed [41, 42]. However, molecular electronics is still very much in its infancy and although the large scale production of fully functional molecular devices remains some time away, there is a growing body of experimental, theoretical and computational work investigating the wide range of challenges posed by the field.

In recent times, the possibility of making electronic devices using organic molecules has been the focus of intense research as the field of molecular electronics [4, 5, 6] aims to provide a viable alternative to conventional semiconductor electronics. Organic electronic devices offer the advantages of low-cost, low-temperature production through chemical methods, instead of expensive high-temperature solid-state growth (e.g. molecular beam epitaxy) and patterning (lithography) techniques. Furthermore, the rich chemistry of or-

ganic systems affords endless possibilities of chemical synthesis, end-group and side-chain engineering to conceptualize new kinds of devices and tune device properties. Of particular relevance to the data storage industry in the on going effort towards ever increasing storage densities are *molecular spintronics* devices. Prototypical in this class of devices are molecular spin valves [43, 44] which essentially comprise of a non-magnetic organic tunneling layer of molecules sandwiched between magnetic leads. Magnetoresistance effects of upto about 18% have been demonstrated in these devices [43, 44]. However a different type of stand-alone molecular spintronic device based on a novel class of molecules called *Single molecule magnets* (SMMs) or *molecular nanomagnets* [45, 46] holds much promise. SMMs are usually formed from a central cluster of transition metal and ligand ions surrounded by carefully engineered organic functional groups and are characterized by a non-zero total spin on the molecule. They exhibit remarkable physical properties such magnetic hysteresis [45] with entirely intra-molecular origins and magnetization reversal in external fields due to quantum tunneling [47] between different spin states of the molecule. A variety of such SMMs have been widely studied since the mid 1990s both from a fundamental theoretical perspective as well as from the point of view of spintronic applications [46]. In particular, molecules formed from a cluster of 12 Mn ions (Mn_{12}), have received a lot of attention. These Mn_{12} molecules act as isolated spin systems with a high local spin ($S = 10$) and a large intrinsic magnetic anisotropy barrier [45]. If such molecules could be engineered so that the blocking temperature for their magnetization is above room temperature, they could potentially be used as individual “bits” for data storage at terabit/in² densities or by suitably exploiting their exotic spin physics, even as “qubits” for quantum computing. Recently such molecules were successfully deposited as extended arrays on gold surfaces with the possibility of individually addressing them in scanning probe microscopy experiments [48]. One of the questions with direct related to these SMMs being used for data storage is whether the electrical read out from these molecules is different for different spin states of the molecule. Thus if information is written to the molecule in the form of a particular spin state, can it then be “read” as an electrical signal? In this thesis we present the first *ab initio* theoretical electronic transport calculations on these Mn_{12} based SMMs that attempt to answer the question.

1.3 Dissertation layout

The main focus of the work presented in this thesis is to study using first principles theoretical calculations, some problems of current interest in the field of spintronics. Some widely debated issues regarding the phenomenon of ferromagnetism in dilute and disordered wide-gap oxides are addressed. Advanced density functional theory (DFT) based approximations, necessary to accurately model such wide-gap oxides and other materials that are problematic for conventional DFT methods, are introduced and their implementation within an efficient numerical DFT platform is discussed. The electronic transport properties, focusing in particular on the interplay between charge transport and the intramolecular spin degrees of freedom of a prototypical Mn_{12} molecular magnet are also presented.

For clarity, the thesis is mainly divided into three parts. In part I consisting of chapters 2 to 4, the theoretical tools employed for various first principles calculations carried out during the course of this work are discussed. Most of the computational coding and implementation work carried out during the course of this research work is presented in this part.

In chapter 2 we provide a general introduction to the many electron problem and briefly discuss some of the ways of tackling it. An overview of Kohn-Sham density functional theory [49] is then presented followed by a quick review of some of the more popular numerical approaches to practical density functional calculations. We then discuss in some detail the numerical framework within the density functional code SIESTA. The last section in chapter 2 presents the general scheme for non equilibrium Green's functions (NEGF) [50] based electronic transport calculations as implemented in the SMEAGOL [51] code.

Chapter 3 presents a discussion on orbital dependent exchange correlation functionals [52]. In particular, the optimized effective potential method is reviewed with emphasis on the Krieger-Li-Iafrate approximation [53]. The exact exchange functional [52] and self interaction corrected (SIC) [52] approximate functionals are discussed in this context and some details of their implementation in the SIESTA [54] code are presented. As an application of the methods developed, the long standing problem of polymer polarizabilities in density functional theory is revisited and the performance of SIC functionals is analyzed in that regard.

In chapter 4, a computationally efficient approximate self interaction correction scheme based on atomic orbital based correction terms is presented. The implementation of this approximate scheme (abbreviated ASIC) [55] within the SIESTA code is also discussed in

detail. The scheme is also compared to other methods such as the fully self consistent SIC scheme [32] and the LDA+ U method [31] for treating strongly correlated systems. The performance of ASIC in describing the electronic structure of various molecular as well as solid state systems is then analyzed.

Part II of the thesis consisting of chapters 5 and 6, deals mainly with materials simulations investigating ferromagnetism in wide-gap oxide systems.

In chapter 5 the problem of *phantom* ferromagnetism in un-doped Hafnium Oxide (HfO_2) [28] is investigated. First the electronic structure of oxygen vacancy defects is discussed and the effect of introducing additional electron or hole doping into n-type HfO_2 is also studied. Then, the case of p-type HfO_2 is considered by looking at Hafnium vacancies. Some interesting differences in the electronic structure of Hafnium vacancies in the three different crystalline phases of HfO_2 are discussed.

Chapter 6 presents a detailed study of the role of native n-type donor defects in the ferromagnetism of Cobalt doped ZnO (ZnO:Co). The ASIC method developed in chapter 4 is employed. Defects such as oxygen vacancies (V_{O}), interstitial Zn (Zn_{I}) and Hydrogen (H_{I}) are analyzed for their effect on the electronic structure of substitutional Co ions. Magnetic interactions between Co ions in clustered as well as spatially well separated configurations are calculated in the presence of donor defects. A model based on donor and dopant ion pair complexes capable of explaining the observed experimental trends in ZnO:Co is proposed.

Part III of the dissertation is still somewhat related to magnetism but in the context of electronic transport.

In Chapter 7 we study the electronic transport properties of a prototypical Mn_{12} based magnetic molecule functionalized by organic thio-ether functional groups [48] and attached to gold electrodes. Firstly the electronic structure of the molecule is studied using a semi-local approximate GGA exchange correlation functional [56] as well as the more advanced LDA+ U method [31]. Differences in the electronic structure of the molecule in the two approaches are discussed. Current-voltage characteristics as well as transmission coefficients calculated using the SMEAGOL code [51] are then presented. In particular, the question of whether the local spin configuration of the molecule effects its current-voltage characteristics, is addressed.

Finally, towards the end of the dissertation we draw some general conclusions on the work presented in this thesis. We also highlight some issues and questions related to the topics discussed in this work that need further theoretical investigation.

Part I

Theoretical tools



Chapter 2

Theoretical and Numerical framework

2.1 The Quantum Many body problem

The systems of interest in condensed matter physics and quantum chemistry consist essentially of an ensemble of electrons and nuclei interacting via Coulombic forces. At the molecular level or indeed at the nano-scale in condensed matter, one wishes to describe the collective structure and mechanics of systems typically ranging between a few tens to several hundreds of electrons and nuclei. However, no analytic solution exists for the quantum many body problem involving any more than two particles and one must resort to solving the problem numerically with the aid of high speed computers. Furthermore even exact numerical solutions are computationally prohibitive except in the simplest of cases involving only a few electrons. One is therefore forced to rely upon useful approximations that help to simplify the problem as much as possible while not sacrificing the accuracy of the final solution. Since electrons in most of the lighter elements and the chemically active subset of valence electrons in heavier elements travel at speeds much slower than the speed of light, they can be treated as non-relativistic. The nuclei meanwhile are much slower than the electrons and can in fact be treated as classical particles to a good approximation. When one is interested in the steady state solution of a quantum system one must solve the the time independent Schrödinger equation which takes the form of an eigenvalue problem

$$\hat{H}\Psi = E\Psi \tag{2.1}$$

where in \hat{H} is the Hamiltonian operator, Ψ is the many body wave function and E is the energy of the system. For a non-relativistic Coulomb system consisting of a set of N_e electrons each of mass m_e , moving under the influence of N_N nuclei with masses Z_I and position coordinates \mathbf{R}_I , the full Hamiltonian operator takes the form

$$\begin{aligned} \hat{H} = & \sum_i^{N_e} -\frac{\hbar^2}{2m_e} \nabla_{\mathbf{r}_i}^2 + \sum_I^{N_N} -\frac{\hbar^2}{2M_I} \nabla_{\mathbf{R}_I}^2 + \frac{1}{2} \sum_{I \neq J}^{N_N} \frac{e^2 Z_I Z_J}{|\mathbf{R}_I - \mathbf{R}_J|} \\ & - \sum_{i,I}^{N_e, N_N} \frac{e^2 Z_I}{|\mathbf{r}_i - \mathbf{R}_I|} + \frac{1}{2} \sum_{i \neq j}^{N_e} \frac{e^2}{|\mathbf{r}_i - \mathbf{r}_j|} \end{aligned} \quad (2.2)$$

where the first and second terms are the electronic and nuclear kinetic energy respectively. The third term is the Coulombic interaction between the nuclei, the fourth term is the Coulombic attraction between the electrons and nuclei while the fifth term is the electron-electron interaction. \mathbf{r}_i denotes the position of the i^{th} electron. The many-body wave function Ψ in equation 2.1 is a complex object being a function of the coordinates of all the electrons and nuclei in the system, thus

$$\Psi = \Psi(\mathbf{x}_1, \mathbf{x}_2, \dots, \mathbf{x}_i, \dots, \mathbf{x}_{N_e}, \mathbf{X}_1, \mathbf{X}_2, \dots, \mathbf{X}_I, \dots, \mathbf{X}_{N_N}) \quad (2.3)$$

Note that the electronic (nuclear) coordinates $\{\mathbf{x}_i\}$ ($\{\mathbf{X}_I\}$) include both the position coordinates $\{\mathbf{r}_i\}$ ($\{\mathbf{R}_I\}$) and the spin coordinates $\{\mathbf{s}_i\}$ ($\{\mathbf{S}_I\}$). A major step towards simplifying this object is encompassed in the Born-Oppenheimer (BO) approximation [57]. As the nuclear masses are much heavier than the electron mass, and since the nuclei usually move much slower than the electrons, nuclear motion occurs over a much longer time scale in comparison to electronic motion. In the reference frame of the electrons, the nuclei are almost stationary and one can therefore separate the electronic and nuclear degrees of freedom.

$$\Psi = \Psi^e(\{\mathbf{x}_i\}) \otimes \Psi^N(\{\mathbf{X}_I\}) \quad (2.4)$$

Thus one only needs to worry about the electronic degrees of freedom $\{\mathbf{x}_i\}$ while the nuclear coordinates $\{\mathbf{X}_I\}$ enter merely as parameters in the electronic Hamiltonian.

$$\hat{H}^e = \hat{T}(\{\mathbf{x}_i\}) + \hat{V}_{ee}(\{\mathbf{x}_i\}) + \hat{V}_{ext}(\{\mathbf{x}_i\}; \{\mathbf{X}_I\}) \quad (2.5)$$

where

$$\hat{T}(\{\mathbf{x}_i\}) = \sum_i^{N_e} \frac{-\hbar^2}{2m_e} \nabla_{\mathbf{r}_i}^2 \quad (2.6)$$

$$\hat{V}_{ee}(\{\mathbf{x}_i\}) = \frac{1}{2} \sum_{i \neq j}^{N_e} \frac{e^2}{|\mathbf{r}_i - \mathbf{r}_j|} \quad (2.7)$$

$$\hat{V}_{ext}(\{\mathbf{x}_i\}) = \sum_{i,I}^{N_e, N_N} \frac{e^2 Z_I}{|\mathbf{r}_i - \mathbf{R}_I|} \quad (2.8)$$

Note that \hat{V}_{ext} can be easily generalized to also include additional external electric and magnetic fields. Thus within the BO approximation, the Schrödinger equation for the electronic system reduces to

$$\hat{H}^e \Psi^e = E(\{\mathbf{X}_I\}) \Psi^e \quad (2.9)$$

and the energy of the electronic system is obtained as a parametric function of the nuclear coordinates.

2.2 Wavefunction methods

In spite of the considerable simplification afforded by the BO approximation, the electronic Hamiltonian in equation (2.5) still represents an interacting many-body problem whose solution is not a trivial task. The presence of the electron-electron interaction \hat{V}_{ee} couples the coordinates of all the electrons and the many electron wavefunction cannot be decomposed into a product of single particle wavefunctions. Indeed if we consider the special case of non-interacting electrons, the electronic Hamiltonian for N electrons reduces to a sum of one particle Hamiltonians

$$\hat{H}_{non} = \sum_i^N \left[\frac{-\hbar^2}{2m_e} \nabla_{\mathbf{r}}^2 + \sum_I^{N_N} \frac{e^2 Z_I}{|\mathbf{r} - \mathbf{R}_I|} \right] \quad (2.10)$$

and the eigenfunctions Φ of \hat{H}_{non} satisfying

$$\hat{H}_{non} \Phi = E_{non} \Phi \quad (2.11)$$

can be written as an anti-symmetrized product or Slater determinant of single particle wavefunctions ϕ

$$\Phi = \frac{1}{\sqrt{N!}} \begin{vmatrix} \phi_1(\mathbf{x}_1) & \phi_2(\mathbf{x}_1) & \dots & \phi_N(\mathbf{x}_1) \\ \phi_1(\mathbf{x}_2) & \phi_2(\mathbf{x}_2) & \dots & \phi_N(\mathbf{x}_2) \\ \vdots & \vdots & \ddots & \vdots \\ \phi_1(\mathbf{x}_N) & \phi_2(\mathbf{x}_N) & \dots & \phi_N(\mathbf{x}_N) \end{vmatrix} = \frac{1}{\sqrt{N!}} \det[\phi_i(\mathbf{x}_j)] \quad (2.12)$$

This takes into account the Pauli exclusion principle as the electrons are fermions. The total energy in this case is simply a sum over the eigenvalues of the N occupied single particle states and the total electron density is given by a sum over the N single particle densities $|\phi'_i(\mathbf{r})|^2$ where ϕ' represents the spatial part of the wavefunction ϕ . For the more general interacting problem the Slater-determinant eigenstates of \hat{H}_{non} form a complete orthonormal basis in which to expand the many-body wavefunction.

The Schrödinger equation (2.9) for the ground state of a many electron system can be mapped onto the wavefunction variational principle [59] which provides the following prescription: to obtain the ground state energy and wavefunction, find the extremal point of $\langle \Psi | H | \Psi \rangle$ subject to the constraint $\langle \Psi | \Psi \rangle = 1$, i.e., solve the following:

$$\delta \left\{ \frac{\langle \Psi | H | \Psi \rangle}{\langle \Psi | \Psi \rangle} \right\} = 0 \quad (2.13)$$

The Rayleigh-Ritz method then attempts to find the extrema of H within a restricted space of wavefunctions. One of the earliest and more popular methods based on the above is the Hartree-Fock (HF) approximation [57, 58] where in a single Slater determinant wavefunction Φ that minimizes $\langle \Phi | H | \Phi \rangle / \langle \Phi | \Phi \rangle$ is sought. The HF approximation describes light atoms and small molecules adequately well and was widely used in the quantum chemistry community during the early years but falls short of the desired chemical accuracy. Due to the single-determinant nature of the ground state wavefunction, HF theory cannot describe electron correlations and one must seek to incorporate the correlation energy through other means. In quantum chemistry calculations Moller-Plesset perturbation theory (MP2,MP4) [60] and configuration interaction (CI)[60] are among the most commonly used methods to calculate the correlation energy. In solid state physics, strong correlations are handled by Green's Function (GF) methods. Quantum Monte Carlo [61] also offers an alternate method to directly tackle the many-particle wavefunction. However all of the above methods are computationally demanding and exhibit poor scaling with system

size which makes them prohibitive for large systems. Table 2.1 lists the typical scaling behaviour with number of orbitals N for some commonly used *ab initio* methods.

Hartree Fock	$N^3 - N^4$
MP2	N^5
MP4	N^6
Configuration Interaction	$N^6 - N^{10}$
Density Functional Theory	$N^2 - N^3$

Table 2.1: The typical scaling behaviour with number of orbitals N for some commonly used *ab initio* methods is listed

For large scale molecular and solid state calculations where one needs to handle extended systems with hundreds of atoms, a completely different approach that significantly reduces the number of variables involved is required. For the restricted but all important class of ground state properties Density Functional theory (DFT) achieves exactly that by replacing the many-body wavefunction $\Psi(\mathbf{x}_1, \mathbf{x}_2, \dots, \mathbf{x}_N)$ with the electron density $n(\mathbf{r})$ as the basic quantity of interest.

2.3 Density Functional theory

The foundations of modern DFT lie in the celebrated theorem of 1964 due to Hohenberg and Kohn (HK) [62] in which they demonstrate that the problem of finding the many electron wavefunction can be reduced to that of calculating just the equilibrium charge density $n(\mathbf{r})$. The charge density $n(\mathbf{r})$ of an N electron system is defined by

$$n^\sigma(\mathbf{r}) = N \sum_{\sigma_2, \sigma_3, \dots, \sigma_N} \int d\mathbf{r}_2 d\mathbf{r}_3 \dots d\mathbf{r}_N |\Psi(\mathbf{x}_1, \mathbf{x}_2, \dots, \mathbf{x}_N)|^2 \quad (2.14)$$

where $\sigma \in \{\uparrow, \downarrow\}$ indicates the spin-coordinate and

$$n(\mathbf{r}) = n^\uparrow(\mathbf{r}) + n^\downarrow \quad (2.15)$$

provided

$$\langle \Psi | \Psi \rangle = \sum_{\sigma_1, \dots, \sigma_N} \int d\mathbf{r}_1, \dots, d\mathbf{r}_N |\Psi(\mathbf{x}_1, \dots, \mathbf{x}_N)|^2 = 1 \quad (2.16)$$

Also

$$\sum_{\sigma} \int n^\sigma(\mathbf{r}) d\mathbf{r} = N \quad (2.17)$$

2.3.1 The Hohenberg-Kohn theorem

The HK theorem can be summarized in the following three statements.

1. The ground-state density $n_0(\mathbf{r})$ uniquely determines the external potential $V = V[n_0]$ as well as the ground-state wave function $\Psi[n_0]$. Therefore, any ground-state observable of a many-particle system is a functional of its ground-state density.
2. The total energy functional for a given external potential V_0

$$E_{V_0}[n] = \langle \Psi[n] | \hat{T} + \hat{V}_{ee} + \hat{V}_0 | \Psi[n] \rangle \quad (2.18)$$

is equal to the ground-state energy E_0 if and only if the ground-state density n_0 is used in equation 2.18. For all other densities $n \neq n_0$ the following holds

$$E_0 < E_{V_0}[n] \quad (2.19)$$

Thus the ground-state energy is variational with respect to the density and the exact ground-state density (n_0) and energy (E_0) can be determined by solving the Euler-Lagrange equation

$$\frac{\delta}{\delta n(\mathbf{r})} E_{V_0}[n] = 0 \quad (2.20)$$

3. The functional

$$F[n] = \langle \Psi[n] | \hat{T} + \hat{V}_{ee} | \Psi[n] \rangle \quad (2.21)$$

is a universal functional of the density for all systems as it is independent of the external potential defining a particular system and only depends upon the form of the particle-particle interaction V_{ee} . Note that the HK theorem is valid for any given form of the particle-particle interaction V_{ee} and in particular for the trivial case $V_{ee} = 0$ defining non-interacting systems.

2.3.2 The Kohn-Sham scheme

Although the HK theorem establishes a one to one mapping between the external potential V_0 and the ground state density n_0 , it does not prescribe a way to actually obtain one quantity given the other and vice versa. However, in 1965, Kohn and Sham [63] proposed a clever way of mapping the interacting many body problem onto a system of non-interacting particles moving under the influence of a fictitious effective potential that produces the same ground state density and total energy as the interacting system. It is

this mapping that forms the basis of all modern day practical DFT calculations. Thus in the KS formalism one deals with a non-interacting Hamiltonian of the form

$$\hat{H}^{KS} = \hat{T} + \hat{V}_s \quad (2.22)$$

where $V_s(\mathbf{r}) = V_s[n](\mathbf{r})$ is the local KS effective single-particle potential that is uniquely determined by the ground state density $n(\mathbf{r})$. The KS orbitals are the one-particle orbitals satisfying a set of one-particle Schrödinger like equations known as the KS equations

$$\left[\frac{-\hbar^2}{2m} \nabla^2 + V_s(\mathbf{r}) \right] \psi_i = \varepsilon_i \psi_i \quad (2.23)$$

With $\langle \psi_i | \psi_j \rangle = \delta_{ij}$, the ground state density can be constructed from the occupied subset of KS orbitals as

$$n(\mathbf{r}) = \sum_i |\psi_i(\mathbf{r})|^2 f_i \quad (2.24)$$

where $f_i \in [0, 1]$ is the occupation number usually given by $f_i = F(\varepsilon_i - \varepsilon_F)$ where F is the Fermi distribution function and ε_F is the Fermi energy or chemical potential chosen so that

$$\int d\mathbf{r} n(\mathbf{r}) = N \quad (2.25)$$

is satisfied. The total KS energy can be written as

$$E_{KS} = T_s[n] + \int d\mathbf{r} n(\mathbf{r}) V_{ext}(\mathbf{r}) + U_{ee}[n] + E_{xc}[n] \quad (2.26)$$

where

$$T_s[n] = \sum_i \langle \psi_i | \frac{-\hbar^2}{2m} \nabla^2 | \psi_i \rangle f_i \quad (2.27)$$

is the non-interacting kinetic energy which can be shown to be a functional of the density. The second term represents the interaction of the electrons with the external potential V_{ext} . The third term is the electro-static Hartree energy of the electronic density

$$U_{ee}[n] = \frac{1}{2} \int d\mathbf{r} \int d\mathbf{r}' \frac{n(\mathbf{r})n(\mathbf{r}')}{|\mathbf{r} - \mathbf{r}'|} \quad (2.28)$$

The last term is the so-called exchange-correlation (xc) energy E_{xc} , whose exact functional dependence on the electronic density is not known and must be approximated. It is defined to include all the remaining contributions to the total energy that are omitted in the first

three terms of equation 2.26. The KS effective potential $V_s(\mathbf{r})$ is then given by

$$V_s[n](\mathbf{r}) = V_{ext}(r) + \int d\mathbf{r}' \frac{n(\mathbf{r}')}{|\mathbf{r} - \mathbf{r}'|} + V_{xc}[n](\mathbf{r}) \quad (2.29)$$

where $V_{xc}[n](\mathbf{r})$ is the exchange-correlation potential defined as the functional derivative of the exchange-correlation energy with respect to the density

$$V_{xc}[n](\mathbf{r}) = \frac{\delta E_{xc}[n]}{\delta n(\mathbf{r})} \quad (2.30)$$

Note that the KS ground state energy can also be written as

$$E_{KS} = \sum_i \epsilon_i f_i + E_{xc}[n] - \int d\mathbf{r} V_{xc}[n](\mathbf{r}) - \frac{1}{2} \int \frac{n(\mathbf{r})n(\mathbf{r}')}{|\mathbf{r} - \mathbf{r}'|} \quad (2.31)$$

where in the last three terms are referred to as the *double counting* corrections to the first term which represents a sum over the eigenvalues. As mentioned earlier the positions of the atomic nuclei enter only as parameters into the electronic Hamiltonian. Once the KS equations have been solved for a given arrangement of the atomic nuclei one can also extract the forces acting on the (static) nuclei in their current configuration using the Hellman-Feynman theorem [59]. Let \mathbf{r}_i be the position of the i^{th} electron and \mathbf{R}_I the position of the static nucleus I with atomic number Z_I . The BO Hamiltonian

$$\hat{H} = \sum_{i=1}^N \frac{-\hbar^2}{2m} \nabla_{\mathbf{r}_i}^2 + \sum_i \sum_I \frac{-Z_I e^2}{|\mathbf{r}_i - \mathbf{R}_I|} + \frac{1}{2} \sum_i \sum_{j \neq i} \frac{e^2}{|\mathbf{r}_i - \mathbf{r}_j|} + \frac{1}{2} \sum_I \sum_{J \neq I} \frac{Z_I Z_J e^2}{|\mathbf{R}_I - \mathbf{R}_J|} \quad (2.32)$$

only has a parametric dependence on the positions \mathbf{R}_I and the force on nucleus I is simply given by

$$\begin{aligned} \frac{-\partial E}{\partial \mathbf{R}_I} &= \left\langle \Psi \left| - \frac{\partial \hat{H}}{\partial \mathbf{R}_I} \right| \Psi \right\rangle \\ &= \int d\mathbf{r} n(\mathbf{r}) \frac{Z_I e^2 (\mathbf{r} - \mathbf{R}_I)}{|\mathbf{r} - \mathbf{R}_I|^3} + \sum_{J \neq I} \frac{Z_I Z_J e^2 (\mathbf{R}_I - \mathbf{R}_J)}{|\mathbf{R}_I - \mathbf{R}_J|^3} \end{aligned} \quad (2.33)$$

Equation (2.33) can be used to calculate equilibrium geometries of molecules and solids on the BO surface by varying all the \mathbf{R}_I until the energy is a minimum or equivalently $\frac{-\partial E}{\partial \mathbf{R}_I} = 0$.

2.3.3 Approximate density functionals

The KS formalism presented thus far is exact and completely general in that if the exact functional dependence of E_{xc} upon $n(\mathbf{r})$ were known, the method would produce the exact ground-state total energy and density of the interacting N electron problem. However as the exact form of E_{xc} is unknown we resort to various levels of approximations while incorporating the exchange-correlation energy. In fact one might even choose to use an approximate density functional for the non-interacting kinetic energy $T_s[n]$ as one could then bypass the calculation of the KS orbitals entirely and directly minimize the total energy over $n(\mathbf{r})$. From a historical perspective, the so called *first generation* density functional calculations approximated both $T_s[n]$ and $E_{xc}[n]$ as in the Thomas-Fermi model [58]. Most practical KS calculations carried out these days come under the category of *second generation* DFT where in one employs the exact functional for the non-interacting kinetic energy (equation 2.27) and an approximate density functional for the xc energy. The total xc energy is usually a fraction ($\sim 10\%$) of the total energy and therefore errors made in approximating E_{xc} are expected to be less critical although certain physical quantities such as bond dissociation energies in molecules have a crucial dependence on E_{xc} .

Present-day approximate xc functionals provide a satisfactory compromise between accuracy and computational cost for most day to day applications, allowing much larger systems to be treated than traditional *ab initio* methods, while retaining much of their accuracy. The local spin density approximation (LSDA) [63, 64] has been very popular among the solid state community over a long period of time. The LSDA xc energy is given by

$$E_{xc}^{LSDA}[n^\uparrow, n^\downarrow] = \int d\mathbf{r} n(\mathbf{r}) e_{xc}(n^\uparrow, n^\downarrow) \quad (2.34)$$

where $e_{xc}(n^\uparrow, n^\downarrow)$ is the exactly known [65] exchange-correlation energy per particle for a homogenous electron gas of spin densities $n^\uparrow(\mathbf{r}), n^\downarrow(\mathbf{r})$. Note that e_{xc} at any point in space only depends upon the spin densities at that point and E_{xc}^{LSDA} is therefore a local functional. More recently, various flavours of the generalized gradient approximation (GGA) [66, 67, 68, 69] have become popular in quantum chemistry:

$$E_{xc}^{GGA}[n^\uparrow, n^\downarrow] = \int d\mathbf{r} f(n^\uparrow, n^\downarrow, \nabla n^\uparrow, \nabla n^\downarrow) \quad (2.35)$$

The GGAs include gradient corrections to the xc energy that are missing in the LSDA and therefore also require as input the density gradients $\nabla n^\uparrow(\mathbf{r}), \nabla n^\downarrow(\mathbf{r})$ at each point in space.

They fall under the category of semi-local functionals. Both empirical and non-empirical versions of LSDA and GGA exist and the choice of the functional usually varies from application to application. LSDA is known to perform well in the solid state for a number of metallic as well as semiconducting systems and usually reproduces bulk properties such as lattice constants and bulk moduli within a few percent of experiments. GGAs are also sometimes used in simulating bulk materials but are not known to afford any systematic advantages over LSDA with regards to bulk properties and in some cases such as simple metals do not do as well LSDA. However GGAs have had their biggest impact in quantum chemistry in the accurate prediction of bond lengths, molecular geometries and reaction paths in organic systems.

Still, there are several systems both in molecular as well as solid state physics for which LSDA/GGA are either not accurate enough or even fail drastically. Such limitations of LSDA/GGA will be discussed later in the context of orbital-dependent functionals but for now it suffices to note that the search for ever more accurate approximations to E_{xc} is of central importance in DFT. In principle, one way in which to improve over LSDA/GGA is by systematically adding more ingredients to the E_{xc}^{GGA} approximation to produce what are known as meta-GGAs [59]. These are more sophisticated functionals that depend on semi-local and non-local quantities such as the Laplacian of the spin densities $\nabla^2 n^\uparrow, \nabla^2 n^\downarrow$ and the kinetic energy densities $\tau^\uparrow, \tau^\downarrow$ where

$$\tau^\sigma(\mathbf{r}) = \frac{1}{2} \sum_i f_i |\nabla \psi_{i\sigma}(\mathbf{r})|^2 \quad (2.36)$$

The larger the number of such ingredients in a functional, the heavier is its computational cost and in some cases (but not all), the greater is its accuracy. The so called *third generation* of density functionals however, follow a different approach where one employs along with the exact expression for $T_s[n]$ also the exact exchange energy expression which is orbital-dependent:

$$E_x^{exact}[n] = -\frac{1}{2} \sum_{\sigma=\uparrow,\downarrow} \sum_{i,j=1}^{N_{occ}^\sigma} \int d\mathbf{r} \int d\mathbf{r}' \frac{\psi_{i\sigma}^*(\mathbf{r}) \psi_{j\sigma}^*(\mathbf{r}') \psi_{j\sigma}(\mathbf{r}) \psi_{i\sigma}(\mathbf{r}')}{|\mathbf{r} - \mathbf{r}'|} \quad (2.37)$$

Thus only the correlation part of $E_{xc}[n]$ needs to be approximated in this approach. Moreover, the *third generation* functionals allow for both closed form expressions such as the local and semi-local approximations as well as explicitly orbital-dependent functionals for the correlation energy E_c and are thus more flexible in the construction of such approx-

imations. Note that orbital-dependence of E_{xc} in the *third generation* functionals makes the calculation of the xc potential $V_{xc}[n](\mathbf{r})$ more complicated. The general procedure to construct $V_{xc}[n](\mathbf{r})$ for an orbital-dependent E_{xc} functional is called the optimized effective potential (OEP) [70] method or simply the optimized potential method (OPM) [71]. However, the solution of the full OEP integral equation is rather complicated to be practical, and useful approximations to the OEP need to be considered. One such approximation due to Krieger, Li and Iafrate (KLI) [72] is discussed in a later chapter. One can also envisage hybrid density functionals that include a fraction of the exact exchange energy mixed with GGA exchange and correlation. A simple hybrid functional would takes the form

$$E_{xc}^{hyb} = aE_x^{exact} + (1 - a)E_x^{GGA} + E_c^{GGA} \quad (2.38)$$

where the constant a is either fitted empirically or estimated theoretically. A value of $a = 1/4$ is commonly employed for molecules. The most popular among such functionals is the B3LYP [73] functional widely used in quantum chemistry and more recently has also found favour among solid state simulators. For a more indepth review of various functional approximations we direct the reader to reference [59]. An alternate approach to improving upon the local approximations LSDA/GGA is to incorporate certain corrections into these functionals tailored to rectify a subset of problems. Thus one might adopt the explicit Self Interaction Correction (SIC) scheme of Perdew and Zunger[65] which seeks to correct for the spurious self interaction error (SIE) inherent to all local/semi-local approximations to E_{xc} . This scheme also belongs to the general class of orbital-dependent potentials and is discussed in detail in subsequent chapters. For certain so called “strongly correlated” solids in which localized electrons occupying atomic d and f shells are poorly described in LSDA/GGA, the “Hubbard- U ” correction due to Anisimov [74] is also commonly employed. This method commonly referred to as LDA+ U is based on the Hubbard model and involves two parameters viz., the on-site coulomb repulsion parameter U and the exchange parameter J which in-principle can be calculated [74]. For an appropriate choice of the parameters this method affords a good description of transition metal and rare-earth oxides.

2.3.4 Interpretation of Kohn Sham eigenvalues

As stated previously, the KS formalism provides a way of mapping an interacting N particle problem onto a fictitious non-interacting problem with the same ground state density

and total energy. This process is facilitated by the set of KS equations (2.23) whose eigenvectors ψ_i produce the exact ground-state density via equation (2.24). Meanwhile the KS eigenvalues ε_i are merely the Lagrange multipliers that help to impose the orthonormality of the KS eigenvectors. Therefore the physical significance of the KS orbitals and eigenvalues needs to be established. It can be shown that the KS Slater determinant wavefunction Ψ^{KS} is not the same as the true N particle wave function Ψ and strictly speaking, KS orbitals cannot be equated to the molecular orbitals or the valence and conduction band orbitals of the real physical system [75, 76]. The true meaning of the the KS eigenvalues was first discussed by Janak [77] who showed that the KS eigenvalue ε_i^{KS} is equal to the derivative of the total energy E with respect to the occupation number f_i of the state ψ_i .

$$\varepsilon_i^{KS}(f_1, f_2, \dots, f_i, \dots, f_N) = \frac{\partial E}{\partial f_i} \quad (2.39)$$

In contrast the real eigenvalues ε_i^{real} that correspond to the excitation energies of the real system are defined by Koopman's theorem to be

$$\varepsilon_i^{real} = E(f_1, f_2, \dots, f_i, \dots, f_N) - E(f_1, f_2, \dots, f_i - 1, \dots, f_N) \quad (2.40)$$

$$= \int_0^1 df \frac{\partial E(f_1, f_2, \dots, f_i - 1 + f, \dots, f_N)}{\partial f} \quad (2.41)$$

$$= \int_0^1 df \varepsilon_i^{KS}(f_1, f_2, \dots, f_i - 1 + f, \dots, f_N) \quad (2.42)$$

However, it has also been shown [78] that although the KS eigenvalues in general do not represent the true excitation energies of the system, there exists an exception to the rule in the highest occupied molecular orbital (HOMO) of a finite system whose KS eigenvalue ε^{HOMO} must equal the negative of the first ionization energy of the real system. Thus only the highest occupied orbital of a KS system has physical meaning. Nevertheless in practice KS eigenstates and band structures are routinely compared to experiment. Molecular level orderings and orbitals shapes obtained from DFT are usually in agreement with those obtained from wavefunction methods. Similarly valence band widths and band curvatures at high-symmetry points in the Brillouin zone of simple semiconductors usually compare favourably with experiment. From empirical experience, it is fairly well accepted that the KS spectrum especially in the case of simple metals and semiconductors is a reasonably good first approximation to the real excitation spectra. Also, in the case of molecules, the KS eigenvalues predicted in standard semi-local approximations such as LSDA/GGA

consistently under-estimate the excitation energies but the spectra obtained with more advanced functionals are seen to be in good agreement with experiment. The interpretation of the predicted KS bandgap (HOMO-LUMO gap) in semi-conductors (molecules) is also an issue that needs to be addressed [79]. The real optical bandgap of a semiconductor/molecule is given by

$$E_{gap}^{real} = E(N+1) - E(N) - [E(N) - E(N-1)] \quad (2.43)$$

$$= \begin{cases} \mu(N+1) - \mu(N) & \text{(semiconductor)} \\ -E.A + I.P & \text{(molecule)} \end{cases} \quad (2.44)$$

where μ is the chemical potential and E.A, I.P are the electron affinity and ionization potential respectively. The KS bandgap given by $E_{gap}^{KS} = \varepsilon_{N+1}^{KS} - \varepsilon_N^{KS}$ differs from the true gap by the derivative discontinuity Δ [79] in the xc energy E_{xc} or equivalently the discontinuity in the xc potential V_{xc} . Thus $E_{gap}^{KS} = (E_{gap}^{real} - \Delta)$ and Δ being a positive quantity, the KS gap is always smaller than the real bandgap. Notably, the size of the derivative discontinuity Δ is usually unknown. Therefore one must be careful in DFT calculations while extracting information that depends upon the size of the band gap or the position of the un-occupied KS eigenstates.

2.4 Computational Methods

These days, a wide variety of numerical Kohn-Sham DFT implementations both commercial as well as non-commercial are readily available for carrying out practical electronic structure calculations. The choice of a particular implementation is usually dictated by several factors such as the capabilities of the implementation, the desired level of accuracy and the computational resources at ones disposal. The two most basic features of any numerical DFT code that have a major bearing on its efficiency and accuracy are:

1. The basis set employed over which the KS eigenvectors, density and potential are expanded.
2. The way in which the *core* electrons which reside in atomic shells close to the nuclei are treated.

2.4.1 Basis sets

Plane wave basis sets are extremely popular in solid state physics where in the validity of Bloch's theorem in a periodic potential naturally facilitates the expansion of the wave function $\psi_i(\mathbf{r})$ as a Fourier expansion over a set of plane waves [80]

$$\psi_j(\mathbf{r}) = \sum_{\mathbf{k}} C_{\mathbf{k}}^j e^{i\mathbf{k}\cdot\mathbf{r}} \quad (2.45)$$

where the number of \mathbf{k} vectors included in the summation is large enough to represent $\psi_i(\mathbf{r})$ to the required degree of accuracy. Usually the quality of a plane wave basis set is determined by a single parameter called the *energy cutoff* $E_{cut} = \frac{\hbar^2|\mathbf{k}|^2}{2m}$ which is equivalent to a cutoff on the highest electronic kinetic energy. Thus if one wishes to describe localized electronic states with large kinetic energies, a sufficiently large value of E_{cut} is required which translates into an increase in computational cost both in terms of time and memory. However the availability of efficient fast fourier transform (FFT) techniques [81] has made plane wave calculations practicable for relatively large solid state systems. For molecular calculations in quantum chemistry, Gaussian type orbitals (GTOs) have long been very popular for representing molecular wavefunctions and densities [60]. More generally, atom centered analytic functions such as Slater type orbitals (STOs), or numerical atomic orbital basis functions are also employed. Typically, eigenstates are expanded over a finite number of atom centered basis functions

$$\psi_j(\mathbf{r}) = \sum_a C_a^j \phi_a \quad (2.46)$$

where ϕ_a can be a GTO, STO or any numerical function that decays radially outwards from the nucleus. For finite systems lacking periodicity such as molecules, the use of planewave basis sets is not computationally efficient. In contrast atom centered basis functions such as GTOs/STOs capture the exponential decay of the electronic wavefunction into the vacuum region much more effectively. Furthermore the quasi-localized nature of these basis functions means that they have a finite effective interaction range. Thus two STOs that are far apart in space have a vanishing interaction and Hamiltonian and overlap matrices represented over such localized basis functions exhibit a great degree of sparsity for large systems which can lead to substantial savings in computational resources. While GTOs have traditionally been popular as most of the integrals involving GTOs are analytic, STOs and numerical orbitals describe atomic wave functions better than GTOs and relatively

fewer such functions are therefore necessary. Recent times have also seen the increased use of direct space methods where in the KS equations are solved directly in real space by expanding the orbitals over a fine numerical grid. Just as in plane wave calculations one single parameter viz., the fineness of the grid determines the accuracy of the calculation. Still a relatively large number of grid points are usually required in any simulation and one has to handle very large matrices as a result. On the bright side these methods are easily implemented on massively parallel architectures.

2.4.2 Pseudopotentials

The chemical behaviour of atoms in molecules and solids is almost exclusively determined by interactions between the outer or *valence* electrons while the deeper lying *core* electrons are usually part of closed shells and are chemically inactive. The core electrons are very close to the nucleus and their energy levels are very deep and remain unperturbed in most chemical environments. Therefore it is not necessary to explicitly describe the core region in electronic structure simulations. This is achieved through the pseudopotential [82, 83] method which essentially involves eliminating the individual nuclear and core electron potentials and replacing them by a single effective potential that describes their net effect on the valence electrons. This effective potential is called the *pseudopotential* and offers massive advantages both in terms of drastically reducing the number of electronic states in the calculation and also reducing the number of basis functions required. This is absolutely unavoidable for heavier elements as describing a large number of core electrons with very high kinetic energies would be prohibitively expensive. Both empirical and *ab initio* pseudopotentials are commonly employed but in what follows we shall only discuss the latter. A pseudopotential needs to be calculated for each atomic species that one wishes to use in a particular simulation. One starts by solving the atomic radial Schrödinger equation¹ in the spherically symmetric potential $V[\rho](r)$ for a particular valence shell $\{n, l\}$

$$\left[-\frac{1}{2} \frac{d^2}{dr^2} + \frac{l(l+1)}{2r^2} + V[\rho](r) \right] r\psi_{nl}^{AE} = \epsilon_{nl} r\psi_{nl}^{AE} \quad (2.47)$$

where in $V[\rho](r)$ is the KS effective potential for the density atomic density $\rho(r)$

$$V[\rho](r) = -\frac{Z}{r} + V_H[\rho](r) + V_{xc}[\rho](r) \quad (2.48)$$

¹Note that atomic units are employed

The real all-electron (AE) wave function ψ_{nl}^{AE} of valence electrons often fluctuates wildly in the core region to maintain orthogonality with the core states. This is however replaced by a nodeless pseudo (PS) wavefunction ψ_{nl}^{PS} which is smooth throughout but which matches the real wavefunction outside a chosen matching radius r_c . In the particular class of *norm conserving* pseudopotentials, the following conditions are satisfied:

$$\psi_{nl}^{PS}(r) = \psi_{nl}^{AE}(r), \quad r > r_c \quad (2.49)$$

$$\int_0^{r_c} |\psi_{nl}^{PS}(r)|^2 r^2 dr = \int_0^{r_c} |\psi_{nl}^{AE}(r)|^2 r^2 dr \quad (2.50)$$

The norm conserving pseudo-wavefunction for the 4s atomic wave function of a Zn atom is shown in figure. 2.1. The pseudo-wavefunctions then also reproduce the same eigenvalues

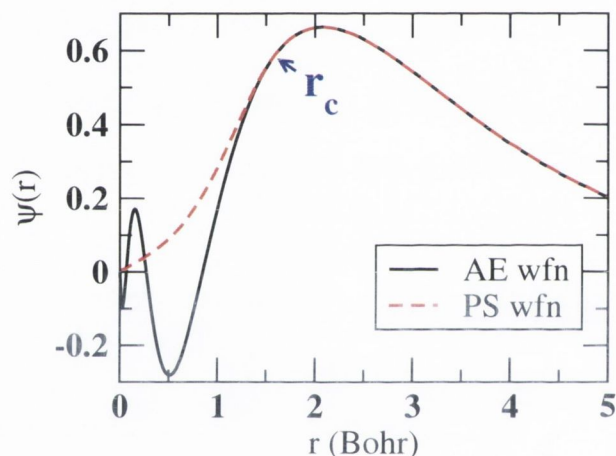


Figure 2.1: The all-electron and pseudo wavefunctions for the 4s atomic state of a Zn atom are shown. The PS wavefunction is constructed so as to match the AE wavefunction outside r_c and also to have the same norm.

ϵ_{nl} as ψ_{nl}^{AE} . Once ψ_{nl}^{PS} is obtained, the pseudopotential is calculated by simply inverting the Schrödinger equation.

$$V_{nl}^{PS}(r) = \epsilon_{nl} - \frac{l(l+1)}{2r^2} + \frac{1}{2r\psi_{nl}^{PS}(r)} \frac{d^2}{dr^2} r \psi_{nl}^{PS}(r) \quad (2.51)$$

However, in this form the pseudopotential includes the screening due to the valence electrons and cannot be used in a solid state or molecular calculation where one needs to treat the valence region self-consistently. Therefore the Hartree and exchange-correlation potential from all of the valence electrons is subtracted from $V_{nl}^{PS}(r)$ to obtain the so called

bare ion pseudopotential.

$$V_{nl}^{PS,I}(r) = V_{nl}^{PS}(r) - V_H^{val}[\rho_{val}](r) - V_{xc}^{val}[\rho_{val}](r) \quad (2.52)$$

where ρ_{val} is the valence electronic density. Note that a different pseudopotential is obtained for each $\{n, l\}$ shell. In the widely used *non-local* pseudopotential scheme due to Klienman and Bylander (KB) [84] the different $V_{nl}^{PS,I}(r)$ are combined into one single pseudopotential with a *nl*-independent part termed the *local* pseudopotential and a *nl*-dependent part called the *non-local* part by means of special projector functions called “KB projectors”. The scheme offers significant computational advantages by confining the long range interactions in the pseudopotential to the *nl*-independent part as the *nl*-dependent parts are usually short-ranged. Thus a representation such as

$$V^{PS,I}(r) = V_{local}^{PS,I}(r) + \sum_{n,l} |\chi_{nl}\rangle\langle\chi_{nl}| \quad (2.53)$$

where the χ_{nl} represent the KB projectors is commonly employed. For some atomic species in which the core shells and valence shells are not well separated leading to a substantial overlap between the core and valence electron density, the subtraction of $V_{xc}^{val}[\rho_{val}]$ in equation (2.52) is not exact owing to the non-linearity of the xc potential. In such cases one has to carry additional *core corrections* [85] in the pseudopotential. The quality of a pseudopotential is usually determined by two quantities namely its *softness* and *transferability*. Softness refers to the smoothness of a pseudopotential. In general, the softer the pseudopotential the easier it is to describe in planewave calculations. However, a pseudopotential should ideally also be transferable in the sense that it should be accurate in a range of chemical environments. The softness and transferability can usually be tuned by changing the matching radius r_c . Larger r_c s tend to produce softer pseudopotentials but it might sometimes be at the cost of transferability. In general, a pseudopotential must be tested for its quality before it is extensively used in material simulations.

2.4.3 The SIESTA code

All of the density functional calculations and methodological implementations presented in this thesis are carried out within the numerical framework of the SIESTA (Spanish Initiative for the Estimation of Systems with Thousands of Atoms) code [86, 87, 88]. SIESTA belongs to the general class of pseudopotential-localized basis orbital implementations and

in particular, uses norm-conserving pseudopotentials similar to the ones described earlier. The main philosophy behind SIESTA was the development of a general purpose DFT platform that makes efficient use of locality i.e., the weak dependence of the properties of a region of the system to perturbations sufficiently far away from it, in order to achieve favourable scaling with increasing system sizes. To this end, SIESTA employs a localized basis set consisting of numerical atomic orbitals which are the product of a numerical radial function and a real spherical harmonic. Thus for an atom I located at \mathbf{R}_I

$$\phi_{lmn}^I(\mathbf{r}) = \phi_{ln}^I(r_I) Y_{lm}(\hat{\mathbf{r}}_I) \quad (2.54)$$

where $\mathbf{r}_I = \mathbf{r} - \mathbf{R}_I$, $r = |\mathbf{r}|$ and $\hat{\mathbf{r}} = \frac{\mathbf{r}}{r}$. The angular momentum (labelled by l, m) may be arbitrarily large and, in general, there will be several orbitals (labelled by index n) with the same angular dependence, but a different radial dependence, forming what is conventionally called a *multiple- ζ* basis. The first among a group of such basis orbitals termed the *first- ζ* orbital is constructed as an eigenfunction of the pseudo-atom within a hard wall spherical potential of chosen radius r_c . In other words, it is an angular-momentum dependent numerical eigenfunction $\phi_l(r)$ of the atomic pseudopotential $V_l(r)$, for an energy $\epsilon_l + \delta\epsilon_l$ chosen so that the first node occurs at the desired cutoff radius r_c .

$$\left(-\frac{1}{2r} \frac{d^2}{dr^2} r + \frac{l(l+1)}{2r^2} + V_l(r) \right) \phi_l(r) = (\epsilon_l + \delta\epsilon_l) \phi_l(r) \quad (2.55)$$

with the boundary condition $\phi_l(r_c) = 0$. (The indices I and $n = 1$ are omitted here for simplicity). Thus SIESTA basis functions are also called pseudo atomic orbitals (PAOs). Second and higher ζ -functions are constructed in the spirit of the ‘‘split valence’’ scheme. For instance the *second- ζ* function $\phi_l^{2\zeta}(r)$ has the same tail as the *first- ζ* orbital $\phi_l^{1\zeta}(r)$ but changes to a simple polynomial behaviour inside a ‘split radius’ r_l^s

$$\phi_l^{2\zeta}(r) = \begin{cases} r^l (a_l - b_l r^2) & \text{if } r < r_l^s \\ \phi_l^{1\zeta}(r) & \text{if } r > r_l^s \end{cases} \quad (2.56)$$

where a_l and b_l are determined by imposing the continuity of value and slope at r_l^s . Thus the SIESTA basis functions exhibit the smooth exponential decay of atomic eigenfunctions but are of finite extent being strictly zero beyond the cutoff radius r_c . SIESTA also implements *polarization* orbitals constructed from a perturbed atomic Hamiltonian in order to account for the deformation induced by bond formation. The polarization orbital corresponding to

a given pseudo atomic orbital $\phi_{lm}(\mathbf{r}) = \phi_l(r)Y_{lm}(\hat{\mathbf{r}})$ is of the form

$$\phi_{l+1,m}(\mathbf{r}) = N\phi_{l+1}(r)Y_{l+1,m}(\hat{\mathbf{r}}) \quad (2.57)$$

where N is a normalization constant. One of the main advantages of SIESTA is that a relatively small number of basis functions are adequate to accurately describe the charge density. A typical double zeta plus polarization (DZP) basis set might consist of about 16 to 23 PAOs per atom.

SIESTA features the standard KS one-electron Hamiltonian within the non-local pseudopotential approximation

$$\hat{H} = \hat{T} + \sum_I V_I^{local}(\mathbf{r}) + \sum_I \hat{V}_I^{KB} + V_H[\rho](\mathbf{r}) + V_{xc}[\rho](\mathbf{r}) \quad (2.58)$$

where $\hat{T} = -\frac{1}{2}\nabla^2$ is the kinetic energy operator, I is an atom index, $V_H(\mathbf{r})$ and $V_{xc}(\mathbf{r})$ are the total Hartree and xc potentials, and $V_I^{local}(\mathbf{r})$ and \hat{V}_I^{KB} are the local and non-local (Kleinman-Bylander) parts of the pseudopotential of atom I . The overlap matrix $S_{\mu\nu} = \langle \phi_\mu | \phi_\nu \rangle$ and several parts of the Hamiltonian viz., kinetic energy and non-local pseudopotential matrix elements are evaluated as two center integrals. A general two center integral is of the form

$$A(\mathbf{R}) \equiv \langle \xi_1 | \xi_2 \rangle = \int \xi_1^*(\mathbf{r}) \xi_2(\mathbf{r} - \mathbf{R}) d\mathbf{r} \quad (2.59)$$

where the integral is over all space and ξ_1, ξ_2 may be basis functions ϕ_{lmn} , KB pseudopotential projectors χ_{lmn} , or more complicated functions centered on the atoms. The function $A(\mathbf{R})$ is then treated as a convolution and transformed into reciprocal space

$$A(\mathbf{R}) = \int \varphi_1^*(\mathbf{k}) \varphi_2(\mathbf{k}) e^{-i\mathbf{k}\cdot\mathbf{R}} d\mathbf{k} \quad (2.60)$$

where $\varphi(\mathbf{k})$ is the Fourier transform of $\xi(\mathbf{r})$. Provided that the functions $\xi(\mathbf{r})$ can be expanded over a finite number of spherical harmonics,

$$\xi(\mathbf{r}) = \sum_{l=0}^{l_{max}} \sum_{m=-l}^l \xi_{lm}(r) Y_{lm}(\hat{\mathbf{r}}) \quad (2.61)$$

(the above holds true for all the atom centered functions in SIESTA), it can be shown that $A(\mathbf{R})$ may be transformed as

$$A(\mathbf{R}) = \sum_{l=0}^{2l_{max}} \sum_{m=-l}^l A_{lm}(R) Y_{lm}(\hat{\mathbf{R}}) \quad (2.62)$$

For each pair of functions $\xi_{1,2}(\mathbf{r})$ the functions $A_{lm}(R)$ are calculated numerically on a fine one dimensional grid for all values of R upto $R_{max} = r_c^1 + r_c^2$ and stored in memory once and for all. Here $r_c^{1,2}$ are the cutoff radii of the two atom centered functions. Values of $S_{lm}(R)$ for R in-between grid points are easily interpolated. The spherical harmonics $Y_{lm}(\hat{\mathbf{R}})$ are easily obtained using standard special function algorithms.

Integrals involving other parts of the Hamiltonian such as the local pseudopotential $V_I^{local}(\mathbf{r})$ ², the Hartree potential $V_H[\rho](\mathbf{r})$ and xc potential $V_{xc}[\rho](\mathbf{r})$ are efficiently evaluated on a real-space grid. The grid fineness is controlled by a single energy cutoff E_{cut} which is equivalent to the highest energy of planewaves that can be represented on the same grid. Before the required integrals can be evaluated the electron density first needs to be represented on the grid which is done as follows: Let $\psi_i(\mathbf{r})$ be the Hamiltonian eigenstates, expanded in the PAO basis set

$$\psi_i(\mathbf{r}) = \sum_{\mu} \phi_{\mu} c_{\mu i} \quad (2.63)$$

where $c_{\mu i} = \langle \tilde{\phi}_{\mu} | \psi_i \rangle$ and $\tilde{\phi}_{\mu}$ is the dual of ϕ_{μ} such that $\langle \tilde{\phi}_{\mu} | \phi_{\nu} \rangle = \delta_{\mu\nu}$. We use the compact notation $\mu = \{l m n\}$ to index the basis orbitals as defined in equation (2.54). The electron density is then given by

$$\rho(\mathbf{r}) = \sum_i f_i |\psi_i(\mathbf{r})|^2 \quad (2.64)$$

where n_i is the occupation number of the state ψ_i . By substituting (2.64) into (2.63) and defining the SIESTA density matrix as

$$\rho_{\mu\nu} = \sum_i c_{\mu i} f_i c_{i\nu} \quad (2.65)$$

where $c_{i\nu} \equiv c_{\nu i}^*$, the electron density can be written in terms of the basis orbitals as

$$\rho(\mathbf{r}) = \sum_{\mu\nu} \rho_{\mu\nu} \phi_{\nu}^*(\mathbf{r}) \phi_{\mu}(\mathbf{r}) \quad (2.66)$$

²SIESTA actually replaces $V_I^{local}(\mathbf{r})$ with the so called neutral atom potential via a clever partitioning of the charge density but we neglect that detail during this discussion.

Note that the conjugate $\phi_\nu^*(\mathbf{r})$ is used for generality although the PAOs are real functions. Thus the density can be expanded on the real-space grid by interpolating the values of the basis functions on grid points. Owing to the locality of the PAOs this operation is relatively inexpensive and scales as $O(N)$. Once the density $\rho(\mathbf{r})$ is available on the grid, the Hartree potential $V_H[\rho](\mathbf{r})$ is calculated by solving the Poisson equation. Note that SIESTA always assumes periodic boundary conditions (PBC) and a FFT Poisson solver is therefore very efficient. For neutral isolated molecules the strictly finite nature of the PAOs ensures minimal interaction between periodic images and the convergence of $V_H[\rho](\mathbf{r})$ with simulation cell size is rapid. For charged molecules and solid state supercells, a uniform neutralizing background charge is applied and appropriate Madelung correction terms are added to the total energy. Similarly, by knowing $\rho(\mathbf{r})$ on the grid, the calculation of $V_{xc}[\rho](\mathbf{r})$ is straightforward especially for local and semi-local xc functionals such as LSDA/GGA. Note that for GGAs, the density gradient at every point on the grid is calculated using finite differences. The local pseudopotential potential $V_I^{local}(\mathbf{r})$ for each atom I can be directly interpolated on the grid from look up tables. Thus the total grid potential $V^g(\mathbf{r}) = V_I^{local}(\mathbf{r}) + V_H[\rho](\mathbf{r}) + V_{xc}[\rho](\mathbf{r})$ is collected and the matrix elements $V^g(\mathbf{r})\phi_\nu^*(\mathbf{r})\phi_\mu(\mathbf{r})\delta\mathbf{r}^3$ for each pair of non-zero PAOs $\phi_{\mu,\nu}$ at every grid point are added to the Hamiltonian matrix elements $H_{\mu\nu}$. $\delta\mathbf{r}^3$ is the volume element of the grid.

Brillouin zone(BZ) integration over various k-point meshes is necessary in order to treat solid state systems of small and moderately large unitcells and especially metals. As mentioned earlier SIESTA always assumes periodic boundary conditions and therefore finite as well as extended systems are treated on the same footing with regards to the evaluation of matrix elements. For periodic systems the definition of the two and three center integrals is easily generalized to include PAO basis functions outside the unitcell. Thus two and three center integrals of the respective forms $A_{\mu\nu'}^{per} = \langle \phi_\mu | \phi_{\nu'} \rangle$ and $B_{\mu'\nu''}^{per} = \langle \phi_{\mu'} | V^g(\mathbf{r}) | \phi_{\nu''} \rangle$ are evaluated where in the primed quantities indicate PAOs not just centered in the unitcell but over all space. Note however that due to the periodicity of the potential, \mathbf{r} in $B_{\mu'\nu''}^{per}$ only needs to be within the unitcell. Furthermore the finite range of the PAOs means that only a finite number of basis functions situated inside an auxiliary supercell spanning a few lattice vectors in all 3 directions are ever required in the evaluation of $A_{\mu\nu'}^{per}$ and $B_{\mu'\nu''}^{per}$. Once all the real matrix elements are thus calculated, the complex Hamiltonian in the Bloch representation at a given k-point \mathbf{k} in the BZ is accumulated as :

$$H_{\mu\nu}(\mathbf{k}) = \sum_{(\nu' \equiv \nu)} H_{\mu\nu'} e^{i\mathbf{k} \cdot (\mathbf{R}_\mu - \mathbf{R}_{\nu'})} \quad (2.67)$$

where ($\nu' \equiv \nu$) indicates that $\phi_{\nu'}$ and ϕ_{ν} are equivalent orbitals under lattice translation. Note that ϕ_{μ} and ϕ_{ν} are centered in the unitcell. This yields a complex $N \times N$ matrix eigenvalue problem, N being the number of basis functions in the unitcell, which needs to be solved at every \mathbf{k} -point in the sampled BZ. The resulting Bloch state expansion coefficients $c_{\mu'i}(\mathbf{k})$ are used to construct the wavefunctions

$$\psi_i(\mathbf{k}, \mathbf{r}) = \sum_{\mu'} e^{i\mathbf{k} \cdot \mathbf{R}_{\mu'}} \phi_{\mu'}(\mathbf{r}) c_{\mu'i}(\mathbf{k}) \quad (2.68)$$

where i is the band index and $c_{\mu'i} = c_{\mu i}$ if ($\mu' \equiv \mu$). The $\psi_i(\mathbf{k}, \mathbf{r})$ are normalized in the unitcell. The periodic electron density is then given by

$$\rho(\mathbf{r}) = \sum_i \int_{BZ} n_i(\mathbf{k}) |\psi_i(\mathbf{k}, \mathbf{r})|^2 d\mathbf{k} \quad (2.69)$$

$$= \sum_{\mu'\nu'} \rho_{\mu'\nu'} \phi_{\nu'}^* \phi_{\mu'} \quad (2.70)$$

and the density matrix

$$\rho_{\mu\nu} = \sum_i \int_{BZ} c_{\mu i}(\mathbf{k}) n_i(\mathbf{k}) c_{i\nu}(\mathbf{k}) e^{i\mathbf{k} \cdot (\mathbf{R}_{\nu} - \mathbf{R}_{\mu})} \quad (2.71)$$

is real and periodic such that $\rho_{\mu\nu} = \rho_{\mu'\nu'}$ provided ($\mu \equiv \mu'$ and $\nu \equiv \nu'$). In practice, the integral in (2.71) is performed in a finite, uniform grid of \mathbf{k} -points in the Brillouin zone set up using the Monkhorst-Pack scheme [89]. Thus periodic supercells of bulk type materials as well as systems such as metallic or semiconductor surfaces, nanowires and nanotubes which are periodic in some directions while being finite in others can all be handled conveniently.

Once the KS electronic ground state has been calculated for a given arrangement of the atomic positions, the total energy of a system of electrons and (stationary) nuclei can be calculated. Thus the KS total energy expression in SIESTA takes the form

$$E^{KS} = \sum_{\mu\nu} H_{\mu\nu} \rho_{\mu\nu} - \frac{1}{2} \int V_H(\mathbf{r}) \rho(\mathbf{r}) d\mathbf{r} \quad (2.72)$$

$$+ \int (\epsilon_{xc}(\mathbf{r}) - V_{xc}(\mathbf{r})) \rho(\mathbf{r}) d\mathbf{r} + \sum_{I < J} \frac{Z_I Z_J}{R_{IJ}} \quad (2.73)$$

where I, J are the atomic indices, $R_{IJ} = |\mathbf{R}_I - \mathbf{R}_J|$, Z_I, Z_J are the valence ion pseudo-atom charges and $\epsilon_{xc}(\mathbf{r})\rho(\mathbf{r})$ is the exchange-correlation energy density. The first term is equivalent to a sum over the occupied eigenvalues and is called the band structure (BS) term. Note that in practice, within SIESTA, some of the terms in above expression are re-arranged for the sake computational efficiency and the final energy expression used is a slightly modified form of equation (2.73) [86]. SIESTA also implements standard Hellman-Feynman forces and stress tensors together with a Conjugate-Gradients (CG) [81] scheme for geometry optimizations and fullscale Car-Parinello Molecular dynamics [90]. From the perspective of large scale computation, SIESTA is also parallelized for distributed memory architectures. The main layer of parallelism is over the orbital basis functions which are distributed among different nodes in a multi-processor simulation although certain subroutines also involve parallelism over grid points in the real-space mesh or over k-points in the BZ. For a more complete description of the capabilities of SIESTA we point the reader to the extensive published literature [86, 87, 88]

2.4.4 Additions to SIESTA

During the course of the research work presented in this thesis, we have implemented several new functionalities within a development version of SIESTA, mostly in the context of improved exchange-correlation functionals. Details of some of these additions are presented in later chapters but we briefly list them below.

- Some previously unavailable semi-local LDAs and GGAs such as OLYP [91] , LB94 [92] have been added to the xc modules of SIESTA.
- Explicitly orbital-dependent functionals such as the exact exchange functional and the self-interaction corrected LSDA/GGA functionals in the KLI [72] approximation have been incorporated.
- A computationally efficient approximate self interaction correction scheme (ASIC) [94] based on the idea of Fillipetti and Spaldin [93] has been integrated in the code.
- A new level of parallelism has been added in which the code is simultaneously parallelized over both basis orbitals and k-points which improves the scalability of SIESTA for medium to large scale solid state simulations.

2.5 Electronic transport at the nanoscale

Theoretical calculations of the electronic transport properties of nanoscale devices are at the forefront of modern computational physics. The rules of Ohmic transport valid in all metallic and semi-conductor based devices breakdown at the nanoscopic level and transport across individual molecules or other atomic scale structures is strongly influenced by quantum mechanical effects. Therefore one needs to adopt a fully quantum mechanical description for the electrons in such devices and transport needs to be described in terms of wave function scattering and transmission probabilities. Among the various theoretical treatments of the quantum transport problem the non-equilibrium Green's function formalism (NEGF) [95, 96, 97, 98, 99] combined with an electronic structure method such as density functional theory [58] is by far the most popular. The electronic transport calculations presented in this work are performed within the framework of the SMEAGOL program [98, 100, 101], in which an efficient NEGF algorithm is interfaced with the DFT platform provided by the SIESTA code [88]. In the following section we present a brief overview of the SMEAGOL algorithm focusing primarily on how a typical transport problem is set up and solved.

2.5.1 NEGF and SMEAGOL

The general set up used in SMEAGOL to model the transport properties of a nanoscale device is presented in figure 2.2. The calculations described in this work consist typically of a molecule sandwiched between two metallic electrodes. However the device region in figure 2.2 could also represent a more general arrangement such as a nano constriction in a metallic or semiconductor nanowire or even a multilayer tunnel junction. The electrodes, usually referred to as *leads*, are treated as being semi-infinite and periodic in the direction of electronic transport. Therefore the Hamiltonian describing the leads and the device or *scattering* region is essentially infinite. However, unlike in normal solid state systems, Bloch's theorem cannot be invoked in this case as the presence of the scattering region between the leads breaks the translational symmetry of the whole system and thus one effectively has to treat an infinite yet non-periodic system. For this problem to be solved numerically, the infinite system has to be mapped onto an effective finite system and this is achieved within the NEGF formalism. As shown in figure 2.2 the whole device is partitioned into three distinct regions viz., the left lead, the scattering region and the right lead. The leads are further partitioned into so called *principal* layers defined so that each

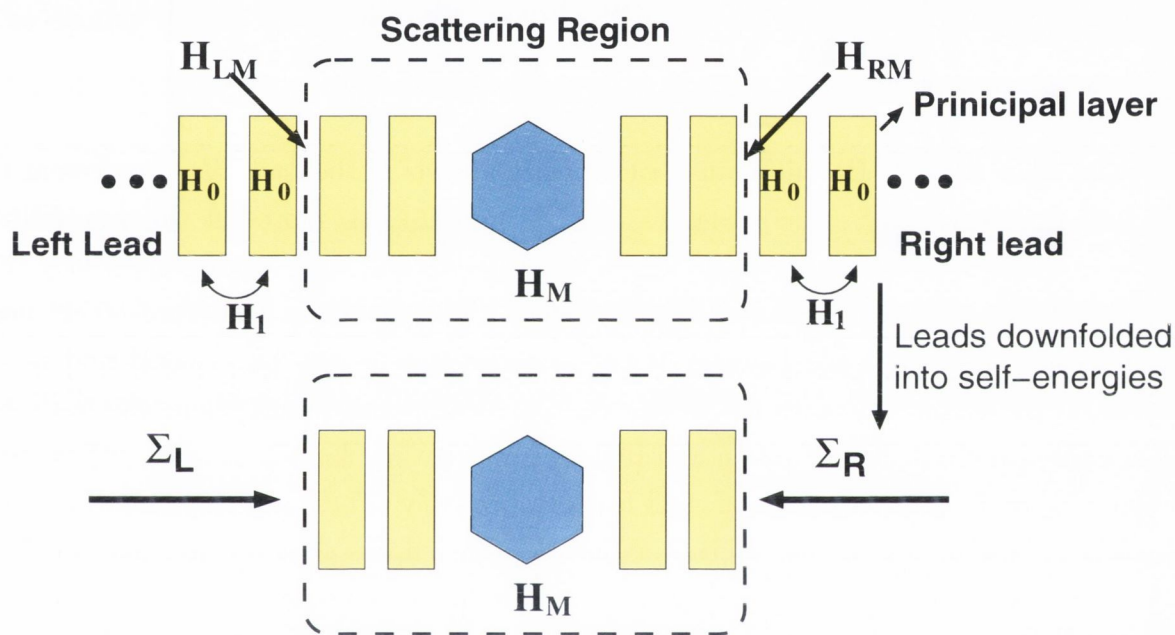


Figure 2.2: A schematic representation of the device set up in SMEAGOL is presented. The system is partitioned in three distinct regions the left lead, the scattering region and the right lead. The leads are subsequently replaced by effective self energies that act on the finite Hamiltonian H_M of the scattering region.

principal layer only interacts with two other principal layers one on either side of it. In practice a certain number of principal layers on either side of the device are included in the scattering region. Thus the Hamiltonian for the whole system can be written as

$$H = \begin{pmatrix} \cdot & \cdot & \cdot & \cdot & \cdot & \cdot & \cdot & \cdot & \cdot & \cdot & \cdot \\ \cdot & 0 & H_{-1} & H_0 & H_1 & 0 & \cdot & \cdot & \cdot & \cdot & \cdot \\ \cdot & \cdot & 0 & H_{-1} & H_0 & H_{LM} & 0 & \cdot & \cdot & \cdot & \cdot \\ \cdot & \cdot & \cdot & 0 & H_{ML} & H_M & H_{MR} & 0 & \cdot & \cdot & \cdot \\ \cdot & \cdot & \cdot & \cdot & 0 & H_{RM} & H_0 & H_1 & 0 & \cdot & \cdot \\ \cdot & \cdot & \cdot & \cdot & \cdot & 0 & H_{-1} & H_0 & H_1 & 0 & \cdot \\ \cdot & \cdot & \cdot & \cdot & \cdot & \cdot & \cdot & \cdot & \cdot & \cdot & \cdot \end{pmatrix} \quad (2.74)$$

where in, H_0 is the bulk Hamiltonian of each principal layer in the lead. $H_{-1,1}$ represent the interactions between the principal layers. $H_{ML,LM}$ and $H_{MR,RM}$ represent the semi-infinite interaction matrices of the scattering region with the left and right leads respectively. H_M is the finite Hamiltonian of the scattering region. The electronic structure of principal layers deep inside the leads however is the same as that in the bulk metal and is not influenced by perturbations in the device region. Within this assumption, the leads can be re-normalized out of the system and replaced by what are known as *leads self energies* denoted Σ_L and Σ_R for the left and right leads respectively. These self energies which in general can be complex and non-Hermitian matrices encompass all of the information about how the leads effect the scattering region. Note that the self energies are energy dependent quantities and need to be evaluated for different values of the chemical potentials of leads. In SMEAGOL, the scheme proposed by Sanvito *et al* is used to calculate Σ_L , Σ_R and we direct the reader to reference [102] for more details. One can then focus ones attention on the region of interest which is the scattering region and in place of the infinite Hamiltonian H in equation (2.74), consider a finite effective Hamiltonian for the scattering region given by

$$H_{\text{EFF}} = H_M + \Sigma_L + \Sigma_R \quad (2.75)$$

However, H_{EFF} is in general non-Hermitian as the number of particles inside the scattering region is not conserved due to particale interchange between the scattering region and the leads. As a result, one does not solve an eigenvalue problem but instead calculates the the so called *retarded Green's function* G_M for the scattering region defined as:

$$G_M(E) = [\lim_{\delta \rightarrow 0} (E + i\delta)S_M - H_M - \Sigma_L - \Sigma_R]^{-1} \quad (2.76)$$

where S_M is the overlap matrix for the scattering region. Having obtained $G_M(E)$ one can then calculate the *lesser Green's function* $G^<(E)$ given by

$$G^<(E) = iG_M(\Gamma_L f(E - \mu_L) + \Gamma_R f(E - \mu_R))G_M^\dagger \quad (2.77)$$

where in f represents the Fermi distribution and $\mu_L(\mu_R)$ is the chemical potential of the left (right) lead and

$$\Gamma_L = i(\Sigma_L - \Sigma_L^\dagger), \quad \Gamma_R = i(\Sigma_R - \Sigma_R^\dagger) \quad (2.78)$$

The density matrix of the scattering region is directly obtained from $G^<(E)$ as

$$\rho = \frac{1}{2\pi i} \int_{-\infty}^{\infty} G^<(E) dE \quad (2.79)$$

Within a DFT based treatment of the problem, the density ρ obtained in equation (2.79) can be used to calculate a new Hamiltonian for the scattering region $H_M[\rho]$ and one can thus enter a self consistent field (SCF) cycle until a converged solution is obtained. Note that the leads self energies are only calculated at the beginning and do not change during the SCF cycle. With a converged solution for ρ and $G_M(E)$ at hand, quantities of interest such as the current and the transmission coefficients can be obtained. The expression for the current I is

$$I = \frac{e}{h} \int Tr[\Gamma_L G_M^\dagger \Gamma_R G_M](f(E - \mu_L) - f(E - \mu_R)) dE \quad (2.80)$$

and that for the transmission coefficients is

$$T(E, V) = Tr[\Gamma_L G_M^\dagger \Gamma_R G_M] \quad (2.81)$$

where $V = (\mu_L - \mu_R)$ is the potential bias applied to the system. From equations (2.80) and (2.81) the current I is simply the integral over energy of the transmission coefficients $T(E, V)$ in the region in which the Fermi functions of the leads are not equal to each other (i.e., the bias window). The transmission coefficients $T(E, V)$ correspond to the probability of an electron being transmitted from one side of the scattering region to the other at an energy E .

Thus within the NEGF+DFT framework of SMEAGOL, the effects of finite bias that cannot be deduced from zero bias calculations can be modelled self-consistently and accurate transmission coefficients and I-V curves can be plotted. Furthermore, the SMEAGOL

code is specifically designed to treat large systems and is also efficiently parallelized to run on distributed memory architectures. For a more detailed discussion about the capabilities of SMEAGOL or indeed the NEGF formalism in general, we point the reader to reference [103]

2.6 Conclusions

Among the various approaches to tackling the many electron problem, density functional theory comes across as the most elegant and practical. The theory is in-principle exact and the accuracy of modern day DFT calculations is only limited by the level of approximation involved in the exchange correlation energy functional $E_{xc}[\rho(\mathbf{r})]$. LSDA/GGA have been long been the “work horse” functionals in solid state physics and quantum chemistry but more advanced functionals are increasingly being adopted in day to day simulations.

SIESTA is a robust and numerically efficient Kohn-Sham density functional platform ideally suited for large scale materials simulations. It uses a numerical atomic orbital basis set that makes efficient use of locality to achieve favourable scaling. The code is capable of handling both finite as well as periodic systems and is suited to large scale distributed computing.

A combination of the non equilibrium Green’s functions formalism (NEGF) and DFT is the most commonly used theoretical framework for practical electronic transport calculations. SMEAGOL is an efficient NEGF algorithm that interfaces with the SIESTA code and it can be used to calculate electron transport processes in a variety of systems, from metal-molecule junctions, to nanowires and multilayer devices.

Chapter 3

Orbital dependent functionals

3.1 Introduction

The local spin density approximation (LSDA) and the generalized gradient approximation (GGA) in all its varying forms feature in a vast majority of Density functional theory (DFT) [104] calculations carried out to date. While LSDA has long been the exchange-correlation (xc) functional of choice in solid state physics, the GGAs since they first arrived have rapidly taken over in quantum chemistry. The main reason for the popularity of LSDA/GGA is that they seem to offer a useful compromise between accuracy and computational cost for most day to day calculations such as lattice parameters, bulk moduli and defect formation energies in solids and bond lengths, formation enthalpies in chemistry. These functionals belong to the class of local/semi-local functionals that only need information about the electronic density in the immediate vicinity of the point in question. This feature makes the evaluation of the xc potentials and energies for these functionals trivially easy. However numerous situations in which local functionals fail to be accurate enough or even fail catastrophically can be listed and its a list that keeps growing as physicists and chemists investigate previously unexplored areas. Examples of some scenarios in which LSDA/GGA fail to be accurate include [105]

- a) Heavy atoms and large angular momenta such as d and f
- b) Negative ions which are almost always predicted to be un-bound
- c) Dispersion or van der Waals type forces
- d) Strongly correlated oxides with localized 3d transition metal states.

Also quantities such as band gaps in semi-conductors and insulators are routinely under-

estimated¹. The eigenvalues of the highest occupied orbitals of molecules (HOMOs) must equal the negative ionization potential (IP) of the molecule but LSDA/GGA consistently underestimate IPs by about 3 to 4 eV. In most cases the source of the error can be traced to one of two fundamental flaws in the local xc functionals

- (1) Incorrect asymptotic behaviour. The LSDA/GGA xc potentials decay exponentially instead of as $-\frac{1}{r}$.
- (2) Incomplete cancellation of the self interaction in the Hartree energy by its counterpart in the exchange-correlation energy

Note that rectifying the latter usually corrects the former but not necessarily the other way around.

When faced with one of the situations listed above one has to look towards a different class of xc functionals commonly termed *orbital dependent functionals* (ODF). Orbital dependent functionals come in various forms but if constructed correctly are free of problems (1) and (2) listed above.

3.2 Orbital dependent functionals

As the name suggests, an orbital dependent xc functional in the context of Kohn-Sham (KS) DFT is any functional that is explicitly dependent upon the Kohn-Sham orbitals. The prototypical example of an ODF is the the exact exchange functional [105] of DFT

$$E_x^{exact}[\{\phi_{i\sigma}\}] = -\frac{1}{2} \sum_{\sigma=\uparrow,\downarrow} \sum_{i,j=1}^{N_{occ}^{\sigma}} \int d\mathbf{r} \int d\mathbf{r}' \frac{\phi_{i\sigma}^*(\mathbf{r})\phi_{j\sigma}^*(\mathbf{r}')\phi_{j\sigma}(\mathbf{r})\phi_{i\sigma}(\mathbf{r}')}{|\mathbf{r}-\mathbf{r}'|} \quad (3.1)$$

This form for the exchange energy guarantees exact cancellation with the self interaction contained in the Hartree energy.

One of the basic requirements of the KS scheme is that the KS effective single particle potential be a local multiplicative type potential which means a potential of the type $V_{\text{eff}}^{KS}(\mathbf{r})$ that depends upon only one coordinate \mathbf{r} . Therefore the xc potential in $V_{\text{eff}}^{KS}(\mathbf{r})$ must also be local. However, given the expression for the orbital dependent xc energy, the corresponding xc potential is not readily available. This is because

$$V_{xc}^{\sigma}(\mathbf{r}) \equiv \frac{\delta E_{xc}}{\delta \rho^{\sigma}(\mathbf{r})} \quad (3.2)$$

¹The bandgap error itself is not the problem but the lack of the derivative discontinuity

but unlike LSDA/GGA, E_{xc} is only an implicit functional of the density $\rho^\sigma(\mathbf{r})$ and extracting $V_{xc}^\sigma(\mathbf{r})$ given $E_x^{exact}[\{\phi_{i\sigma}\}]$ is not a trivial task. Nevertheless, there does exist a systematic prescription to construct $V_{xc}^\sigma(\mathbf{r})$ for an orbital dependent E_{xc} and it is called the optimized effective potential (OEP) method [118]. In the following we outline the general OEP approach and a practical approximation to the OEP due to Krieger, Li, and Iafrate (KLI) [119]. We then apply the KLI approximation to two orbital dependent functionals viz., the exact exchange functional and the Self Interaction Correction (SIC) functional.

3.3 The optimized effective potential

The exact total energy within the Kohn-Sham spin density functional formalism can be written as

$$E_{KS}[\rho^\uparrow, \rho^\downarrow] = T_S[\{\phi_{i\sigma}\}] + J[\rho] + E_{xc}[\rho^\uparrow, \rho^\downarrow] + \int d\mathbf{r} \rho(\mathbf{r}) v_{ext}(\mathbf{r}) \quad (3.3)$$

where T_S is the non-interacting kinetic energy, J the Hartree energy and E_{xc} is the xc energy.

$$T_S = \sum_{\sigma=\uparrow,\downarrow} \sum_{i=1}^{N_\sigma} \langle \phi_{i\sigma} | -\frac{1}{2} \nabla^2 | \phi_{i\sigma} \rangle \quad (3.4)$$

$$J = \frac{1}{2} \int \int d\mathbf{r} d\mathbf{r}' \frac{\rho(\mathbf{r})\rho(\mathbf{r}')}{|\mathbf{r} - \mathbf{r}'|} \quad (3.5)$$

The last term is the interaction energy E_{ne} of the electrons with the external potential (nuclei).

The total electronic density is constructed as

$$\rho(\mathbf{r}) = \sum_{\sigma=\uparrow,\downarrow} \sum_{i=1}^{N_\sigma} \phi_{i\sigma}^*(\mathbf{r}) \phi_{i\sigma}(\mathbf{r}) \quad (3.6)$$

where the spin-orbitals $\phi_{i\sigma}$ satisfy the KS equation

$$\left(-\frac{1}{2} \nabla^2 + v_{\text{eff}}^\sigma(\mathbf{r})\right) \phi_{i\sigma}(\mathbf{r}) = \varepsilon_{i\sigma} \phi_{i\sigma}(\mathbf{r}) \quad (3.7)$$

and

$$v_{\text{eff}}^{\sigma}(\mathbf{r}) = \int d\mathbf{r}' \frac{\rho(\mathbf{r}')}{|\mathbf{r} - \mathbf{r}'|} + v_{\text{ext}}(\mathbf{r}) + \frac{\delta E_{xc}}{\delta \rho^{\sigma}(\mathbf{r})} \quad (3.8)$$

The basic OEP equation is

$$\left. \frac{\delta E_{KS}}{\delta V_{\sigma}} \right|_{V_{OEP}^{\sigma}} = 0 \quad (3.9)$$

which means that the OEP is obtained when the total energy is minimized. Also V_{OEP}^{σ} must satisfy the KS equation i.e.,

$$\left(-\frac{1}{2}\nabla^2 + V_{OEP}^{\sigma}(\mathbf{r})\right)\phi_{i\sigma}(\mathbf{r}) = \varepsilon_{i\sigma}\phi_{i\sigma}(\mathbf{r}) \quad (3.10)$$

Using the chain rule arguments from perturbation theory, equation (3.9) can be transformed as

$$\sum_i \int d\mathbf{r}' \frac{\delta E_{KS}}{\delta \phi_{i\sigma}(\mathbf{r}')} \sum_{\substack{k=1 \\ k \neq i}}^{\infty} \frac{\phi_{k\sigma}^*(\mathbf{r})\phi_{k\sigma}(\mathbf{r}')}{\varepsilon_{i\sigma} - \varepsilon_{k\sigma}} + c.c = 0 \quad (3.11)$$

where *c.c* indicates the complex conjugate. From equation (3.3), $\frac{\delta E_{KS}}{\delta \phi_{i\sigma}(\mathbf{r})}$ can be evaluated and we get

$$\begin{aligned} \sum_i \int d\mathbf{r}' \left[-\frac{1}{2}\nabla^2 + \int d\mathbf{r}'' \frac{\rho(\mathbf{r}'')}{|\mathbf{r}'' - \mathbf{r}'|} + v_{\text{ext}}(\mathbf{r}') + \frac{1}{\phi_{i\sigma}^*(\mathbf{r}') \delta \phi_{i\sigma}(\mathbf{r}')} \frac{\delta E_{xc}}{\delta \rho^{\sigma}(\mathbf{r}')} \right] \\ \times \left[\sum_{\substack{k=1 \\ k \neq i}}^{\infty} \frac{\phi_{k\sigma}^*(\mathbf{r})\phi_{k\sigma}(\mathbf{r}')}{\varepsilon_{i\sigma} - \varepsilon_{k\sigma}} \phi_{i\sigma}^*(\mathbf{r}')\phi_{i\sigma}(\mathbf{r}) \right] = 0 \end{aligned} \quad (3.12)$$

Using the KS equation (3.10), the above can be written in terms of V_{OEP}^{σ} as

$$\begin{aligned} \sum_i \int d\mathbf{r}' \left[V_{OEP}^{\sigma}(\mathbf{r}') - \int d\mathbf{r}'' \frac{\rho(\mathbf{r}'')}{|\mathbf{r}'' - \mathbf{r}'|} - v_{\text{ext}}(\mathbf{r}') - \frac{1}{\phi_{i\sigma}^*(\mathbf{r}') \delta \phi_{i\sigma}(\mathbf{r}')} \frac{\delta E_{xc}}{\delta \rho^{\sigma}(\mathbf{r}')} \right] \\ \times \left[\sum_{\substack{k=1 \\ k \neq i}}^{\infty} \frac{\phi_{k\sigma}^*(\mathbf{r})\phi_{k\sigma}(\mathbf{r}')}{\varepsilon_{k\sigma} - \varepsilon_{i\sigma}} \phi_{i\sigma}^*(\mathbf{r}')\phi_{i\sigma}(\mathbf{r}) \right] = 0 \end{aligned} \quad (3.13)$$

We then define the quantities

$$V_{xc\sigma}^{OEP}(\mathbf{r}) = V_{OEP}^{\sigma}(\mathbf{r}) - \int d\mathbf{r}'' \frac{\rho(\mathbf{r}'')}{|\mathbf{r}'' - \mathbf{r}|} - v_{\text{ext}}(\mathbf{r}) \quad (3.14)$$

and

$$u_{xc}^{i\sigma}(\mathbf{r}) = \frac{1}{\phi_{i\sigma}^*(\mathbf{r})} \frac{\delta E_{xc}}{\delta \phi_{i\sigma}(\mathbf{r})} \quad (3.15)$$

which leads us to equations (3.13) and (3.10) in their final form

$$\sum_i \int d\mathbf{r}' \left[V_{xc\sigma}^{OEP}(\mathbf{r}') - u_{xc}^{i\sigma}(\mathbf{r}') \right] \times \left[\sum_{\substack{k=1 \\ k \neq i}}^{\infty} \frac{\phi_{k\sigma}^*(\mathbf{r}) \phi_{k\sigma}(\mathbf{r}')}{\varepsilon_{k\sigma} - \varepsilon_{i\sigma}} \phi_{i\sigma}^*(\mathbf{r}') \phi_{i\sigma}(\mathbf{r}) \right] = 0 \quad (3.16)$$

$$\left(-\frac{1}{2} \nabla^2 + \int d\mathbf{r}'' \frac{\rho(\mathbf{r}'')}{|\mathbf{r}'' - \mathbf{r}|} + v_{ext}(\mathbf{r}) + V_{xc\sigma}^{OEP}(\mathbf{r}) \right) \phi_{i\sigma}(\mathbf{r}) = \varepsilon_{i\sigma} \phi_{i\sigma}(\mathbf{r}) \quad (3.17)$$

The Equations (3.16), (3.17) represent the full OEP equations. In principle one can start from a guess for $V_{xc\sigma}^{OEP}(\mathbf{r})$, obtain a set of orbitals $\{\phi_{i\sigma}\}$ and then solve equation (3.16) for a new $V_{xc\sigma}^{OEP}(\mathbf{r})$ and iterate until convergence. However the equation (3.16) is an integral equation whose solution is computationally expensive and only systems with spherical symmetry could be treated until recently. Krieger, Li, and Iafrate put forward a scheme called the KLI approximation [119], in which one avoids the infinite sum in equation (3.16) and the optimized effective KLI potential can in fact be written directly as

$$V_{xc\sigma}^{KLI}(\mathbf{r}) = \sum_{i=1}^{N_\sigma} \frac{\rho_{i\sigma}(\mathbf{r}) u_{xc}^{i\sigma}(\mathbf{r})}{\rho^\sigma(\mathbf{r})} + \sum_{i=1}^{N_\sigma-1} \frac{\rho_{i\sigma}(\mathbf{r}) [\bar{V}_{xc\sigma,i}^{KLI} - \bar{u}_{xc}^{i\sigma}]}{\rho_\sigma(\mathbf{r})} \quad (3.18)$$

The second sum in the above equation is restricted to run over all spin-orbitals except the highest occupied spin-orbital which insures the correct asymptotic behavior of the potential. $\bar{u}_{xc}^{i\sigma}$ denotes the orbital average

$$\bar{u}_{xc}^{i\sigma} = \int d\mathbf{r} \rho_{i\sigma}(\mathbf{r}) u_{xc}^{i\sigma}(\mathbf{r}) \quad (3.19)$$

and $\bar{V}_{xc\sigma,i}^{KLI}$ is obtained by solving the system of linear algebraic equations

$$\sum_{i=1}^{N_\sigma-1} (\delta_{ij} - M_{ij}^\sigma) (\bar{V}_{xc\sigma,i}^{KLI} - \bar{u}_{xc}^{i\sigma}) = \bar{V}_{xc\sigma,j}^S - \bar{u}_{xc}^{j\sigma} \quad (3.20)$$

with $j=1,2,3,\dots,N_\sigma-1$. Furthermore, $\bar{V}_{xc\sigma,i}^S$ represents the orbital average

$$\bar{V}_{xc\sigma,i}^S = \int d\mathbf{r} \rho_{i\sigma}(\mathbf{r}) \sum_{j=1}^{N_\sigma} \frac{\rho_{j\sigma}(\mathbf{r}) u_{xc}^{j\sigma}(\mathbf{r})}{\rho^\sigma(\mathbf{r})} \quad (3.21)$$

and the quantities M_{ij}^σ are given by

$$M_{ij}^\sigma = \int d\mathbf{r} \frac{\rho_{j\sigma}(\mathbf{r}) \rho_{i\sigma}(\mathbf{r})}{\rho^\sigma(\mathbf{r})} \quad (3.22)$$

The first term in equation (3.18) is called the *Slater* term and the second term is referred to as the *response* or the *orbital-shift* part. The OEP and KLI equations presented thus far are completely general and can be used with any orbital dependent xc functional.

3.3.1 The exact exchange functional

The exact exchange functional (EXX) defined in equation (3.1) is reproduced here for convenience.

$$E_x^{exact}[\{\phi_{i\sigma}\}] = -\frac{1}{2} \sum_{\sigma} \sum_{i,j=1}^{N_\sigma} \int d\mathbf{r} \int d\mathbf{r}' \frac{\phi_{i\sigma}^*(\mathbf{r}) \phi_{j\sigma}^*(\mathbf{r}') \phi_{j\sigma}(\mathbf{r}) \phi_{i\sigma}(\mathbf{r}')}{|\mathbf{r} - \mathbf{r}'|} \quad (3.23)$$

The primary component that goes into building the optimized effective KLI potential is simply $u_{xc}^{i\sigma}(\mathbf{r})$ defined in equation (3.15). For the EXX functional we drop the subscript c to indicate an exchange only functional and thus $u_x^{i\sigma}(\mathbf{r})$ is given by

$$u_x^{i\sigma}(\mathbf{r}) = \frac{1}{\phi_{i\sigma}^*(\mathbf{r})} \sum_j \int d\mathbf{r}' \frac{\phi_{i\sigma}^*(\mathbf{r}') \phi_{j\sigma}(\mathbf{r}') \phi_{j\sigma}^*(\mathbf{r})}{|\mathbf{r} - \mathbf{r}'|} \quad (3.24)$$

Once $u_x^{i\sigma}(\mathbf{r})$ is calculated, $V_{x\sigma}^{KLI}(\mathbf{r})$ follows from equations (3.18-3.22)

3.3.2 The SIC functional

The methodology for the Self Interaction Corrected functionals is slightly more involved and so we present the SIC functional in more detail. In what follows we briefly discuss the SIC functional as originally proposed by Perdew and Zunger[115] and then explain the generation of the SIC-KLI potential.

In DFT, the total energy functional $E[\rho^\uparrow, \rho^\downarrow]$ (ρ^σ , $\sigma = \uparrow, \downarrow$ is the spin density, $\rho = \sum_\sigma \rho^\sigma$)

can be written as

$$E[\rho^\uparrow, \rho^\downarrow] = T_S[\rho] + \int d^3\mathbf{r} \rho(\mathbf{r})v(\mathbf{r}) + U[\rho] + E_{xc}[\rho^\uparrow, \rho^\downarrow], \quad (3.25)$$

where T_S is the kinetic energy of the non-interacting system, $v(\mathbf{r})$ the external potential, U the Hartree electrostatic energy and E_{xc} the exchange and correlation (XC) energy. This last term is not known exactly and various semilocal approximations to E_{xc} are commonly employed. For any such semilocal approximation (SLA) to E_{xc} , the SIC involves subtracting directly the SI energy of all the occupied Kohn-Sham (KS) orbitals from the total XC energy. Thus the SIC energy functional is defined as

$$E_{xc}^{\text{SIC}}[\{\rho_n^\sigma\}] = E_{xc}^{\text{SLA}}[\rho^\uparrow, \rho^\downarrow] - \sum_{n\sigma}^{\text{occupied}} (U[\rho_n^\sigma] + E_{xc}^{\text{SLA}}[\rho_n^\sigma, 0]). \quad (3.26)$$

Employing the above functional and following the Levy minimization scheme, one arrives at a set of single particle Kohn-Sham (KS) like equations for the orbitals ϕ_n^σ with corresponding eigenvalues $\epsilon_n^{\sigma, \text{SIC}}$ and occupation numbers p_n^σ

$$\left[-\frac{1}{2}\nabla^2 + v_{\text{eff},n}^\sigma(\mathbf{r}) \right] \phi_n^\sigma = \epsilon_n^{\sigma, \text{SIC}} \phi_n^\sigma, \quad (3.27)$$

such that

$$\rho^\sigma = \sum_n^{N^\sigma} p_n^\sigma \rho_n^\sigma = \sum_i^{N^\sigma} p_n^\sigma |\phi_n^\sigma|^2 \quad (3.28)$$

The effective potential $v_{\text{eff},n}^\sigma(\mathbf{r})$ appearing in (3.27) however is orbital dependent and cannot be classified as a Kohn-Sham like potential. Several different approaches have been pursued in the literature [116, 117] to deal with $v_{\text{eff},n}^\sigma(\mathbf{r})$. The simplest approach is to solve equation (3.27) directly under a normalization constraint on the orbitals with the resulting non-orthogonal orbitals being subjected to an orthogonalization procedure. Apart from leading to a non KS problem, the orbital dependent $v_{\text{eff},n}^\sigma(\mathbf{r})$ also leaves the Hamiltonian for the unoccupied states in the system ambiguous as the SIC is only defined for occupied states. Furthermore the SIC energy functional $E_{xc}^{\text{SIC}}[\{\rho_n^\sigma\}]$ in equation (3.26) is not invariant under unitary transformations of the set $\{\phi_n^\sigma\}$ of occupied orbitals. To obtain a SIC procedure that is size consistent, one usually has to work with an auxiliary set of localized orbitals $\{\psi_n^\sigma\}$ in constructing $v_{\text{eff},n}^\sigma(\mathbf{r})$. The set $\{\psi_n^\sigma\}$ is related to $\{\phi_n^\sigma\}$ in (3.27) by a unitary transformation that is chosen so as to minimize $E_{xc}^{\text{SIC}}[\{\rho_n^\sigma\}]$. However, using the Optimized

Effective Potential (OEP) method[118], the orbital dependent SIC potential $v_{\text{eff},n}^\sigma(\mathbf{r})$ can conveniently be recast into a local multiplicative orbital independent potential with the obvious advantage that the SIC problem can then be solved as a normal KS problem. The Krieger-Li-Iafrate (KLI) approximation [119] to the OEP while being computationally easier to handle, retains most of the advantages of the full OEP and is well suited to the SIC problem[120]. Thus within the KLI framework, the orbital independent effective SIC Kohn Sham potential takes the form

$$v_{KS}^\sigma(\mathbf{r}) = v_{\text{ext}}(\mathbf{r}) + v_H(\mathbf{r}) + v_{xc,SLA}^\sigma[\rho^\uparrow, \rho^\downarrow](\mathbf{r}) + v_{xc,SIC}^\sigma(\mathbf{r}) \quad (3.29)$$

where in $v_{\text{ext}}(\mathbf{r}), v_H(\mathbf{r}), v_{xc,SLA}^\sigma[\rho^\uparrow, \rho^\downarrow](\mathbf{r})$ and $v_{xc,SIC}^\sigma(\mathbf{r})$ are the external, Hartree, the approximate XC and the SIC potential respectively. Furthermore, $v_{xc,SIC}^\sigma(\mathbf{r})$ can be written as

$$v_{xc,SIC}^\sigma(\mathbf{r}) = v_{xc,SIC}^{S,\sigma}(\mathbf{r}) + \sum_{i=1}^{N^\sigma} \frac{\tilde{\rho}_i^\sigma[\Delta v_{SIC}^{i\sigma} - C^\sigma]}{\rho^\sigma(\mathbf{r})} \quad (3.30)$$

with

$$v_{xc,SIC}^{S,\sigma}(\mathbf{r}) = \sum_{i=1}^{N^\sigma} \frac{\tilde{\rho}_i^\sigma(\mathbf{r}) u_{SIC}^{i\sigma}(\mathbf{r})}{\rho^\sigma(\mathbf{r})} \quad (3.31)$$

being a Slater average over the orbital dependent $u_{SIC}^{i\sigma}(\mathbf{r})$ defined as

$$u_{SIC}^{i\sigma}(\mathbf{r}) = -\frac{\delta E_{xc}^{SLA}[\tilde{\rho}_i^\sigma, 0]}{\delta \tilde{\rho}_i^\sigma} - \int d\mathbf{r}' \frac{\tilde{\rho}_i^\sigma(\mathbf{r}')}{|\mathbf{r} - \mathbf{r}'|} \quad (3.32)$$

Note that the orbital density $\tilde{\rho}_i^\sigma$ appearing in equations (3.30-3.32) is calculated from the auxiliary set of localized orbitals $\{\psi_i^\sigma\}$ instead of the canonical $\{\phi_i^\sigma\}$. Both sets of orbitals of course give the same total density ρ^σ . The orbital shift terms $\Delta v_{SIC}^{i\sigma}$ (C^σ being a constant), are obtained by solving the algebraic equation

$$\sum_{i=1}^{N^\sigma} (\delta_{ij} - M_{ij}^\sigma) \Delta v_{SIC}^{i\sigma} = \bar{v}_{xc,SIC}^{S,j\sigma} - \bar{u}_{SIC}^{j\sigma}, \text{ with } j = 1, 2, \dots, N^\sigma \quad (3.33)$$

where in

$$M_{ij}^\sigma = \int d\mathbf{r} \frac{\tilde{\rho}_j^\sigma(\mathbf{r}) \tilde{\rho}_i^\sigma(\mathbf{r})}{\rho^\sigma(\mathbf{r})} \quad (3.34)$$

$$\bar{u}_{SIC}^{j\sigma} = \int d\mathbf{r} \tilde{\rho}_j^\sigma(\mathbf{r}) u_{SIC}^{j\sigma}(\mathbf{r}) \quad (3.35)$$

and

$$\bar{v}_{xc,SIC}^{S,j\sigma} = \int d\mathbf{r} \tilde{\rho}_j^\sigma(\mathbf{r}) v_{xc,SIC}^{S,\sigma} \quad (3.36)$$

Furthermore, the following relations hold

$$\sum_{i=1}^{N^\sigma} M_{ij}^\sigma = 1 \quad (3.37)$$

$$\sum_{i=1}^{N^\sigma} (\bar{v}_{xc,SIC}^{S,i\sigma} - \bar{u}_{SIC}^{i\sigma}) = 0 \quad (3.38)$$

which means that the linear system in (3.33) is of rank $(N^\sigma - 1)$ and must be solved using a least squares approach. Setting the constant $C^\sigma = \Delta v_{SIC}^{\text{HO},\sigma}$ (HO stands for the highest occupied orbital) corresponds to the choice where by the HO orbital energy satisfies the Janak theorem.

3.4 Implementation in SIESTA

The optimized effective potential method in the KLI approximation has been implemented in a development version of the SIESTA[121]. In SIESTA, the molecular wave functions $\phi_{i\sigma}(\mathbf{r})$ are expanded over a localized pseudo-atomic orbital basis set φ_p

$$\psi_{i\sigma}(\mathbf{r}) = \sum_p C_{ip}^\sigma \varphi_p(\mathbf{r}) \quad (3.39)$$

where $C_{ip}^\sigma = \langle \tilde{\varphi}_p | \psi_{i\sigma} \rangle$ are the expansion coefficients and $\tilde{\varphi}_p$ is the dual of φ_p such that $\langle \tilde{\varphi}_p | \varphi_q \rangle = \delta_{pq}$. Once the coefficients C_{ip}^σ are available, the wave functions $\psi_{i\sigma}(\mathbf{r})$ are directly represented on a real space mesh as the values of the basis functions $\varphi_p(\mathbf{r})$ in space can be readily interpolated from look-up tables. Potentials of the general form

$$V_{ij}^\sigma(\mathbf{r}) = \int d\mathbf{r}' \frac{\psi_{i\sigma}^*(\mathbf{r}') \psi_{j\sigma}(\mathbf{r}')}{|\mathbf{r} - \mathbf{r}'|} \quad (3.40)$$

are obtained by solving the Poisson equation for the effective density $\rho_{ij}(\mathbf{r}) = \psi_{i\sigma}^*(\mathbf{r}') \psi_{j\sigma}(\mathbf{r}')$. Note that an EXX calculation requires $N(N - 1)/2$ such solutions required to build $u_x^{i\sigma}$ in equation (3.24) while a KLI-SIC calculation requires only N such solves to build $u_{SIC}^{i\sigma}$ in

equation (3.32) where N is the number of occupied orbitals. For the KLI-SIC calculations, the Pipek-Mezey [122] localization measure is employed to obtain the auxiliary set of localized orbitals required to generate the SIC potential. Although strictly speaking, the auxiliary set of orbitals should be chosen to maximize the orbital self-interaction energy, most commonly used localization schemes such as the ones due to Edmiston-Ruedenberg, Boys, von Niessen and Pipek-Mezey give similar results (see [120, 122] and references therein). The Pipek-Mezey (PM) localization procedure in general seeks to minimize the number of atoms over which a molecular orbital extends and is naturally suited to atomic orbital basis sets. Thus, for an atom centered basis set $\{|\mu\rangle\}$, one can define the Hermitian operators,

$$P_\mu = P_\mu^\dagger = \frac{1}{2}\{|\tilde{\mu}\rangle\langle\mu| + |\mu\rangle\langle\tilde{\mu}|\} \quad (3.41)$$

where

$$|\tilde{\mu}\rangle = \sum_\nu (\mathbf{S}^{-1})_{\mu\nu} |\nu\rangle \quad (3.42)$$

such that $\langle\tilde{\mu}|\nu\rangle = \delta_{\mu\nu}$ and \mathbf{S} represents the atomic overlap matrix

$$S_{\mu\nu} = \langle\mu|\nu\rangle \quad (3.43)$$

The atomic population operators for the set of n atoms $\{A\}$ in the molecular system are defined by

$$P_A = P_A^\dagger = \sum_{\mu \in A} P_\mu \quad (3.44)$$

where the summation is over the atomic orbitals (AO) that belong to the atom A . For a set of N molecular orbitals $\{\phi_i\}$, one then seeks the $N \times N$ unitary rotation matrix U that minimizes the population localization functional defined by

$$\mathcal{P}\{\phi_i\} = \sum_{i=1}^N \sum_{A=1}^n [\langle i|P_A|i\rangle]^2 \quad (3.45)$$

The minimization is usually carried through a sequence of pairwise two by two rotations [122] over the set of molecular orbitals and the overall procedure scales as N^3 with the number of molecular orbitals N . Usually, the computational time spent during the PM localization procedure is much smaller than that spent for calculating the orbital wise electrostatic self-repulsion and exchange potentials from equation (3.40). However, the convergence of the pairwise rotation algorithm can be slow for larger systems that exhibit

a complex molecular orbital structure and one might need to employ a more sophisticated unconstrained minimization algorithm.

3.5 Application: Polarizability of molecular chains from SIC functionals

The problem of massive overestimation of the static polarizability and hyperpolarizability of molecular chains in Density Functional calculations using standard LDA and GGA approximations has been the subject of several recent investigations [106, 107, 108, 109, 110, 111, 112, 113, 114]. It has been shown that instrumental to the failure of conventional local and semi-local XC functionals is the absence of a field counteracting term in the response part of the XC potential [107, 108, 111] that ought to be present in the exact XC potential. The Self Interaction error (SIE) inherent to all semi-local functionals is a significant factor behind their poor performance in this regard. One way to improve electrical response prediction within DFT that has been widely investigated thus far is the EXX approach which completely avoids the SI problem by treating exchange exactly. An alternate orbital dependent approach that can potentially tackle the problem is Self Interaction Corrected (SIC) DFT [115], wherein the XC energy functional still employs a semi-local approximate functional but incorporates an explicit correction for the Self Interaction Error (SIE). While SIC-DFT is definitely expected to improve the performance of semi-local functionals to some degree, there exists indirect evidence in the EXX literature which suggests that SIC-DFT may not be quite adequate to match high quality wave function methods. The authors of references [107, 114] have shown that the KLI approximation to exact exchange (X-KLI) which is in principle SI free falls short of matching Hartree Fock (HF) and that a Density Functional treatment at the level of exact OEP exchange (X-OEP) is needed. However, it's difficult to predict exactly how well or how poorly SIC-DFT will perform from the above and the quantitative accuracy of SIC-DFT is still worth investigating.

To facilitate easy comparison with previous quantum Chemistry and EXX-DFT calculations [114] in the literature, we chose the widely studied test system consisting of linear hydrogen chains made up of H atoms with alternating H-H distances of 2 and 3 a_0 . The calculations are carried out using the localized orbital basis set SIESTA. An optimized atomic orbital basis set consisting of double zeta s, triple zeta p and polarized s,p functions was employed. The Pipek-Mezey [122] localization scheme was used to transform the

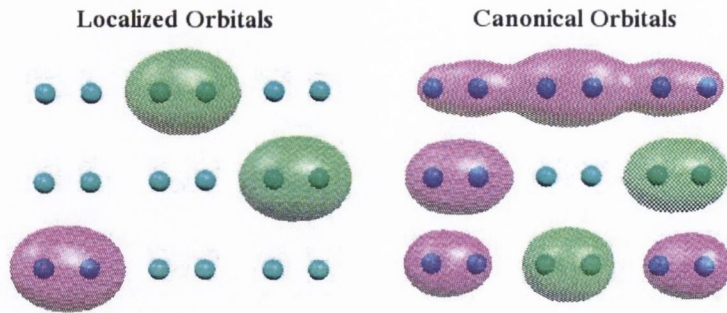


Figure 3.1: The Pipek-Mezey localized molecular orbitals (left) and Kohn-Sham orbitals (right) for the occupied subspace of the H_6 chain are shown.

canonical Kohn-Sham orbitals into the Localized Molecular Orbitals (LMOs) required to calculate the SIC potential. The occupied LMOs for the H_6 chain are shown in figure 3.1 along with the occupied KS orbitals. The static polarizability $\alpha = \delta\mu_z/\delta F_z$ was calculated numerically using finite differences.

In Table 3.1 we list the calculated α for various semi-local approximate XC functionals.

Table 3.1: static polarizability α of hydrogen chains calculated using various approximate semi-local XC functionals

H_N	$\alpha = \delta\mu_z/\delta F_z$				
	LDA	PBE	BLYP	OLYP	LB94
H_4	37.26	35.62	35.61	34.76	36.27
H_6	73.10	69.35	69.20	67.05	72.49
H_8	116.58	109.74	109.38	105.31	117.285
H_{10}	166.36	155.31	154.42	148.49	169.46
H_{12}	220.55	204.53	202.95	193.83	226.25

As one would expect the LDA [115] massively over estimates α compared to MP4 results (see Table 3.2 below) with the result worsening with increasing chain length. The GGA functionals such as PBE [123], BLYP [124, 125] and OLYP [126] are seen to marginally improve over the LDA. The OLYP functional which features Handy and Cohen's optimized exchange functional [127], seems to be the best GGA for electrical response and provides approximately a 5% improvement over the other GGAs. Also the LB94 functional [128] which has built in the right asymptotic $\frac{1}{r}$ behaviour in the tail of the XC potential, is seen to be quite poor in fact performing slightly worse than the LDA. Table 3.2 presents a comparison between α calculated from the KLI-SIC method for various underlying approximate

Table 3.2: comparison between static polarizability α of hydrogen chains calculated using the KLI-SIC method with different XC functionals, various exact exchange DFT and wavefunction methods

H_N	$\alpha = \delta\mu_z/\delta F_z$							HF	MP4
	SIC-LDA	SIC-PBE	SIC-BLYP	SIC-OLYP	EXX-KLI	EXX-OEP			
H_4	33.38	33.14	32.73	32.72	33.11	32.2	32.0	29.5	
H_6	58.56	58.07	56.99	56.81	60.64	56.6	56.4	51.6	
H_8	86.94	86.48	84.42	83.97	91.56	84.2	82.3	75.9	
H_{10}	117.28	116.16	112.64	112.54	124.87	NA	NA	NA	
H_{12}	147.96	145.98	141.75	140.90	159.27	138.1	137.6	126.9	

Table 3.3: DFT and SIC-DFT values of the static polarizability α of hydrogen chains for the exchange only (X-only) LDA and OLYP functionals

H_N	$\alpha = \delta\mu_z/\delta F_z$			
	LDA _X	OLYP _X	SIC-LDA _X	SIC-OLYP _X
H_4	38.90	34.96	33.37	32.91
H_6	76.16	67.45	58.84	57.11
H_8	121.64	105.40	87.08	83.99
H_{10}	173.89	148.07	116.77	112.45
H_{12}	231.35	193.31	147.188	140.46

XC functionals and other methods including X-KLI, X-OEP and MP4. The SIC-DFT results for α are clearly much improved in comparison to the conventional LDA/GGA results. Also, the various SIC-GGAs are seen to perform better than SIC-LDA and the same trend that is seen among the conventional GGA's is reproduced for the SIC-GGAs with SIC-OLYP doing better than the others. Overall, the best SIC-DFT results are within 2% of the exact exchange X-OEP result. Surprisingly, all the SIC-DFT results are seen to be slightly better than the KLI exact exchange results (X-KLI). In principle, the X-KLI potential is SI free and there is no reason why it should under perform w.r.t SIC-DFT. Since the X-KLI calculations were calculated at an exchange-only (X-only) level, we carried out separate X-only calculations for both the normal DFT and SIC-DFT functionals in order to filter out the effect of correlation. Results for the LSDA and OLYP functionals are listed in Table 3.3. Only in the case of conventional LDA does the correlation seem to have a sizeable effect with X-only LDA doing worse than XC-LDA. The X-only OLYP, SIC-LDA and SIC-OLYP results are seen to be very close to the corresponding full XC

results and in fact for the longer chains, the X-only results are slightly better. Its worth mentioning although the data is not presented that the same trend is seen with the other GGAs. This suggests that overall, local correlation both within normal DFT and SIC-DFT has a very minor effect on the polarizability.

At least part of the improvement in the electrical response afforded by orbital dependent

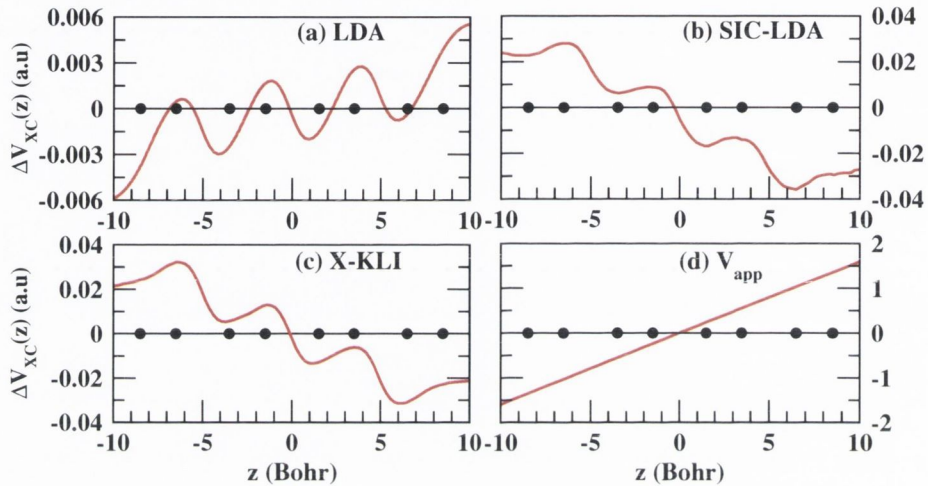


Figure 3.2: $V_{XC}^{resp}(z) = V_{XC}^{F=0.006}(z) - V_{XC}^{F=0}(z)$ is plotted against z for (a) LDA, (b) SIC-LDA, and (c) X-KLI. The applied external field is shown in (d)

methods can be traced to the so called induced depolarization field. Under an applied external electric field the XC potential in exact DFT exhibits a response term whose gradient opposes the external field. However, with semi-local approximate functionals, the gradient of the XC response term erroneously points in the same direction as the external field. Orbital dependent XC potentials on the other hand include relevant non-local information such as orbital polarization effects essential to correctly describe the XC response. Figure 3.2 plots ΔV_{XC} defined as the difference between the XC potential with and without the external field $\Delta V_{XC}(z) = V_{XC}^{F=0.006}(z) - V_{XC}^{F=0}(z)$ for LDA, SIC-LDA and X-KLI cases. Clearly the LDA potential seems to respond along the applied field direction while ΔV_{XC} for SIC-LDA and X-KLI clearly opposes the external field. Moreover, the gradient in ΔV_{XC} from SIC-LDA and X-KLI is seen to be quite similar suggesting that the depolarization field is of comparable strength in both cases. Its also informative to look at the performance of the KLI-SIC and X-KLI methods when the orbital shift terms in the potential are dropped and only the Slater average potential is retained. Its obvious comparing the α values in table 3.4 with those from tables 3.2 and 3.3 that the bulk of the correction

Table 3.4: Static polarizability α of hydrogen chains obtained from KLI-SIC and X-KLI calculations where only the Slater term in the KLI potential is used (indicated by the super-script S). Both XC and X-only results are shown for the SIC-LDA^S and SIC-OLYP^S cases.

H_N	$\alpha = \delta\mu_z / \delta F_z$				
	SIC-LDA ^S	SIC-OLYP ^S	SIC-LDA ^S _X	SIC-OLYP ^S _X	X-KLI ^S
H ₄	35.37	35.22	36.25	35.33	35.78
H ₆	67.74	66.63	68.92	66.84	69.17
H ₈	105.91	103.73	107.57	103.30	108.72
H ₁₀	148.64	144.38	150.86	143.93	152.90
H ₁₂	193.94	187.08	197.05	186.55	199.91

obtained in both KLI-SIC and X-KLI is due to the orbital shift terms in the potential. However, most of the quantitative difference in α between KLI-SIC and X-KLI is already seems to be present at the level of the Slater potential approximation. Figure 3.3 plots

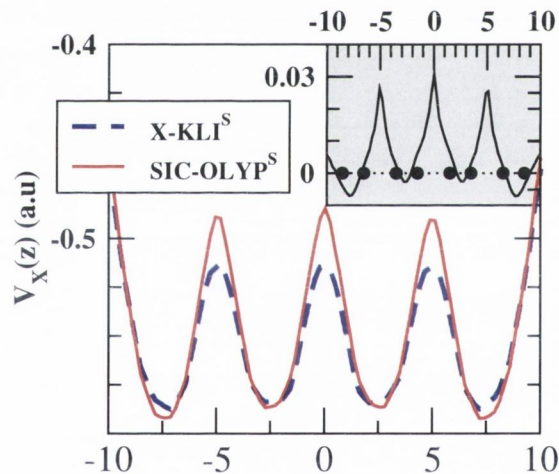


Figure 3.3: $V_{XC}(z)$ is plotted against z for SIC-OLYP^S (solid line) and X-KLI^S. The grey inset plots the difference between the two potentials.

the of XC potential from SIC-OLYP^S and the exchange potential from X-KLI^S when no external field is applied. It is apparent that SIC-OLYP potential exhibits higher peaks in the inter-molecular space between H₂ units than X-KLI. This might explain the quantitative difference in α between the two cases. It is worth noting that the improved performance of X-OEP over X-KLI can be attributed [114] to similar barriers in the inter-molecular region which however arise from the response part of the X-OEP potential.

3.6 Conclusions

Orbitals dependent functionals (ODFs) represent a class of advanced density functional approximations usually constructed to overcome some of the shortcomings in local or semi-local xc functionals. ODFs are capable of accurately describing a wider range of physical systems including some where local functionals fail completely. An elegant way to incorporate ODFs into Kohn-Sham density functional schemes is given by the optimized effective potential (OEP) methodology. However, the full OEP equations are numerically intensive to solve and approximations such as the one due to Krieger, Li and Iafrate (KLI) are commonly employed for handling larger physical systems.

We discuss two of the more popular ODFs viz., the exact exchange functional (EXX) and the self interaction correction (SIC) functional and present their implementation within the numerically efficient DFT platform of the SIESTA code. We then study the problem of overestimation of the static polarizability in density functional theory and compare the performance of SIC functionals and EXX functionals at the KLI level of approximation. We find that SIC-DFT functionals do exhibit a field counteracting term in the response part of the XC potential which is missing in LDA/GGA. As a result, the calculated polarizability in SIC-DFT is much improved in comparison to normal LDA/GGA and is found to be within a few percent of exact exchange(EXX) DFT results. The SIC-DFT results also exhibit a systematic dependence on the flavour of the underlying LDA/GGA approximation with the OLYP functional performing best among the various GGA functionals investigated. We demonstrate that SIC functionals at the KLI level, in general, perform better than X-KLI at computing the static polarizability of hydrogenic chains. This is an interesting result in view of the considerably smaller computational overheads involved with the SIC method in comparison to EXX. This work therefore opens the prospect of using SIC for evaluating the electrical response of complex polymeric materials.

Chapter 4

Atomic self-interaction correction for molecules and solids

4.1 Introduction

Density functional theory (DFT), in both its static [130] and time-dependent [131] forms, has become by far the most successful and widely used among all the electronic structure methods. The most obvious reason for this success is that it provides accurate predictions of numerous properties of atoms, inorganic molecules, bio-molecules, nanostructures and solids, thus serving different scientific communities.

In addition DFT has a solid theoretical foundation. The Hohenberg-Kohn theorem [130] establishes the existence of a unique energy functional $E[\rho]$ of the electron density ρ which alone is sufficient to determine the exact ground-state of a N -electron system. Although the energy functional itself is not known, several of its general properties can be demonstrated rigorously. These are crucial for constructing increasingly more predictive approximations to the functional and for addressing the failures of such approximations[132].

Finally, but no less important, the Kohn-Sham (KS) formulation of DFT [133] establishes a one to one mapping of the intrinsically many-body problem onto a fictitious single-particle system and offers a convenient way for minimizing $E[\rho]$. The degree of complexity of the Kohn-Sham (KS) problem depends on the approximation chosen for the density functional. In the case of the local density approximation (LDA) [133] the KS problem typically scales as N^3 , where the scaling is dominated by the diagonalization algorithm. However, clever choices with regards to basis sets and sophisticated numerical methods make order- N scaling a reality [134, 135].

The energy functional $E[\rho^\uparrow, \rho^\downarrow]$ (ρ^σ , $\sigma = \uparrow, \downarrow$ is the spin density, $\rho = \sum_\sigma \rho^\sigma$) can be written as

$$E[\rho^\uparrow, \rho^\downarrow] = T_S[\rho] + \int d^3\mathbf{r} \rho(\mathbf{r})v(\mathbf{r}) + U[\rho] + E_{xc}[\rho^\uparrow, \rho^\downarrow], \quad (4.1)$$

where T_S is the kinetic energy of the non-interacting system, $v(\mathbf{r})$ the external potential, U the Hartree electrostatic energy and E_{xc} the exchange and correlation (XC) energy. This last term is unknown and must be approximated. The construction of an approximated functional follows two strategies: empirical and “constraint satisfaction”.

Empirical XC functionals usually violate some of the constraints imposed by exact DFT, and rely on parameterizations obtained by fitting representative data. One includes in this category, XC functionals which borrow some functional dependence from other theories. This is for instance the case of the celebrated LDA+ U scheme [136, 137], where the Hubbard- U energy takes the place of the LDA energy for certain “strongly correlated” atomic orbitals (typically d and f shells). The method however depends on the knowledge of the Coulomb and exchange parameters U and J , which vary from material to material, and can also be different for the same ion in different chemical environments [138, 139].

In contrast the construction based on “constraint satisfaction” proceeds by developing increasingly more sophisticated functionals, which nevertheless satisfy most of the properties of exact DFT [140]. It was argued that this method constructs a “Jacob’s ladder” [141], where functionals are assigned to different rungs depending on the number of ingredients they include. Thus the LDA, which depends only on the spin-densities is on the first rung, the generalized gradient approximation (GGA) [142], which depends also on $\nabla\rho^\sigma$, is on the second rung, the so-called meta-GGA functionals [143], which in addition to ρ^σ and $\nabla\rho^\sigma$ depend on either the Laplacian $\nabla^2\rho^\sigma$ or the orbital kinetic energy density, are on the third rung and so on. The higher its position on the ladder the more accurate a functional becomes, but at the price of increasing computational overheads. Therefore its worth investigating corrections to the functionals of the lower rungs, which preserve most of the fundamental properties of DFT and do not generate massive additional numerical overheads.

One of the fundamental problems intrinsic to the semi-local functionals of the first three rungs is the presence of self-interaction (SI) [144]. This is the spurious interaction of an electron in a given KS orbital with the Hartree and XC potential generated by itself. Such an interaction is not present in the Hartree-Fock method, where the Coulomb self-interaction of occupied orbitals is cancelled exactly by the non-local exchange. However when using semi-local functionals such a cancellation is not complete and the rigorous

condition for KS-DFT

$$U[\rho_n^\sigma] + E_{xc}[\rho_n^\sigma, 0] = 0 \quad (4.2)$$

for the orbital density $\rho_n^\sigma = |\psi_n^\sigma|^2$ of the fully occupied KS orbital ψ_n^σ is not satisfied. A direct consequence of the self-interaction in LDA/GGA is that the KS potential becomes too repulsive and exhibits an incorrect asymptotic behavior [144].

This “schizophrenic” (self-interacting) nature of semi-local KS potentials generates a number of failures in describing elementary properties of atoms, molecules and solids. Negatively charged ions (H^- , O^- , F^-) and molecules are predicted to be unstable by LDA [145] and transition metal oxides are described as small-gap Mott-Hubbard antiferromagnets (MnO, NiO) [146] or even as ferromagnetic metals (FeO, CoO) [146] instead of charge-transfer insulators. Moreover the KS highest occupied molecular orbital (HOMO), the only KS eigenvalue that can be rigorously associated to a single particle energy [147, 148, 149], is usually nowhere near the actual ionization potential [144].

Finally XC functionals affected by SI do not present a derivative discontinuity as a function of the occupation [147, 148]. Semi-local functionals in fact continuously connect the orbital levels of systems of different integer occupation. This means for instance that when adding an extra electron to an open shell N -electron system the KS potential does not jump discontinuously by $I_N - A_N$ where I_N and A_N are respectively the ionization potential and the electron affinity for the N -electron system. This serious drawback is responsible for the incorrect dissociation of heteronuclear molecules into charged ions [150] and for the metallic conductance of insulating molecules [151].

The problem of removing the SI from a semi-local potential was acknowledged a long time ago when Fermi and Amaldi proposed a first crude correction [152]. However the modern theory of self-interaction corrections (SIC) in DFT is due to the original work of Perdew and Zunger from almost three decades ago [144]. Their idea consists in removing directly the self-Hartree and self-XC energy of all the occupied KS orbitals from the LDA XC functional (the same argument is valid for other semi-local functionals), thus defining the SIC functional as

$$E_{xc}^{SIC}[\rho^\uparrow, \rho^\downarrow] = E_{xc}^{LDA}[\rho^\uparrow, \rho^\downarrow] - \sum_{n\sigma}^{\text{occupied}} (U[\rho_n^\sigma] + E_{xc}^{LDA}[\rho_n^\sigma, 0]) . \quad (4.3)$$

Although apparently simple, the SIC method is more involved than standard KS DFT. The theory is still a density functional one, i.e. it satisfies the Hohenberg-Kohn theorem, however it does not fit into the Kohn-Sham scheme, since the one-particle potential is

orbital-dependent. This means that one cannot define a kinetic energy functional independently from the choice of E_{xc} [144]. Two immediate consequences are that the ψ_n^σ are not orthogonal, and that the orbital-dependent potential can break the symmetry of the system. This last aspect is particularly important for solids since one has to give up the Bloch representation.

In this work we explore an approximate method for SIC to the LDA, which has the benefit of preserving the local nature of the LDA potential, and therefore maintains all of the system's symmetries. We have followed in the footsteps of Filippetti and Spaldin [129], who extended the original idea of Vogel and co-workers [153, 154, 155] of considering only the atomic contributions to the SIC. We have implemented such a scheme into the localized atomic orbital code SIESTA [156] and applied it to a vast range of molecules and solids. In particular we have investigated in detail how the scheme performs as a single-particle theory, and how the SIC should be rescaled in different chemical environments.

4.2 Review of existing methods

The direct subtraction proposed by Perdew and Zunger is the foundation of the modern SIC method. However the minimization of the SIC functional (4.3) is not trivial, in particular for extended systems. The main problem is that E_{xc} itself depends on the KS orbitals. Thus it does not fit into the standard KS scheme and a more complicated minimization procedure is needed.

Following the minimization strategy proposed by Levy [157], which prescribes to minimize the functional first with respect to the KS orbitals ψ_n^σ and then with respect to the occupation numbers p_n^σ , Perdew and Zunger derived a set of single-particle equations

$$\left[-\frac{1}{2}\nabla^2 + v_{\text{eff},n}^\sigma(\mathbf{r}) \right] \psi_n^\sigma = \epsilon_n^{\sigma,\text{SIC}} \psi_n^\sigma, \quad (4.4)$$

where the effective single-particle potential $v_{\text{eff},n}^\sigma(\mathbf{r})$ is defined as

$$\begin{aligned} v_{\text{eff},n}^\sigma(\mathbf{r}) = & v(\mathbf{r}) + u([\rho]; \mathbf{r}) + v_{\text{xc}}^{\sigma,\text{LDA}}([\rho^\uparrow, \rho^\downarrow]; \mathbf{r}) - \\ & - u([\rho_n]; \mathbf{r}) - v_{\text{xc}}^{\sigma,\text{LDA}}([\rho_n^\uparrow, 0]; \mathbf{r}), \end{aligned} \quad (4.5)$$

and

$$u([\rho]; \mathbf{r}) = \int d^3\mathbf{r}' \frac{\rho(\mathbf{r}')}{|\mathbf{r} - \mathbf{r}'|}, \quad (4.6)$$

$$v_{\text{xc}}^{\sigma, \text{LDA}}([\rho^\uparrow, \rho^\downarrow]; \mathbf{r}) = \frac{\delta}{\delta \rho^\sigma(\mathbf{r})} E_{\text{xc}}^{\text{LDA}}[\rho^\uparrow, \rho^\downarrow]. \quad (4.7)$$

These are solved in the standard KS way for atoms, with good results in terms of quasi-particle energies [144]. In this particular case the KS orbitals ψ_n^σ show only small deviations from orthogonality, which is re-imposed with a standard Schmidt orthogonalization.

The problem of the non-orthogonality of the KS orbitals can be easily solved by imposing the orthogonality condition as a constraint to the energy functional, thus obtaining the following single-particle equation

$$\left[-\frac{1}{2} \nabla^2 + v_{\text{eff},n}^\sigma(\mathbf{r}) \right] \psi_n^\sigma = \sum_m \epsilon_{nm}^{\sigma, \text{SIC}} \psi_m^\sigma. \quad (4.8)$$

Even in this case where orthogonality is imposed, two major problems remain: the orbitals minimizing the energy functional are not KS-type and in general do not satisfy the system's symmetries.

If one insists in minimizing the energy functional in a KS fashion by constructing the orbitals according to the symmetries of the system, the theory will become size-inconsistent, or in other words it will be dependent on the particular representation employed. Thus one might arrive at a paradox, where in the self-interaction of N hydrogen atoms arranged on a regular lattice of large lattice spacing (in such a way that there is no interaction between the atoms) vanishes, since the SIC of a Bloch state vanishes for $N \rightarrow \infty$. However the SIC for an individual H atom, when calculated using atomic-like orbitals, accounts for essentially all the ground-state energy error [144]. Therefore a size-consistent theory of SIC DFT must look for a scheme where a unitary transformation of the occupied orbitals, which minimizes the SIC energy is performed. This idea is at the foundation of all modern implementations of SIC.

Significant progress towards the construction of a size-consistent SIC theory was made by Pederson, Heaton and Lin, who introduced two sets of orbitals: localized orbitals ϕ_n^σ minimizing $E_{\text{xc}}^{\text{SIC}}$ and canonical (Kohn-Sham) de-localized orbitals ψ_n^σ [158, 159, 160]. The localized orbitals are used for defining the densities entering into the effective potential (4.5), while the canonical orbitals are used for extracting the Lagrangian multipliers $\epsilon_{nm}^{\sigma, \text{SIC}}$, which are then associated to the KS eigenvalues. The two sets are related by unitary

transformation $\psi_n^\sigma = \sum_m \mathcal{M}_{nm}^\sigma \phi_m^\sigma$, and one has two possible strategies for minimizing the total energy.

The first consists in a direct minimization with respect to the localized orbitals ϕ_n^σ , i.e. in solving equation (4.8) when we replace ψ with ϕ and the orbital densities entering the definition of the one-particle potential (4.5) are simply $\rho_n^\sigma = |\phi_n^\sigma|^2$. In addition the following minimization condition must be satisfied

$$\langle \phi_n^\sigma | v_n^{\text{SIC}} - v_m^{\text{SIC}} | \phi_m^\sigma \rangle = 0, \quad (4.9)$$

where $v_n^{\text{SIC}} = u([\rho_n]; \mathbf{r}) + v_{\text{xc}}^{\text{LDA}}([\rho_n^\uparrow, 0]; \mathbf{r})$. An expression for the gradient of the SIC functional, which also constrains the orbitals to be orthogonal has been derived [161] and applied to atoms and molecules with a mixture of successes and bad failures [162, 163, 164].

The second strategy uses the canonical orbitals ψ and seeks the minimization of the SIC energy by varying both the orbitals ψ and the unitary transformation \mathcal{M} . The corresponding set of equations is

$$H_n^\sigma \psi_n^\sigma = (H_0^\sigma + \Delta v_n^{\text{SIC}}) \psi_n^\sigma = \sum_m \epsilon_{nm}^{\sigma, \text{SIC}} \psi_m^\sigma, \quad (4.10)$$

$$\psi_n^\sigma = \sum_m \mathcal{M}_{nm} \phi_m^\sigma, \quad (4.11)$$

$$\Delta v_n^{\text{SIC}} = \sum_m \mathcal{M}_{nm} v_m^{\text{SIC}} \frac{\phi_m^\sigma}{\psi_n^\sigma}, \quad (4.12)$$

where H_0^σ is the standard LDA Hamiltonian (without SIC). Thus the SIC potential for the canonical orbitals appears as a weighted average of the SIC potential for the localized orbitals. The solutions of the set of equations (4.10) is somehow more appealing than that associated to the localized orbitals since the canonical orbitals can be constructed in a way that preserves the system's symmetries (for instance translational invariance).

A convenient way for solving the equation (4.10) is that of using the so called ‘‘unified Hamiltonian’’ method [158]. This is defined as (we drop the spin index σ)

$$H_{\text{u}} = \sum_n^{\text{occup}} \hat{P}_n H_0 \hat{P}_n + \sum_n^{\text{occup}} (\hat{P}_n H_n \hat{Q} + \hat{Q} H_n \hat{P}_n) + \hat{Q} H_0 \hat{Q}, \quad (4.13)$$

where $\hat{P}_n = |\psi_n^\sigma\rangle\langle\psi_n^\sigma|$ is the projector over the occupied orbital ψ_n^σ , and \hat{Q} is the projector

over the unoccupied ones $\hat{Q} = 1 - \sum_n^{\text{occup}} \hat{P}_n$. The crucial point is that the diagonal elements of the matrix $\epsilon_{nm}^{\sigma, \text{SIC}}$ and their corresponding orbitals ψ_n^σ are respectively eigenvalues and eigenvectors of H_u , from which the whole $\epsilon_{nm}^{\sigma, \text{SIC}}$ can be constructed. Finally, and perhaps most important, at the minimum of the SIC functional, the canonical orbitals diagonalize the matrix $\epsilon_{nm}^{\sigma, \text{SIC}}$, whose eigenvalues can now be interpreted as an analogue of the Kohn-Sham eigenvalues [160].

It is also interesting to note that an alternative way for obtaining orbital energies is that of constructing an effective SI-free local potential using the Krieger-Li-Iafrate method [165]. This has been recently explored by several groups [166, 167, 168]

When applied to extended systems the SIC method demands considerable additional computational overheads over standard LDA. Thus for a long time it has not encountered the favor of the general solid state community. In the case of solids the price to pay for not using canonical orbitals is enormous since the Bloch representation should be abandoned and in principle infinite cells should be considered. For this reason the second minimization scheme, in which the canonical orbitals are in a Bloch form, is more suitable. In this case for each \mathbf{k} -vector one can derive an equation identical to equation (4.10), where $\epsilon_{nm}^{\sigma, \text{SIC}} = \epsilon_{nm}^{\sigma, \text{SIC}}(\mathbf{k})$ and n is simply the band index [169]. The associated localized orbitals ϕ for instance can be constructed as Wannier functions and the minimization scheme proceeds in a similar way to that done for molecules.

The problem here is that in practice, the cell needed to describe the localized states ϕ may be considerably larger than the primitive unit cell. This is not the case for ionic insulators [169], where the localized orbitals are well approximated by atomic orbitals. Such a simplification is however not valid in general. For example supercells as large as 500 atoms have been considered for describing the localized d shells in transition metals oxides [170, 171, 172]. Despite these difficulties the SIC scheme has been applied to a vast range of solid state systems with systematic improvement over LDA. These include, in addition to transition metals monoxides [170, 172, 173], rare-earth materials [174], diluted magnetic semiconductors [175], Fe_3O_4 [176], heavy elements compounds [177], just to name a few.

In order to make the SIC method more scalable several approximations have been proposed. One possibility is that of incorporating part of the SIC into the definition of the pseudopotentials [178]. The idea consists in subtracting the atomic SI from the free atom, and then transferring the resulting electronic structure to the definition of a standard norm-conserving pseudopotential. This approximation is sustained by the fact that the

transformation \mathcal{M} , which relates canonical and localized orbitals does hardly mix core and valence states [160]. Thus the SIC contribution to the total energy can be separated into the contributions from the core and the valence and in first approximation the latter can be neglected [179]. The benefit of this method is that translational invariance is regained and the complicated procedure of minimizing \mathcal{M} is replaced by a pseudopotential calculation.

A further improvement over the pseudopotential method was recently presented by Vogel and co-workers [153, 154, 155] and then extended by Filippetti and Spaldin [129]. The method still assumes separability between the core and the valence contributions to the SIC, but now the SIC for the valence electrons is approximated by an atomic-like contribution, instead of being neglected. This atomic SIC (ASIC) scheme is certainly a drastic approximation, since it implicitly assumes that the transformation \mathcal{M} minimizing the SIC functional leads to atomic like orbitals.

In the work of Vogel this additional contribution is not evaluated self-consistently for the solid, while the implementation of Filippetti assumes a linear dependence of the SIC over the orbital occupation. In spite of the approximations involved, the method has been applied successfully to a range of solids including II-VI semiconductors and nitrides [153, 154, 129], transition metal monoxides [129, 180], silver halides [155], noble metal oxides [181], ferroelectric materials [129, 182, 183], high-k materials [184] and diluted magnetic semiconductors [185, 186]. Interestingly most of the systems addressed by the ASIC method are characterized by semi-core d orbitals, for which an atomic correction looks appropriate, and a similar argument is probably valid for ionic compounds as recently demonstrated for the case of SiC [187].

Here we further investigate the self-consistent ASIC method [129] by examining both finite and extended systems, and by critically considering whether a scaling factor, additional to the orbital occupation, is needed for reproducing the correct single particle spectrum.

4.3 Formalism and Implementation

In this section we derive the fundamental equations of the ASIC method, while looking closely at the main approximations involved in comparison to the fully self-consistent SIC approach. Our practical implementation is also described.

4.3.1 The ASiC potential

The starting point of our analysis is the SIC Schrödinger-like equation (4.10) for the canonical orbitals. Let us assume, as from reference [179], that the rotation \mathcal{M} transforming localized orbitals (to be determined) into canonical orbitals (see equation (4.11)) does not mix core and valence states. We also assume that core electrons are well localized into atomic-like wave-functions and that they can be effectively described by a norm-conserving pseudopotential.

Let us now assume that \mathcal{M} is known and so are the localized orbitals ϕ_m^σ . In this case the canonical orbitals diagonalize $\epsilon_{nm}^{\sigma, \text{SIC}}$ and the equation (4.10) simply reduces to

$$(H_0^\sigma + \Delta v_n^{\text{SIC}})\psi_n^\sigma = \epsilon_n^{\sigma, \text{SIC}}\psi_n^\sigma, \quad (4.14)$$

with Δv_n^{SIC} defined in equation (4.12). The Hamiltonian $H_0^\sigma + \Delta v_n^{\text{SIC}}$ can be then re-written in a convenient form as

$$H_0^\sigma + \Delta v_n^{\text{SIC}} = H_0^\sigma + \sum_m v_m^{\text{SIC}} \hat{P}_m^\phi, \quad (4.15)$$

where v_m^{SIC} is the self-interaction potential for the localized orbital ϕ_m^σ , and \hat{P}_m^ϕ is the projector over the same state

$$\hat{P}_m^\phi \psi_n^\sigma(\mathbf{r}) = \phi_m^\sigma(\mathbf{r}) \int d^3\mathbf{r}' \psi_n^\sigma(\mathbf{r}') \phi_m^{\sigma\dagger}(\mathbf{r}') = \phi_m^\sigma(\mathbf{r}) \langle \phi_m^\sigma | \psi_n^\sigma \rangle. \quad (4.16)$$

Two main approximations are then taken in the ASiC approach [153, 129]. First the localized states ϕ_m^σ are assumed to be atomic-like orbitals Φ_m^σ (ASiC orbitals) and the SIC potential is approximated as

$$\sum_m v_m^{\text{SIC}}(\mathbf{r}) \hat{P}_m^\phi \rightarrow \alpha \sum_m \tilde{v}_m^{\sigma, \text{SIC}}(\mathbf{r}) \hat{P}_m^\Phi, \quad (4.17)$$

with $\tilde{v}_m^{\sigma, \text{SIC}}(\mathbf{r}) = u([\rho_m]; \mathbf{r}) + v_{\text{xc}}^{\sigma, \text{LDA}}([\rho_m^\uparrow, 0]; \mathbf{r})$ and $\rho_m^\sigma = |\Phi_m^\sigma|^2$, \hat{P}_m^Φ is the projector of equation (4.16) obtained by replacing the ϕ 's with the ASiC orbitals Φ , and α is a scaling factor. Note that the orbitals Φ_m are not explicitly spin-dependent and one simply has $\Phi_m^\sigma = \Phi_m p_m^\sigma$ with p_m^σ the orbital occupation ($p_m^\sigma = 0, 1$). The factor α is an empirical factor, which accounts for the particular choice of ASiC orbitals. This first approximation is expected to be accurate for systems retaining an atomic-like charge density as in the case of small molecules. It is also formally exact in the one-electron limit (for $\alpha = 1$). In

the case of extended solids the situation is less transparent, since in general the functions minimizing $E_{\text{xc}}^{\text{SIC}}$ are Wannier-like functions [188].

The second approximation taken in the ASIC method is that of replacing the non-local projector \hat{P}_m^Φ with its expectation value. The idea is that the SIC potential for the canonical orbitals Δv_n^{SIC} is formally a weighted average of the SIC potential for the localized orbitals v_m^{SIC} . For the exact SIC method the weighting factor is the non-local projector $\mathcal{M}_{nm} \frac{\phi_m^\sigma}{\psi_n^\sigma}$. This means that the SIC potential for a given canonical orbital ψ_n is maximized in those regions where the overlap with some of the localized orbitals ϕ_m is maximum. In the ASIC method such non-local projector is replaced more conveniently by a scalar. In the original proposal by Vogel et al. [153, 154, 155] this was simply set to one. Here we consider the orbital occupation p_m^σ of the given ASIC orbital Φ_m , i.e. we replace \hat{P}_m^Φ with its expectation value

$$\hat{P}_m^\Phi \rightarrow \langle \hat{P}_m^\Phi \rangle = p_m^\sigma = \sum_n f_n^\sigma \langle \psi_n^\sigma | \hat{P}_m^\Phi | \psi_n^\sigma \rangle, \quad (4.18)$$

where f_n^σ is the occupation number of the Kohn-Sham orbital ψ_n^σ . The final form of ASIC potential is then

$$v_{\text{ASIC}}^\sigma(\mathbf{r}) = \alpha \sum_m \tilde{v}_m^{\sigma\text{SIC}}(\mathbf{r}) p_m^\sigma. \quad (4.19)$$

Let us now comment on the empirical scaling factor α . In reference [129] α was set to 1/2 in order to capture eigenvalue relaxation. This choice however violates the one-electron limit of the SIC potential, which is correctly reproduced for $\alpha = 1$. We can then interpret α as a measure of the deviation of the ASIC potential from the exact SIC potential. Ultimately α reflects the deviation of the actual ASIC projectors $|\Phi\rangle\langle\Phi|$ from the localized orbitals defining the SI corrected ground state. One then expects α to be close to 1 for systems with an atomic-like charge density, and to vanish for metals, whose valence charge density resembles that of a uniform electron gas [189]. Intermediate values are then expected for situations different from these two extremes, and we will show that a values around 1/2 describe well a vast class of mid- to wide-gap insulators.

4.3.2 Implementation

The final form of the SIC potential to subtract from the LSDA (local spin density approximation) one (equation (4.19)) is that of a linear combination of non-local pseudopotential-like terms. These are uniquely defined by the choice of exchange and correlation potential used and by ASIC orbitals Φ_m . The practical way of constructing such potentials, i.e.

the way of importing the atomic SIC to the solid state, depends on the specific numerical implementation used for the DFT algorithm. At present plane-wave and gaussian orbital implementations are available [129, 153, 154, 155], while here we present our new scheme based on the pseudo atomic orbital (PAO) [193] code SIESTA [156].

We start by solving the atomic all-electron SIC-LSDA equation for all the species involved in the solid state calculation. Here we apply the original Perdew-Zunger (PZ-SIC) formalism [144] and we neglect the small non-orthogonality between the Kohn-Sham orbitals. Thus we obtain a set of SI corrected atomic orbitals Φ_m , which exactly solve the atomic SIC-LSDA problem. The atomic orbitals Φ_m describing the valence electrons are then used to define the ASIC potentials $\tilde{v}_m^{\sigma\text{SIC}}$

$$\tilde{v}_m^{\sigma\text{SIC}}(\mathbf{r}) = u([\rho_m]; \mathbf{r}) + v_{\text{xc}}^{\sigma\text{LDA}}([\rho_m^\dagger, 0]; \mathbf{r}) \quad (4.20)$$

with $\rho_m^\sigma = |\Phi_m|^2$.

At the same time a standard LSDA calculation for the same atoms is used to construct the pseudopotentials describing the core electrons. These are standard norm-conserving scalar relativistic Troullier-Martins pseudopotentials [190] with nonlinear core corrections [191]. Thus we usually neglect the SIC over the core states, when constructing the pseudopotentials. This is justified by the fact that the eigenvalues for the SIC-LSDA-pseudoatom, i.e. for the free atom where the effects of core electrons are replaced by LSDA pseudopotentials but SIC is applied to the valence electrons, are in excellent agreement with those obtained by all-electron SIC-LSDA calculations [153].

The final step is that of recasting the ASIC potentials $\tilde{v}_m^{\sigma\text{SIC}}(\mathbf{r})$, which have a $-2/r$ asymptotic behaviour, in a suitable non-local form. This is obtained with the standard Kleinman-Bylander [192] scheme and the final ASIC potential (equation (4.19)) is written as

$$v_{\text{ASIC}}^\sigma = \sum_m \frac{|\gamma_m^\sigma\rangle\langle\gamma_m^\sigma|}{C_m^\sigma}, \quad (4.21)$$

where the ASIC projectors are given by

$$\gamma_m^\sigma(\mathbf{r}) = \alpha p_m^\sigma \tilde{v}_m^{\sigma\text{SIC}}(\mathbf{r}) \Phi_m'(\mathbf{r}). \quad (4.22)$$

and the normalization factors are

$$C_m^\sigma = \alpha p_m^\sigma \langle \Phi_m' | \tilde{v}_m^{\sigma\text{SIC}} | \Phi_m' \rangle. \quad (4.23)$$

The orbital functions Φ'_m are atomic-like functions with a finite range, which ensure that the ASIC projectors γ_m do not extend beyond that range. These are constructed in the same way as the SIESTA basis set orbitals, i.e. as solutions of the pseudo-atomic problem with an additional confining potential at the cutoff radius r_{cutoff} [193]. The choice of the appropriate cutoff radius for the SIC projectors should take into account the two following requirements. On the one hand it should be sufficiently large to capture most of the SIC corrections. A good criterion [129] is that the SIC-LSDA contribution to the orbital energy of the free atom

$$\delta\varepsilon_{\text{SIC } m}^{\sigma} = \langle \Phi'_m | \tilde{v}_m^{\sigma \text{SIC}} | \Phi'_m \rangle \quad (4.24)$$

is reproduced within some tolerance. On the other hand the cutoff should be reasonably short so as not to change the connectivity of the matrix elements of the PAO Hamiltonian. In other words we need to ensure that orbitals otherwise considered as disconnected in evaluating the various parts of the Hamiltonian matrix are not considered connected for the v_{ASIC}^{σ} matrix elements alone.

As a practical rule we set the cutoff radius for a particular orbital of a given atom to be either equal to the longest among the cutoff radii of the PAO basis set for that particular atom (typically the first ζ of the lowest angular momentum), or, if shorter, the radius at which $\delta\varepsilon_{\text{SIC } m}^{\sigma} < 0.1\text{mRy}$. Typically, when reasonable cutoff radii (6 to 9 Bohr) are used, we find that the atomic SIC-LSDA eigenvalues are reproduced to within 1 to 5 mRy for the most extended shells and to within 0.1 mRy for more confined shells. Thus $\delta\varepsilon_{\text{SIC } m}^{\sigma}$ are rather well converged already for cutoff radii defined by a PAO energies shifts [156] of around 20mRy, although usually smaller PAO energy shifts are necessary for highly converged total energy calculations.

Finally the matrix elements of the SIC potential are calculated as usual over the SIESTA basis set. Additional basis functions χ_m are constructed from the confined localized atomic orbitals described before using the split-norm scheme [193, 194, 195]. The density matrix ρ^{σ} is represented over such basis $\rho_{\mu\nu}^{\sigma}$ and the orbital populations are calculated as

$$p_m^{\sigma} = \sum_{\mu\nu} S_{m\mu} \rho_{\mu\nu}^{\sigma} S_{\nu m} , \quad (4.25)$$

where $S_{m\mu}$ is a matrix element of the overlap matrix. Note that in principle the orbital population should be constructed for the atomic SIC orbital Φ_m . However, we notice that p_m^{σ} is rather insensitive to the specific choice of orbital, once this has a reasonable radial

range. For practical numerical reasons in the present implementation, we always use the orbital populations projected onto the basis set sub-space consisting of the most extended first- ζ orbitals of the atomic species involved. The matrix elements of the SIC potential are simply

$$(v_{\text{ASIC}}^{\sigma})_{\mu\nu} = \sum_m \frac{\langle \chi_{\mu} | \gamma_m^{\sigma} \rangle \langle \gamma_m^{\sigma} | \chi_{\nu} \rangle}{C_m^{\sigma}}, \quad (4.26)$$

and the ASIC-KS equation takes the final form

$$\left[-\frac{1}{2} \nabla^2 + v_{\text{PP}} + u + v_{\text{xc}}^{\sigma, \text{LSDA}} - v_{\text{ASIC}}^{\sigma} \right] \psi_n^{\sigma} = \epsilon_n^{\sigma, \text{SIC}} \psi_n^{\sigma}. \quad (4.27)$$

with v_{PP} the pseudopotential.

4.3.3 Total Energy

The energy corresponding to the SIC-LSDA functional is given by [144]

$$E^{\text{SIC}}[\rho^{\uparrow}, \rho^{\downarrow}] = E^{\text{LSDA}}[\rho^{\uparrow}, \rho^{\downarrow}] - \sum_{n\sigma}^{\text{occ.}} (U[\rho_n^{\sigma}] + E_{\text{xc}}^{\text{LSDA}}[\rho_n^{\sigma}, 0]), \quad (4.28)$$

where

$$U[\rho_n^{\sigma}] = \int d^3\mathbf{r} \frac{1}{2} \rho_n(\mathbf{r}) u([\rho_n]; \mathbf{r}), \quad (4.29)$$

$$E_{\text{xc}}^{\text{LSDA}}[\rho_n^{\sigma}, 0] = \int d^3\mathbf{r} \rho_n(\mathbf{r}) \mathcal{E}_{\text{xc}}^{\text{LSDA}}([\rho_n]; \mathbf{r}), \quad (4.30)$$

with $\mathcal{E}_{\text{xc}}^{\text{LSDA}}$ the LSDA exchange and correlation energy density. The orbital densities entering in the SI term are those associated to the local orbitals ϕ . As we have already mentioned, this functional needs to be minimized with respect to the ϕ 's, which are an implicit function of the total spin density ρ^{σ} . In the ASIC approximation these orbitals are not minimized, but taken as atomic functions. This means that in the present form the theory is not variational, in the sense that there is no functional related to the KS equation (4.27) by a variational principle. With this in mind we adopt the expression of equation (4.28) as a suitable energy, where the orbital densities are those given by the ASIC orbitals

$$\rho_m^{\sigma}(\mathbf{r}) = p_m^{\sigma} |\Phi_m|^2. \quad (4.31)$$

In our implementation the LSDA KS energy E^{LSDA} is directly available as calculated

in the SIESTA code [156] and thus, only the second term of equation (4.28) needs to be calculated. This is easily done by calculating both U and E_{xc}^{LSDA} on an atomic radial grid for each atomic orbital in the system.

4.3.4 ASIC and LDA+ U

We now compare our ASIC method with another atomic-like correction to LSDA, namely the LDA+ U method [136, 137]. In LDA+ U one replaces the LSDA exchange and correlation energy associated to the “correlated” orbitals (d or f shells), with the Hubbard- U energy. Thus the functional becomes

$$E^{\text{LDA}+U}[\rho(\mathbf{r})] = E^{\text{LSDA}}[\rho(\mathbf{r})] + E^U[\{p_m^\sigma\}] - E^{\text{DC}}[\{p_m^\sigma\}], \quad (4.32)$$

where the Hubbard energy E^U and the double counting term E^{DC} depend on the orbital populations p_m^σ of the correlated orbitals. Several forms for the LDA+ U functional have been proposed to date. A particularly simple and transparent one [138, 196], which is also rotationally invariant, redefines the U parameter as an effective parameter $U_{\text{eff}} = U - J$ and the functional takes the form

$$E^U - E^{\text{DC}} = \frac{U_{\text{eff}}}{2} \sum_I \sum_{m\sigma} \left[p_{mm}^{I\sigma} - \sum_n p_{mn}^{I\sigma} p_{nm}^{I\sigma} \right] \quad (4.33)$$

where in we separate out the index for the atomic position I from the magnetic quantum number m , and introduce the off-diagonal populations $p_{mn}^{I\sigma} = \sum_\alpha f_\alpha^\sigma \langle \psi_\alpha^\sigma | \hat{P}_{mn}^{I\Phi} | \psi_\alpha^\sigma \rangle$ with $\hat{P}_{mn}^{I\Phi} = |\Phi_m^I\rangle \langle \Phi_n^I|$. Note that the LDA+ U functional is SI free for those orbitals that are corrected.

Although a rotationally invariant form of the ASIC potential can be easily derived, we assume here for simplicity that the system under consideration is rotationally invariant, or alternatively that we have carried out a rotation, which diagonalizes the $p_{mn}^{I\sigma}$ matrix. In this case the energy becomes simply

$$E^U - E^{\text{DC}} = \frac{U_{\text{eff}}}{2} \sum_{Im\sigma} p_m^{I\sigma} [1 - p_m^{I\sigma}], \quad (4.34)$$

with $p_m^{I\sigma} = p_{mm}^{I\sigma}$. It is then easy to compute the KS potential

$$v^{\text{LDA}+U} = v^{\text{LSDA}} + \sum_{Im\sigma} U_{\text{eff}} \left[\frac{1}{2} - p_m^{I\sigma} \right] \hat{P}_m^{I\Phi}, \quad (4.35)$$

and the orbital energy

$$\epsilon_m^{I\sigma} = \frac{\partial E}{\partial p_m^{I\sigma}} = \epsilon_m^{I\sigma \text{ LSDA}} + U_{\text{eff}} \left(\frac{1}{2} - p_m^{I\sigma} \right). \quad (4.36)$$

These need to be compared with the ASIC potential (equation (4.19)) and orbital energy

$$\epsilon_m^{I\sigma} = \epsilon_m^{I\sigma \text{ LSDA}} - \alpha p_m^{I\sigma} \langle \Phi_m^{I'} | \tilde{v}_{Im}^{\sigma \text{ SIC}} | \Phi_m^{I'} \rangle, \quad (4.37)$$

where the last term follows from $\frac{\partial E}{\partial p_m^{I\sigma}} = C_m^{I\sigma}$ and from equation (4.28). The main difference between the ASIC and LDA+ U method is in the way in which unoccupied states are handled. In fact, while LDA+ U corrects unoccupied states and pushes the orbital energies upwards by $\sim U_{\text{eff}}/2$, ASIC operates only on occupied states, that are shifted towards lower energies by $C_m^{I\sigma}$. This reflects the fact that the SIC is defined only for occupied KS orbitals. An important consequence is that the opening of bandgaps in the electronic structures, one of the main features of both the LDA+ U and ASIC schemes, is then driven by two different mechanisms. On the one hand in LDA+ U , gaps open up since occupied and unoccupied states are corrected in opposite directions leading to a gap of $\sim U_{\text{eff}}$. On the other hand ASIC is active only over occupied states and gaps open only if occupied and unoccupied bands have large differences in their projected atomic orbital content. Thus one should not expect any corrections for covalent materials where conduction and valence bands are simply bonding and antibonding states formed by the same atomic orbitals. This is for instance the case of Si and Ge. In contrast ASIC will be extremely effective for more ionic situations, where the orbital contents of conduction and valence bands are different.

Finally, by comparing the corrections to the orbital energy of a fully occupied state, one finds

$$U = 2\alpha \langle \Phi_m^{I'} | \tilde{v}_{Im}^{\sigma \text{ SIC}} | \Phi_m^{I'} \rangle, \quad (4.38)$$

which establishes an empirical relation between the Hubbard energy and the ASIC correction. Since U is sensitive to the chemical environment due to screening [138], while all the other quantities are uniquely defined by an atomic calculation, we can re-interpret the parameter α as empirically describing the screening from the chemical environment within

the ASIC scheme.

4.4 Results: Extended systems

The test calculations that we present in this work are for two classes of materials: extended and finite. First we investigate how our implementation performs in the solid state. In particular we discuss the rôle of the parameter α in determining the bandstructure of several semiconductors, considering both the KS band-gap and the position of bands associated with tightly bound electrons.

4.4.1 Estimate of α for semiconductors

The quasi-particle band gap E_g in a semiconductor is defined as the difference between its ionization potential I and electron affinity A . These can be rigorously calculated from DFT as the HOMO energy respectively of the neutral and negatively charged systems. This actual gap cannot be directly compared with the KS band-gap E_g^{KS} , defined as the difference between the orbital energy of the HOMO and LUMO states of the neutral system. In fact, the presence of a derivative discontinuity in the DFT energy as a function of the electron occupation establishes the following rigorous relation [148, 197]

$$E_g = E_g^{\text{KS}} + \Delta_{\text{xc}}, \quad (4.39)$$

with

$$\Delta_{\text{xc}} = \lim_{\omega \rightarrow 0^+} \left\{ \frac{\delta E_{\text{xc}}[n]}{\delta n} \Big|_{N+\omega} - \frac{\delta E_{\text{xc}}[n]}{\delta n} \Big|_{N-\omega} \right\}_{n_N}. \quad (4.40)$$

This is valid even for the exact XC potential, and therefore in principle one has to give up KS bandstructures as a tool for evaluating semiconductor band-gaps. The size of Δ_{xc} is however not known for real extended systems and the question of whether most of the error in determining E_g from E_g^{KS} is due to the approximation in the XC potential or due to the intrinsic Δ_{xc} is a matter of debate.

In general SI-free potentials bind more than LSDA and one expects larger gaps. Surprisingly, functionals based on exact exchange, provide KS gaps rather close to the experimental values [198, 199]. The reason for such a good agreement is not fully understood, but it is believed that the exact KS gaps should be smaller than the actual ones.

With this in mind, we adopt a heuristic approach and we use the KS band-gap as a

quality indicator for interpreting the parameter α and for providing its numerical value for different classes of solids. Here we investigate the dependence of E_g^{KS} over α and we determine the value for α yielding the experimental band-gap. Assuming that Δ_{xc} does not vary considerably across the materials investigated, this will allow us to relate α to the degree of localization in a semiconductor and to extract the value useful for ASIC to be an accurate single-particle theory.

In figure 4.1 we present the band-gap of four representative semiconductors as a function of α together with the value needed to reproduce the experimental band-gap. LSDA corresponds to $\alpha = 0$ and while $\alpha = 1$ accounts for the full ASIC. In general E_g^{KS} increases

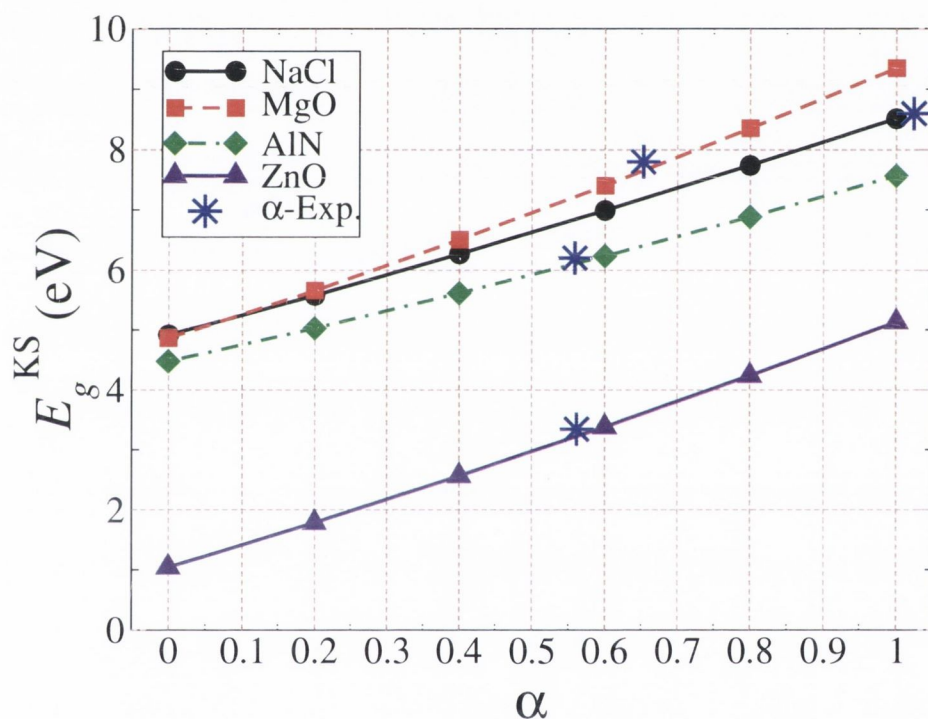


Figure 4.1: Calculated band-gap for NaCl, MgO, AlN and ZnO as a function of the parameter α . $\alpha = 0$ is the LSDA value and $\alpha = 1$ accounts for complete atomic SIC. The lattice parameters used for the calculations are either the equilibrium LSDA or the experimental when available.

as α increases, as a result of the stronger SIC. The $E_g^{\text{KS}}(\alpha)$ curve is almost linear with a slope, which appears to be material-specific.

For the most ionic compound, NaCl, the experimental gap is reproduced almost exactly by $\alpha = 1$, i.e. by the full ASIC. This is somehow expected since the charge density of solid NaCl is rather close to a superposition of the Na^+ and Cl^- ionic charge densities. In

this case of strongly localized charge densities the ASIC approximation is rather accurate yielding results substantially identical to those obtained with full self-consistent PZ-SIC [169]. Indeed earlier calculations for LiCl [169] demonstrate that the SIC band-structure is rather insensitive of the localized orbitals ϕ once these have an atomic-like form.

For the other compounds the localized orbitals ϕ 's are not necessarily atomic-like functions and deviations from $\alpha = 1$ are expected. Interestingly we find that, for all the materials investigated, a value of around 1/2 reproduces the experimental band-gap rather accurately. As an illustration, in table 4.1 we compare the experimental band-gap E_g^{exp} to the calculated E_g^{KS} for ASIC ($\alpha = 1$) and LDA, for several semiconductors ranging from ionic salts to wide-gap II-VI and III-V semiconductors. We also report the value of $\alpha = \alpha^*$ needed for $E_g^{\text{exp}} = E_g^{\text{KS}}$.

Table 4.1: Experimental E_g^{exp} and KS E_g^{KS} band-gap (in eV) for a number of semiconductors. E_g^{KS} are calculated with both LSDA and ASIC ($\alpha = 1$). In the last column we report the value of $\alpha = \alpha^*$ needed for $E_g^{\text{exp}} = E_g^{\text{KS}}$. The lattice parameters used for the calculations are either the equilibrium LSDA or the experimental when available (in Å). RS=rocksalt, WZ=wurtzite, ZB=zinblende. The value for the experimental gaps are from the literature: *a* [200], *b* [201], *c* [202], *d* [203], *e* [204], *f* [205], *g* [206], *h* [207], *i* [208]

Solid	Structure	E_g^{exp}	$E_g^{\text{KS-LSDA}}$	$E_g^{\text{KS-ASIC}}$	α
LiCl	RS ($a = 5.13$)	9.4 ^{<i>a</i>}	6.23	9.76	0.89
NaCl	RS ($a = 5.63$)	8.6 ^{<i>b</i>}	4.91	8.51	1.02
KCl	RS ($a = 6.24$)	8.5 ^{<i>c</i>}	4.90	8.51	0.99
MgO	RS ($a = 4.19$)	7.8 ^{<i>d</i>}	4.86	9.36	0.65
CaO	RS ($a = 4.74$)	7.08 ^{<i>d</i>}	4.93	9.28	0.49
SrO	RS ($a = 5.03$)	5.89 ^{<i>e</i>}	4.20	7.80	0.47
AlN	WZ ($a = 3.11, c = 4.98$)	6.20 ^{<i>f</i>}	4.47	7.56	0.56
GaN	WZ ($a = 3.16, c = 5.13$)	3.39 ^{<i>g</i>}	2.21	5.03	0.44
InN	WZ ($a = 3.54, c = 5.70$)	0.7 ^{<i>h</i>}	0.09	2.09	0.45
ZnO	WZ ($a = 3.23, c = 5.19$)	3.43 ^{<i>i</i>}	0.85	5.13	0.57
ZnS	ZB ($a = 5.40$)	3.78 ^{<i>i</i>}	2.47	4.90	0.53
ZnSe	ZB ($a = 5.63$)	2.82 ^{<i>i</i>}	1.77	3.53	0.58

Clearly for all the strongly ionic compounds (LiCl, NaCl and KCl) the full ASIC correction $\alpha = 1$ reproduces quite accurately the experimental gap and agrees with previous self-consistent SIC calculations [209]. For all the other compounds a value of around 1/2 is always adequate, confirming the initial choice of Filippetti and Spaldin. For these materials we do not find any particular regularity. In general α is large when the experimental gap is large, however there is no direct connection between α and the ionicity or covalency

of a compound. In fact, the improvement of the band-gap is not simply due to a rigid shift of the valence band, but usually corresponds to a general improvement of the whole quasi-particle spectrum. Examples for ZnO and GaN will be presented in the next section.

As a further proof of this point in table 4.2 we present the valence band-width for the semiconductors investigated as calculated from LSDA ΔE_v^{LSDA} and ASIC for both $\alpha = 1$ ($\Delta E_v^{\text{ASIC}_1}$) and $\alpha = \alpha^*$ ($\Delta E_v^{\text{ASIC}_{\alpha^*}}$). We also report the experimental values ΔE_v^{exp} whenever available, although a direct comparison with experiments is difficult, since these values are rather imprecise and sometimes not known. The general feature is that ASIC produces only minor corrections over LSDA, and that these corrections do not follow a generic trend. Thus, while for the nitrites ASIC always increases the band-width, it does just the opposite for KCl, SrO and CaO.

Table 4.2: Valence band experimental bandwidth ΔE_v^{exp} compared with those obtained from ASIC ($\alpha = 1$) $\Delta E_v^{\text{ASIC}_1}$, LSDA (ΔE_v^{LSDA}) and ASIC with the optimal $\alpha = \alpha^*$ from table 4.1 $\Delta E_v^{\text{ASIC}_{\alpha^*}}$ for a number of semiconductors. The lattice parameters used for the calculations are either the equilibrium LSDA or the experimental when available (in Å). The experimental values are from the literature (last column).

Solid	ΔE_v^{exp}	$\Delta E_v^{\text{ASIC}_1}$	ΔE_v^{LSDA}	$\Delta E_v^{\text{ASIC}_{\alpha^*}}$	Reference
LiCl	4-5	3.52	3.06	3.51	[209]
NaCl	1.7-4.5	2.11	2.06	2.11	[209]
KCl	2.3-4.3	1.09	1.21	1.09	[209]
MgO	3.3-6.7	5.16	4.83	5.06	[210, 211]
CaO	0.9	2.72	2.89	2.82	[211]
SrO		2.21	2.53	2.39	
AlN	6.0	7.44	6.27	6.92	[212]
GaN	7.4	8.42	7.33	7.85	[213]
InN	6.0	6.66	6.01	6.34	[214]
ZnO	~5	5.66	4.77	5.54	[215]
ZnS	5.5	6.49	5.57	6.05	[216]
ZnSe	5.6	7.14	5.35	6.38	[216]

4.4.2 Wide-gap semiconductors: ZnO and GaN

Having established $\alpha = 1/2$ as an appropriate value for II-VI and III-V semiconductors, we now look at the whole band-structure (not just the fundamental gap) for a few test cases. Here we consider ZnO and GaN for which photo-emission data disagree quite remarkably

from LSDA calculations. In figure 4.2 we compare the band structure of wurtzite ZnO obtained respectively from LSDA and our ASIC.

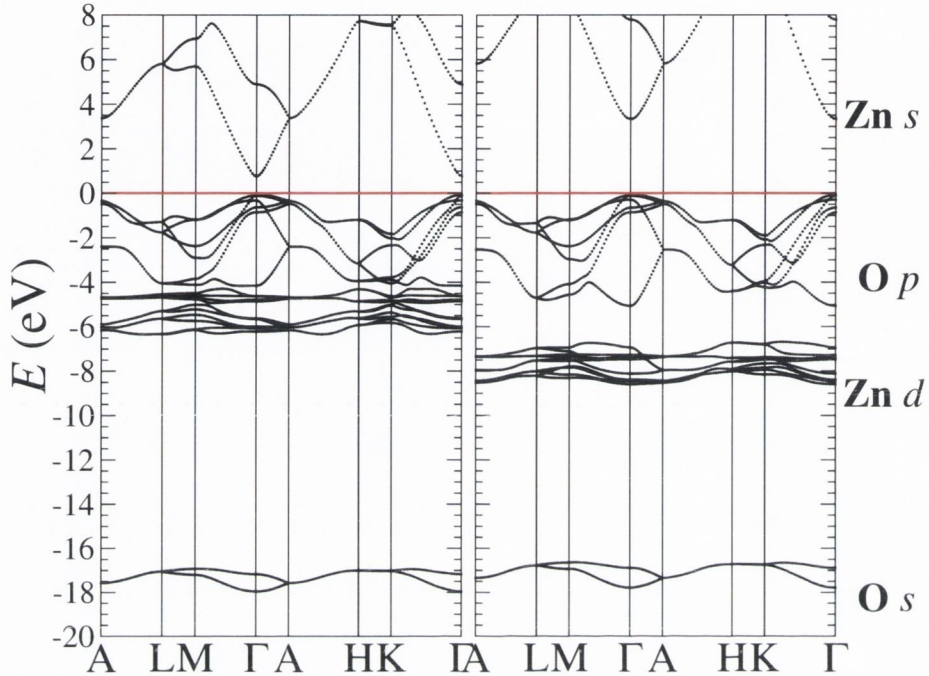


Figure 4.2: Calculated band structure of wurtzite ZnO obtained from LSDA and ASIC. Owing to the ionic character of ZnO each group of bands can be clearly labeled according to a single, dominant orbital character as shown. The VBT is aligned at 0 eV.

In ZnO, the valence band top (VBT) is predominantly oxygen $2p$ in character and the conduction band minimum (CBM) is essentially zinc $4s$. With a value of ~ 0.5 for the scaling parameter α , the ASIC band gap closely matches the experimental gap of $E_g=3.43$ eV, whereas the LDA band-gap is very small (~ 0.85 eV). Some part of the LDA band gap error in ZnO can be traced to an underestimation of the semi-core Zn $3d$ states. The LDA binding energy for the Zn $3d$ states is ~ 5.5 eV while photoemission results place them at around ~ 7.8 eV. ASIC however rectifies the problem and is in very good agreement with experiment. This results furthermore in the removal of the spurious Zn $_{3d}$ -O $_{2p}$ band mixing seen in LDA. An additional feature is that the band-width of the valence band increases considerably as an effect of the downshift of the d manifold. Its worth mentioning that the positions of the Zn $3d$ levels obtained from ASIC in the case of ZnS, ZnSe, and ZnTe also agree remarkably well with experiment.

The wide-gap III-V semiconductor GaN presents similar phenomenology to that of

ZnO. Figure 4.3 compares the band structure for wurtzite GaN obtained from LSDA and ASIC. When compared to X-ray photoemission spectra [217], the LSDA band structure of GaN has several shortcomings. Firstly, the band-gap between N 2*p* bands (VBT) and Ga 4*s* bands (CBM) is underestimated at around 2.2 eV against the experimental value of 3.4 eV. Secondly, the 3*d* states of Ga are too shallow in LSDA, leading to a spurious 3*d*-2*s* hybridization. As a result the Ga 3*d* states overlap with and split the N 2*s* bands. ASIC rectifies the picture on both counts by improving the band gap and lowering the position of the Ga 3*d* bands with respect to the N 2*s* bands. These results corroborate

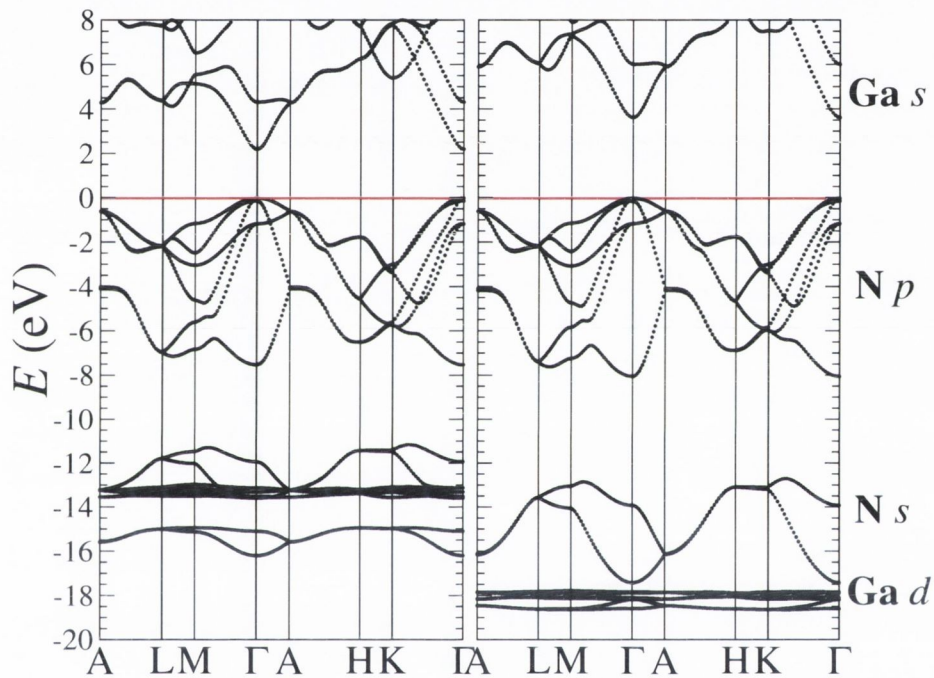


Figure 4.3: Calculated band structure of wurtzite GaN obtained from LDA and ASIC. The primary orbital character of the bands is indicated. The VBT is aligned at 0 eV.

those of references [129, 153, 154] where in ZnO and GaN have previously been discussed in a pseudo-potential based SIC context.

4.4.3 Transition-metal oxide: MnO

Transition metal oxides like MnO and NiO are characterized by partially filled 3*d* orbitals and an associated local magnetic structure. In particular the Mn²⁺ ions in MnO are magnetic with a half-filled 3*d* shell. In the ground state, MnO is an A-type anti-ferromagnetic insulator in the intermediate charge-transfer Mott-Hubbard regime with a band-gap in the

region of 3.8-4.2 eV. The VBT is expected to be of mixed Mn 3d-O 2p character and the CBM pure Mn 3d in character. However the LSDA description of MnO is flawed in several aspects most notably in describing MnO as a narrow gap ($E_g = 0.92$ eV) Mott-Hubbard insulator with both the VBT and CBM composed of purely of Mn 3d states. This is due to the severe underestimation of d electron binding-energies in LSDA. The calculated anti-ferromagnetic band-structures of MnO from LSDA and ASIC ($\alpha = 1/2$) are shown in figure 4.4.

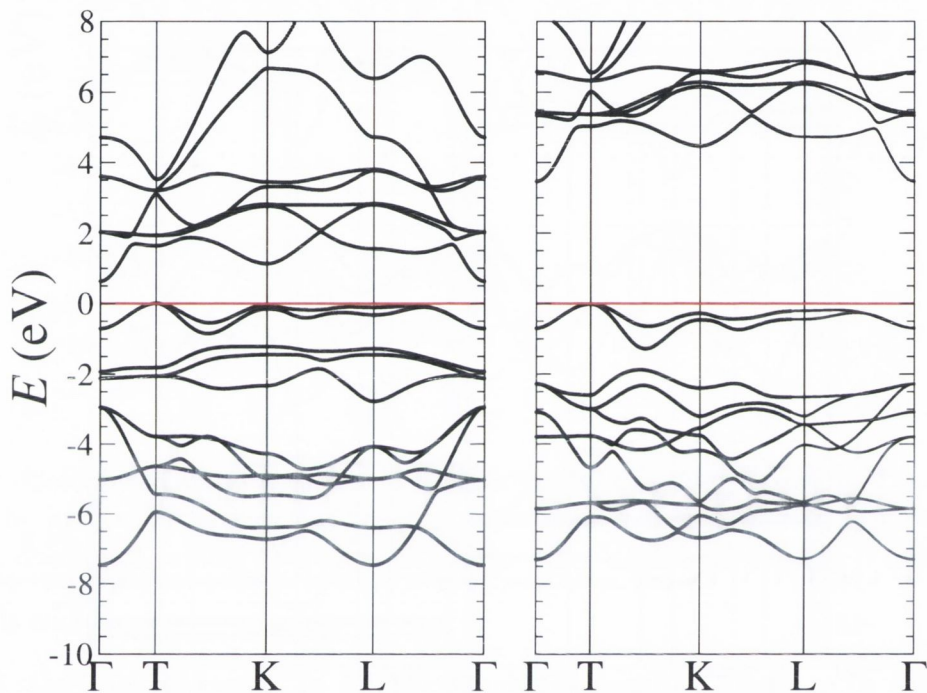


Figure 4.4: Calculated band structure of anti-ferromagnetic MnO obtained from LSDA and ASIC. In our calculation we obtain an LSDA bandgap of ~ 0.65 eV whereas the ASIC bandgap is much improved at ~ 3.5 eV. The VBT is aligned at 0 eV.

Note that these are for the rhombohedral unitcell with 4 atoms per cell. The two Mn ions are anti-ferromagnetically aligned and the oxygen ions are non-magnetic. This results in a layered ferromagnetic order of the (111) planes, which in turn are anti-ferromagnetic coupled to each other. Also in this case, ASIC is a considerable improvement over LSDA. The size of the fundamental gap now resembles the experimental one and the VBT recovers some p character. We point the reader once again to reference [129] where in Transition-metal oxides have been discussed in much more detail.

4.5 Results: Molecules

4.5.1 Ionization potentials

In view of the fact that the ASIC method gives improved eigenvalue spectra for several solid state systems, it is worth taking a cautious look at how it performs with molecules. This is particularly important for assessing whether the ASIC scheme can be adapted to work in DFT electron transport schemes based on the KS spectra [151, 218]. In exact KS DFT only the highest occupied orbital eigenvalue (ϵ^{HOMO}) has a rigorous physical interpretation and corresponds to the negative of the first ionization potential [147, 148]. More generally, for a N electron system, the following equations hold in exact KS-DFT

$$\epsilon^{\text{HOMO}}(M) = -I_N \quad \text{for } (N - 1 < M < N) \quad (4.41)$$

$$\epsilon^{\text{HOMO}}(M) = -A_N \quad \text{for } (N < M < N + 1) \quad (4.42)$$

where $-I_N$ and $-A_N$ are the ionization potential (IP) and the electron affinity (EA) respectively. Therefore we start our analysis by looking at these quantities as calculated by ASIC. Also in this case we investigate different values of α . However here we limit ourselves only to $\alpha = 1$ (ASIC₁) and $\alpha = 1/2$ (ASIC_{1/2}).

In table 4.3 and figure 4.5 we compare the experimental negative IP for several molecules with the corresponding (ϵ^{HOMO}) obtained using LSDA and ASIC. It is clear that LSDA largely underestimates the removal energies in all the cases and that the values obtained from ASIC_{1/2} are also consistently lower than the experimental value. However, as made evident by the figure the agreement between ASIC₁ and experiments is surprisingly good. In fact the mean deviation $\delta(X)$ ($X = \text{LSDA}, \text{ASIC}_{1/2}, \text{ASIC}_1$) from experiment

$$\delta(X) = \sqrt{\frac{\sum_{i=1}^N \left[\epsilon_X^{\text{HOMO},i} + \text{IP}_{\text{Expt}}^i \right]^2}{N}} \quad (4.43)$$

is 3.56 eV for LSDA, 1.69 eV for ASIC_{1/2} and only 0.58 eV for ASIC₁ (N runs over the molecules of table 4.3). It is worth noting that we have excellent agreement over the whole range of molecules investigated going from N₂ to large fullerenes C₆₀ and C₇₀.

For comparison in figure 4.5 we have also included results obtained with a full self-consistent PZ-SIC approach [163]. Surprisingly our atomic approximation seems to pro-

Table 4.3: Experimental Ionization potential (IP) compared to calculated HOMO eigenvalues for neutral molecules. Columns 3 and 4 present the results from ASIC with respectively $\alpha = 1/2$ and $\alpha = 1$. The experimental data are taken from reference [219].

Molecule	$\epsilon^{\text{HOMO}}(\text{eV})$			-IP(eV)
	LSDA	ASIC _{1/2}	ASIC ₁	
CH ₃	-4.65	-7.34	-10.06	-9.84
NH ₃	-5.74	-8.21	-10.79	-10.07
SiH ₄	-7.95	-10.14	-12.41	-11.00
C ₂ H ₄	-6.28	-8.00	-9.74	-10.51
SiCH ₄	-5.89	-7.57	-9.35	-9.00
CH ₃ CHCl ₂	-7.23	-8.97	-10.72	-11.04
C ₄ H ₄ S	-5.95	-7.65	-9.35	-8.87
C ₂ H ₆ S ₂	-5.56	-7.54	-9.53	-9.30
Pyridine	-4.83	-6.57	-8.31	-9.60
Benzene	-5.92	-7.59	-9.28	-9.24
Iso-butene	-5.39	-6.98	-8.6	-9.22
Nitrobenzene	-6.49	-8.76	-10.67	-9.92
Naphthalene	-5.49	-7.04	-8.59	-8.14
C ₆₀	-5.06	-6.53	-8.02	-7.57
C ₇₀	-4.92	-6.40	-7.89	-7.36

duce a better agreement with experiments than the self-consistent scheme, which generally overcorrects the energy levels. This is a rather general feature of the PZ-SIC scheme and it is generally acknowledged that some re-scaling procedure is needed [220, 221].

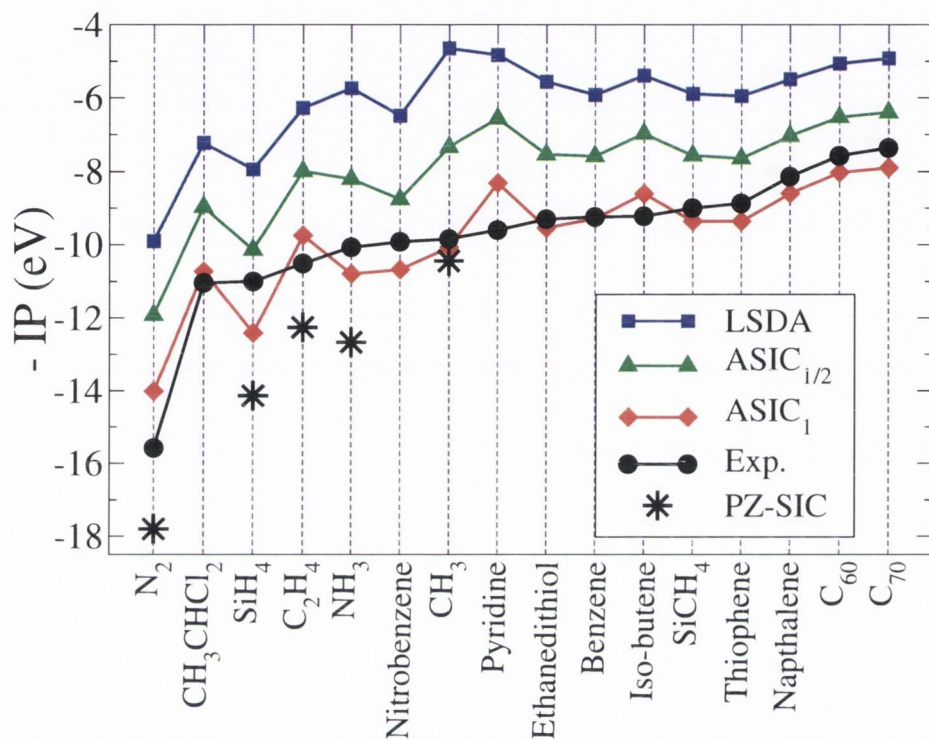


Figure 4.5: Experimental negative ionization potential IP compared to the calculated HOMO eigenvalues for molecules. The experimental data are from reference [219], while the star symbol represents full PZ-SIC calculations from reference [163].

4.5.2 Electron affinities

In Hartree Fock theory where Koopmans' theorem holds [222], the lowest unoccupied molecular orbital (LUMO) energy (ϵ^{LUMO}), corresponds to the vertical EA of the N electron system, if one neglects electronic relaxation. No such interpretation exists for (ϵ^{LUMO}) in DFT and so the EA is not directly accessible from the ground state spectrum of the N electron system. However, as equation (4.42) indicates, the EA is in principle accessible from the ground state spectrum of the $N+1-f$ ($0 < f < 1$) electron system and asserts in particular that it must be relaxation free through non-integer occupation. Unfortunately, the LSDA/GGA approximate functionals usually perform rather poorly in this regard as

Table 4.4: Calculated HOMO eigenvalues for singly negatively charged molecules compared to experimental negative electron affinities (-EA). Columns 6,7 and 8 present the LUMO eigenvalues for the corresponding neutral species.

Molecule	$\epsilon_{N+1}^{\text{HOMO}}$ (eV)			Exp. -EA (eV)	ϵ_N^{LUMO} (eV)		
	LSDA	ASIC _{1/2}	ASIC ₁		LSDA	ASIC _{1/2}	ASIC ₁
CN ⁻	0.84	-0.79	-2.48	-3.86	-8.13	-9.03	-9.42
C ₂ H ⁻	0.94	-0.80	-2.68	-2.97	-6.91	-7.38	-7.48
CH ₃ S ⁻	2.42	0.65	-1.14	-1.87	-5.20	-5.31	-5.34
OH ⁻	3.82	1.09	-1.80	-1.83	-0.16	-0.43	-0.69
SiH ₃ ⁻	4.61	3.13	1.61	-1.41	-2.66	-3.30	-4.07
HOO ⁻	3.10	-0.07	-3.34	-1.08	-5.30	-6.14	-6.40
NH ₂ ⁻	3.83	1.51	-0.98	-0.77	-5.27	-4.80	-4.39
CH ₂ ⁻	3.07	1.21	-0.45	-0.65	-3.80	-3.84	-3.91
CH ₃ CO ⁻	2.90	1.76	0.40	-0.42	-2.94	-3.88	-4.85
CHO ⁻	3.55	2.02	0.42	-0.31	-3.30	-4.40	-5.51
CH ₃ ⁻	4.15	1.99	-0.34	-0.08	-2.73	-2.59	-2.47
C ₆₀ ⁻	0.03	-1.19	-2.45	-2.65	-3.44	-4.66	-5.90
C ₇₀ ⁻	0.00	-1.22	-2.47	-2.73	-3.17	-4.41	-5.66

the $N + 1$ electron state is unbound with a positive eigenvalue. So one resorts instead to extracting electron affinities from more accurate total energy differences [223], or by extrapolating them from LSDA calculations for the N electron system [224]. This failing of approximate functionals has been traced in most part to the SI error and so SIC schemes are expected to be more successful in describing the $N + 1$ electron spectrum.

In table 4.4 we compare HOMO energies (denoted as $\epsilon_{N+1}^{\text{HOMO}}$) of several singly negatively charged molecules with the experimental electron affinities. We also report the LUMO energies for the corresponding neutral species (denoted as ϵ_N^{LUMO}). LSDA relaxed geometries for the neutral molecule are used for both the neutral and charged cases. We find that various $\epsilon_{N+1}^{\text{HOMO}}$ obtained from ASIC₁ once again are in reasonably good agreement with corresponding experimental electron affinities while LSDA and ASIC_{1/2} continue to be poor even in this regard. In this case $\delta(X)$ stands at 4.1 eV, 2.31 eV and 0.83 eV for LSDA, ASIC_{1/2} and ASIC₁ respectively. Notice that $\epsilon_{N+1}^{\text{HOMO}}$ from LSDA is positive in most cases as the states are unbound.

In figure 4.6 we present our data together with $\epsilon_{N+1}^{\text{HOMO}}$ as calculated using the PZ-SIC [163]. Again ASIC₁ performs better than PZ-SIC, that also for the EA systematically overcorrects.

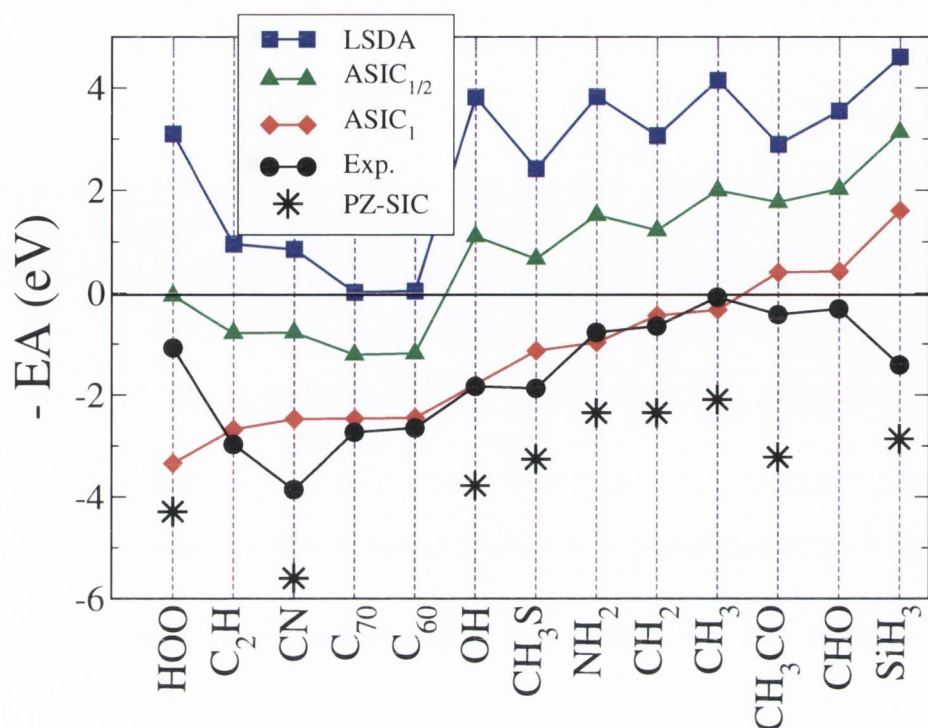


Figure 4.6: Experimental negative electron affinities (-EA) compared to calculated HOMO eigenvalues of negative radicals.

4.5.3 Vertical excitations

Having shown that ASIC offers a good description of both IP and EA for a broad range of molecules, we turn our attention to the remaining vertical ionization potentials. As mentioned before, KS-DFT lacks of Koopmans theorem, and therefore the KS energies are not expected to be close to the negative of the vertical ionization potentials. However, at least for atoms, the introduction of SIC brings a remarkable cancellation between the negative relaxation energy and the positive non-Koopmans corrections [144]. For this reason the SIC KS eigenvalues are a good approximation to the relaxed excitation energies. As an example, in table 4.5 we present the orbital energies calculated with ASIC₁ and ASIC_{1/2} for the N₂ molecule. These are compared with experimental data [225] and orbital energies obtained respectively with Hartree-Fock (HF), self-consistent SIC, and SIC where molecular orbitals are used instead of localized orbitals (D-SIC) [159].

Remarkably ASIC₁ seems to offer good agreement over the whole spectrum, improving considerably over LSDA and in some cases even over SIC and HF results. This improvement is not just quantitative, but also qualitative. For instance while rectifying the LSDA

Table 4.5: Orbital energies of N₂ calculated with various methods. The results for Hartree-Fock and SIC are from reference [159]. Experimental results are from reference [225].

Orbital	HF	SIC	D-SIC	ASIC ₁	ASIC _{1/2}	LSDA	Exp.
2σ _g	-41.49	-38.86	-37.85	-38.29	-33.22	-28.16	
2σ _u	-21.09	-20.27	-16.44	-18.42	-15.64	-12.93	-18.75
3σ _g	-17.17	-17.39	-13.88	-14.01	-11.70	-9.90	-15.58
1π _u	-16.98	-16.33	-16.68	-15.97	-13.74	-11.54	-16.93

Table 4.6: Orbital energies for CO, HF and H₂O calculated with LSDA and ASIC₁. The experimental results are from reference [226] and references therein.

Molecule	Orbital	LSDA	ASIC ₁	Exp.
CO	5σ	-8.74	-12.85	-14.01
	1π	-11.54	-16.64	-16.91
	4σ	-13.97	-19.36	-19.72
HF	1π	-9.83	-16.96	-16.19
	3σ	-13.61	-19.68	-19.90
H ₂ O	1b ₁	-7.32	-13.38	-12.62
	3a ₁	-9.32	-14.66	-14.74
	1b ₂	-13.33	-18.03	-18.55

spectrum of the N₂ molecule, ASIC₁ preserves the correct order between 3σ_g and 1π_u orbitals, which are erroneously inverted by both SIC and HF. So why does ASIC perform better than the other methods with regards to removal energies? In LSDA, electron relaxation typically cancels only half of the non-Koopmans contributions, resulting in energies that are too shallow [144]. In contrast HF lacks energy relaxation and the orbital energies are too deep. The reason why ASIC₁ performs better than self-consistent SIC is less clear. As a general consideration, also for the case of vertical ionization energies self-consistent SIC seems to overcorrect the actual values. Thus the SIC potential appears too deep, and the averaging procedure behind the ASIC approximation is likely to make it more shallow.

As a further test we calculated the orbital energies for a few other molecules and compared them both with LSDA and experiment [226]. These are presented in table 4.6. Again the ASIC₁ results compare rather well with experiment, and we can conclude that the ASIC method offers a rather efficient and inexpensive theory for single particle vertical excitations.

4.5.4 HOMO-LUMO gap and discontinuity of the exchange and correlation potential

We are now in a position to discuss the HOMO-LUMO gap in ASIC. As already mentioned, even for the exact XC functional, the KS gap $E_g^{\text{KS}} = \epsilon^{\text{LUMO}} - \epsilon^{\text{HOMO}}$ does not account for the actual quasi-particle gap $E_g = I_N - A_N$. This in turn is the sum of E_g^{KS} and the discontinuity of the exchange and correlation potential Δ_{xc} . Equivalently

$$\Delta_{\text{xc}} = \lim_{f \rightarrow 0^+} \epsilon_{N+f}^{\text{HOMO}} - \epsilon_N^{\text{LUMO}}, \quad (4.44)$$

i.e. Δ_{xc} is the discontinuity in the eigenvalue of the LUMO state at N . Therefore, in order to extract the actual gap from the KS gap, provided that the spectrum is reasonably well described at integer electron numbers N , what remains is to model the derivative discontinuity at N and ensure that $\epsilon_{N \pm f}^{\text{HOMO}}$ is relaxation free for $(0 < f < 1)$. Local and semi-local (LSDA/GGA) XC functionals lack such a discontinuity, while self-interaction corrections are able to restore it, at least in part. For instance the PZ-SIC scheme is successful in this regard.

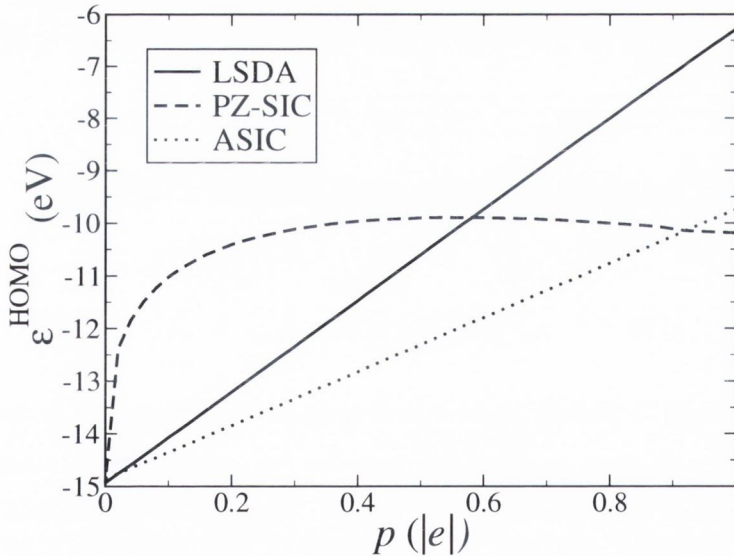


Figure 4.7: Ionization curve for the ethylene (C_2H_4) molecule as the occupation of the HOMO state is varied from 0 to 1 in going from the ionized C_2H_4^+ to the neutral C_2H_4 state.

In figure 4.7 we illustrate the ionization curve for the ethylene (C_2H_4) molecule as the

occupation of the HOMO state is varied from 0 to 1 in going from the ionized $C_2H_4^+$ to the neutral C_2H_4 configuration. It is seen that among the three schemes presented, only the PZ-SIC scheme approximately models the behaviour required by the equation (4.41). The ASIC HOMO eigenvalue roughly agrees with the PZ-SIC eigenvalue at integer occupation but behaves linearly through non-integer values. Thus we find that the derivative discontinuity for the molecule is smoothed out in ASIC, which still connects continuously different integer occupations. This is one of the limitations of the atomic representation employed in ASIC.

In view of the foregoing discussion, the actual size of the HOMO-LUMO gap in ASIC becomes significant with a direct bearing on the physics described. Ideally, we want $\epsilon^{\text{LUMO}}(N)$ (LUMO for the N -electron system) to be as close to $\epsilon^{\text{HOMO}}(N+1)$ so that the range of eigenvalue relaxation through fractional occupation numbers $M \in (N, N+1)$ is minimized. Looking at columns 6,7 and 8 in table 4.4 however, we see that for almost all the molecules, this is hardly the case. The agreement between $\epsilon^{\text{LUMO}}(N)$ and -EA from experiment ($\simeq \epsilon^{\text{HOMO}}(N+1)$) for ASIC₁ is quite poor implying a considerable energy range spanning fractional particle number. We still expect this energy range to be smaller for ASIC₁ than LSDA. It is also apparent from the table 4.4 that $\epsilon_{\text{ASIC}}^{\text{LUMO}}(N)$ usually differs from $\epsilon_{\text{LSDA}}^{\text{LUMO}}(N)$ and in fact by considerable magnitudes in some cases. Thus the ASIC₁ ‘‘correction’’ to the empty LUMO state does not vanish in contrast to the PZ-SIC scheme where, by definition, the empty eigenstates are SIC free.

Since the SIC operator v_{ASIC}^σ is constructed in an atomic orbital representation, the correction to any KS eigenstate ψ_n^σ either filled or empty

$$\delta E_{\text{ASIC}}^{n\sigma} = \langle \psi_n^\sigma | v_{\text{ASIC}}^\sigma | \psi_n^\sigma \rangle \quad (4.45)$$

is not necessarily zero unless ψ_n^σ only projects onto empty atomic orbitals. Also this correction to the LUMO with respect to the LSDA is negative in most cases, exceptions being NH_2 and CH_3 where it is desirably positive. Thus the fundamental HOMO-LUMO gap in ASIC is a combination of both the HOMO and LUMO corrections. Table 4.7 shows how this combination works out in ASIC_{1/2} and ASIC₁ when compared to LSDA. The molecular test set is the same as that in table 4.3.

We see in almost all cases the ASIC gap is systematically larger than the LSDA one. This is expected because the correction to the HOMO is usually much stronger than that to the LUMO. In general, ASIC is expected to work well for systems where the occupied and un-occupied KS eigenstates of the extended system have markedly different atomic orbital

Table 4.7: HOMO-LUMO gap obtained from ASIC compared to the LSDA value. The values marked with * correspond to unbound LUMO levels.

Molecule	$\epsilon^{\text{LUMO}} - \epsilon^{\text{HOMO}}$ (eV)		
	LSDA	ASIC _{1/2}	ASIC ₁
CH ₃	1.92	4.75	7.59
NH ₃	7.1*	9.29*	11.61*
SiH ₄	8.44*	9.68	10.94
C ₂ H ₄	5.81	6.59	7.38
SiCH ₄	6.19	7.07	8.06
CH ₃ CHCl ₂	5.79	6.84	7.88
C ₄ H ₄ S	4.46	5.13	5.8
C ₂ H ₆ S ₂	4.44	6.02	7.6
Pyridine	3.85	4.56	5.26
Benzene	5.22	5.9	6.59
Iso-butene	4.88	5.56	6.26
Nitrobenzene	3.25	4.03	4.42
Naphthalene	3.36	3.83	4.29
C ₆₀	1.62	1.87	2.12
C ₇₀	1.75	1.99	2.23

signatures being derived predominantly from filled and empty atomic orbitals respectively. In such a case, the ASIC correction to the empty states would be nullified in being scaled by near-zero atomic orbital populations. In some cases, provided phase factors combine suitably, the correction to the empty states can even be positive with respect to the same in LSDA.

4.5.5 Final Remarks

Before we conclude, we discuss some general properties of the ASIC method which are relevant to any orbital dependent SIC implementation and also some possible pitfalls. As with other SIC schemes, ASIC is not invariant under unitary transformations of the orbitals used in constructing the SIC potential. Thus the ASIC correction is likely to change as the atomic orbitals used for projecting onto the KS eigenstates of the system are rotated or transformed otherwise. Unlike the Perdew-Zunger method however, there can be no variational principle over all possible unitary transformations of the atomic orbitals because in the general case they do not represent the Hamiltonian of the system under consideration. This also implies that if the scheme is used with a system that is already well described by LSDA, the “correction” additional to the LSDA result does not necessarily vanish. Simple metals and narrow gap systems are likely candidates for this scenario.

Furthermore, it is pertinent to mention that ASIC becomes ineffective if not counterproductive for materials with homonuclear bonding, in which valence and conduction bands have the same atomic orbital character. In this situation the ASIC potential will shift the bands in an almost identical way, without producing any quantitative changes, such as the opening up of the KS gap. Note that this is a pitfall of the ASIC approximation, which distinguishes occupied from empty states only through their projected atomic orbital occupation, but not of the SIC in general. Typical cases are those of Si and Ge. The KS gap in Si goes from 0.48 eV in LSDA to only 0.57 eV for ASIC_{1/2}, while Ge is a metal in both cases. In addition the LSDA calculated valence bandwidths of 12.2 eV for Si and 12.8 eV for Ge, in good agreement with experiments, are erroneously broadened to 14.3 eV and 14.8 eV respectively.

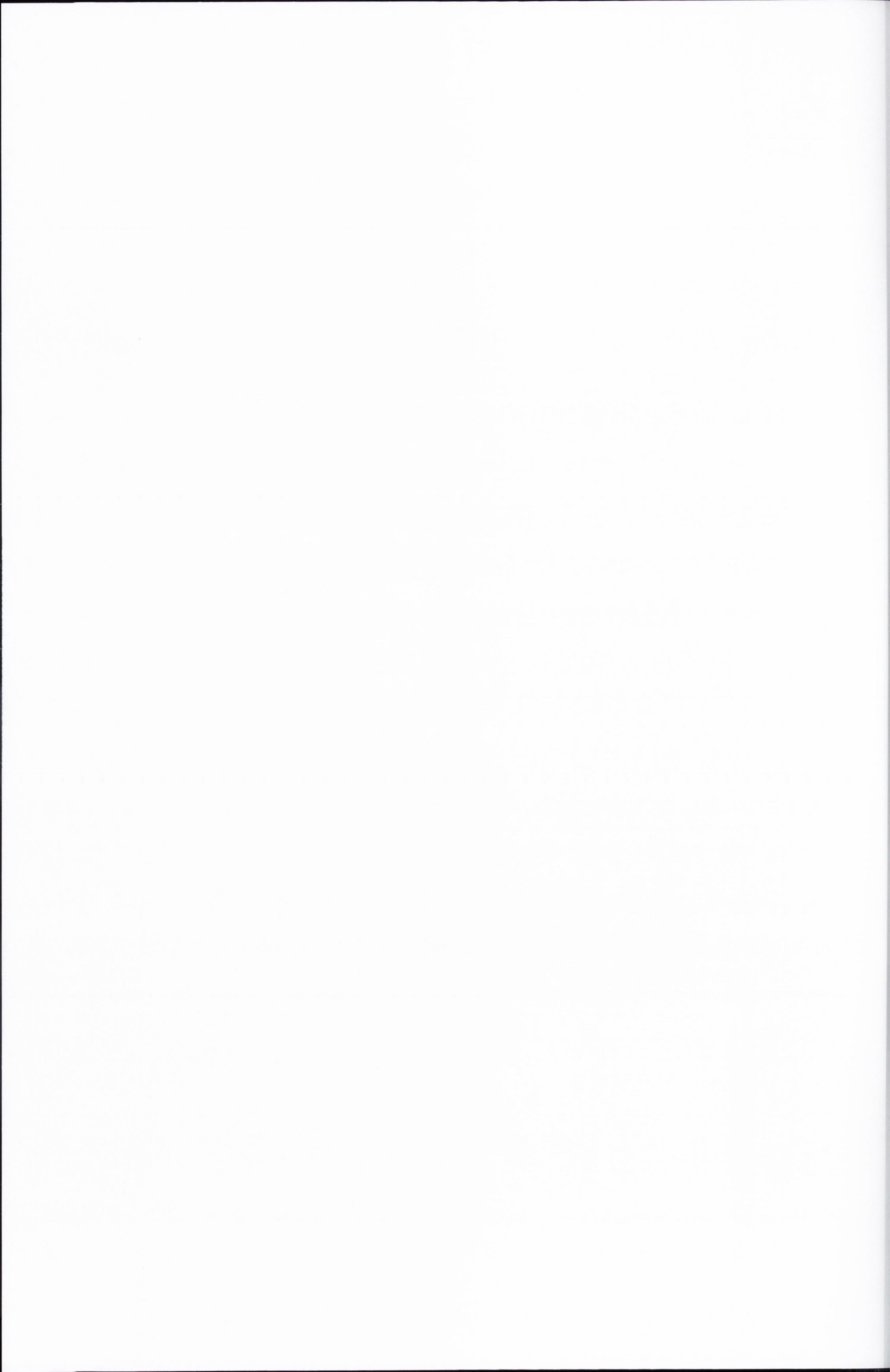
4.6 Conclusions

In conclusion, we have implemented the ASIC scheme proposed by Filipetti and Spaldin within the pseudopotential and localized orbital framework of the SIESTA code. We have then investigated a broad range of semiconductors and molecules, with the aim of providing a reasonable estimate for the scaling parameter α . We found that $\alpha = 1$, which accounts for the full atomic SI, describes surprisingly well ionic semiconductors and molecules. In particular for molecules, both the IP and the EA can be obtained with good accuracy from the HOMO KS eigenvalues respectively for the neutral and singly charged molecule. This makes the ASIC scheme particularly suited for application such as quantum transport, where the position of the HOMO level determines most of the I - V curve.

In contrast III-V and II-VI semiconductors are better described by $\alpha = 1/2$, which corrects the atomic SI for screening. This makes ASIC_{1/2} an interesting effective band theory for semiconductors. The relation of the present scheme with the fully self-consistent SIC methods has been emphasized, and so has been that with LDA+ U .

Part II

Materials simulations



Chapter 5

Ferromagnetism driven by intrinsic point defects in HfO₂

5.1 Introduction

HfO₂ (Hafnia) is a well known wide band gap insulator ($E_g \approx 5.8$ eV) with a high dielectric constant. It also exhibits high thermal stability and is commonly used in optical and protective coatings. HfO₂ occurs in three different bulk crystalline phases at atmospheric pressure, the monoclinic C_{2h}⁵ phase (space group P2₁/c) is predominant at low temperatures while the tetragonal D_{4h}¹⁵ phase (space group P4₂/nmc), and the cubic fluorite O_h⁵ phase (space group Fm3m) are high temperature phases stable above 2000 K and 2870 K respectively. As a member of the family of high-k dielectrics, HfO₂ has been extensively studied in recent times both experimentally and theoretically [227, 228] because of its potential for substituting SiO₂ as a gate dielectric in microelectronic devices. First-principles investigations of the physics of defects in Hafnia [229, 230] also reflect this trend.

In its stoichiometric bulk phase, HfO₂ is diamagnetic with susceptibility $\chi = -1.6 \times 10^{-9} \text{m}^3 \text{kg}^{-1}$ and presents no evidence of any long range magnetic order. However in recent experimental studies [231, 232], it was observed that heating HfO₂ powders in a reducing atmosphere, gives rise to a small but detectable ferromagnetic moment, which can then be reversibly removed by annealing in an oxygen rich atmosphere. The effects were also observed to be more substantial in HfO₂ thin films grown by pulsed-laser deposition on various substrates [232]. Furthermore, the magnetic moment appeared to show no systematic dependence on thin-film thickness and moments in the range of $300 \pm 150 \mu_B \text{nm}^{-2}$, which corresponds roughly to $0.1 \mu_B/\text{Hf}$, were observed for film thicknesses in the range of 45–300 nm. Sig-

nificantly, the Curie temperature was reported to be well above 500 K. These observations suggest that the detected ferromagnetic moments are somehow driven by the presence of lattice defects in the material whose concentration can vary significantly depending upon several factors such as grown conditions, post growth treatment, thin-film texture and morphology. Also the possibility of rogue impurity phases of magnetic materials such as Iron although cannot be completely ruled out, is rather unlikely as the magnetic moments were detected in highly pure samples. Interestingly, the magnetism detected on oriented thin-films was also found to exhibit significant anisotropy with the saturation moment being roughly three times larger when the field is applied perpendicular to the film than when the field is in-plane. This suggests that there might be an orbital contribution to the magnetic moment in these systems. However, in spite of the large anisotropy, the hysteresis is found to be small at any temperature with only a tiny remanence and a weak coercivity of the order of a few millitesla.

With most of the experimental evidence pointing towards intrinsic defects as the likely source behind the observed ferromagnetic moments, the defect physics of Hafnium Oxide needs to be re-visited in an effort to establish the identity and the electronic structure of the lattice defects capable of producing ferromagnetism. First principles density functional theory (DFT) investigations are well suited to addressing this problem as relevant information such as the energetics of defect formation, the structure of impurity bands, the spin state of localized defect states and magnetic coupling energies between defects can be readily obtained from supercell calculations. In fact, theoretical investigations into the possibility of intrinsic point defect driven ferromagnetism in otherwise non magnetic compounds have been previously carried out for several systems such as CaB_6 [233], CaO [234]. The spin states of point defects in semi-conductors are determined by several competing factors such as symmetry driven orbital degeneracy, the possibility of Jahn-Teller distortions and coulomb interactions between localized electrons. For example, vacancy sites in systems such as CaB_6 , CaO or SiC , are characterized by the high symmetry, either octahedral or tetrahedral around the vacancy site. This invariably leads to a highly degenerate single particle spectrum, which may then present high spin states. In CaO for instance Coulomb repulsion stabilizes the two holes occupying the degenerate molecular orbital associated to the Calcium vacancy V_{Ca} in a triplet ground state [234]. However, for a Si vacancy in cubic SiC , the occurrence of a magnetic Jahn-Teller distortion stabilizes the spin singlet relative to the triplet state otherwise expected from the T_d symmetry and the degenerate single particle spectrum [235]. Once it is ascertained that a certain point defect

within the material under investigation indeed exhibits a spin polarized ground state, the question of inter-defect magnetic coupling can then be addressed.

In the case of HfO_2 , it was initially suggested that the detected magnetic moments probably arose from partially filled d -orbitals derived from Hafnium atoms coordinating Oxygen vacancies (V_{O}) in the system. Since the nominal valence of Hf in HfO_2 is 4+, which leaves Hf atoms with an empty d -shell, the name “ d^0 magnetism” fits the case in question rather well. However, upon testing the above conjecture using DFT electronic structure calculations, we find that Oxygen vacancies in monoclinic HfO_2 exhibit a doubly occupied singlet ground state that cannot support a magnetic moment. Further investigations reveal that the observed ferromagnetism is most likely due to the presence of Hafnium (cation) vacancy sites (V_{Hf}) that form high spin states derived mainly from the Oxygen 2p orbitals coordinating the V_{Hf} . Interestingly, Hafnium vacancies in monoclinic HfO_2 , are radically set apart from cation vacancies in systems such as CaO, by the complete lack of symmetry around the vacancy site. The defect single particle spectrum is completely non-degenerate and yet, as our DFT calculations show, they exhibit magnetic ground states. In what follows, we present a detailed account of our DFT calculations that investigate both the local electronic structure of the relevant point-defects and the inter-defect magnetic couplings needed to produce a ferro-magnetic ground state in HfO_2 . After a brief glance first at the ground state electronic structure of stoichiometric HfO_2 in the monoclinic phase, we look at the nature of Oxygen vacancies in HfO_2 . We then present results for the case of Hafnium vacancies and also investigate some interesting differences between the V_{Hf} s in monoclinic, tetragonal and cubic HfO_2 .

5.2 Computational Details

The DFT calculations are carried out using the LCAO electronic structure code SIESTA [236]. The local spin density approximation (LSDA) is chosen as the approximate exchange-correlation (XC) potential and in particular, the Ceperly-Alder [237] parameterization of the XC potential is employed. Test calculations using the generalized gradient approximation (GGA), are seen to yield qualitatively similar results. We use the numerical localized atomic orbital basis set implemented in SIESTA including polarized orbitals with an energy shift of 0.01 eV [236]. Standard norm-conserving scalar relativistic pseudo-potentials generated using the Troullier-Martins scheme [238] are employed. The pseudo-atomic orbital (PAO) basis set and pseudo-potential configurations employed for each of the atomic

species involved in the calculations are listed in table 5.1. Note that the Hf-4f states are included in the core. k -point sampling is done over a 6x6x6 Monkhorst-Pack (MP) mesh for the twelve atom monoclinic unit cell and the mesh is scaled appropriately for larger cells. For instance, a 3x3x3 MP mesh is used for a 2x2x2 supercell containing 96 atoms. The energy cutoff defining the equivalent planewave cutoff for the numerical integration grid is set at a value of 250.0 Rydbergs. In all cases, the atoms in the supercell are relaxed until all the forces are smaller than 0.05 eV/Å.

Atomic Species	Electronic Configuration	Basis set
Hf	[Xe 4f ¹⁴] 6s ² 5d ²	6s-DZP,5d-DZ
O	[He]2s ² 2p ⁴	2s-DZ,2p-DZP
N	[He]2s ² 2p ³	2s-DZ,2p-DZP

Table 5.1: The electronic configuration used for the generation of the pseudo-potentials and the PAO basis sets employed for various atomic species are shown. SZ - single zeta, DZ - double zeta, DZP - double zeta plus polarization

5.3 Defect free HfO₂

Monoclinic HfO₂ crystallizes in the Baddeleyite structure with 12 atoms or 4 formula units in the primitive unit cell (Fig. 5.1(a)). Within this structure, each Hf cation is coordinated by 7 O ions, while two non-equivalent O ion sites coordinated respectively by 3 or 4 Hf ions can be identified. Henceforth in the text, the O ions surrounded by 3 nearest neighbour (NN) Hf ions are labeled as O3 and the ones surrounded by 4 NN Hf ions are labeled O4. Each Hf ion therefore has 3 O3 and 4 O4 nearest neighbours. Some calculated and experimental structural parameters for the bulk unit-cell of monoclinic Hafnia are shown in table 5.2. As is usually the case, LDA is seen to slightly under-estimate the lattice constant in comparison to experiment. The LDA band structure of stoichiometric HfO₂ is shown in Fig. 5.1(b). The band gap E_g although under-estimated in comparison to the experimental value of 5.8 eV, is still substantially large at ~ 3.6 eV. One would therefore expect the position of various mid-gap defect states to be relatively insensitive to the band gap error and the defect physics to be accurately described within LDA/LSDA for a range of Fermi energies. The top of the valence band (VB) in HfO₂ is composed predominantly of O-2p states while the conduction band (CB) is chiefly Hf-5d in character. Also, the O-2s states are seen to be very deep in energy and do not hybridize strongly with any of

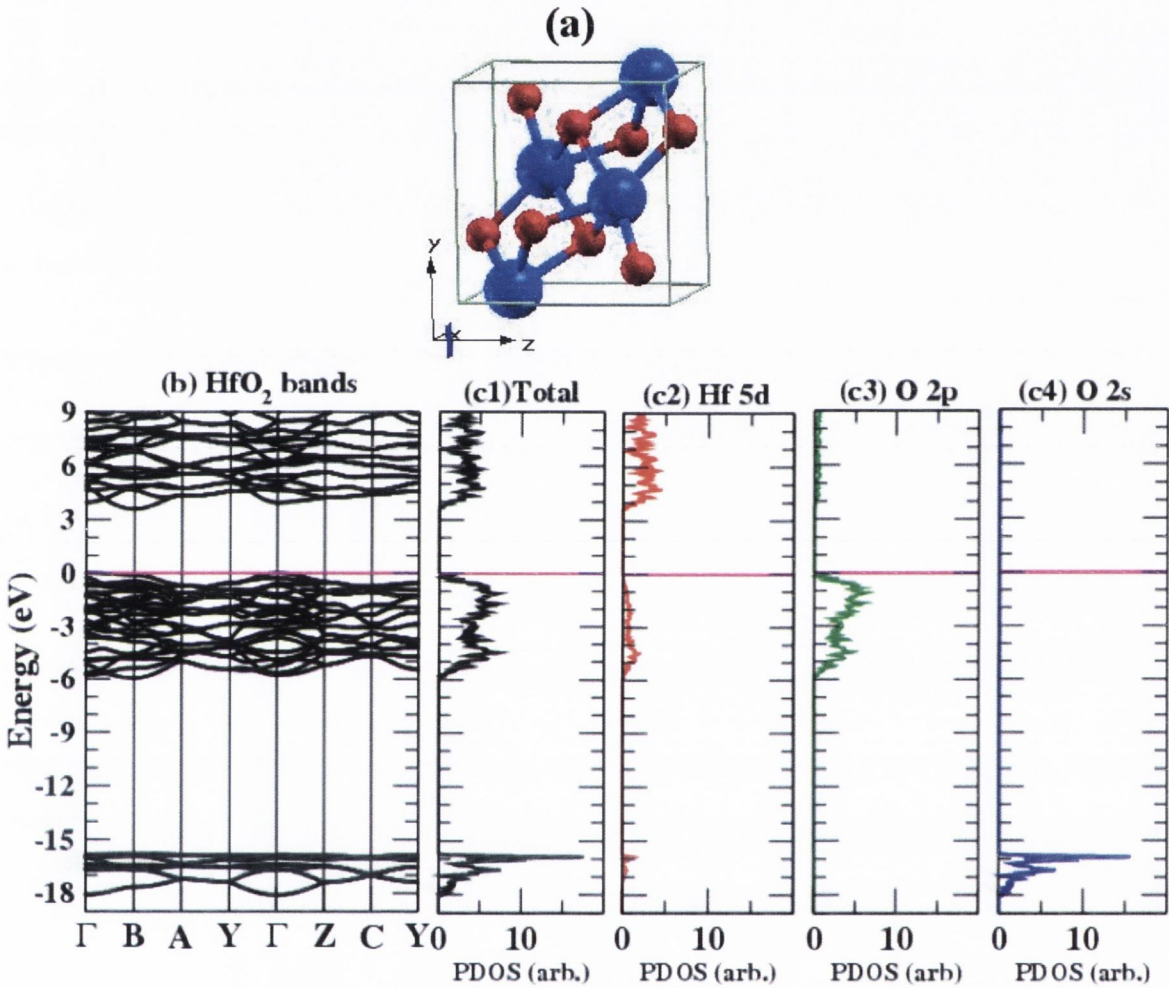


Figure 5.1: (a) The bulk unit-cell of monoclinic HfO_2 is shown with the larger Hf ions shown in blue and O ions in red. Panel (b) shows the LDA band structure of monoclinic HfO_2 . The Fermi level at 0 eV, is aligned with the top of the valence band. In (c1) the total density of states corresponding to the band structure shown in Fig. 5.1(b) is plotted. (c2) PDOS for the Hf-5d states (c3) PDOS for the O-2p states (c4) PDOS for the O-2s states. Clearly the top of the VB of HfO_2 is composed mostly of O-2p orbitals while the bottom of the CB is Hf-5d in character.

Parameter	Calculated	Experimental
$a(\text{\AA})$	5.103	5.1187
b/a	1.018	1.010
c/a	1.032	1.035
$\beta(\text{degrees})$	99.29	99.18
Volume(\AA^3)	34.44	34.62

Table 5.2: Comparison between calculated and experimental parameters [229] for the bulk unit-cell of monoclinic HfO_2 . a, b, c are the lengths of the 3 cell vectors while β is the angle between cell vectors a and c . The volume indicated is the volume per formula unit.

the other states. This is evident from the partial density of states (PDOS) depicted in Fig. 5.1(c1-c4)

5.4 Oxygen Vacancies

We investigate first the electronic structure of Oxygen vacancies (V_O) in HfO_2 to test the hypothesis that partially occupied Hf-5d states centered around V_O sites could support ferromagnetism [231]. In the monoclinic structure there are two inequivalent V_O sites : i) V_O coordinated by three Hf atoms (V_{O3}), and ii) V_O coordinated by four Hf atoms (V_{O4}). The local geometry around both kinds of V_{O3} is shown in Fig. 5.2. A description of the various defect formation energetics is outside the scope of our work (see reference [229]), as our main focus is on the electronic and magnetic structure of the defects. However its worth noting that V_{O3} is stabler than V_{O4} by about 62 meV suggesting that the former might be the slightly more predominant form of V_O .

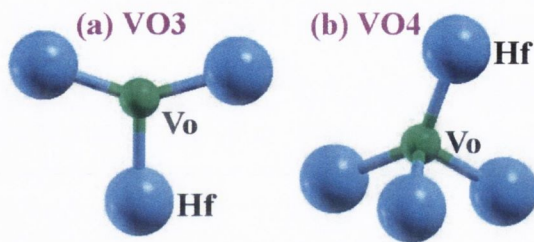


Figure 5.2: The geometries around Oxygen vacancies V_{O3} , V_{O4} are shown. The dummy atom at the site of the O vacancy is included for clarity and shown in green. The V_{O4} site forms an imperfect tetrahedron while the V_{O3} site forms an almost planar trigonal structure with the coordinating Hf atoms.

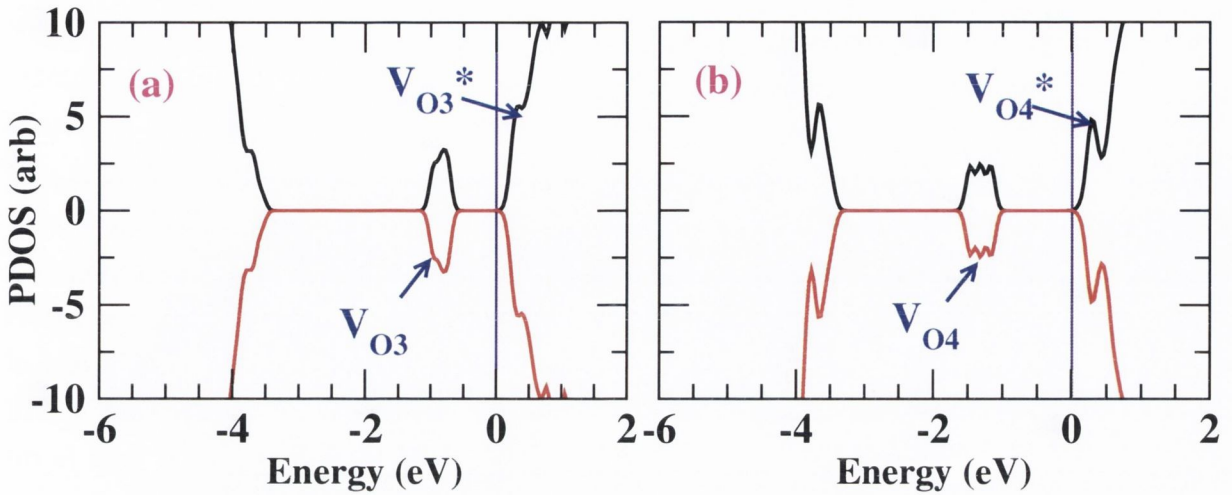


Figure 5.3: Spin resolved total DOS for Oxygen deficient HfO_2 . The defect states are labeled according to figure 5.2 based on the type of V_{O} they represent. $V_{\text{O}3}$ and $V_{\text{O}4}$ represent occupied mid-gap states while $V_{\text{O}4}^*$ and $V_{\text{O}3}^*$ denote the empty anti-bonding type states at the bottom of the conduction band. The vertical line indicates the position of the Fermi level ($E_{\text{F}} = 0$ eV). Note that both $V_{\text{O}3}$ and $V_{\text{O}4}$ are doubly occupied in their neutral ground state and are non-magnetic.

An Oxygen vacancy in both the three and four fold coordinated case leads to the formation of a set of impurity levels, with a low lying level in the HfO_2 band gap (labeled $V_{\text{O}3}$ and $V_{\text{O}4}$) and a set of higher lying levels just below the conduction band (labeled $V_{\text{O}3}^*$ and $V_{\text{O}4}^*$, see figure 5.3). These impurity levels are formed from a re-hybridization of the dangling 6s and 5d orbitals of Hf atoms coordinating the vacancy site. Of these states, the lower lying one in the band gap is filled by two electrons while the higher lying states are empty. Thus V_{O} is an n-type defect as it results in two electrons occupying conduction band derived cation orbitals. These electrons in the perfect crystal would nominally occupy O-2p orbitals which form part of the valence band. The LDOS shown in Fig. 5.4 provide a view of the charge density distribution of the various V_{O} states in space. Its interesting to note that the doubly occupied mid-gap states ($V_{\text{O}3}$ and $V_{\text{O}4}$) are localized in the interstitial region of the vacancy with lobes pointing towards the dangling Hf ions. The higher lying empty defect states ($V_{\text{O}3}^*$ and $V_{\text{O}4}^*$) meanwhile are localized on the Hf ions around the vacancy and the Hf-5d contribution to the charge density is also apparent.

The non-magnetic nature of the ground state for both $V_{\text{O}3}$ and $V_{\text{O}4}$ is apparent from the the PDOS in Fig. 5.3 wherein the doubly occupied defect state is seen to be completely non-spinpolarized. Furthermore, the system remains effectively semiconducting and the

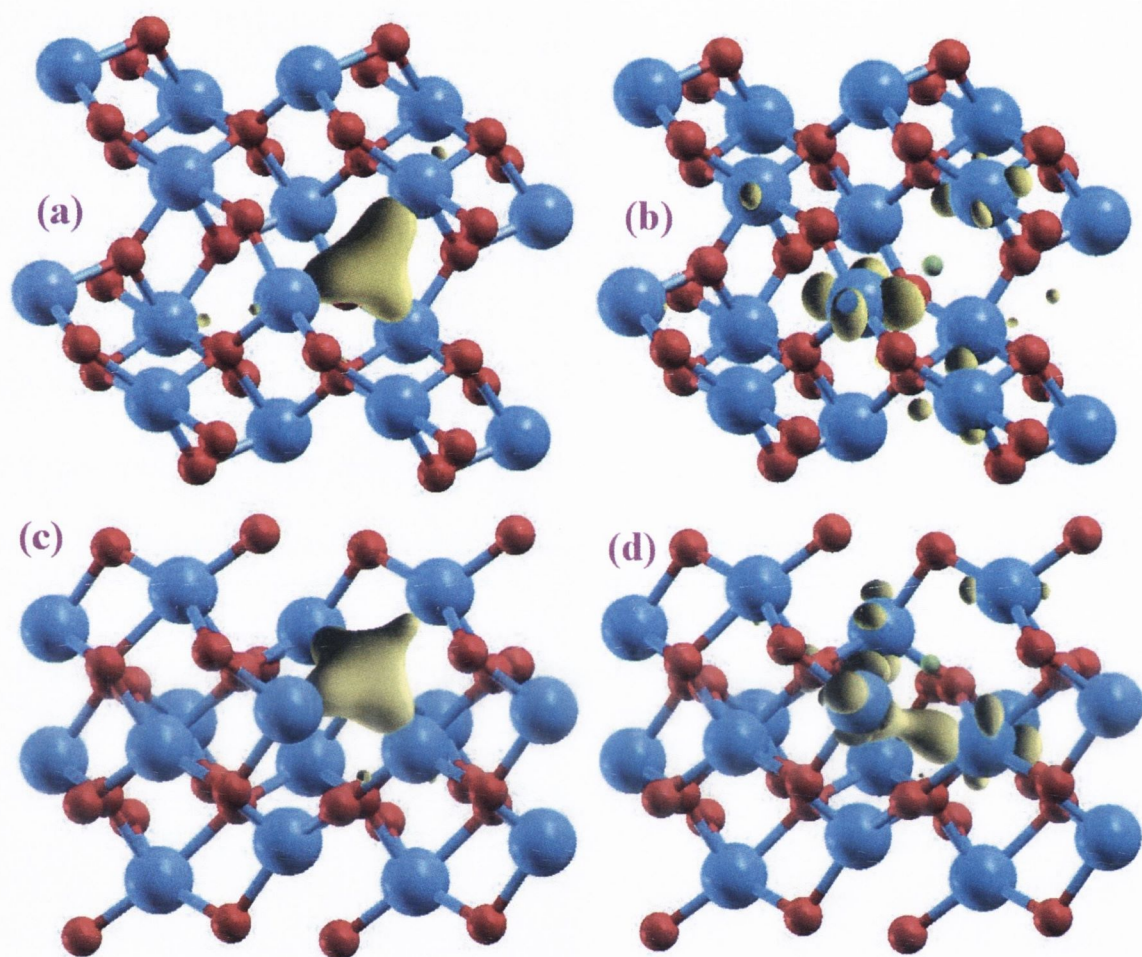


Figure 5.4: Iso-surfaces showing the spatial distribution of the charge density for the V_{O} derived defect states are shown. Panels (a) and (c) show the density iso-surfaces for the low lying mid-gap states $V_{\text{O}3}$ and $V_{\text{O}4}$ respectively. Panels (b) and (d) present the density iso-surfaces for the higher lying sub-CB states $V_{\text{O}3}^*$ and $V_{\text{O}4}^*$ respectively. Clearly the bonding states $V_{\text{O}3}$ and $V_{\text{O}4}$ are well localized within the interstitial region at the vacancy site while the anti-bonding type $V_{\text{O}3}^*$ and $V_{\text{O}4}^*$ show significant amplitude on the Hf ions directly coordinating the vacancy.

V_{O} are unlikely to contribute any free carries to the system. It is worth analyzing the orbital symmetry of the V_{O} states in order to understand why they do not lead to a magnetic ground state. If we assume for the moment that the Hf atoms coordinating the $V_{\text{O}4}$ and the $V_{\text{O}3}$ sites form a perfect tetrahedron and a perfect trigonal plane respectively, resulting in local T_d and C_{3h} symmetries, then the single particle molecular orbital ground state in each case would be a completely symmetric and non-degenerate a_1 and a'_1 singlet respectively. Similarly the higher lying σ -bonding single particle states would be a t_2 triplet in the $V_{\text{O}4}$ case and a e' doublet in the $V_{\text{O}3}$ case. Deviation from perfect symmetry, as in the actual case, of course means that the degeneracies of the higher lying states are lifted and the energy levels suitably reordered. Nevertheless, the ground state remains an orbital singlet. The higher lying states (labeled $V_{\text{O}3}^*$, $V_{\text{O}4}^*$ in either case) are well separated in energy from the low-lying singlet level. Configurations with one electron promoted to the higher lying states lie prohibitively higher in energy relative to the ground state thus ruling out electron promotion. Since two electrons occupying an orbital singlet anti-align their spins, the resulting ground state is non-magnetic.

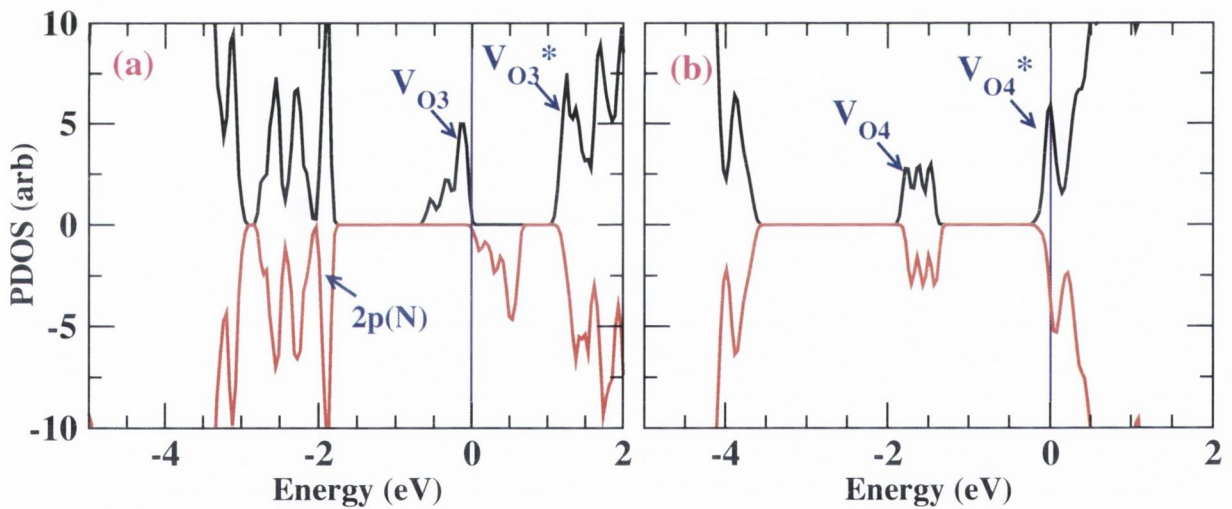


Figure 5.5: Spin resolved total DOS for Oxygen deficient HfO_2 under additional p and n doping is presented. (a) Calculated DOS in the p -doping case for a $(V_{\text{O}3}, N_{\text{O}})$ system in a 48 atom supercell. The $V_{\text{O}3}$ state is singly ionized and spin-splits with a magnetic moment of $1\mu_{\text{B}}$. The N-2p states are also indicated. (b) Calculated DOS in the n -doped scenario for a $V_{\text{O}4}$ type vacancy in a 48 atom supercell. The higher lying $V_{\text{O}4}^*$ state is now partially occupied and exhibits a weak spin-polarization. The Fermi level is set at 0.0 eV.

We then investigate the effect of additional doping of the Oxygen deficient system starting with partial p -doping achieved by substituting an electron acceptor like N at an

O site (N_O). In figure 5.5(a) we present the DOS for a ($\text{V}_{\text{O}3}$, N_O) system, bearing in mind that the situation for a ($\text{V}_{\text{O}4}$, N_O) system is qualitatively the same. In this case one electron is removed from the V_O level, and it compensates the hole in the N-2p states. This therefore represents the oxygen vacancy state in its singly ionized (V_O^+) configuration. The V_O^+ configuration would be stable in real samples when the Fermi level occupies a mid-gap position between 1 eV to 0.5 eV from the conduction band minimum (CBM). Owing to its localized nature, the defect level spin splits with a magnetic moment of $1 \mu_B$ per vacancy. We then check whether these localized moments on the V_O^+ interact with each other by considering a larger supercell containing two $\text{V}_{\text{O}3}$ and two N_O and comparing total energies for ferromagnetic and anti-ferromagnetic alignment of the magnetic moments on the two $\text{V}_{\text{O}3}$ sites. We find very little difference in the total energy irrespective of the $\text{V}_{\text{O}3}$ - $\text{V}_{\text{O}3}$ separation and so we conclude that the isolated moments are not magnetically coupled. Thus the mid gap V_O states cannot support ferromagnetism either at double or single occupation and the system can at best be paramagnetic.

Although HfO_2 is a wide gap dielectric material with very low n-type carrier concentrations in the conduction band, we study the prospect of additional n-doping in Oxygen deficient HfO_2 in order to investigate the effect of occupying the higher lying $\text{V}_{\text{O}3}^*$ and $\text{V}_{\text{O}4}^*$ states. We consider 48 atom supercells containing one V_O site with an extra electron added to the supercell. A neutralizing positive background charge is also applied. Since the $\text{V}_{\text{O}3}^*$ and $\text{V}_{\text{O}4}^*$ states are situated just below the conduction band the extra electron occupies these states. Interestingly both the $\text{V}_{\text{O}3}^*$ and $\text{V}_{\text{O}4}^*$ states exhibit some degree of spin-polarization with a magnetic moment of $\sim 0.04\mu_B$ and $\sim 0.4\mu_B$ per cell for $\text{V}_{\text{O}3}^*$ and $\text{V}_{\text{O}4}^*$ respectively. Figure 5.5(b) presents the calculated DOS for one $\text{V}_{\text{O}4}$ with additional electron doping. Therefore even the higher-lying V_O derived states seem capable of supporting local moments provided they are fractionally occupied. To check however, if these defect states are capable of giving rise to ferromagnetism, we consider a 96 atom supercell with two $\text{V}_{\text{O}4}$ defects and introduce two extra electrons into the cell. We compare the total energies of the parallel and anti-parallel configurations of the local moments around each vacancy site. In the parallel configuration, the total magnetic moment on the supercell is $\sim 0.6\mu_B$ and in the anti-parallel case the total moment is seen to be $\sim 0\mu_B$. This indicates that the two electrons added are approximately localized one on either V_O site with a moment of $\sim 0.3\mu_B$ per site. However the magnetic coupling between the two V_O sites is seen to rather small at ~ 1 meV. Hence it seems that none of the defect states associated to Oxygen vacancies in Hafnia are capable of producing long range ferro-magnetism.

5.5 Hafnium Vacancies

In this section we present the electronic structure of Hafnium vacancies (V_{Hf}) in monoclinic HfO_2 and investigate whether V_{Hf} derived defect states can lead to ferromagnetic order. In monoclinic HfO_2 , each Hf atom is coordinated by seven O atoms three of which are of type O3 and the remaining four of type O4. The two types of O ions differ in their Hf coordination number in the crystal as described previously. For the purposes of the following discussion, around a given Hf ion site, we label the 3 first NN O3 type ions around the site as O_A and the 4 NN O4 type ions by O_B . O ions beyond a first NN distance from the Hf site under consideration are labeled as O_C regardless of their local coordination. The local geometry around a Hf site is shown in Fig.5.6(a). In the perfect crystal, the O-2p levels are fully filled and form the bulk of the valence band. Since Hf is a cation with a 4+ valence, the removal of a neutral Hf atom introduces four empty states among the O-2p levels. The spin occupation of these four states establishes whether or not the V_{Hf} system is magnetic.

At this point we present our LSDA results for the ground state of Hf deficient HfO_2 . We consider a $2 \times 2 \times 2$ supercell containing 96 atoms. Only one Hf vacancy is introduced in the supercell and upon relaxation the O atoms are seen to move outwards around the vacancy site by about 0.15 Å. In figure. 5.6(b) we present the DOS for the supercell in the fully re-

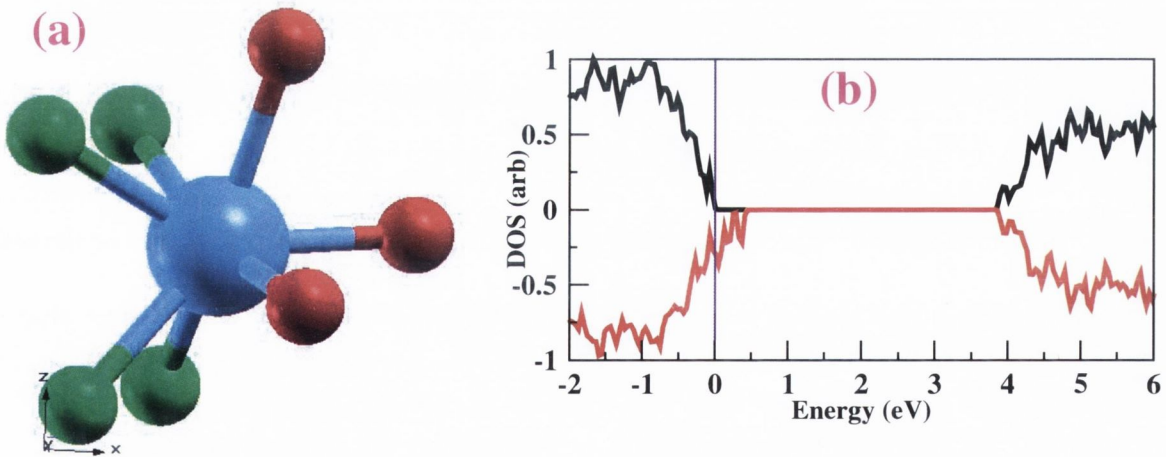


Figure 5.6: (a) Local geometry at a Hf site in monoclinic HfO_2 is shown. The two types of O ions directly coordinating a Hf site (see text) are indicated with the O_A type ions shown in red and the O_B type ions in green. The larger Hf ion is shown in blue. (b) Spin resolved DOS for one V_{Hf} in a 96 atom HfO_2 supercell. The top of the VB is spin-polarized with hole states mostly confined to the minority spin. E_F is set at 0.0 eV.

laxed geometry. The valence band is clearly spin split, with the compensating holes mostly confined to the down spin states resulting in an almost half metallic ground state with a magnetic moment of $3.52 \mu_B$ per vacancy. Prior to relaxation the system is completely half metallic with an integer magnetic moment of $4 \mu_B$ per vacancy. The relaxation involves a considerable redistribution of the hole density over the O atoms around the vacancy site as shown in figure 5.7, with the magnetism coming predominantly from the O_A type atoms. The observed charge re-ordering is driven by large scale re-hybridization, upon relaxation,

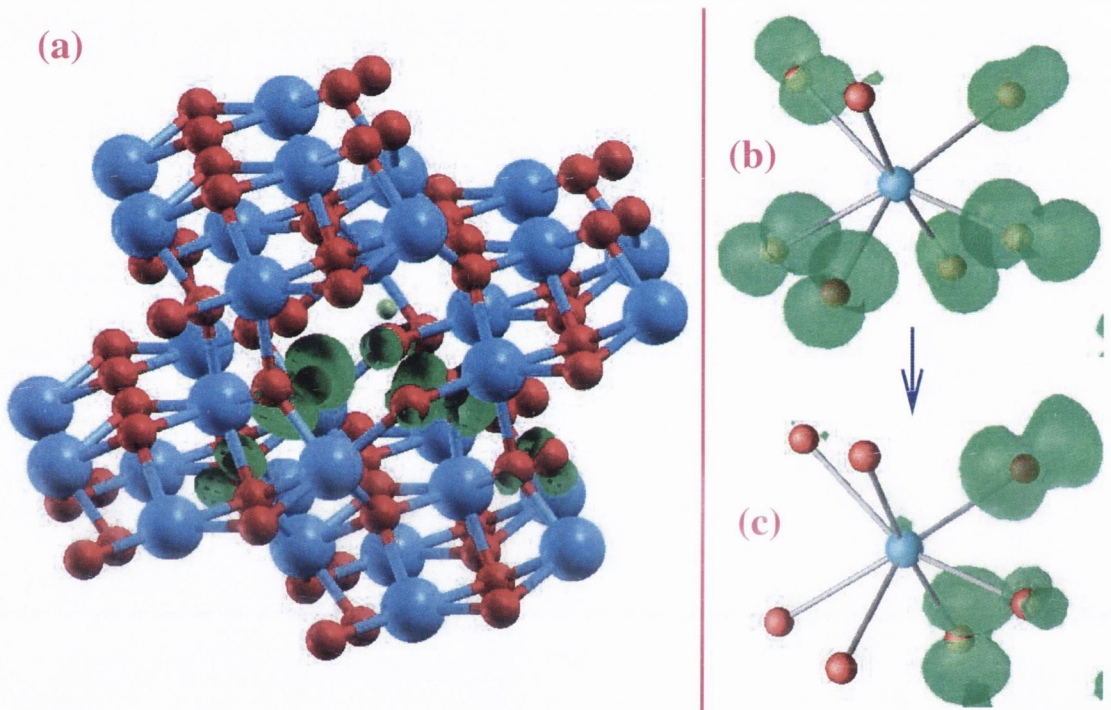


Figure 5.7: (a) Density iso-surface (in green) for the highest, minority-spin V_{Hf} derived hole state in the fully relaxed geometry is shown. In panels (b) and (c), the hole density before (b) and after (c) geometric relaxation is presented. For clarity only the O ions directly surrounding the V_{Hf} site are shown. During the course of relaxation the charge density (hole density) is re-distributed clumping mainly on the three O_A type O atoms. As a result the O_B type atoms lose most of their spin polarization. The central atom is a dummy atom included only for clarity.

of the orbitals constituting the impurity levels with the crystalline surroundings. We find that the holes clump together on and around the O_A atoms and their nearest O_C type neighbours. Figure 5.8 shows the localization of the magnetic moment around the vacancy site, where this outward spread in the spin polarization during the course of relaxation is

evident.

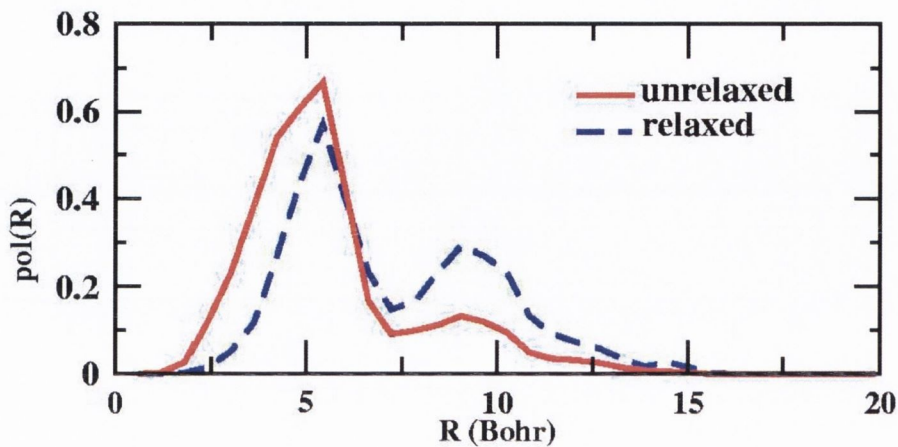


Figure 5.8: Localization plot for the magnetic moment inside the supercell before and after relaxation. The quantity presented is $pol(R) = \int_R^{R+dR} r^2 dr \int d\Omega [\rho_{\uparrow}(\vec{r}) - \rho_{\downarrow}(\vec{r})]$ against R . $pol(R)$ is the spin polarization from a shell of thickness dR at radius R where R is measured radially outward from the vacancy site. Note the redistribution of the magnetic moment towards outer shells upon relaxation.

Having studied the real space distribution of the magnetic moment, we now look at the symmetry aspect of the defect states. Looking at the local symmetry around the V_{Hf} site, in the spirit of a defect molecule model, we find a trivial C_1 point group for the seven coordinating O ions. Thus the localized defect orbitals generated from combining the dangling O-2p orbitals form a set of non-degenerate levels, and the high spin state arises from single occupation of the four topmost defect levels (insets of figure 5.9). Interestingly the calculated magnetic moment ($\sim 4\mu_B$) cannot originate from a single set of orbitally degenerate defect levels even in the most symmetric octahedral coordination. In fact the largest orbital degeneracy allowed is just three fold, and a total spin $\mathbf{S}=2$ for a configuration of four spin 1/2 particles is ruled out by the Pauli principle. This means that in any case a set of non degenerate orbitals must be involved in the high spin configuration. As non-degenerate orbitals differ in single particle properties (kinetic and ionic energies), the final configuration of the four spin 1/2 particles is decided not just by mutual Coulomb repulsion or exchange energy but by an interplay between all contributions in the Hamiltonian.

Looking at the relative energetics of different possible electronic configurations of the defect levels helps to see what stabilizes the high spin ground state. To this end, we perform fixed spin moment calculations, for the two limiting cases of $\mathbf{S}=2$ and $\mathbf{S}=0$ (see table 5.3).

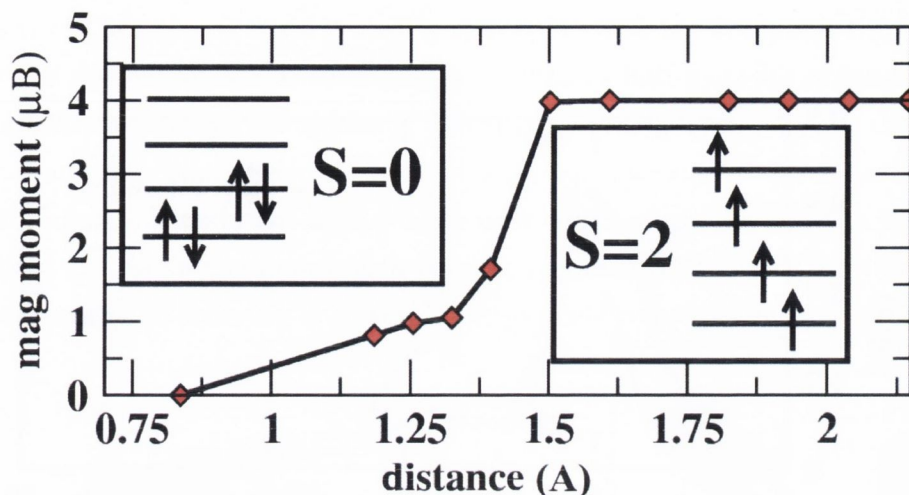


Figure 5.9: Magnetic moment per V_{Hf} as a function of the average distance from the vacancy site of the seven coordinating Oxygen ions. If the O ions are artificially forced to move inwards towards the V_{Hf} center, the magnetic moment is seen to decay. In the two insets, schematic representations of the high spin $S=2$, and non-magnetic $S=0$ state are depicted.

From the calculations it emerges that the high spin configuration is expensive with regards

	ΔE_{FS} (meV)	
	Un-relaxed	Relaxed
Kinetic	440.79	194.99
Electrostatic	-435.59	-136.42
Exch-corr	-176.57	-204.75
Total	-171.38	-146.18

Table 5.3: Energy differences $\Delta E_{FS} = E_{S=2} - E_{S=0}$ between the fixed-spin configurations $S = 2$ and $S = 0$ for various contributing terms in the Hamiltonian are shown. Both the relaxed and un-relaxed geometries around the V_{Hf} site are considered. The kinetic energy terms favour the low-spin $S = 0$ configuration while the electrostatic and exchange-correlation energies favour the high-spin $S = 2$ state.

to kinetic energy but favourable exchange and Coulomb energy stabilize it. It is likely that the higher lying orbitals are anti-bonding in character with larger kinetic energies. In fact, one expects that analogous to what happens in molecules, if the O ions around the vacancy (in the crystal) are artificially squeezed in towards the vacancy, thus driving the system highly kinetic, the higher lying defect levels would be emptied out accompanied by a fall in the magnetic moment. This is indeed seen to be the case as shown in figure 5.9.

As it turns out, at the equilibrium distance in the crystal ($\sim 2.28\text{\AA}$), the magnetic moment is close to $4\mu_B$.

Next we address the question of the magnetic coupling between isolated vacancies, by calculating the total energy of a supercell containing two V_{Hf} and comparing the energy between the ferromagnetic (E_{FM}) and antiferromagnetic (E_{AF}) alignments of the local moments on the two V_{Hf} sites. We consider 96, 144 and 192 atom supercells corresponding to V_{Hf} concentrations of 6.25%, 4.16% and 3.12% respectively. The strength of the calculated magnetic coupling as a function of the nominal V_{Hf} concentration is presented in table 5.4. Clearly the ferromagnetic alignment is always energetically favorable, and most remarkably

V_{Hf} concentration	ΔE (meV)
6.25% (1)	-113.66
4.16% (2)	-50.56
3.12% (3)	-13.81

Table 5.4: Energy differences $\Delta E = E_{\text{FM}} - E_{\text{AF}}$ between ferromagnetic and antiferromagnetic alignment of the magnetic moments of two different vacancy sites. The first column indicates the defect concentration and the number in bracket the number of Hf sites separating the two vacancies.

the coupling appears rather strong, in particular for short $V_{\text{Hf}}-V_{\text{Hf}}$ distances. This leads us to attribute the observed ferromagnetism in HfO_2 thin-films [231] to Hf vacancies. Mapping the calculated values of ΔE onto a simple first neighbour Heisenberg model suggests Curie temperatures above room temperature for concentrations above 6.25%.

In order to achieve a better understanding of the origin of this ferromagnetic ordering we perform an extensive study of the charge distribution by means of Mülliken population analysis. The main features are: (a) the O ions in the cell are polarized to different degrees depending on their orientation and distance relative to the vacancy site but always with the same sign, (b) the Hf ions in the cell are also polarized but importantly, the sign of polarization is opposite to that of the O, and (c) the total polarization of all the O ions in the cell is $3.92\mu_B$ and that for the Hf ions is $-0.40\mu_B$, leaving a moment of the cell of $3.52\mu_B$. This suggests that the magnetic coupling between the O ions in the cell is mediated by minority spin electron delocalization across the Hf bridge connecting the O ions. This applies also to O ions belonging to two different V_{Hf} sites. The delocalization is larger when local moments on the two V_{Hf} are ferromagnetically aligned resulting in lower kinetic and exchange energies relative to the anti-ferromagnetic case.

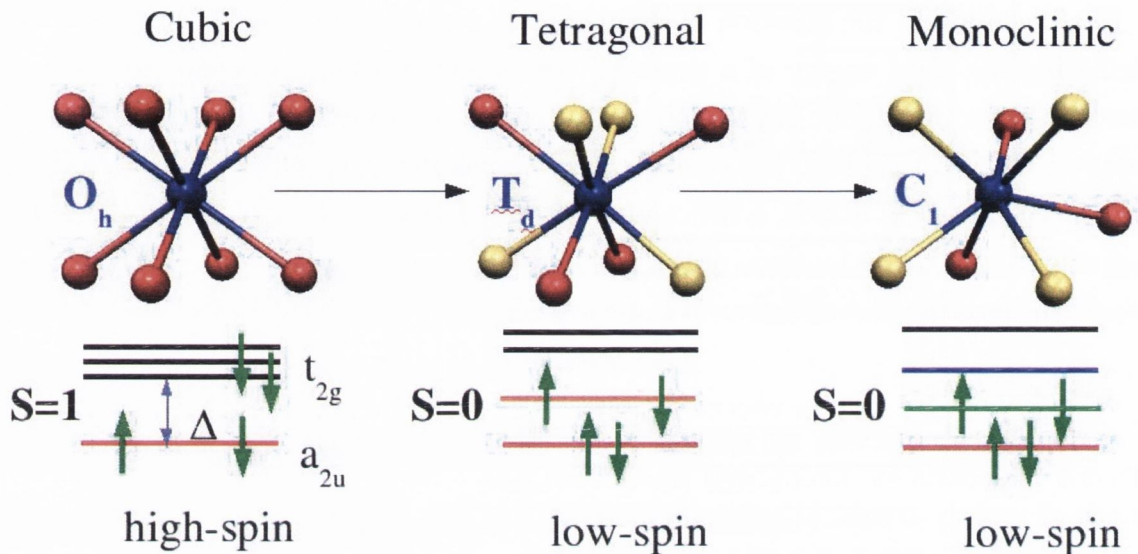
5.6 V_{Hf} in cubic and tetragonal Hafnia

Figure 5.10: Schematic showing the spin occupation of defect molecular orbitals formed at cation vacancies under different symmetries as predicted by simple molecular theory. In the cubic O_h symmetry a high-spin $S=1$ ground state is expected while a low-spin $S=0$ configuration is expected for the less symmetric T_d and C_1 geometries.

Having looked at the electronic structure of Hafnium Vacancies in monoclinic Hafnia in some detail, we now study some interesting differences between V_{Hf} s in the monoclinic phase and the more symmetric tetragonal and cubic phases. Although the tetragonal and cubic phases occur at very high temperatures where ferromagnetism is not an issue, the local magnetic structure of the V_{Hf} s in these phases is still worth investigating especially to see how the higher symmetry effects the results. Note that the Hf ion coordination number in the tetragonal and cubic phases is eight as opposed to seven in the monoclinic phase. In the cubic phase all of the eight O ions are equivalent because of the O_h symmetry while in the tetragonal phase with T_d symmetry around a Hf ion, the eight O ions form two groups of four equivalent O ions. The two sets of four O ions differ in their Hf-O bond distance by about $\sim 0.2\text{\AA}$. However, in all three phases the formation of a V_{Hf} leads to the creation of four hole states at the top of the O-2p valence band. In a simple defect molecule model, the spin-occupation of the four hole states is determined simply by the local symmetry around the defect. Thus a $S=1$ high-spin ground state is predicted for the O_h symmetry in the cubic phase while a $S=0$ low spin state is predicted for the T_d

and C_1 symmetries of the tetragonal and monoclinic phases as illustrated schematically in Fig. 5.10. However, as seen earlier for V_{Hf} in the monoclinic phase, the localized nature of the defect states invariably brings electron-electron interaction into play which might lead

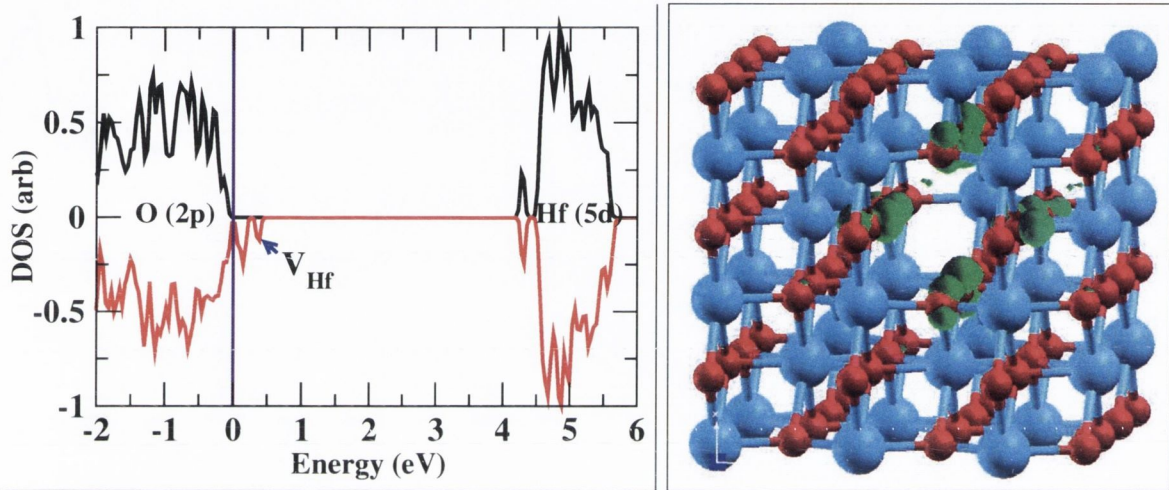


Figure 5.11: Calculated density of states for a 108 atom supercell of tetragonal Hafnia with one V_{Hf} (left panel). The top of the VB is spin polarized with the hole density confined to down-spin states. In the right panel, the spatial distribution of the charge density for the V_{Hf} derived hole states. The holes are seen to be mostly localized on the eight O ions directly coordinating the V_{Hf} site.

DOS for a 108 atom supercell of tetragonal Hafnia with one V_{Hf} is shown in Fig. 5.11. The supercell exhibits an integer magnetic moment of $4.0\mu_{\text{B}}$ and is half metallic with the holes confined to the minority spin channel. The hole density is also seen to be localized on the eight O ions coordinating the V_{Hf} with a slightly larger contribution coming from the four O ions that are closer to the vacancy site. Note that the eight O ions relax outwards by $\sim 0.11\text{\AA}$. In the case of cubic Hafnia, one would expect a similar high-spin ground state for V_{Hf} this time also aided by the higher O_h symmetry. However, rather counter-intuitively, the ground state is seen to be a low-spin state driven by a localized to delocalized transition of the hole charge density. We consider an 81 atom supercell of cubic Hafnia containing one V_{Hf} . Prior to geometric relaxation around the vacancy site, a high-spin $S=2$ configuration is obtained for the V_{Hf} derived hole states with a magnetic moment of $4.0\mu_{\text{B}}$ on the supercell. Furthermore the hole density is seen to be localized on the eight O ions coordinating the V_{Hf} site. When the geometry around the V_{Hf} is allowed to relax

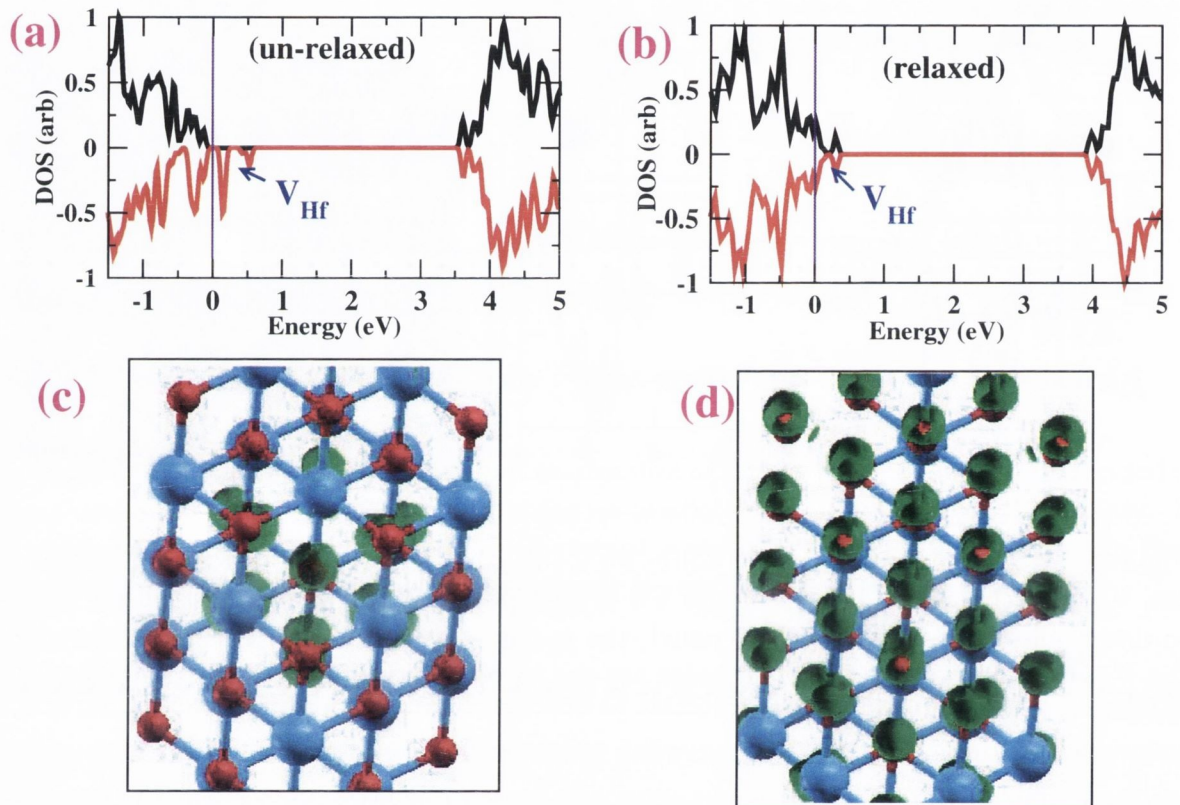


Figure 5.12: Calculated DOS for an 81 atom supercell of cubic Fluorite Hafnia containing one V_{Hf} site. In the un-relaxed geometry, the V_{Hf} derived hole states are fully spin polarized (a). Post geometric relaxation around the V_{Hf} site, the hole density is no longer spin polarized (b). The corresponding charge density iso-surfaces (in green) for the V_{Hf} derived hole states before (c) and after (d) relaxation are presented. The delocalization of the hole density over the supercell is apparent in (d)

however, the magnetic moment on the cell vanishes and a $\mathbf{S}=0$ low-spin configuration is stabilized. It is seen that the magnetic moment on the cell decreases during the process of geometric relaxation as the O ions coordinating the V_{Hf} move outwards by $\sim 0.15\text{\AA}$ as shown in Fig.5.13. The relaxation is also seen to be symmetric with no distortion of the octahedral cage formed by the O ions. In the relaxed configuration, the hole density in real space is found to be delocalized over almost all of the O ions in the supercell (see Fig.5.12). A Mlliken population analysis of the atomic charge on representative O ions situated at first and third NN separation from the V_{Hf} site is presented in table 5.5. The changes in the atomic charge and local spin-polarization on the two O ions considered clearly bring out the delocalization of the hole density with relaxation. One might understand the reason for this localized to delocalized transition as follows. In all of the three crystalline phases considered, the geometric relaxation of the O ion cage around the V_{Hf} is outwards from

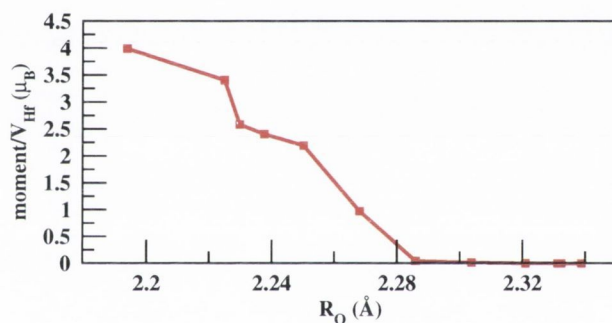


Figure 5.13: Decay of the magnetic moment on the V_{Hf} center with geometric relaxation around the site. The average distance from the vacancy site of the eight coordinating O ions (R_{O}) serves as a measure of the degree of relaxation.

the center of the V_{Hf} site as if in a breathing mode. Thus the overlap between the dangling O-2p orbitals decreases as the O ions move away from the V_{Hf} center and away from each other. This in turn leads to a decrease in amplitude of the defect molecular orbitals in the interstitial regions and the holes are effectively forced to localize in more atomic-like orbitals. In the monoclinic and cubic phases where all the O ions are not equivalent the hole density is able to re-distribute itself amongst a subset of the O ions whose 2p orbitals still overlap to a sufficient degree. Thus in the monoclinic phase about 80% the hole density post relaxation is found on the O_A type ions. In the cubic phase however, in the absence of any distortion, all the eight O ions are equivalent and the increased confinement of the hole density around the ions is energetically unfavourable owing to an increase in coulomb-repulsion most of which comes from self-interaction. Thus the holes delocalize

	O_{NN1}		O_{NN3}	
	$N_{\text{ion}}^{\downarrow}$	m_{ion}	$N_{\text{ion}}^{\downarrow}$	m_{ion}
LSDA(un-relaxed)	3.025	0.431	3.362	0.002
LSDA(relaxed)	3.271	0.0	3.357	0.0
ASIC(relaxed)	3.267	0.2	3.423	0.03

Table 5.5: A Mülliken population analysis of the charge and spin-polarization on representative O ions in the supercell is presented. O_{NN1} represents an O ion directly coordinating the V_{Hf} center. O_{NN3} represents an O ion at a 3^{rd} NN distance from the V_{Hf} . $N_{\text{ion}}^{\downarrow}$ is the total down-spin charge on the ion and m_{ion} is the total spin-polarization on the ion. LSDA results both pre and post relaxation are shown. For the ASIC calculation the relaxed LSDA geometry is used.

completely in an effort to minimize the coulomb self-repulsion. In order to study whether self-interaction indeed has a role, we recalculate the ground state for the V_{Hf} center in cubic Hafnia using the approximate self interaction correction scheme ASIC. The α parameter of ASIC is set to 0.5 as is appropriate for mid to wide gap Oxides and we use the fully relaxed LSDA geometry for consistency. As expected, within the ASIC scheme a more localized configuration for the holes is obtained and the spin-polarization of the hole density is also partially restored. The total moment on the supercell is found to be $\sim 2.7\mu_B$ which suggests that the localization achieved is not perfect. The bulk of the hole density and magnetic moment are however located on the eight O ions around the V_{Hf} site as is apparent from the Mülliken population analysis in table 5.5.

5.7 Summary and conclusions

In summary we perform DFT calculations investigating the possibility of intrinsic defect driven ferromagnetism in HfO_2 . We find that Oxygen vacancies as such form non-magnetic impurity levels unless p-type co-dopants are present. The presence of a sub CBM resonance state also leads to the formation of weak local moments on V_{O} sites in the presence of extra electron doping when the Fermi-level is just above the CBM. However, in both cases the V_{O} derived states are rather localized and show little magnetic interaction, ruling out the hypothesis of d^0 ferromagnetism [231] in bulk HfO_2 . In contrast Hf vacancies show a high spin state with an associated magnetic moment of $\sim 3.5\mu_B$. In contrast to cation vacancies in highly symmetric lattices, V_{Hf} centers in monoclinic Hafnia offer a more general mechanism for a magnetic ground state based on two facts: (1) symmetry driven orbital degeneracy is not a pre-requisite for the existence of a high-spin defect ground state

(2) a set of closely spaced single particle levels together with strong exchange might be sufficient for the same. These findings suggest that a wider class of systems, not restricted by symmetry and free from the possibility of Jahn-Teller like distortions, might actually be open to the possibility of intrinsic defect ferromagnetism. Significantly, the V_{Hf} centers are also ferromagnetically coupled via minority spin electron delocalization across the bridging Hf sites, with a large coupling strength at short inter-defect distances. However, while the magnetic coupling strength in itself is strong enough to sustain Curie temperatures above room temperature, the short range of the interaction requires rather large V_{Hf} concentrations. Recent calculations by Osorio-Guillèn *et.al* [239] show that the equilibrium concentration of V_{Hf} defects in bulk Hafnia are several orders of magnitude lower than that required for magnetic percolation. On the other hand, ferro-magnetic response is experimentally detected only in badly treated and highly granular thin-film samples and never in the bulk crystalline phase. Furthermore, the magnetic moment in the thin-film samples is seen to decay with time [232]. These observations in turn suggest that there might be significant out-of-equilibrium contributions to the defect concentration in the as grown thin-film samples. Nevertheless given the lack of systematic controlled experiments and indeed detailed experimental characterization of such “ferromagnetic” thin-film samples, theoretical calculations [240, 241] on the subject carried out to date remain speculative.

Chapter 6

Investigation of n-type donor defects in Co doped ZnO

6.1 Introduction

ZnO is a piezoelectric [242] transparent conductive oxide [243], in which free-carriers coexist with optical transparency [244]. If magnetism could also be successfully incorporated through transition metal ion doping, ZnO would become the ultimate multifunctional material, with semiconducting, magnetic, optical and mechanical properties. This would indeed have a profound impact on the emerging field of spintronics [245] with applications in optoelectronics [246] and quantum computing [247]. Moreover it would allow us to go beyond the (Ga,Mn)As paradigm [248], whose practical use is severely hampered by the low ferromagnetic critical temperature. This is why Co doped ZnO (ZnO:Co) is perhaps the most studied among all the dilute magnetic oxides. Since room-temperature ferromagnetism (RTF) in ZnO:Co thin films, was first demonstrated in 2001 by Ueda et al. [249], a number of experimental groups have reported similar findings [250, 251, 252, 253]. However, over the same period, several other groups have also reported the absence of ferro-magnetism in ZnO:Co thin-films [254, 255, 259, 257, 260] detecting either paramagnetism or spin-glass behaviour in some cases while in others the ferro-magnetic response was attributed to metallic Co nano-particles. While it has not been possible to reach a universal consensus on the problem in the face of several conflicting reports, numerous trends systematically linking the presence or absence of ferro-magnetic response in these thin-films to the experimental growth and processing conditions have nevertheless emerged. In what follows we list some of the more commonly reported experimental findings that

help to clarify the current state of affairs with regards to ZnO:Co.

i) Spectroscopy confirms that Co^{2+} substituting Zn is the center responsible for all the different magnetic phases found experimentally. These include RTF [256, 257, 258], paramagnetism [259, 257] and spin-glasses [260].

ii) RTF is detected experimentally from magnetometry [249, 251, 252, 253] or from magnetic circular dichroism [261, 250]. The critical temperature (T_C) is not usually measured and magnetic hysteresis at room temperature is taken as the smoking gun for RTF.

iii) The saturation magnetization (M_s) and the remanence (M_r) are always small. Hence a secondary phase as the source of RTF is often difficult to rule out. However, except for metallic Co, the phase diagram of ZnO:Co is populated only by non-magnetic materials or antiferromagnets with low Néel temperatures (CoO , Co_2O_3 , Co_3O_4 , ZnCo_2O_4). The coercive field is typically small (~ 100 Oe) and weakly temperature dependent.

iv) M_s is usually smaller than $3\mu_B/\text{Co}$ expected for Co^{2+} , with values as low as $0.01 \mu_B/\text{Co}$ [257]. This suggests antiferromagnetic interaction among Co^{2+} leading to spin-compensation [259, 258, 262]. Notably there are reports of moments exceeding the spin-only value [253, 263, 264].

v) Growth conditions and post-growth processing are crucial for the magnetic state. Chemical methods [250, 259, 262] and molecular beam epitaxy [265] generally lead to paramagnetism, while pulse laser deposition produces RTF films [249, 251, 252, 253]. Typically oxygen deficient growth [253] at tuned substrate temperatures [266, 267, 268] promotes the RTF. Similarly annealing in vacuum enhances the magnetic moment and produces ferromagnetism [257, 268, 269, 270], while annealing in oxygen has the opposite effect [270, 271]. Clearly sample morphology and intrinsic defects are important for the magnetic state.

vi) The role of free carriers is unclear. Exposure to Zn vapors, supposed to produce free carriers via the generation of interstitial Zn (Zn_i) donors, turns paramagnetic samples into ferromagnets [272]. However, measurements on samples sequentially annealed in reducing and oxidizing atmospheres, reveal little correlation between the electrical conductivity and the magnetic state [273]. Similar conclusions are valid for Al- and H-doping [274].

vii) Recent experimental [275] and theoretical [276, 277] evidence on ZnO points to oxygen vacancies (V_O) as the main source of oxygen deficiency but not of free carriers. These instead are attributed to unintentional H-doping. Exposure of ZnO to Zn increases the V_O concentration but not that of Zn_i . Thus the promotion of RTF due to Zn vapour exposure [272] must be re-attributed to an increase of the V_O and not of the free carriers.

viii) Electron paramagnetic resonance [278] suggests the presence of two magnetic cen-

ters. These are both related to Co^{2+} , although they present fine differences in the signal. Interestingly for a nominal Co concentration in the region of 5% the two centers appear with similar abundance.

Existing mechanisms for ferromagnetism in the diluted limit cannot explain this complex collection of phenomena. The Zener model, remarkably effective for dilute magnetism in the III-Vs [279], lacks of its foundations when applied to $\text{Zn}_{1-x}\text{Co}_x\text{O}$. First, there is little correlation between carriers and magnetism [273, 274], and, when present, carriers are electrons and not holes. The exchange coupling between electrons and local spins is about five times smaller than that for holes [279] and typical T_C 's are tiny at realistic carrier densities. Similarly super-exchange must be ruled out [280]. This produces only short range coupling and RTF can be obtained only for a Co concentration, x , above the nearest neighbour (NN) percolation threshold. For the wurtzite lattice this is 20 %, much greater than the typical experimental concentration.

Finally a modification of the Zener scheme, where the magnetic interaction is mediated by large hydrogenic orbitals associated to intrinsic defects was recently proposed [281]. This “donor impurity band exchange” (DIBE) model predicts ferromagnetism below the donor percolation threshold and therefore does not need free carriers. Although the mean field T_C obtained with realistic parameters for $\text{Zn}_{1-x}\text{Co}_x\text{O}$ is extremely small (~ 10 K) [281], the model is frequently used to justify the experimental results.

Thus, we turn to atomistic density functional theory (DFT) simulations in order to investigate in detail the electronic structure of Co doped ZnO at the microscopic level with the eventual aim of proposing a mechanism capable of explaining the myriad experimental observations.

6.2 Computational setup

Our DFT calculations are carried out within the LCAO basis set and pseudo-potential framework implemented in the SIESTA [282] code. Standard norm-conserving pseudopotentials constructed using the Troullier-Martins [283] scheme are employed. The electronic-configuration used in constructing the various pseudo-potentials and the basis set employed for each atomic species are listed in table 6.1 The basis set is specially optimized for bulk ZnO and extra “ghost” basis functions [282] are included at vacancy sites to accurately describe the charge density in empty regions. Nonlinear core corrections are included in the pseudo-potential for the transition metal atoms viz., Zn and Co. k-point sampling

Atomic Species	Electronic Configuration	Basis set
Zn	[Ar]4s ² 3d ¹⁰	4s-DZ,4p-DZ,3d-SZ
O	[He]2s ² 2p ⁴	2s-DZ,2p-DZ,3d-SZ
Co	[Ar]4s ¹ 4p ^{0.5} 3d ^{7.5}	4s-DZ,4p-DZP,3d-DZ
H	1s ¹	1s-DZP,2p-DZ

Table 6.1: The electronic configuration used for the generation of the pseudo-potentials and the pseudo-atomic orbital (PAO) basis sets employed for various atomic species are shown. SZ - single zeta, DZ - Double zeta, DZP - double zeta plus polarization

for Brillouin zone integration is done using a k-grid cutoff of 16 Å⁻¹ which translates to a 10x10x6 Monkhorst-Pack mesh for the primitive ZnO unitcell and a 3x3x3 mesh for a 128 atom supercell. The k-point grids for other supercell sizes are scaled appropriately. For the real space integrations involved in the solution of the Poisson equation and the estimation of the exchange-correlation potential, a grid cutoff (equivalent to plane wave-cutoff) of 650 Ry is chosen. Note that the use of core-corrections in the pseudo-potentials necessitates the use of a large real space cutoff to ensure proper convergence of total energy and forces. Geometrical relaxations are performed using standard conjugate gradient minimization until all the Hellmann-Feynman forces are smaller than 0.04 eV/Å. For supercell geometry relaxations, the cell volume is held fixed at the equilibrium volume of a pure ZnO supercell of the same size. Thus the volume relaxation due to the presence of dopants and defects which is usually expected to be rather small is neglected and only the internal degrees of freedom are allowed to relax. The exchange-correlation (XC) potential is treated within our approximate self interaction correction scheme (ASIC) previously introduced (see chapter 4). The α parameter in ASIC is set to a value of 0.5 which is appropriate for wide-gap semiconductor systems [285, 286]. For the LSDA component of the XC potential, the Ceperley-Alder [284] parameterization of the correlation energy functional is used. As discussed earlier, local and semi-local XC potentials such as LSDA/GGA are found to be severely inadequate in their description of strongly-corellated and magnetic systems such as transition metal oxides that contain localized d-electrons. In addition to overcoming most of the problems with LSDA/GGA in the electronic structure, the ASIC scheme also improves on the exchange parameters for the magnetic transition metal oxides [286].

6.3 Defect free ZnO

In this section we briefly review the ground state electronic structure of pure un-doped ZnO, focussing in particular on the shortcomings of the LSDA approximation and the improvements afforded by the ASIC scheme. ZnO crystallizes in the wurtzite structure where in each Zn and O ion is tetrahedrally coordinated by 4 O and Zn ions respectively. Table 6.2 shows some of the calculated (LSDA) and experimental cell parameters for the primitive unit cell of ZnO. Note that since the ASIC energy functional strictly speaking is not variational and thus does not satisfy the Hellman-Feynman theorem, for consistency we carry out all geometry optimizations using the LSDA energy functional. In spite of several short comings in describing the electronic spectrum of transition metal oxides, the LSDA geometries are usually accurate to within a few percent of experiment. The error made in the lattice constant of ZnO is seen to be less than 1% with the LSDA slightly overbinding the structure. Also structural relaxations around various defect centers in ZnO are expected to be qualitatively accurate within LSDA. The ground state band-structures

Parameter	Calculated	Experimental
a(Å)	3.23	3.25
c(Å)	5.18	5.21
u	0.380	0.382
Volume(Å ³)	23.39	23.83

Table 6.2: Comparison between calculated and experimental parameters [287] for the bulk unit-cell of wurtzite ZnO. The parameters a and c respectively are the lattice vectors lying in and perpendicular to the hexagonal plane while u is the internal parameter of the wurtzite structure. The volume indicated is the volume per formula unit.

of perfect ZnO calculated within LSDA and ASIC are shown in Fig. 6.1(a) together with the corresponding DOS. The top of the valence band (VBT) in ZnO is primarily O-2p in character while the bottom of the conduction band (CBM) is mainly composed of empty Zn-4s states. One of the main shortcomings of LSDA is the severe underestimation of the band-gap E_g in ZnO. The predicted LSDA gap in our calculation is ~ 0.96 eV well below the experimental gap of ~ 3.4 eV. The band gap error in LSDA although not critical for the description of pure ZnO itself, has major implications for the electronic structure of ZnO when defects and dopants, which might exhibit mid-gap states, are introduced. Thus formation energies of various native defects in ZnO as a function of the chemical potential calculated using LSDA must be corrected for the error in E_g [276, 288]. Furthermore, due to the small value of E_g , deep donor (acceptor) states derived from conduction (valence)

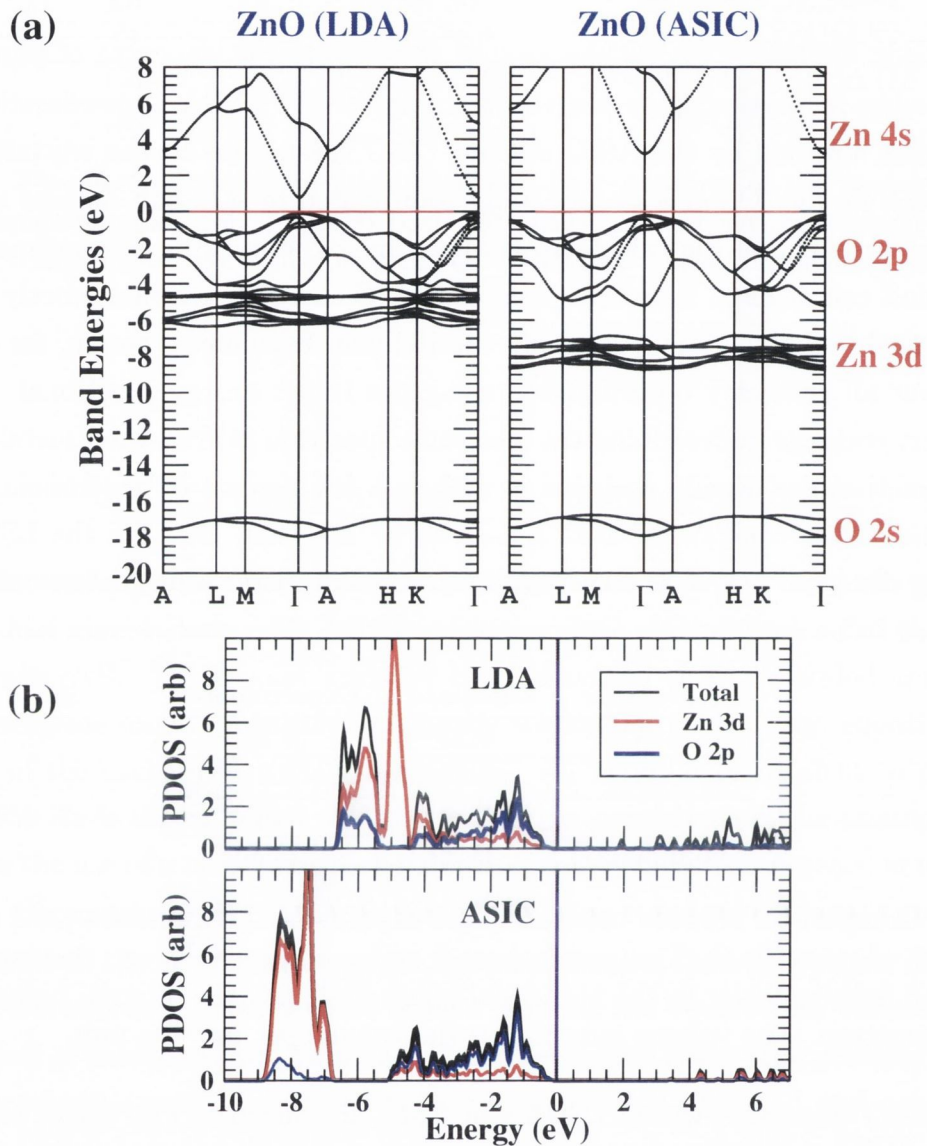


Figure 6.1: The calculated ground state band-structures of defect free ZnO from both LDA and ASIC are shown (panel a). ZnO exhibits a 2p-4s gap with the CBM being primarily Zn-4s in character while the VBT is built mainly from O-2p states. The Zn-3d manifold occurs at about 7-8 eV below the VBT while the O-2s states are very deep. In (b) valence band PDOS for ZnO from LSDA and ASIC showing the inter-mixing between the Zn-3d and O-2p states is presented. ASIC lowers the energy of the localized Zn-3d states and reduces the amount of Zn-3d+O-2p mixing in comparison with LDA. The Fermi level aligned to the VBT is set at 0.0 eV

band orbitals might be incorrectly described as being shallow. A second discrepancy in the LSDA electronic structure of ZnO is the incorrect placement of the Zn-3d states in the valence band spectrum. Valence band photo-emission spectra of ZnO [287] place the Zn-3d manifold about 7-8 eV from the valence band top (VBT). However LSDA under-estimates the binding energy of the localized Zn-3d states due to the self-interaction error. This results in an over-delocalization of the Zn-3d electronic states and some excessive Zn-3d and O-2p mixing. This is apparent from the PDOS shown in Fig 6.1(b). ASIC however improves the description on both counts, firstly by opening up the band gap to $\sim 3.2\text{eV}$ which is much closer to the experimental gap and secondly by lowering the energy of the Zn-3d states thus avoiding spurious band mixing between Zn-3d and O-2p states. The valence band spectrum of ZnO in ASIC is in fact in very good agreement with experimental photo emission spectra (PES) [287].

6.4 Co in ZnO

We now look at the electronic structure of ZnO both in LSDA and ASIC when a small percentage of Co is substituted at the Zn site. For this purpose we consider a 128 atom supercell of ZnO in which two Zn ions are replaced by Co, which translates to a Co concentration of $\sim 3.0\%$. The two Co ions are well separated to minimize Co-Co interaction. The valency of Co in ZnO:Co is nominally Co^{2+} . Since the ionic radii of Zn^{2+} (0.74 \AA) and Co^{2+} (0.72 \AA) are quite similar, there is only a rather small relaxation of the geometry around the Co site with the coordinating O ions relaxing inwards by $\sim 0.01 \text{ \AA}$. However, the shortcomings in the LSDA spectrum of ZnO carry over into the description of ZnO:Co and are further compounded by the presence of Co states in the gap. As the local symmetry of the ligand field around substitutional Co is tetrahedral, the Co-3d orbitals split into a set of e and t_2 states in the crystal. Note that the symmetry of the states is not strictly e and t_2 as the tetrahedral symmetry is not perfect in ZnO and the degeneracy of the two e and three t_2 states is thus slightly lifted. However the e and t_2 labels provide a useful way to group the two well separated sets of states. Furthermore the exchange splitting is larger than the crystal field and Co^{2+} stabilizes in a high-spin state with 5 up-spin and 2 down-spin electrons resulting in a local moment of $3\mu_B$ per ion. The 2 down-spin electrons occupy the two e derived states which are lower in energy leaving a set of 3 empty t_2 states. Experimental X-ray photoemission spectra (XPS) measurements on ZnO:Co thin films [289, 258] exhibit two main Co derived features (1) a peak in the

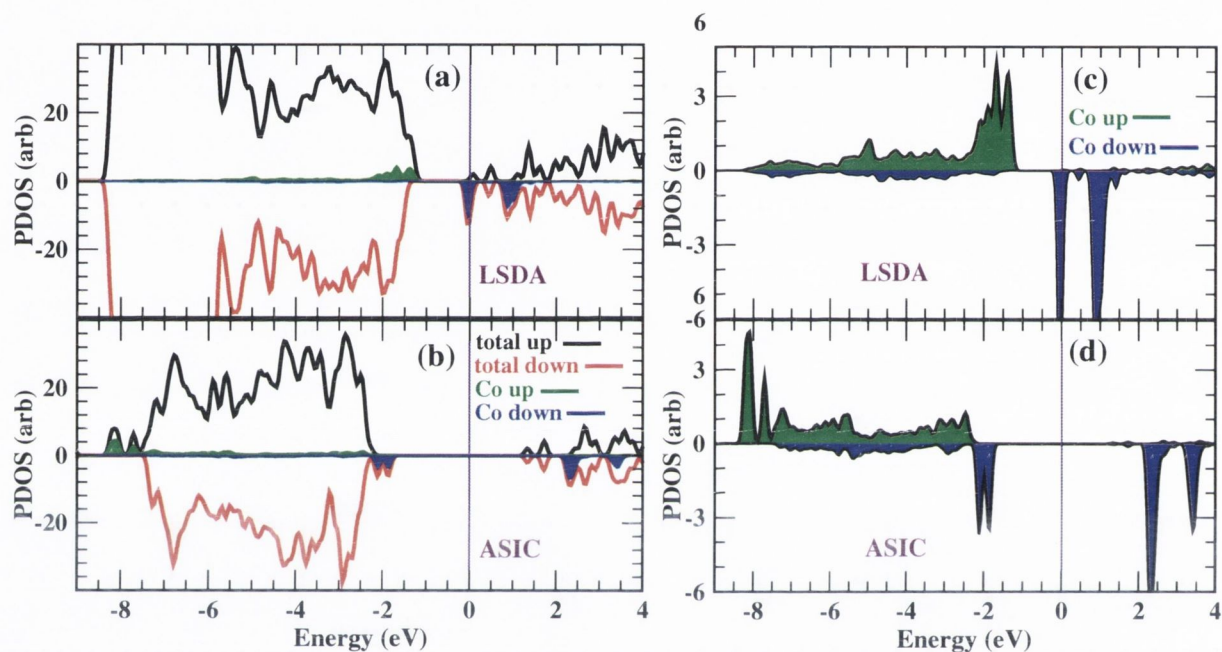


Figure 6.2: Spin resolved density of states for $\sim 3\%$ Co doped ZnO calculated from LSDA (a) and ASIC (b) are shown. The green and blue shaded regions indicate up-spin and down-spin Co PDOS respectively. Panels (c) and (d) present a magnified view of the PDOS for Co. LSDA underbinds the Co-3d states and incorrectly places the occupied down-spin 3d states just at the conduction band minimum (CBM). ASIC rectifies the problem by lowering the energy of the occupied Co-3d manifold. Accordingly the first primary Co-3d peak occurs at a binding energy of ~ 2.5 eV in good agreement with experiment

Co-3d partial density of states (PDOS) near the top of the valence band (VB) at a binding energy E_B of $\sim 2.0 - 3.0$ eV and (2) a broad secondary peak at around an E_B of 7.0-8.0 eV with a diffuse tail due to hybridization with O-2p states from the VB. However, as evident from Fig 6.2 and also supported by earlier literature [290], the binding energy of the electrons in the partially filled Co-3d orbitals is underestimated in LSDA and the minority e states of Co^{2+} are placed incorrectly at the Fermi level virtually pinned at the CBM. In fact a slight charge transfer between the e states and the conduction band results in a magnetic moment of $\sim 3.1\mu_B$ per Co in LSDA. ASIC rectifies this erroneous description by lowering the energy of the Co states and seems to be in remarkably good agreement with experimental spectra. Firstly, the minority spin e states are placed at about ~ 2.5 eV from the CBM. Secondly, the fully filled majority Co-3d states exhibit a strong hybridization with the O-2p valence band states but show two prominent peaks at an E_B of ~ 3.0 eV and $\sim 8.0 - 9.0$ eV. The calculated magnetic moment per supercell is exactly $3.0\mu_B$ and the system remains semi-conducting. The local magnetic moment on the Co^{2+} ion calculated from a Mülliken population analysis is found to be $2.7\mu_B$. Its also worth noting the position of the empty minority t_2 states that are placed roughly about 1.0 eV above the CBM. Thus, as neither the occupied nor the empty Co derived states are close to the CBM, the electronic structure of Co in ZnO is somewhat incompatible with a carrier mediated picture of ferromagnetism in the DIBE form. Carriers introduced by hydrogenic donors typically occupy states very close to the CBM and its difficult to envisage the charge transfer necessary for strong exchange coupling [281] between such donor states and the Co derived states. Nevertheless, in order to investigate the feasibility of the DIBE model in closer detail, one needs to look at how the introduction of various intrinsic defects alters the electronic structure of ZnO:Co. Several n-type intrinsic donor defects most notably Oxygen vacancies (V_O), Zinc interstitials (Zn_I) and incorporated Hydrogen (H_I) have recently been proposed in the experimental literature [253, 272, 274] as being responsible for introducing the carriers mediating the ferromagnetic interaction between Co^{2+} sites in ZnO:Co. In the following section, we present the electronic structure of defective ZnO containing each of the above three native defects before we go on to look at the effect that each defect individually has on ZnO:Co.

6.5 Native n-type defects in ZnO

We consider first the electronic structure of the Oxygen vacancy (V_O) in ZnO. V_O has a relatively small formation energy [276, 288] and is expected to be present in abundance in defective ZnO samples. Experimentally, concentrations of the order of $\sim 10^{20} \text{ cm}^{-3}$ are achievable which translates to roughly about 1%. Although there has been some debate until recently in the experimental literature on the role of V_O in the observed conductivity of ZnO, it is now widely accepted that V_O is a deep lying donor state that does not contribute any free carries to the system at room temperature. It has also been shown theoretically that V_O is likely to be responsible for the persistent photo-conductivity in ZnO [291]. The energetics of formation of V_O under various conditions have been widely addressed in the theoretical literature and are not discussed in this work. To model Oxygen deficient ZnO, we consider a 128 atom supercell with one Oxygen atom removed. In the neutral configuration the 4 nearest neighbour (NN) Zn ions around the V_O site relax inwards towards the center of the vacancy by $\sim 0.23 \text{ \AA}$. The V_O defect state is formed from the re-hybridization of the dangling Zn-4s orbitals around the site and at neutrality is occupied by two electrons thus making it a double donor impurity. In Fig. 6.4(a) the ASIC band structure of Oxygen deficient ZnO is shown. V_O exhibits a deep defect state in the band gap at about $\sim 2.2 \text{ eV}$ below the CBM. This is in good agreement with experimental deep level non-linear spectroscopy data [292] that place the V_O state at 2.1 eV below the CBM. Furthermore the defect state is spatially localized around the vacancy site extending out as far as the next nearest shell of O ions.

Fig. 6.3 shows the spatial distribution of the charge density for the doubly occupied mid-gap V_O state (see also Fig. 6.4(a)). For clarity, Fig 6.4(b) also shows the density of states (DOS) around the CBM for ZnO with V_O .

Zinc interstitials (Zn_I) in ZnO are characterized by large formation energies [276, 288] and under equilibrium conditions are formed in much lower concentrations compared to V_O . There has been some debate in the literature as to the identity of the native shallow donor in ZnO that is responsible for the high n-type conductivity at room temperature. This shallow donor has a small binding energy (E_B) of $\sim 30 \text{ meV}$ and both Zn_I and H_I have been proposed as possible candidates. It has been shown recently [293] that Zn_I can be stabilized in irradiated ZnO in special Nitrogen rich atmospheres in the form of a Zn_I+N_O complex, N_O being a Nitrogen impurity substituting an Oxygen site. However, under standard growth conditions, the formation energy of Zn_I is quite large [276, 293] and it is unlikely to be present in concentrations high enough to explain the measured carrier

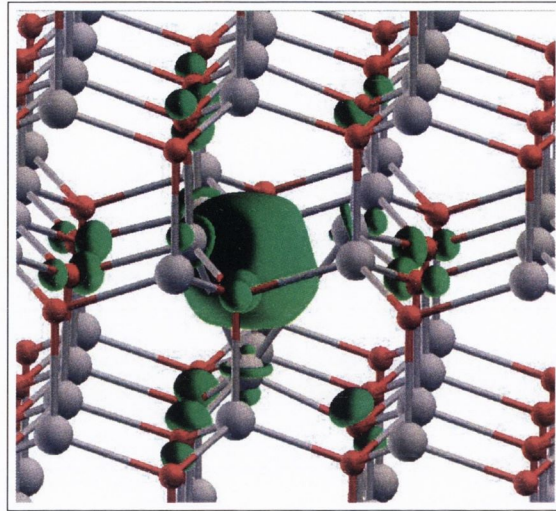


Figure 6.3: Isosurface (in green) depicting the spatial extent of the doubly occupied V_O defect state is shown. This corresponds to the mid-gap state seen in Fig. 6.4(a). Clearly most of the charge density is localized at the vacancy site between the 4 coordinating Zn ions. However there are significant contributions from the next nearest shell of O ions. The Zn ions are shown in grey, O ions in red.

concentrations in n-type ZnO. There are two possible interstitial sites in the ZnO lattice, one with octahedral coordination and the other with tetrahedral coordination. Among the two, the octahedral site is energetically much lower and we consider Zn_I only in this position. Due to the relatively large size of Zn atom, there is substantial lattice relaxation around the Zn_I site. The Zn_I ion stabilizes off the centroid of the octahedral cage closer to the three O ions while the three Zn ions forming the octahedral cage are pushed farther away from the Zn_I ion. Fig.6.5(a) shows the local geometry around Zn_I . In terms of electronic structure, as is the case with V_O , the Zn_I is also a double donor in that the defect state is occupied by two electrons in its neutral state. However, unlike V_O , the Zn_I defect state is not a mid-gap state but is resonant in the conduction band above the CBM and therefore ionizes spontaneously with the electrons dropping down into states at the CBM in the ground state. Thus Zn_I acts as a shallow Hydrogenic donor as it produces electrons in states close to the CBM which contribute to the electrical conductivity in ZnO. The band structure and DOS of ZnO with Zn_I are shown in Fig.6.4(c,d). The Fermi level (E_F) now lies in the conduction band as states near the CBM are occupied with the electrons from Zn_I .

Hydrogen is always incorporated into ZnO during growth and because of its low formation energy can be present in substantial amounts. It is most likely to be the shallow

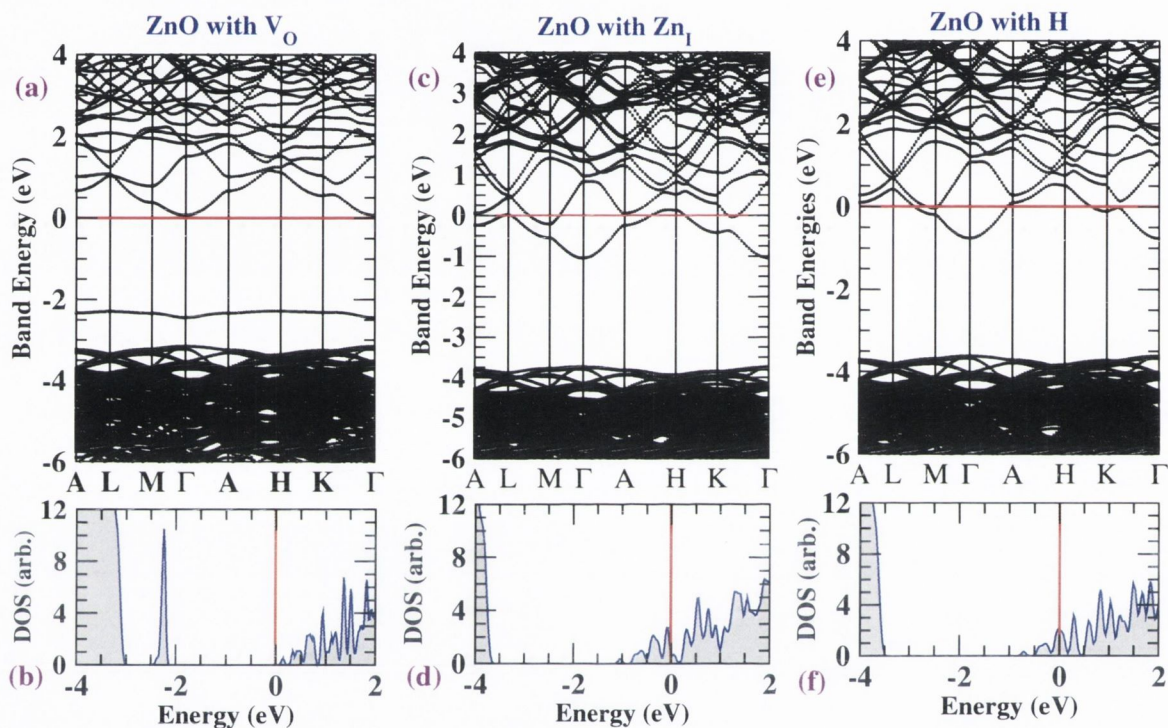


Figure 6.4: Calculated band structures of ZnO with $\sim 1.5\%$ V_O (panel a), Zn_I (panel c) and H_I (panel e) are presented. V_O exhibits a deep donor state while Zn_I and H_I exhibit defect states that resonate in the conduction band. These states are spontaneously ionized with the electrons occupying states at the CBM. Thus Zn_I and H_I act as shallow donors. The DOS corresponding to the band structures are also shown in panels (b), (d) and (f) for V_O , Zn_I and H_I respectively. The Fermi level is set at 0.0 eV

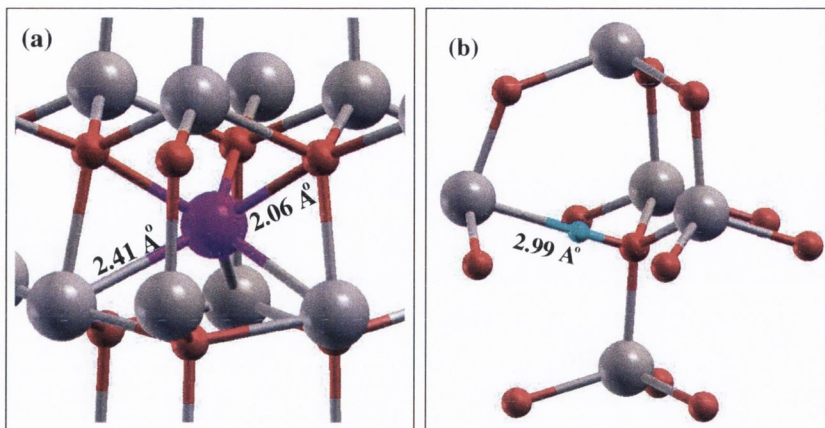


Figure 6.5: (a) The local geometry around the Zn_I in the octahedral position is shown. The Zn_I is highlighted in magenta. Due to the large size of Zn, substantial geometric relaxation occurs around Zn_I . (b) The local geometry at the H_I site is shown. The H ion (shown in blue) is incorporated in the middle of a Zn-O bond. As a result the Zn ion is pushed outwards increasing the Zn-O distance to ~ 3.0 Å. The H ion itself is located ~ 1.0 Å from the O ion.

donor responsible for the n-type conductivity of ZnO. There are several possible sites for H_I in the ZnO lattice and its energetics at various sites have been previously discussed [294]. In this work we consider H_I at two of the possible sites where the formation energy is low and the resulting electronic structure is that of a shallow donor. The first of these sites commonly referred to as the bond-center (BC) site, has the Hydrogen located in the middle of a Zn-O bond. H_I is incorporated between the O ion and the Zn ion and the subsequent geometric relaxation increases the Zn-O bond length to ~ 3.0 Å with the equilibrium position for the H ion a third of the way between O and Zn. The local geometry around this H_I site is shown in Fig.6.5(b). A second site where H is easily accommodated in ZnO is at an Oxygen vacancy site. This is equivalent to substituting an O ion with H. We therefore label this defect H_O for clarity. Both H_I and H_O are effectively shallow single donor defects as they produce one extra electron to occupy states near the CBM in the ground state. Qualitatively the electronic structure of H_I and H_O is similar to that of Zn_I except that for a given defect concentration the Fermi level is set lower in the conduction band as they produce only one electron whereas Zn_I produces two. This is apparent from the band structure and DOS shown in Fig. 6.4(e,f).

Although other n-type donors such as Al, Ga have been doped into ZnO:Co in an attempt to boost the observed ferro-magnetism, we do not study such extrinsic donors in our work. It seems reasonable to expect that qualitatively, the mechanisms responsible for

the observed trends in the ferromagnetism when intrinsic donors are introduced must still be valid in the case of extrinsic donors.

6.6 Donor-dopant interactions

The basic premise of the DIBE model is that the introduction of native shallow donors into ZnO:Co gives rise to an exchange interaction between the Co-3d states and the hydrogenic defect states resulting in a spin-split impurity band. When the concentration of the native donors is large enough so that the overlapping defect states percolate through the system, global ferromagnetism results. Thus in order for the system to exhibit long range ferromagnetism the defect-dopant system must essentially satisfy two requirements:(1) The exchange-interaction between Co and the defect states must be strong as it is the strength of the exchange interaction that determines T_C and (2) the defect states must have a sufficiently large spatial extent enough to achieve percolation at realistic experimental concentrations typically $\leq 1\%$. In this section we look specifically at requirement (1) by studying the electronic structure of ZnO:Co in the presence of various native defects. Of particular interest would be the identification of a spin-split defect band if at all present and the relative spatial arrangements of Co and the defect center in the ZnO lattice that are energetically favourable.

6.6.1 Zn_I -Co interaction

We consider a 128 atom supercell containing one Zn_I and one substitutional Co. Several different relative spatial arrangements of the Co ion and Zn_I are studied in order to gauge the range of Co- Zn_I interaction and to extract the binding energy for Co+ Zn_I pairs. We find that the range of Co- Zn_I interaction is rather short extending no farther than a second nearest neighbour distance ($\sim 2.65\text{\AA}$) from the Zn_I position. However there is a relatively strong binding energy of ~ 292 meV stabilizing the formation of Co+ Zn_I pairs with respect to separated Co and Zn_I configurations. Therefore, if both Co and Zn_I are incorporated during high temperature film-growth, Co+ Zn_I pairs are more likely to be formed. However, the normally achievable experimental concentrations of Zn_I ($\sim 10^{17}\text{cm}^{-3}$) and Co ($\sim 10^{21}\text{cm}^{-3}$) are vastly different and the amount of Co+ Zn_I is expected to be negligibly small compared to the amount of Co. In Fig. 6.6(c,d) we show two different supercell arrangements one in which the Co is at a third NN separation from the Zn_I (Fig. 6.6(c)) and a second in which the Co is part of the octahedral cage directly coordinating the Zn_I

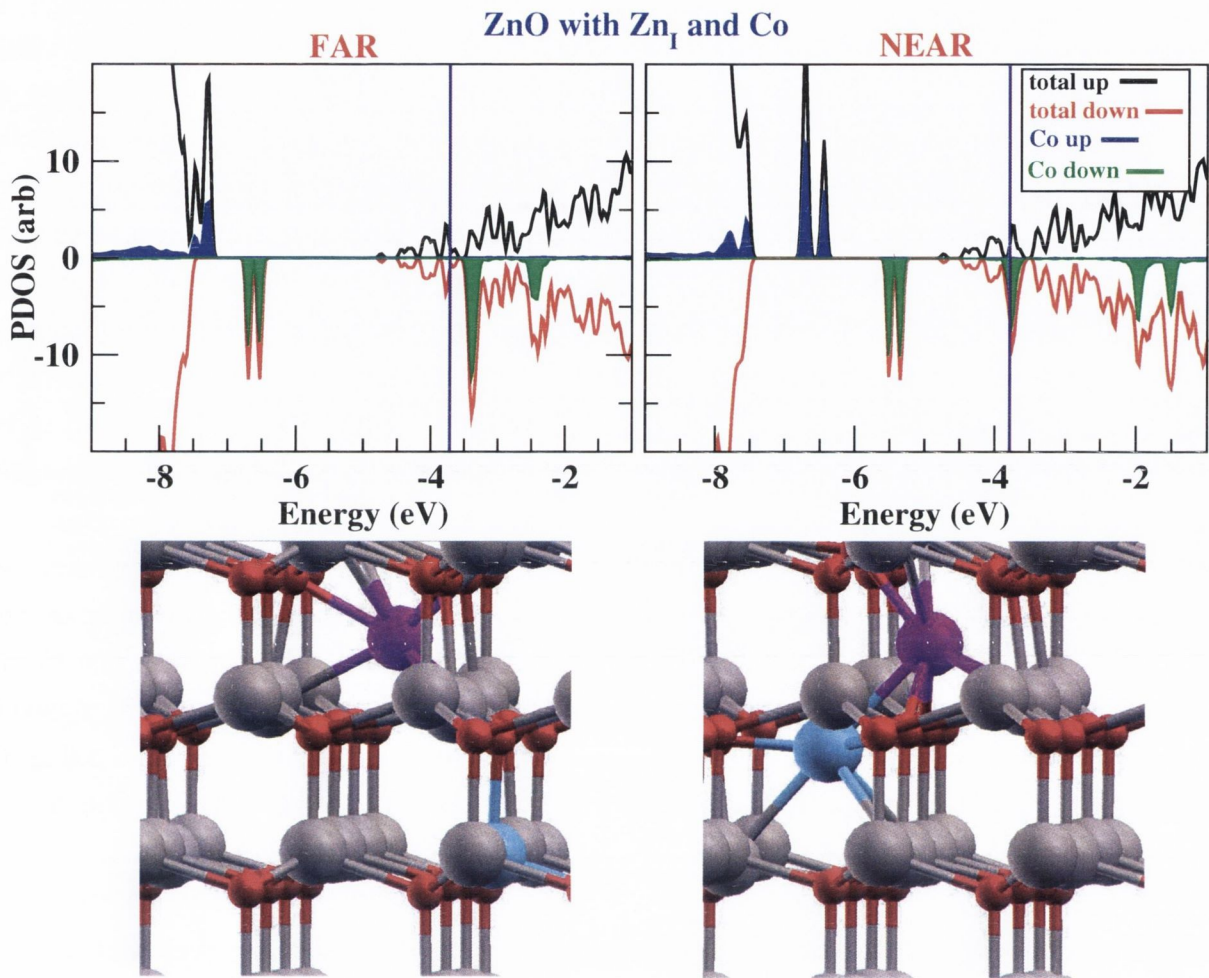


Figure 6.6: In (a) & (b) spin resolved DOS calculated from supercells containing one substitutional Co and one Zn_I are presented. The shaded regions indicate the Co contributions to the DOS. The vertical line in indigo indicates the Fermi-level. In the *far* configuration (panel a), the PDOS is simply a super-position of the PDOS for an isolated Co ion and Zn_I as interaction is minimal. In the *near* configuration (panel b), substantial charge transfer occurs from the CB states onto the spin-down Co- t_2 states. The resulting on-site repulsion between the Co-3d states increases the energy of the occupied up-spin Co-3d manifold which now lies in the band gap. However, the CB states themselves show little spin-splitting. Panels (c) and (d) show the supercell arrangements used for the *far* (a) and *near* (b) configurations respectively. The Zn ions are shown in grey, O ions in red and Co ions in blue. The Zn_I is highlighted in magenta. The same color code is used for Zn, O, Co and Zn_I from here on in unless specified otherwise.

(Fig. 6.6(d)). The former configuration is labelled *far* and the latter *near*. Note that in the *near* configuration, the Co ion sits closer to the Zn_I after geometric relaxation by about $\sim 0.06\text{\AA}$ compared to the other two Zn ions that form part of the octahedral cage around the Zn_I site. The PDOS corresponding to both the configurations are shown in Fig. 6.6(a,b). It is apparent that in the *far* configuration, the combined PDOS is essentially a superposition of the PDOS for the isolated Co and Zn_I species. Furthermore, there seems to be little exchange-interaction between the conduction band states near the Fermi level and the Co derived states with the former showing no spin-polarization. The local electronic structure of the Co ion is also found to be almost identical to that of an isolated substitutional Co. The total magnetic moment on the simulation cell is still $3.0\mu_B$. The local magnetic moment on the Co^{2+} ion calculated from a mülliken analysis is found to be $2.73\mu_B$ as compared to $2.71\mu_B$ for an isolated Co^{2+} when no Zn_I is present in the supercell. The situation is markedly different however for the *near* configuration. The proximity of the Co ion to the Zn_I results in substantial charge transfer from the CB states to some of the otherwise empty minority spin t_2 states of Co and the local magnetic moment on the Co ion drops to $\sim 2.0\mu_B$. The on-site repulsion resulting from an increase in the Co-3d occupation moves upwards in energy all the Co-3d manifold and now the majority t_2 levels occupy the ZnO bandgap. The total moment per supercell also decreases from $3.0\mu_B$ to $2.1\mu_B$ which shows that both majority and minority CB states are involved in the charge transfer to the minority spin Co- t_2 states. Crucially however, there is only a very weak spin-splitting of the CB states which one would expect from their delocalized nature and thus the spin-polarization of the CB electrons is negligible. It therefore seems that in spite of its charge transfer interaction with the Co ion, the Zn_I does not lead the formation of a spin-split impurity band with carriers capable of mediating long range ferromagnetism.

6.6.2 V_O -Co interaction

The V_O -Co interaction is studied by considering once again a 128 atom supercell containing one substitutional Co and one V_O in various relative spatial arrangements. Given that the V_O state itself is rather localized in space, the V_O -Co interaction cannot be expected to be of very long range. Accordingly, we find negligible interaction except when the Co substitutes one of the four Zn sites directly coordinating the V_O . However, there is a substantial pairing energy of ~ 340 meV favouring V_O +Co pairs over well separated V_O and Co arrangements. Two different supercell arrangements one in which the V_O and Co are separated (*far*) and the other with a V_O +Co pair (*near*) are shown in Fig.6.7(c,d).

The separation between the V_O and Co in the two cases is 7.20 Å and 1.72 Å respectively. A small degree of geometric relaxation occurs in the *near* configuration placing the Co ion closer towards the vacancy site by about 0.01 Å compared to the three remaining Zn ions. The PDOS corresponding to the supercells of Fig.6.7(c) and Fig.6.7(d) are shown

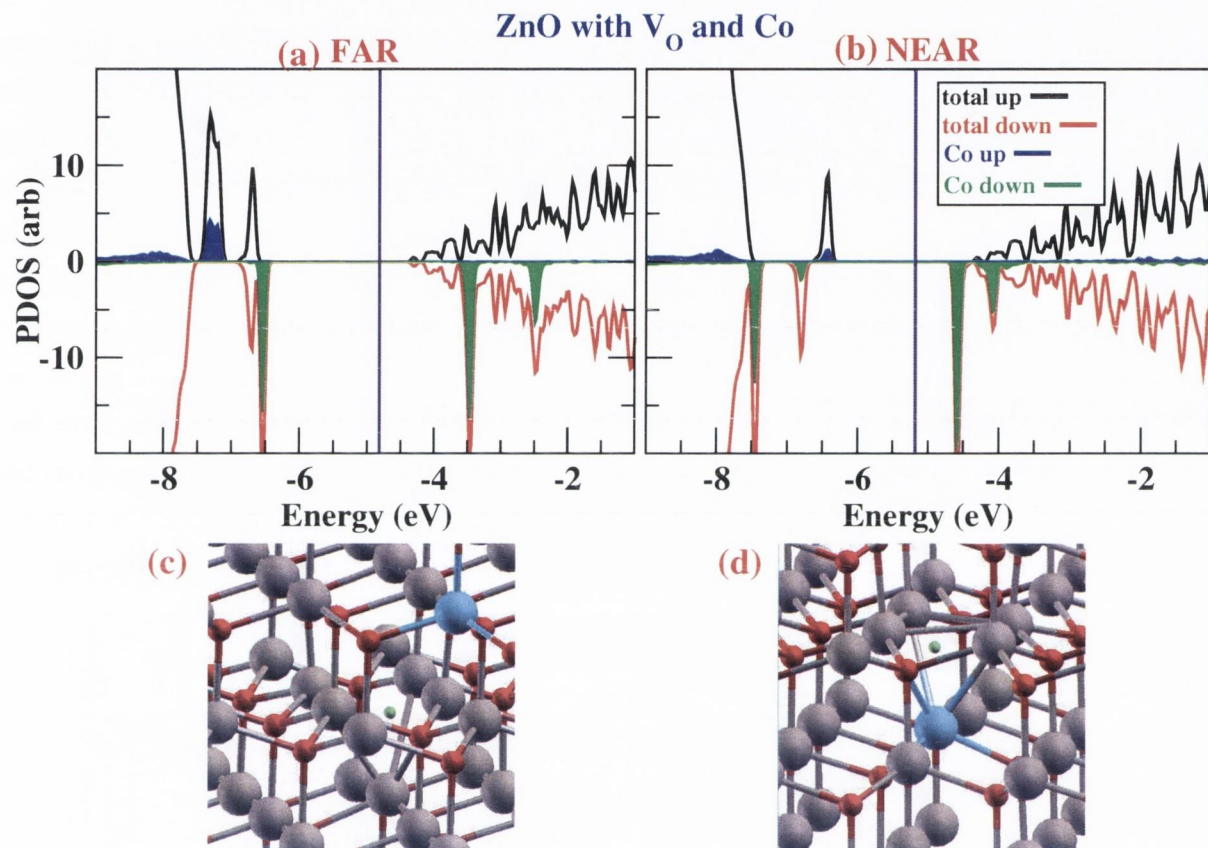


Figure 6.7: In (a) & (b) spin resolved DOS calculated from supercells containing one substitutional Co and one V_O are presented. The shaded regions indicate the Co contributions to the DOS. The vertical line in indigo indicates the Fermi-level. (a) In the *far* configuration, scenario remains Co- V_O interaction is minimal and neither the Co-3d states and the mid-gap V_O defect state are perturbed (b) In the *near* configuration the V_O state is clearly spin-split by about 0.5 eV. The energy of the Co-3d manifold is also lowered by hybridization and a part of empty minority spin Co- t_2 states now lie just below the CBM. (c) and (d) show the supercell arrangements used for the *far* (a) and *near* (b) configurations respectively. The small green atom indicates the V_O site.

in figures 6.7(a) and 6.7(b) respectively. Clearly the PDOS for the *far* configuration is just a superposition of the PDOS for isolated V_O and Co^{2+} . In this arrangement, the calculated magnetic moment per cell is also $3.0\mu_B$ as one would expect for Co^{2+} and the

local magnetic moment on the Co ion is also identical to that of isolated Co^{2+} in ZnO. Meanwhile the V_{O} mid-gap defect state remains un-perturbed by the presence of Co in the cell and shows no spin-splitting. In contrast the *near* configuration presents a much more interesting picture. The hybrid $V_{\text{O}}+\text{Co}$ state is clearly spin-split by ~ 0.5 eV in a direction opposite to that of the 3d states in Co^{2+} . However, unlike in the case of the $\text{Zn}_{\text{I}}+\text{Co}$ pair, no charge is transferred to the 3d states in the Co ion. The excess of electrons on the Co ion that results from it being a part of the V_{O} site, is seen to reside in the 4s and 4p states of the Co. The total magnetic moment on the supercell remains $3.0\mu_B$ and the local magnetic moment on the Co ion at $2.63\mu_B$ is very similar to the moment on isolated Co^{2+} ($2.71\mu_B$). Interestingly, the Co-3d manifold is actually slightly lowered in energy as a result of re-hybridization and the change in the ligand field due to the missing Oxygen ion. The empty t_2 subset of states are in fact shifted downward and a part of them is now seen to lie just at the CBM. A closer look at the spatial distribution of the charge density of this new t_2 derived sub-CBM state (see Fig.6.8) shows that it is in fact a hybrid state that is mainly Co-3d in character but also with some contribution from the neighbouring O ions. This re-arrangement of the Co- t_2 states is significant as these states are now accessible to electrons produced at the CBM from shallow donor like defects.

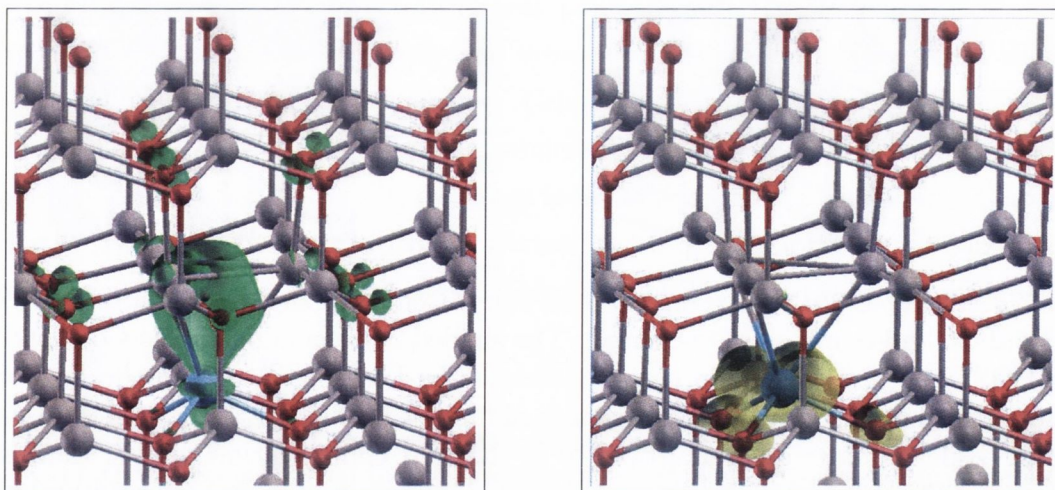


Figure 6.8: Spatial distributions of the hybrid $\text{Co}+V_{\text{O}}$ states formed in the *near* configuration are presented. On the left, the minority spin component of the spin-split mid-gap V_{O} state is depicted. The up-spin component has a similar spatial distribution. Most of the charge density resides at the V_{O} site but the next nearest shell of O ions also contribute. On the right, the Co- t_2 derived state at the CBM is shown. The d_{xy} character of the charge around the Co ion is apparent but the orbitals on the O-ions surrounding the Co also make significant contributions to the density.

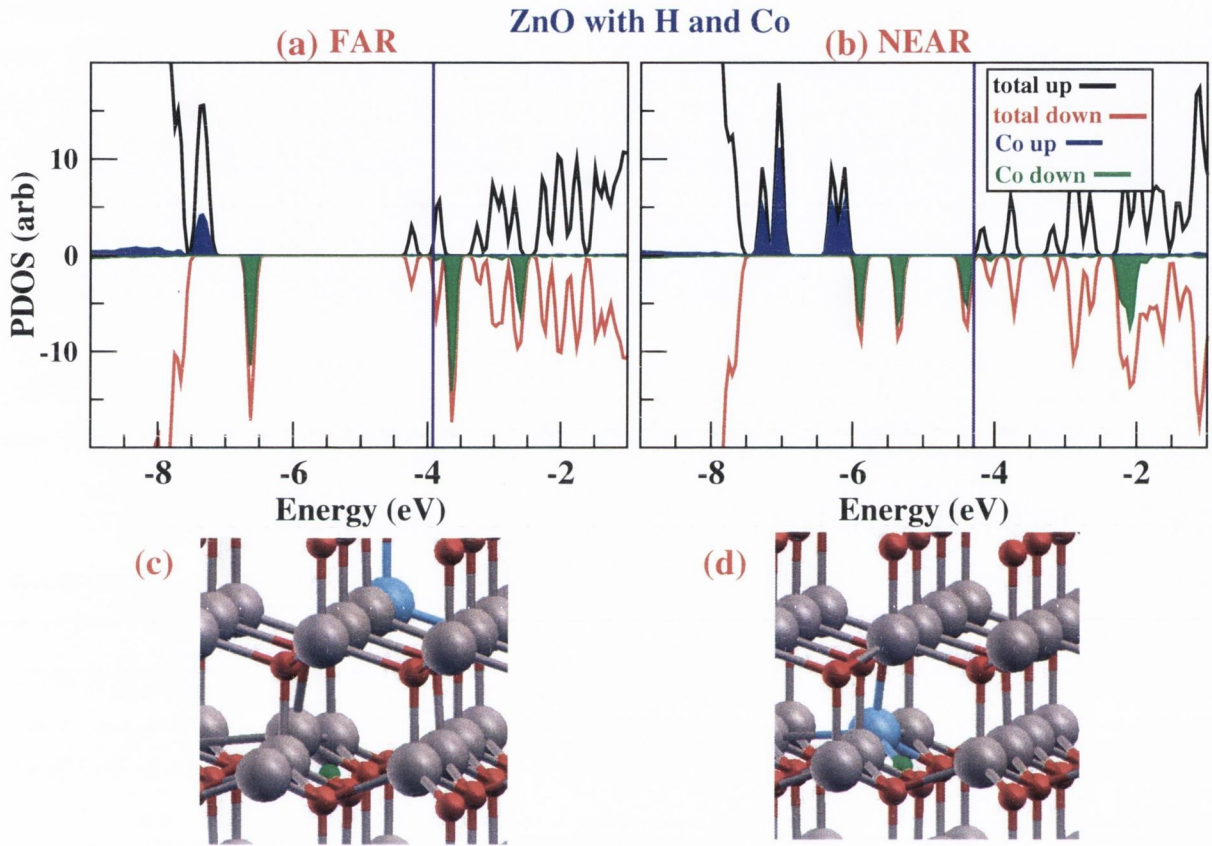
6.6.3 H_I -Co interaction

Figure 6.9: In (a) & (b) spin resolved DOS calculated from supercells containing one substitutional Co and one H_I are presented. The shaded regions indicate the Co contributions to the DOS. The vertical line in indigo indicates the Fermi-level. (a) In the *far* configuration, the PDOS is almost a superposition of that obtained for isolated Co^{2+} and H_I . (b) In the *near* configuration, substantial charge is transferred onto the empty Co- t_2 states and the resulting on-site repulsion on the Co ion, increases the energy of the majority Co-3d states. (c) and (d) show the supercell arrangements used for the *far* (a) and *near* (b) configurations respectively. The H_I site is shown in green.

As H_I is also a shallow donor type defect, its interaction with substitutional Co is qualitatively similar to that of Zn_I . As before, both *far* and *near* spatial arrangements are setup in a 128 atom supercell with one substitutional Co and one H_I . The PDOS and supercell configurations for the *far* and *near* cases are shown in figures 6.9(a-d). There is negligible interaction once again in the *far* configuration and the local electronic structure and geometry around both H_I and Co is virtually identical to that of the corresponding

isolated species. The *near* configuration is created by replacing with Co, the Zn ion of the Zn-O bond in which the H_I is incorporated. This configuration is favoured by a substantial pairing energy of ~ 487 meV and the resulting geometric relaxation involves a shrinking of the equilibrium bond length between Co and H_I to ~ 1.75 Å as compared to what was originally ~ 2.0 Å between Zn and H_I. The electronic occupation of the Co is also substantially altered as almost a full electron is transferred into one of the Co- t_2 states effectively changing the valence of the Co ion from Co²⁺ to Co⁺. The states at the CBM as a result are now almost emptied out. Also the on-site repulsion among the localized Co-3d states from the extra electron increases the energy of the occupied Co-3d manifold and the majority Co-3d states now sit in the middle of the band gap. The total magnetic moment on the supercell falls to $2.1\mu_B$ and the local moment on the Co site to $\sim 2.0\mu_B$. Interestingly, the states at the CBM exhibit a weak spin-split of ~ 0.05 eV in the same direction as the Co-3d states. Therefore additional carriers introduced into states at the CBM might be capable of mediating weak ferro-magnetism in this case.

Before we conclude this section it is worth emphasizing that although defect-dopant pair formation is favoured in all of the three cases studied above, only V_O+Co pairs are compatible with spectroscopical evidence available thus far. Zn_I+Co and H_I+Co pairs if present in abundance must be spectroscopically visible from the substantial increase in Co-3d PDOS in the gap. In contrast the spectroscopic signature of the Co ion in V_O+Co pairs is still very similar to Co²⁺ which is expected to constitute a major fraction of all the Co present in any sample.

Table 6.3: Calculated magnetic energy E_M for various magnetic centers and different dopants configurations. C1 and C2 are the two magnetic centers included in the simulation cell and their relative concentration (concentration of each center), D is the dopant with its concentration y , d_{C1-C2} is the distance between the two magnetic centers expressed both in Å and in NN shells (in parenthesis). Some of the supercell configurations for which Figures are provided are also referenced in the last column.

C1 (x)	C2 (x)	D (y)	d_{C1-C2} (Å)	Position D	E_M (meV)	Fig.
Co (0.015)	Co (0.015)	-	3.19 (1)	-	-38	6.10
Co (0.015)	Co (0.015)	-	3.11 (1)	-	62	6.10
Co (0.015)	Co (0.015)	-	4.54 (2)	-	-1	-
Co (0.010)	Co (0.010)	Zn _I (0.010)	8.01 (3)	<i>far</i>	-1	-
Co (0.010)	Co (0.010)	Zn _I ⁺ (0.010)	8.01 (3)	<i>far</i>	1	-
Co (0.010)	Co (0.010)	H (0.010)	8.01 (3)	<i>far</i>	1	-
Co (0.010)	Co (0.010)	V _O (0.010)	8.01 (3)	<i>far</i>	-1	-
Co (0.015)	Co (0.015)	Zn _I (0.015)	3.180 (1)	<i>near</i>	629	6.12(a)
Co (0.015)	Co (0.015)	Ghost-Zn _I (0.015)	3.180 (1)	<i>near</i>	-77	6.12(a)
Co (0.015)	Co (0.015)	Zn _I (0.015)	3.551 (1)	<i>near</i>	3	6.12(b)
Co (0.015)	Co (0.015)	Zn _I (0.015)	2.914 (1)	<i>near</i>	512	6.12(c)
Co (0.015)	Co (0.015)	Zn _I (0.015)	2.557 (1)	<i>near</i>	731	6.12(d)
Co (0.015)	Co (0.015)	V _O (0.010)	2.585 (1)	<i>near</i>	10	6.13(c)
Co (0.015)	Co (0.015)	V _O (0.010)	2.795 (1)	<i>near</i>	-103	6.13(d)
Co (0.015)	Co (0.015)	V _O (0.010) & Zn _I (<i>far</i>)	2.315 (1)	<i>near</i>	899	-
Co (0.015)	Co (0.015)	H (0.010)	3.829 (1)	<i>near</i>	12	6.13(a)
Co (0.015)	Co (0.015)	H (0.010)	2.713 (1)	<i>near</i>	296	6.13(b)
CoV (0.015)	CoV (0.015)	-	5.55 (2)	-	-6	-
CoV (0.015)	CoV (0.015)	H (0.010)	2.30 (1)	<i>far</i>	423	-
CoV (0.015)	CoV (0.015)	H (0.010)	2.27 (1)	<i>far</i>	614	-
CoV (0.015)	CoV (0.015)	H (0.010)	5.55 (2)	<i>far</i>	84	-
CoV (0.015)	CoV (0.015)	H (0.010)	4.51 (2)	<i>far</i>	9	-
CoV (0.015)	CoV (0.015)	H (0.010)	6.94 (3)	<i>far</i>	20	-

6.7 Magnetic coupling Interactions

Having looked at the electronic structure of the dopants (Co) and some of the defects that are likely to have a bearing on the ferromagnetism in ZnO:Co, we are now in a position to address the question of magnetic coupling. The approach is to consider supercells of various sizes containing two substitutional Co ions and possibly some donor defects in a variety of relative spatial arrangements. For each supercell arrangement, the total energies of two configurations $E_{\uparrow\uparrow}$ and $E_{\uparrow\downarrow}$ where the local spin moments on the two Co^{2+} ions are aligned respectively parallel ($\uparrow\uparrow$) and anti-parallel ($\uparrow\downarrow$) are calculated. The difference $E_M = E_{\uparrow\uparrow} - E_{\uparrow\downarrow}$ is a measure of the magnetic coupling energy. For the sake of clarity we

classify various supercell calculations as belonging to one of two categories based on the relative spatial arrangement of the donor defects and the Co ions in the system. In the first category donor defects if present in the supercell are always placed beyond a second NN distance from the nearest substitutional Co ion. Thus slightly generalizing the *far* and *near* classification discussed in the previous section, only arrangements of the *far* kind are used in such supercells. In the second category of supercells, only arrangements of the *near* kind are used where in substitutional Co ions always occur together with donor defects situated no farther than a second NN distance. A summary of the calculated magnetic coupling energies for various supercell configurations is presented in table 6.3.

6.7.1 *far* Configurations

First the case of two Co^{2+} ions in the supercell with no other donor defect present is considered using 128 atom supercell setups. These may be looked at as trivial *far* type configurations with donor defects situated at infinity. As Co^{2+} in ZnO does not create any carriers on its own, the only possible mechanism in this case is super-exchange which tends to be very short-ranged. Accordingly, we find negligible magnetic coupling except at first NN separation. In Fig. 6.10 we show the two possible arrangements in which two Co^{2+} ions can be a first NN distance apart. We find that the coupling is anti-ferromagnetic (38 meV) for the in-plane arrangement and ferro-magnetic (62 meV) for the out of plane arrangement. At second NN and beyond the magnetic interaction is virtually zero (≤ -1 meV). Furthermore, we find that the first NN configuration for the two Co^{2+} ions is favoured over the separated configurations by a substantial pairing energy of ~ 210 meV. Thus a certain degree of clustering of the substitutional Co is likely under high temperature growth conditions. Next we look at the case where additional donor defects are introduced into 192 atom supercells containing two Co ions as before so that the donors are *far* from either Co. This kind of arrangement reproduces the general scenario proposed by the DIBE model wherein a hydrogenic donor orbital centered on a defect site is presumed to interact with multiple Co ions located inside a characteristic effective radius causing them to line up ferromagnetically. However, as described in the previous section, none of the most commonly formed native defects have a strong enough interaction with substitutional Co except when they happen to be located directly next to the Co. As a result the magnetic coupling between the Co ions in the *far* configurations remains essentially unchanged with respect to the case with no donor defect in the supercell, as evident from rows 4 to 7 in table 6.3. The results of this sub-section are schematically summarized in Fig. 6.11.

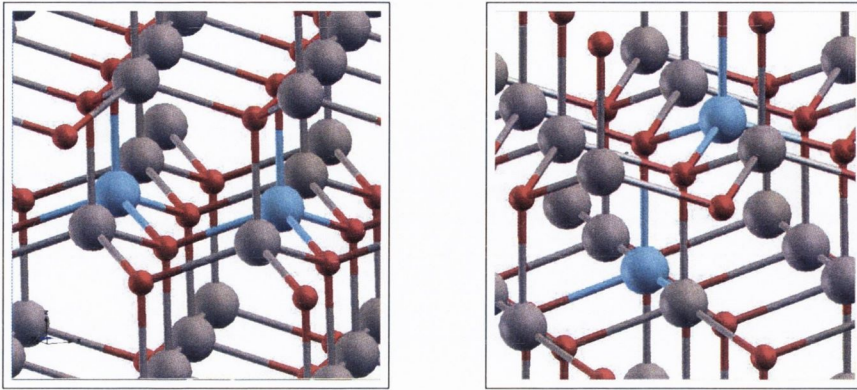


Figure 6.10: The two different arrangements possible for two substitutional Co ions at a first NN separation are shown. Left panel: the “in-plane” configuration wherein the two Co ions lie in the hexagonal plane is shown. The magnetic coupling is AF for this case. Right panel: the “out of plane” arrangement in which the two Co ions sit in adjacent hexagonal planes is presented. In this case the coupling is FM.

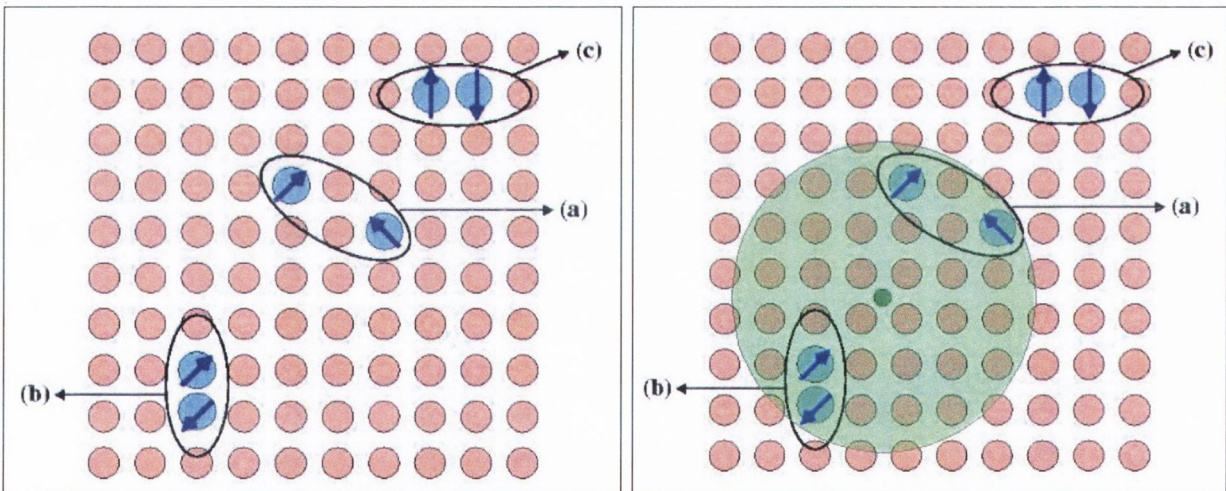


Figure 6.11: The general physical scenario modelled by the *far* category of supercell calculations is schematically described. In the absence of any donor defects, substitutional Co ions in any sample are either locked in AF or FM alignment (pairs (b) and (c)) at first NN separation or un-coupled otherwise (pair (a)). The scenario remains unchanged if donor defects are introduced homogeneously and at random locations in the crystal with no preference for sites close to substitutional Co. Thus the system is likely to be globally paramagnetic with some quenching of the measured saturation magnetic moment due to local AF interactions.

6.7.2 *near* Configurations

From the evidence presented in the previous section, random and homogeneous distributions of Co^{2+} and donor defects clearly cannot produce ferro-magnetism in ZnO:Co. A certain degree of aggregation between Co^{2+} and the donor defects seems necessary in order to *activate* the localized Co-3d states either by charge-transfer or direct hybridization. This implies that in real samples, the number of Co ions that can possibly take part in long range ferromagnetism would also be limited by the defect concentration. As the achievable defect concentrations (x^d) are typically an order of magnitude smaller than the Co doping concentration (x^{Co}), only a fraction of the Co ions can find themselves in close proximity to donor defects. In this sub-section magnetic interactions between Co ions located in *near* type configurations with respect to donor defects are considered. First we look at clustered configurations where the Co ions themselves are at first NN separation. Then we consider the magnetic interaction between distinct Co+donor pair complexes such that the Co ions are separated by several NN distances.

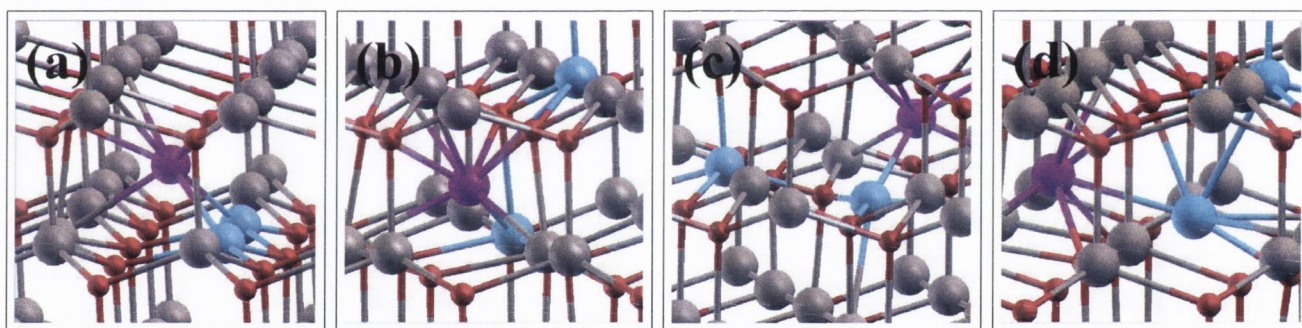


Figure 6.12: Four different supercell arrangements in which one Zn_I is placed in a *near* type configuration (see text) with respect to two Co ions are shown. Note that the large geometric relaxation around the Zn_I can significantly alter the distance between the two Co ions either increasing or decreasing the Co-Co separation.

In Fig. 6.12 sections of 128 atom supercells showing different arrangements of two Co ions and a Zn_I next to them are presented. The corresponding coupling energies are presented in Table 6.3. Clearly the presence of Zn_I next to either or both the Co when the two Co themselves are at first NN separation drastically increases the magnetic coupling strength and the FM alignment is favoured. For the case of the setup in Fig. 6.12(b), the calculated coupling energy is small as the distance between the two Co ions is increased drastically by the geometric relaxation around the Zn_I and only one of the two Co ions has charge transferred into its minority t_2 states. In Fig. 6.13 configurations where two Co ions

are in close proximity to a Hydrogen and a V_O are shown and the corresponding magnetic coupling energies are reported in table 6.3. Once again, in the case where the H_I is directly attached to both the Co ions, the magnetic coupling is very large and ferro-magnetic. It therefore seems that at first NN separation between the Co ions, the charge-transfer into the $Co-t_2$ states from donor defects, as in the case of both Zn_I and H_I , has a drastic influence on the magnetic interaction. To test this conjecture, the Zn_I atom in the supercell of Fig. 6.12(a) is replaced by a set of ghost orbitals but retaining the same geometry so that the system is the same as that of Fig. 6.12(a) except that the extra electrons introduced into the minority $Co-t_2$ states are now absent. In this case the coupling is seen to drop to 77 meV and is also anti-ferromagnetic (row 9 of table 6.3).

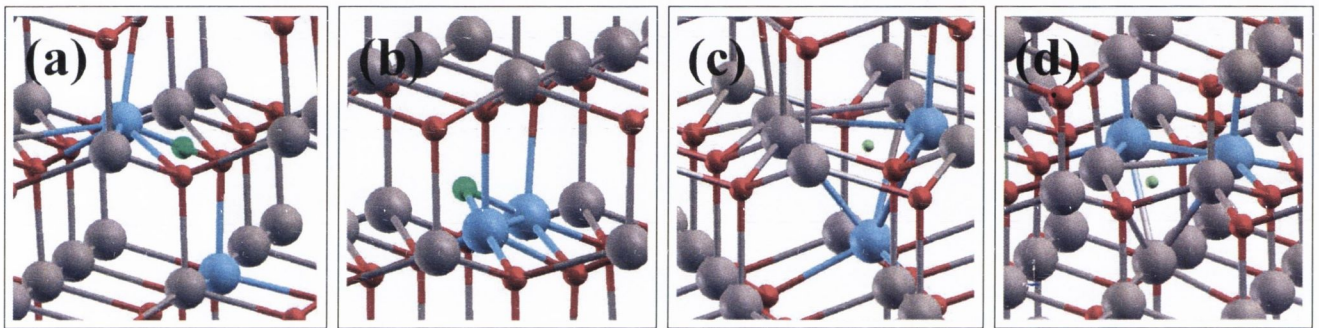


Figure 6.13: Four different supercell arrangements are presented in which either a V_O or an H_I is located in a *near* type configuration (see text) with respect to two Co ions. Panels (a) and (b) show the cells with H_I while (c) and (d) show the cells for V_O . Magnetic coupling energies for these configuration are presented in Table 6.3. In (c) and (d) the position of the V_O is indicated by a small dummy atom (in green).

Meanwhile in the case of the V_O directly coordinating the Co ions where no charge-transfer on the $Co-t_2$ sub-set occurs, only the in-plane (Fig. 6.13(d)) AF interaction between the Co ions is strengthened (relative to the corresponding case in Fig. 6.10) while the out of plane (Fig. 6.13(c)) FM interaction is in fact weakened. Note however that as shown previously, the V_O -Co interaction lowers the energy of the minority $Co-t_2$ states so that they lie just at the CBM (see Fig. 6.7) and are accessible to electrons introduced by shallow donors. To test whether the charging of the $Co-t_2$ states boosts the strong FM coupling even in this case, an extra Zn_I is introduced into the supercell of Fig. 6.13(d) such that it is located *far* from both the Co ions. Still, some of the electrons introduced at the CBM by the Zn_I are transferred onto the minority $Co-t_2$ states and the sign of the magnetic coupling is seen to change from AF (-103 meV) to FM (899 meV). Thus, strong FM interactions can be realized in clustered arrangements of Co ions when the minority $Co-t_2$ states are

activated by charge transfer from shallow donor defects. However, this mechanism is not very relevant to long range ferro-magnetism as it requires percolation of Co ions through out the system which is only possible for large Co doping concentrations ($x^{Co} > 20\%$).

We now investigate if the FM interactions activated by donor to Co- t_2 charge transfer persist at longer Co-Co separations. Since donor-Co interactions themselves are significant only at first NN separation, we consider donor+Co complexes as the effective magnetic centers during this discussion. Thus 192 atom supercells are setup in which two substitutional Co ions are placed beyond a first NN separation. Also a donor defect is placed next to each Co ion forming a complex. The magnetic coupling energy between Co+Zn_I and Co+H_I is reported in table 6.3 and is seen to be negligible. This result however is not surprising if one looks back at the electronic structure of Co+Zn_I and Co+H_I presented earlier (see Figs.6.6 and 6.9). Although these complexes involve local charge transfer onto Co- t_2 states, they do not lead to the formation a spin-polarized hybrid state with a sufficiently large spatial extent. The delocalized states at the CBM are partially emptied out but exhibit no spin polarization as the s-d exchange interaction between the CB states and localized Co- t_2 states is negligible. Thus it seems that charge transfer from Zn_I and H_I derived states is ineffective with regards to boosting the FM interaction except when there is direct over-lap between the Co- t_2 orbitals which happens only at first NN separation.

The magnetic coupling energies between Co+V_O centres (abbreviated as CoV) at various distances are also reported in table 6.3. In the case where there are just two CoV units separated by a second NN distance in the supercell with no other shallow donors present, the magnetic coupling is very weak and anti-ferromagnetic (Table 6.3). Note that in this configuration, the minority Co- t_2 derived states are empty although they reside just below the CBM. However when additional carriers are introduced by adding an extra Hydrogen atom to the supercell, reasonable FM coupling is obtained for Co-Co separations extending to a third NN distance. Recall that hybridization between the Co-3d orbitals and the defect state from V_O, leads to the formation of a set of localized and spin-split hybrid states in the band gap. Fig. 6.14 shows the PDOS calculated for a supercell with two CoV centres separated by a second NN distance and with some additional electron doping. The extra electrons introduced now occupy the hybrid CoV state just under the CBM. The spatial distribution of the charge density at the Fermi level is also depicted in the right panel of Fig. 6.14 which shows that the density is mainly localized on the Co ions and some of the O ions surrounding them. Thus it seems that the impurity band formed from the overlap of such hybrid CoV states is able to mediate ferromagnetic interaction between Co ions

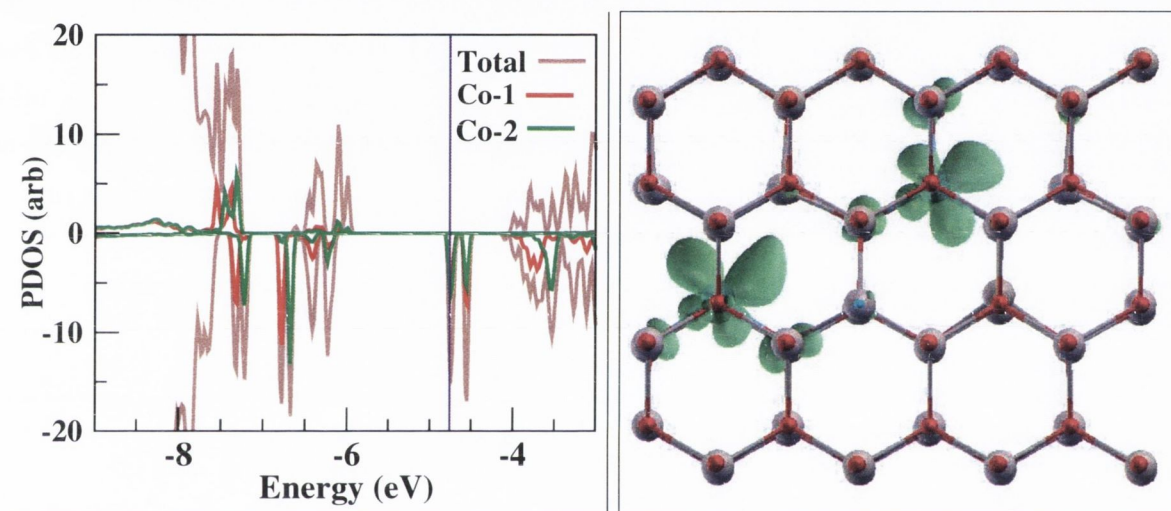


Figure 6.14: (Left panel) Calculated DOS for a supercell with two CoV centres and some additional electron doping is presented. The PDOS from the two Co ions in the supercell are plotted in red and green. The spin on the two Co ions is set parallel in this case. The Fermi-level (vertical indigo line) is seen to cut through the partially occupied hybrid CoV states just below the CBM. (Right panel) The spatial density distribution of the hybrid states at the Fermi level is depicted. A top-view of the supercell is shown with the c -axis pointing out of the page. The density is seen to be localized on the Co ions with a d_{xy} like symmetry but with some contributions from neighbouring O ions.

across a few NN distances. The formation of this CoV impurity band in an energy range that is easily n-dopable is schematically described in Fig. 6.15(a). We also studied the evolution of the magnetic coupling strength as a function of the occupation of the impurity band. This is done by artificially adding or removing electrons to the supercell so that the position of the Fermi level is swept across the band. Clearly, the coupling is weak-AF when the band is empty but turns FM and increases almost linearly as it starts to be occupied. The coupling strength shows a maximum at an optimal electron concentration (n_{opt}^e) which is equal to half that of the CoV concentration (x^{CoV}). Beyond n_{opt}^e the coupling strength decreases. It is also seen to flatten-out in some cases. This is because as electrons are added to the CoV hybrid states forming the impurity band, their energy increases and they eventually merge with the states at the CBM. After this happens, any further charge added preferably goes into CB states and the occupancy of the impurity band stays constant and so does the magnetic coupling strength. The general conclusions of this sub-section are summarized in Fig. 6.16

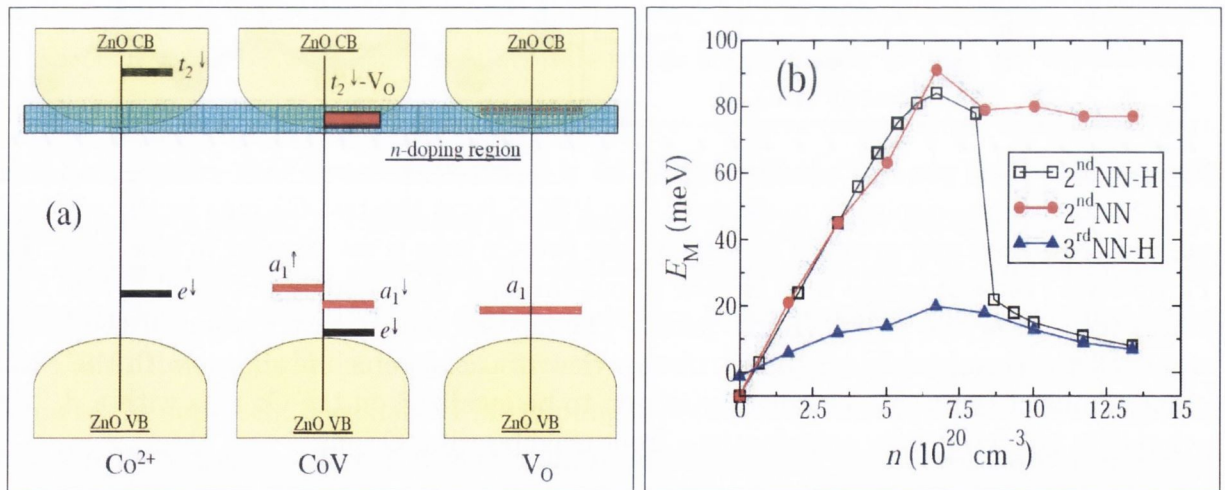


Figure 6.15: (a) A schematic level diagram for Co^{2+} , V_O and CoV is presented. Crucially the CoV center exhibits a defect state in the “n-doping” region, something not possible for Co^{2+} alone. (b) The magnetic coupling energy E_M for two 2nd NN CoV centers as a function of the defect band electron density is shown. The electron density $6.7 \times 10^{20} \text{ cm}^{-3}$ corresponds to one electron every two CoV .

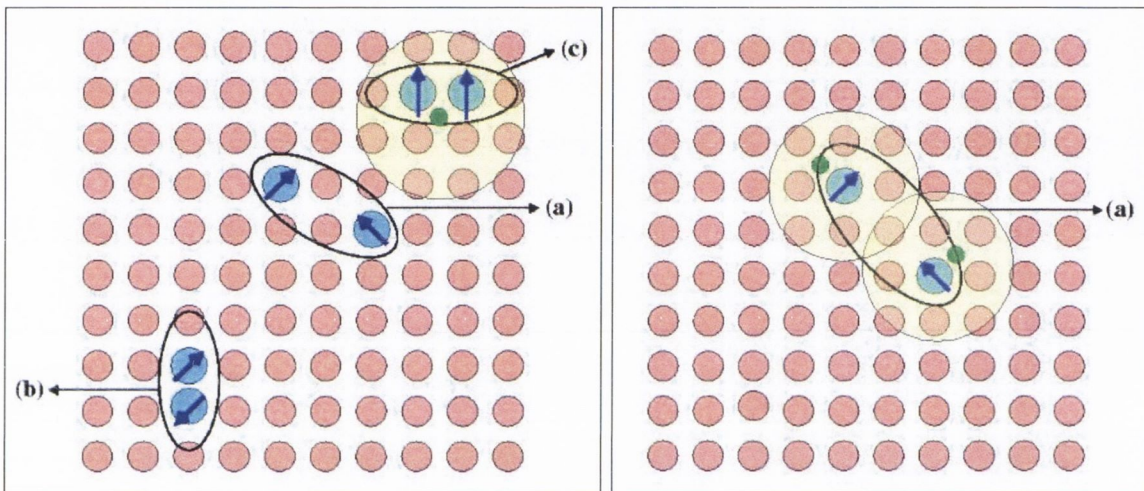


Figure 6.16: The general physical scenario modelled by the *near* type supercell configurations is schematically described. Left panel: donor defects situated close to Co-Co pairs (such as (c)) promote strong local ferromagnetic coupling between such pairs. Meanwhile other Co ions in the system are unaffected and pairs such as (b) are still locked in AF coupling while pairs such as (a) are uncoupled. Right panel: Co ions otherwise isolated can interact via Co+donor hybrid defect states that extend over a few NN shells (represented by the yellow shaded region). The CoV complexes form such a system that can couple ferromagnetically over a 3rd NN separation. This is equivalent to a modified DIBE mechanism wherein the active Co dopants occur together with defect centers.

6.8 Implications for Room Temperature Ferromagnetism

Taking stock of the DFT results presented in the previous sections, we now discuss the implications for room temperature ferro-magnetism (RTF) in ZnO:Co. We consider a mechanism which aims at explaining the experimentally observed trends in ZnO:Co based on two magnetic centers viz., substitutional Co^{2+} ions and CoV complexes. The first of these centers is responsible only for short range coupling, while the second can instead sustain relatively long range interaction via a fractionally filled impurity band. Can this alone produce RTF? As with other diluted systems, percolation theory [295] sets a strict condition for a magnetic ground state in the thermodynamic limit, that is, the concentration of the relevant magnetic impurity should exceed the percolation threshold x_c . This threshold depends on the range of the interaction and for the fcc lattice x_c is 19.8%, 13.7%, 6.2%, 4.9% and 3.4% for magnetic interaction ranges extending respectively to 1st, 2nd, 3rd, 4th and 5th NN distances [296]. Thus, the percolation threshold for Co^{2+} with a first NN interaction range in ZnO:Co is $x_c^{\text{Co}} \sim 20\%$. On the other hand, since the range of the magnetic interaction between CoV complexes extends as far out as a 3rd NN separation, our two-center model predicts long range RTF if $x^{\text{CoV}} > x_c^{\text{CoV}} (= 6\%)$. However, to obtain a global CoV concentration of $\sim 6\%$ experimentally in macroscopic samples is a near impossible task. The V_O concentrations that can be achieved experimentally are of the order of $\sim 1\%$ at best and even if we assume that a majority of V_O are likely to form CoV complexes driven by the favourable pairing energy, x^{CoV} measured over the entire sample cannot be expected to be very different from $\sim 1\%$. Therefore long range RTF from a globally percolating structure of CoV complexes is unlikely.

However, we do not need such a large x^{CoV} in order to explain most of the experimental magnetometry results such as the observed hysteresis in the M-H curve at room temperature. Magnetic hysteresis can be achieved for the global x^{CoV} well below x_c since one just needs a number of percolating clusters of CoV large enough to be superparamagnetically blocked. We define an active cluster of CoV as a region in the sample where locally, x^{CoV} is larger than x_c^{CoV} . There exists therefore a second global concentration threshold, that we call the measurability threshold x_m , setting the limit of what can be detected experimentally as RTF. The required size of the CoV clusters can be estimated by considering coherent rotation of the magnetization over an anisotropy barrier $DN_B S^2$ (D is the zero-field split, N_B the number of magnetic ions magnetically blocked and S the Co^{2+} spin).

By taking $D = 2.76 \text{ cm}^1$ from EPR measurements [265] we obtain an estimate $N_B = 800$ for a blocking temperature $T_B = 300 \text{ K}$. This however is rather conservative. In granular magnets random dipolar interaction [297] or random magnetic anisotropy [298] can push T_B to values considerably larger than those predicted for single particle coherent rotation (by up to a factor 5). A similar effect can be also found in magnetic clusters arranging according to spinodal decomposition [299]. Thus an estimate for N_B in the range of 250 magnetic ions is more realistic. This implies that, in order to measure hysteresis at room temperature, one needs to find regions where around 250 CoV complexes interacting at 3rd NN exist at concentrations larger than 6%. This seems a rather modest requirement and calculations presented in [300] show that even for a completely homogenous and random distribution of CoV neglecting the tendency for Co ions to aggregate, large clusters with more than 10^4 CoV units can be formed at $x^{\text{CoV}} \sim 2\%$. Thus the measurability threshold x_m^{CoV} can be expected to be of the order of 1-2%. Reference [300] also presents Monte Carlo simulations investigating the evolution of the thermodynamic properties of CoV clusters as the concentrations of Co^{2+} and CoV are varied. We are now in a position to propose

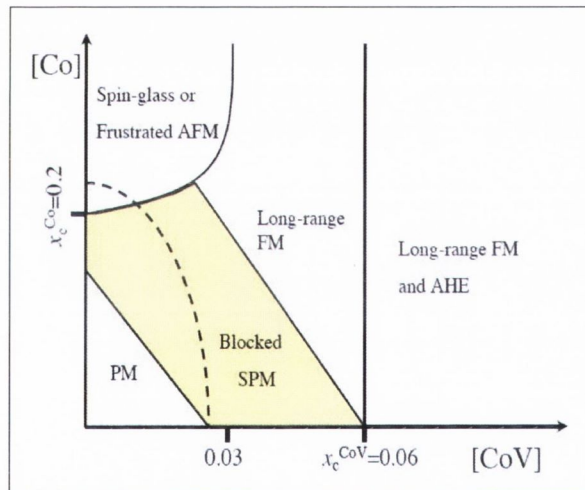


Figure 6.17: Proposed phase diagram for ZnO:Co as a function of the relative concentrations of Co^{2+} and CoV. The yellow area is the blocked superparamagnetic (SPM) region, where both magnetic moment and hysteresis can be detected. The dashed line at small x marks the region where most of the experiments are conducted. Finally the FM region is partitioned into two regions depending on whether or not anomalous Hall effect can be detected.

a phase diagram (see Fig.6.17) for ZnO:Co based on the relative concentration of Co^{2+} and CoV. At low x^{Co} and x^{CoV} the system is paramagnetic. As x^{CoV} is increased, the system evolves into what we call a blocked superparamagnetic phase which is the most

important feature of the phase diagram as it is the region relevant to most experimental observations. This occurs for $x^{\text{CoV}} < x_c^{\text{CoV}}$ and $x^{\text{Co}} < x_c^{\text{Co}}$, but nevertheless allows one the detection of both a net magnetic moment and hysteresis at room-temperature. For larger x^{CoV} ($\geq 6\%$) a global thermodynamic FM ground state emerges. Importantly bulk measurements (hysteresis or magnetization) can hardly distinguish between the FM and the blocked superparamagnetic phase, and more local probes are needed. In particular we believe that a thorough analysis of neutron scattering data [298] would be highly desirable. On the other hand as x^{Co} is increased, the short range AFM interactions between the Co ions become more relevant. Therefore we predict either a frustrated antiferromagnet or a spin-glass for $x^{\text{Co}} > x_c^{\text{Co}}$ and $x^{\text{CoV}} \ll x^{\text{Co}}$. Finally we partition the thermodynamic FM region into two regions separated by the CoV percolation threshold x_c^{CoV} . For $x^{\text{CoV}} > x_c^{\text{CoV}}$ percolation among CoV is achieved and one expects measurable conductivity from the impurity band. Since this is strongly exchanged an anomalous Hall effect (AHE) should be detected. This is not expected for ferromagnetism below x_c^{CoV} since the conductivity is then dominated by band conductivity which is only weakly affected by Co^{2+} since the exchange is small. Note that this phase diagram says little about the overall conductivity of ZnO:Co which in turn can be determined by electrons in the conduction band, which contribute little to the magnetism. Moreover the boundary between the different phases are somehow arbitrary and depend critically on the presence of electron donors. For instance the blocked superparamagnetic region can disappear entirely for fully compensated samples, since the long range interaction between CoVs vanishes.

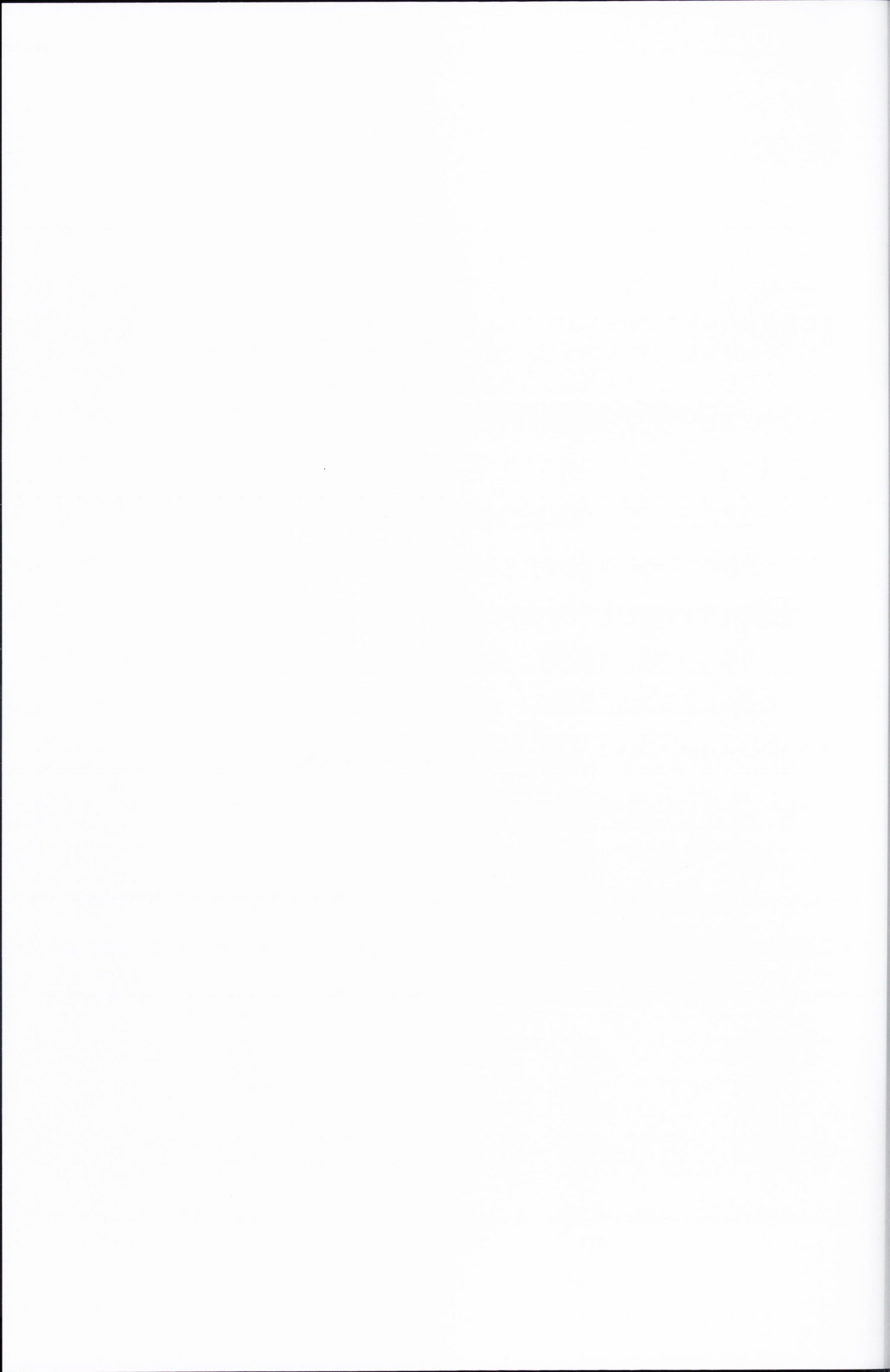
6.9 Conclusions

In conclusion, using DFT calculations incorporating self interaction correction, we have investigated the electronic structure of ZnO:Co in the presence of commonly occurring n-type donor defects in an effort to explain the experimentally reported ferromagnetism and related trends in thin-films of ZnO:Co. We attribute the observed room temperature ferromagnetism in ZnO:Co to blocked superparamagnetism. This superparamagnetic phase develops at Co concentrations below those required for ferromagnetism in the thermodynamical limit. However, in order to explain the widely observed enhancement in room-temperature magnetization and hysteresis in ZnO:Co thin-films upon post growth processing under Oxygen deficient conditions, we invoke a second active magnetic center in ZnO:Co namely the $\text{Co}+\text{V}_\text{O}$ (CoV) complex in addition to substitutional Co^{2+} . Ferro-

magnetic interactions between these CoV complexes extend over a few nearest neighbour distances in the presence of additional electron doping and are strong enough to persist up to room-temperature. This is in stark contrast to the magnetic interactions between Co^{2+} which are extremely short range and can also be antiferromagnetic. We show that the introduction of CoV centres into the system can lead to the formation of ferromagnetic clusters with a high blocking temperature. These findings draw a new roadmap for designing diluted magnetic oxides, where the engineering of intrinsic defects plays the leading role. For instance paramagnetic samples can be turned ferromagnetic by prolonged exposure to Ti vapours, which produce high concentration of V_O [275].

Part III

Electronic transport calculations



Chapter 7

Electronic transport properties of Mn_{12} single molecule magnets

7.1 Introduction

Single-molecule magnets (SMMs) often also called molecular nanomagnets, represent a novel class of magnetic materials, wherein each individual molecule is a self contained spin system whose magnetic properties are determined solely by intra-molecular exchange interactions. Such magnetic molecules usually contain one or more transition metal centers or rare-earth ions or even just organic radicals and occur as molecular crystals wherein they are locked in their lattice positions by a careful chemistry of surrounding organic fragments. Interactions between the individual molecular entities in these crystals are however weak, and the magnetic behavior probed by experiments is often governed by intramolecular effects. The discovery of the Mn_{12} class of magnetic molecules [301] that exhibit a magnetic ground state of $S = 10$ with a characteristic magnetic hysteresis [301] has boosted interest in this field enormously. The observed hysteresis in molecular magnets unlike in conventional ferromagnets is not due to re-magnetization of domains, but arises due to *magnetization tunneling* [302] between quantum spin states of the molecule, as the external magnetic field realigns the degeneracies of different states. This remarkable phenomenon can be observed in these SMMs as they have a very long spin relaxation time, which is much larger compared to the measurement time. Indeed relaxation times of the order of several months have been observed at very low temperatures ($\sim 2\text{K}$). A single molecule therefore effectively behaves like a single domain and is relatively independent of the magnetization of its neighboring molecules. These properties make SMMs

very attractive for a host of technological applications such as single molecule “bits” for magnetic storage, working units “qubits” in quantum computing or as magnetic switches which exhibit spin cross-over behaviour under external impulses such as light. The first of these possibilities viz., the potential for use in information storage has mainly driven research in the field over the past decade. These molecules have been successfully fabricated in single-molecule transistor geometries [303, 304, 305] and phenomena such as Coulomb blockade and the Kondo effect have been demonstrated. More recently signatures of the magnetic properties of these SMMs have been reported in transport measurements through these molecules [306, 307]. Regions of negative differential conductance (NDC) and complete current suppression in low energy excited states of these Mn_{12} molecules were also observed [306]. To date however, there have been no *ab initio* theoretical investigations of the transport properties of these Mn_{12} based magnetic molecules. In fact, the investigation of the coupling between charge transport and the molecular spin degrees of freedom presents a fascinating and challenging problem for first principles theoretical methods, but the large system sizes (typically hundreds of atoms) that are needed to model SMMs have made such calculations impractical. Nevertheless, with the availability in recent times, of efficient numerical transport codes such as SMEAGOL [317], an *ab initio* treatment of transport through Mn_{12} SMMs can be undertaken. In this work we study the steady state transport properties of Mn_{12} molecules attached to gold electrodes, within the non equilibrium green’s functions (NEGF) formalism. One of the questions we wish to answer is whether a static change in the potential in the region of the molecule due to a change in its local spin configuration can be detected in a transport measurement.

7.2 Structural properties of Mn_{12} clusters

The prototype SMM of the Mn_{12} class is the so called $Mn_{12}Ac$ with molecular formula $Mn_{12}O_{12}(CH_3COO)_{16}(H_2O)_4$ and is the most intensively studied among all SMMs. However, a more recently synthesized Mn_{12} based molecule abbreviated $Mn_{12}TE$ has been shown [308] to be stable on gold surfaces with the potential to self organize into extended arrays and thus facilitate the individual addressing of molecules in scanning probe microscopy (SPM) type experiments. In figure 7.1, two different views of the $Mn_{12}TE$ molecule are presented. The full chemical formula of the $Mn_{12}TE$ single-molecule magnet is $[Mn_{12}O_{12}(L)_{16}(H_2O)_4]$ where $L = 4$ -(methylthio)benzoate. This system basically consists of a Manganese-Oxygen core ($Mn_{12}O_{12}$) with 12 Mn ions and 12 O ions. The Mn

ions in the core are arranged in an almost planar geometry with 4 of the Mn ions in a central oxide cube and the remaining 8 Mn ions forming an outer ring. The core region is surrounded by organic dendrimers which are essential for keeping the molecule stable in solution and more so on metallic surfaces. However, they do not directly influence the electronic structure of the Mn_{12} core and as such play no role in the magnetic properties of these systems. Each of the sixteen 4-(methylthio)benzoate dendrimers has a sulphur atom at one end that provides the necessary bonding with gold surfaces. Mn_{12} clusters are usually synthesized as molecular crystals made of weakly interacting individual molecules. The crystal exhibits a tetragonal symmetry (space group $I\bar{4}$) while individual clusters such as $Mn_{12}TE$ possess an S_4 symmetry axis perpendicular to the plane formed by the Mn ions. In all, this Mn_{12} system consists of 12 Mn atoms, 48 O atoms and including all of the organic functional groups has a total of 324 atoms.

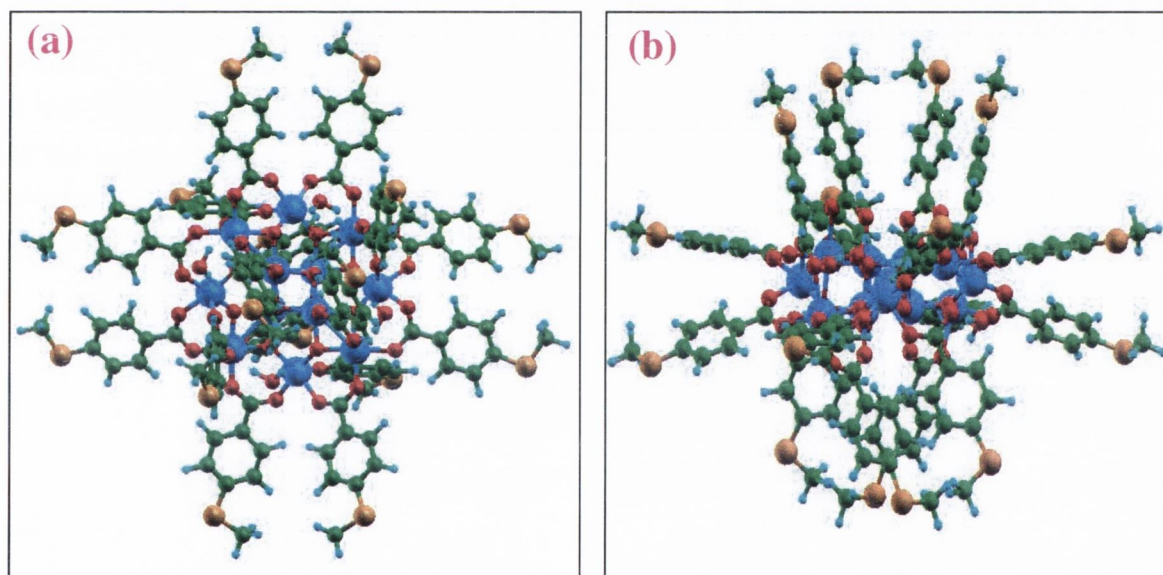


Figure 7.1: Panel (a) presents a *top* view of the $Mn_{12}TE$ molecule along the S_4 symmetry axis perpendicular to the plane of the $Mn_{12}O_{12}$ core. The organic thio-ether groups help to keep the molecule stable in solution and on metal surfaces. The molecule features 16 peripheral sulphur atoms (shown in orange) which provide as many surface bonding sites when placed on gold. Panel (b) shows a *side* view of the molecule. The following colour code is used for various atomic species: C - green, O - red, S - orange, Mn - blue, H - cyan

For a preliminary investigation of the basic electronic structure of a free standing Mn_{12} core, one does not need to consider the organic thio-benzoate functional groups. Thus we strip off the thio-ether(TE) groups and replace them by much simpler COOH groups

on the periphery of the Mn_{12} core. Thus we are left with a $[Mn_{12}O_{12}(COOH)_{16}(H_2O)_4]$ molecule. Note that the prototypical $Mn_{12}Ac$ cluster can simply be obtained by replacing the H ions in the (COOH) groups with methyl groups. The resulting bare bones Mn_{12} system which now contains only 100 atoms is shown in figure 7.3. The Mn ions in these clusters are six-fold coordinated by O ions but exhibit a significant Jahn-Teller distortion which lowers the local O_h symmetry. From here on we label this stripped down version of the molecule $Mn_{12}f$ where “f” indicates the formate (COOH) groups surrounding the Mn_{12} core.

7.3 Computational setup

To study the electronic structure of the Mn_{12} system we use the DFT implementation within the SIESTA package [309] which employs a numerical pseudo-atomic orbital (PAO) basis set and standard norm-conserving [310] pseudopotentials. The electronic-configuration used in constructing the various pseudopotentials and the basis set employed for each atomic species are listed in table 7.1. GGA pseudopotentials generated using the PBE [311]

Atomic Species	Electronic Configuration	Basis set
Mn	$[Ar]4s^14p^13d^5$	4s-DZP,4p-SZP,3d-DZ
O	$[He]2s^22p^4$	2s-DZ,2p-DZP,3d-SZ
C	$[He]2s^22p^2$	2s-DZ,2p-DZP
H	$1s^1$	1s-DZP,2p-SZ
S	$[Ne]3s^23p^4$	3s-DZ,3p-DZP,3d-SZ
Au	$[Xe\ 4f^{14}\ 5d^{10}]\ 6s^1$	6s-DZ

Table 7.1: The Electronic Configuration used for the generation of the pseudopotentials and the pseudo-atomic orbital (PAO) basis sets employed for various atomic species are shown. SZ - single zeta, DZ - Double zeta, DZP - double zeta plus polarization

functional are employed for most of the ground state DFT calculations presented as well as the transport calculations. LDA pseudopotentials are used for test calculations with the LSDA+ U method. Scalar relativistic pseudopotentials are used for S, Mn and Au. Non-linear core corrections are also included in the case of Mn and Au. Note that fully filled the 4f and 5d states of Au are included in the core and only the 6s electrons are explicitly described. Although the 5d states in Au are relatively shallow and need to be treated in the valence for describing structural properties of Au, the density of states at the Fermi level of Au is dominated by 6s electrons and for transport calculations at low

bias ($V < 1$ eV), this minimal description of Au is mostly adequate. Since the Mn-O sub system is the main region of interest in these molecules, the Mn and O basis functions are based on an optimized basis set for bulk MnO and extra polarization orbitals are added for increased variational freedom. For representing the charge density in real space, a uniform mesh with a grid cutoff of 450 Ry (equivalent to plane wave-cutoff) is used. For both the $Mn_{12}TE$ and $Mn_{12}f$ systems geometrical optimizations are performed using standard conjugate gradient minimization of forces until all the Hellmann-Feynman forces are smaller than 0.04 eV/Å. Most of the calculations presented in this work are carried out using the PBE-GGA exchange-correlation functional. Since the environment in the Mn-O core of the Mn_{12} system is similar to that in the strongly correlated oxide MnO, one generally needs to employ extra corrections to LSDA/GGA functionals to obtain a proper description of the system especially while calculating quantities such as exchange parameters and anisotropy barriers which depend upon accurate total energies. From the point of view of electronic transport calculations, for a quantitatively accurate description of the I-V characteristics, the level alignments of the various molecular states and especially of the highest occupied (HOMO) and lowest un-occupied (LUMO) molecular orbitals relative to the chemical potential of the metallic leads must be correct. With these issues in mind, we carry out both GGA and LSDA+ U [312] calculations of the static ground state of the $Mn_{12}f$ system. We then discuss some implications for GGA based transport calculations on Mn_{12} in terms of the qualitative and quantitative differences one might expect with respect to a LSDA+ U description.

7.4 Ground state properties

The overall ground state electronic properties of Mn_{12} clusters are relatively well known and several theoretical works have addressed the magnetic properties of these systems in detail [313]. In the $Mn_{12}f$ cluster shown in figure 7.3 two different kinds of Mn ions are indicated (blue and grey shading). The four inner Mn ions (shaded grey) which form a slightly distorted cube with 4 O ions, have a charge state closer to Mn^{4+} with a total spin ($s=3/2$) while the eight outer Mn ions have a Mn^{3+} charge state with total spin ($s=2$). Furthermore, the inner Mn^{4+} ions are coupled anti-ferromagnetically to the Mn^{3+} ions which results in a ferrimagnetic ground state for the whole molecule with a net spin of $S = 8 \times 2 - 4 \times (3/2) = 10$. The $M_S = 10$ ground state has been detected experimentally while the grouping of the Mn ions into Mn^{3+} and Mn^{4+} can be inferred from structural data

as the outer Mn^{3+} have partially occupied e_g states and undergo significant Jahn-Teller distortions that are typical of Mn(III) systems.

7.4.1 Electronic structure of $Mn_{12}f$

In figure 7.2 we present the partial density of states (PDOS) for $Mn_{12}f$ calculated both with the GGA and LSDA+ U functionals. Values of $U=6$ eV and $J=1$ eV are chosen for the Hubbard- U parameter and exchange parameter J respectively. Recent photoemission results on Mn_{12} systems [314] place the HOMO-LUMO gap of these molecules in the region of ~ 2 eV. In comparison, the GGA gap is rather small at ~ 0.5 eV. LSDA+ U opens up the gap as one would expect and for a value of $U = 6$, the HOMO-LUMO gap is 1.92 eV. From the PDOS in figure 7.2 is apparent that the molecular orbitals on either side of the Fermi level are made up mostly of Mn derived orbitals with some contributions from O due to hybridization. In particular the HOMO level seen in the PDOS is actually a collection of closely spaced Mn- e_g states and this description is the qualitatively the same both in GGA and LDA+ U . Furthermore there is very little PDOS near the Fermi level coming from C atoms and the HOMO-states are therefore expected to be well localized on the Mn-O core. A closer look at the nature of the HOMO-LUMO gap is presented in right hand side panel of figure 7.3 where in the contributions of the Mn^{3+} and Mn^{4+} ions to the Mn-PDOS are shown separately. It is clear that the HOMO-LUMO gap in this system is essentially a distortion induced gap in a partially occupied manifold of e_g states whose degeneracy has been lifted.

A Mülliken analysis of the local magnetic moment of representative Mn^{3+} and Mn^{4+} ions is presented in table 7.2. Two slightly different Mn^{3+} ions can be identified which have different bond-lengths to the coordinating O ions. For clarity, we label them Mn_1^{3+} and Mn_2^{3+} in the table. The local magnetic moments predicted in both GGA and LSDA+ U are quite similar. Although the theoretical moments seem consistently larger than the experimental ones, a Mülliken analysis is in general, strongly basis set dependent and calculated local moments cannot strictly be compared to experiment. However both GGA and LSDA+ U rightly predict the total moment to be 20.0. Thus one might conclude that GGA and LSDA+ U descriptions of the ground state of Mn_{12} are qualitatively similar.

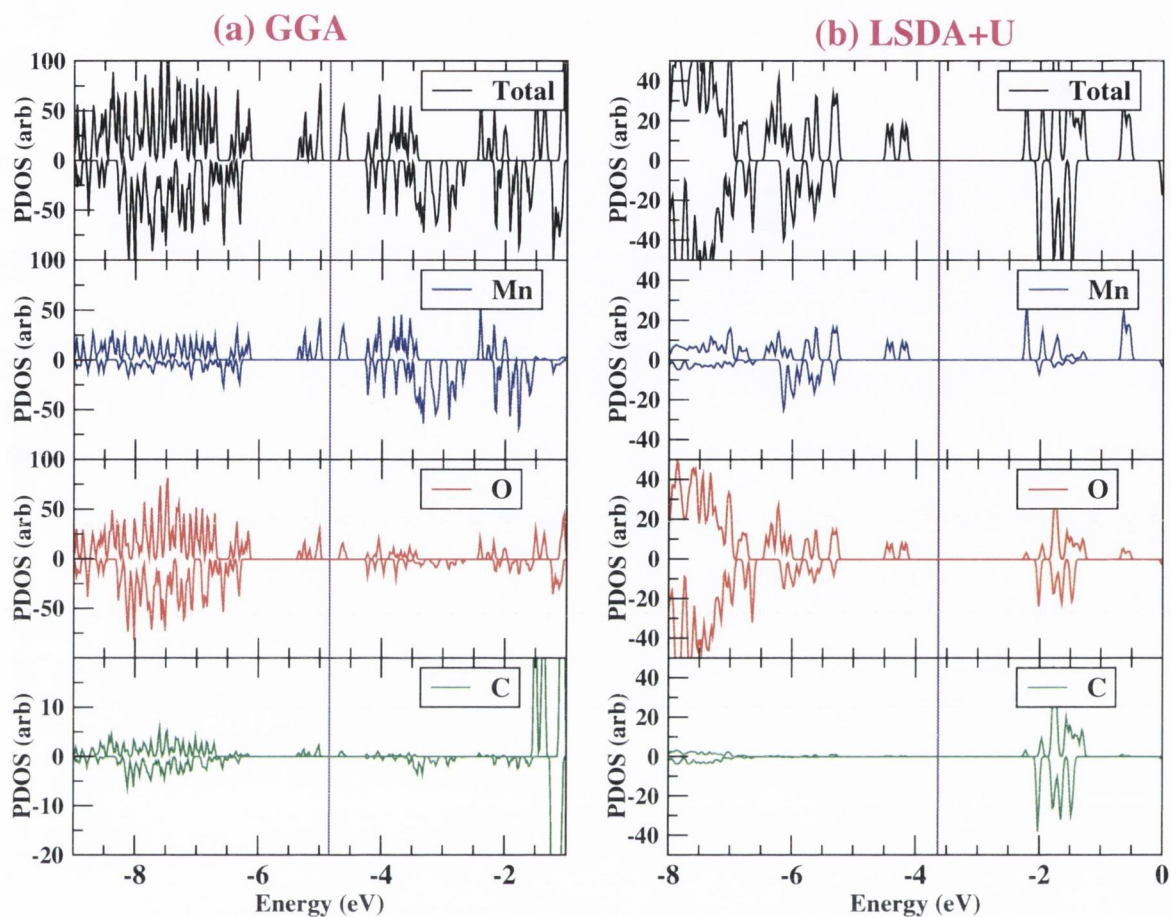


Figure 7.2: GGA and LSDA+ U partial density of states are shown for the $Mn_{12}f$ cluster. PDOS around the Fermi level is mainly Mn-O in character. The HOMO-LUMO gap is underestimated in GGA at ~ 0.5 eV while LSDA+ U predicts a gap of ~ 1.9 eV ($U = 6$, $J = 1$). Also C atoms in the molecule show very little PDOS around the Fermi level (vertical indigo line) and do not seem to interact strongly with the d states on the Mn ions

	GGA	LSDA+ U	Expt.
Mn_1^{3+}	3.90	3.87	3.69
Mn_2^{3+}	3.93	3.99	3.79
Mn^{4+}	-2.89	-3.02	-2.34
Total	20.0	20.0	20.56

Table 7.2: A Mülliken analysis of the local magnetic moments of the Mn ions in the $Mn_{12}f$ system is presented. GGA and LSDA+ U moments are very similar although over-estimated with respect to experiment [315]

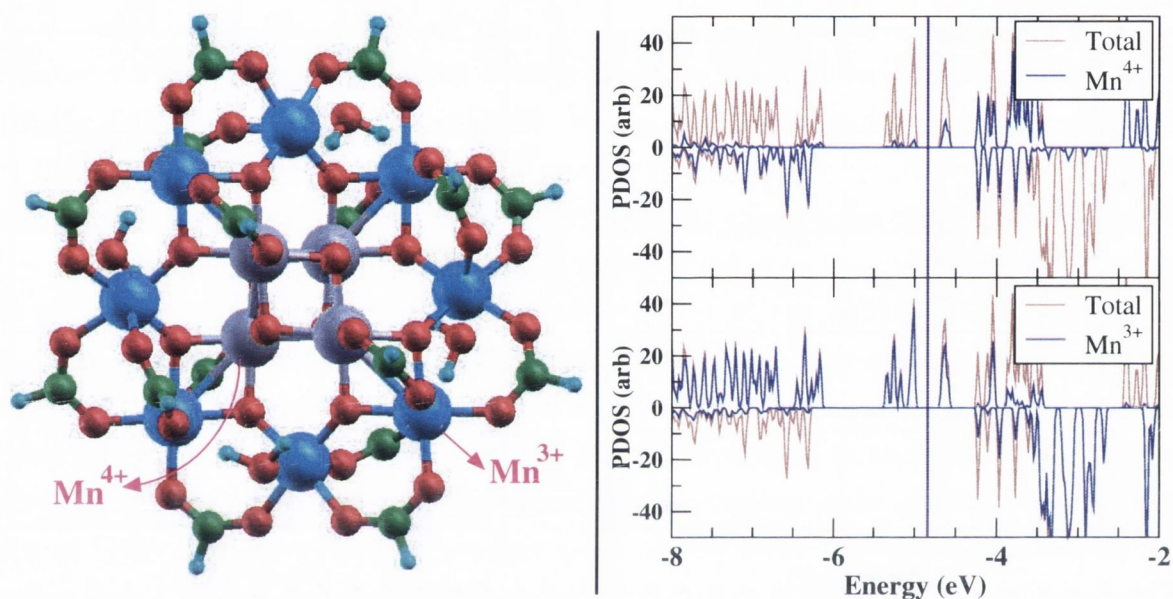


Figure 7.3: (left) The geometry of the $Mn_{12}f$ cluster is shown. The 4 inner Mn ions (shaded grey) are closer to a Mn^{4+} valence while the outer 8 ions (blue) are closer to Mn^{3+} . (right) The PDOS for Mn^{3+} (lower-right) and Mn^{4+} (upper-right) ions, as calculated within GGA, are shown separately. The total Mn PDOS is shown as a brown background. The occupied and empty subsets of the e_g states of the Mn^{3+} ions form the highest occupied and lowest un-occupied molecular orbitals in the system and there is very little Mn^{4+} contribution to the PDOS around the Fermi level.

7.4.2 Electronic structure of $Mn_{12}TE$

We now consider the full $Mn_{12}TE$ molecule (see figure 7.1) to analyze the effects of attaching the organic functional groups. In figure 7.4(a) we present the calculated GGA PDOS for the $Mn_{12}TE$ molecule. Clearly the organic TE groups have little effect on the Mn-O derived states around the Fermi level. The HOMO-LUMO gap is still ~ 0.5 eV as before and retains its $Mn^{3+} - e_g$ character. A set of C and S derived states lie about ~ 1 eV below the Fermi level and show little mixing with any of the Mn states. Similarly, there are no C and S derived states immediately above the Fermi level. The $Mn_{12}TE$ molecule also has a total magnetic moment of $20\mu_B$ corresponding to a $M_S = 10$ ground state. The next issue to address is the interaction of the $Mn_{12}TE$ molecule with a gold surface.

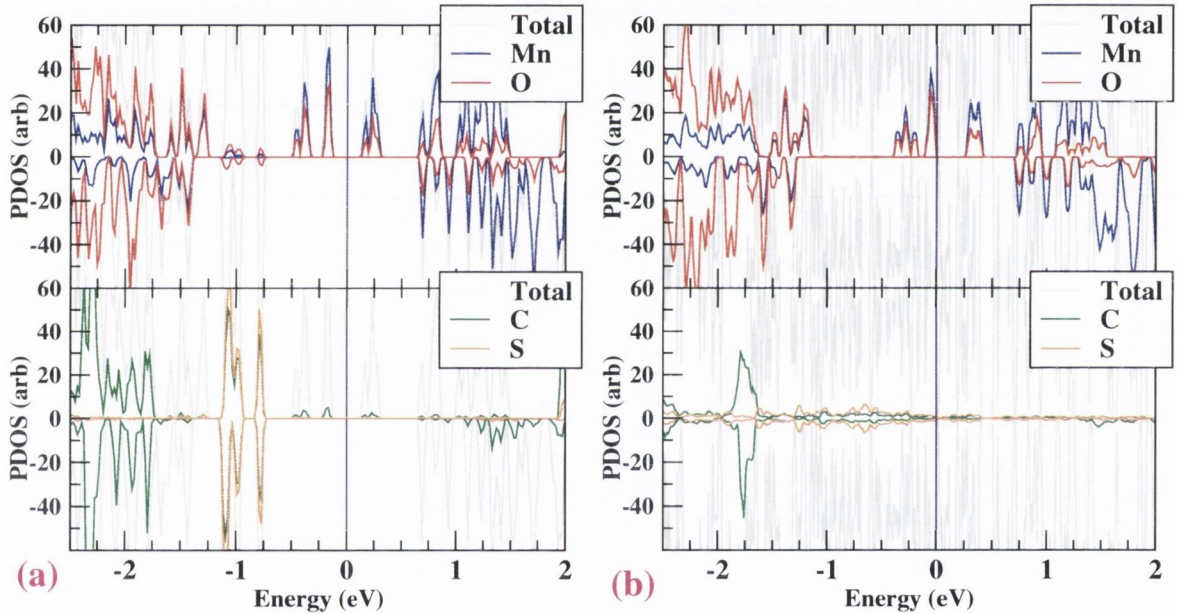


Figure 7.4: In panel (a), the PDOS (GGA) for a free standing $Mn_{12}TE$ molecule is shown. The electronic structure of the Mn-O sub-system in $Mn_{12}TE$ is identical to that in $Mn_{12}f$. The only effect of the additional C and S atoms are a set of states about 1 eV below the Fermi level which show little mixing with the Mn-O system. The total DOS for the molecule is shown as a grey background. In panel (b), the PDOS for the device region in 7.5 is shown. A small charge transfer from the $Mn_{12}TE$ molecule to the Au contacts pins the Fermi level (set at 0 eV) to the HOMO of $Mn_{12}TE$

It has been assumed in recent transport experiments [306] that the rather long organic functional groups act to shield the $Mn_{12}O_{12}$ core from metallic surfaces and that therefore the molecule retains its magnetic properties in the vicinity of gold. In our simulations

we assume that the overall structure of $Mn_{12}TE$ remains the same when anchored to gold surfaces through the thiol groups at the periphery of the molecule. Therefore we do not perform molecular dynamic simulations for the $Mn_{12}TE$ and gold system and restrict our DFT study to an investigation of the static charging or discharging behavior of the molecule on gold. The geometrical setup of the $Mn_{12}TE$ -Au system studied is shown in figure 7.5 which is the same as the setup to be used for transport calculations. The molecule is arranged in between two gold surfaces with the anchoring groups roughly perpendicular to the surfaces. Periodic boundary conditions are applied in the transverse direction to minimize finite size effects. Since the organic TE groups act only as spacers while providing anchorage, those TE groups that do not make direct contact with the gold can be left out of the simulation. This affords considerable savings in the computational resources as otherwise, the lateral dimensions of the simulation cells employed would have to be much bigger. Therefore we retain only 4 of the 16 TE groups and replace the rest by (COOH)

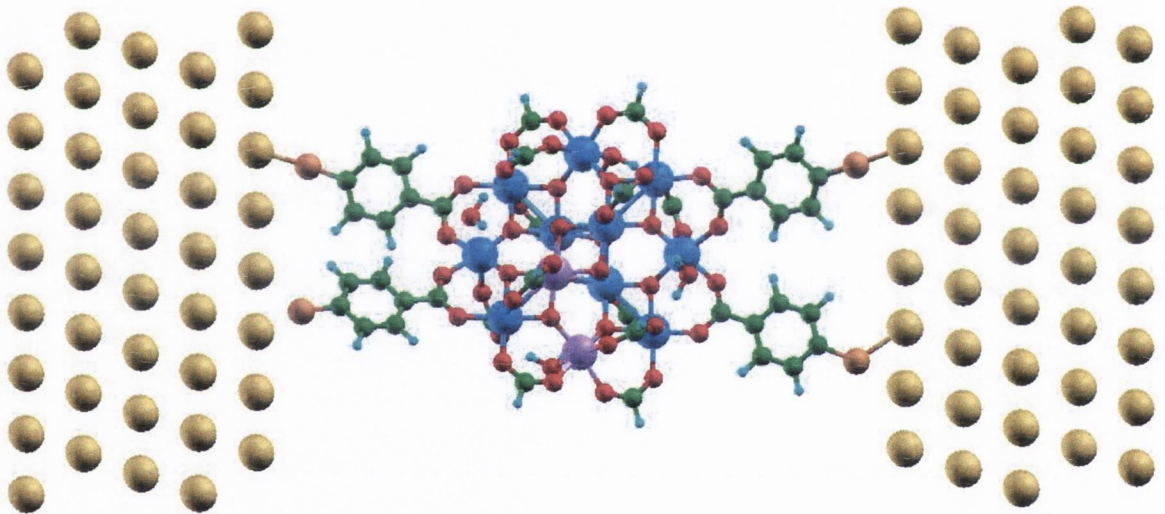


Figure 7.5: The set up of the scattering region used in the transport calculations is shown. Note that 12 out of the 16 TE groups have been replaced by (COOH) groups keeping only those TE that bond to the surface. Because of the low symmetry at the periphery $Mn_{12}TE$, it is not possible for all the 4 surface bonding S atoms to make identical contact. The two Mn ions shaded light-purple represent the two ions whose local magnetic moments are flipped to make the $M_S = 9$ spin configuration. The transport (z) direction is parallel to the page from left to right.

groups as before. It is not known from experiments exactly how many of the S atoms on TE groups make strong contact with gold surfaces. We orient the molecule so that

two S atoms are anchored to the gold surface on either side. As the TE groups are not exactly parallel to each other, it's not possible to obtain perfect hollow site positions for all 4 of the S atoms. Therefore we place one of the S atoms at a hollow site and adjust the orientation of the molecule so that the other three are as close to hollow sites on the Au surface as possible. We then keep the orientation of the molecule with respect to the surface fixed and vary the S-Au distance by rigidly moving the Au surfaces along the z-direction. The calculated PDOS for this “device region” is shown in figure 7.4. It is apparent that the HOMO of the $Mn_{12}TE$ molecule is now pinned at the Fermi-level and is in fact slightly discharged. The magnetic moment of the cell is found to be $\sim 19.7\mu_B$ which means about ~ 0.3 electrons are transferred from the molecule to the gold. Still, this is a relatively small perturbation and the overall magnetic structure of the molecule is retained. Also, the PDOS from the S and some of the C atoms is seen to be broadened out because of their strong interaction with the gold surface. Since we are interested in studying the effect of the local magnetic structure of the $Mn_{12}TE$ molecule on its electrical transport properties, we need to consider the Mn_{12} core in alternate spin configuration and compare the I-V characteristics for the two different configurations. Although “pure” spin excitations of the real Mn_{12} system that are eigenfunctions of the total spin operator \mathbf{S} are different from spin configurations wherein the local moments on some of the Mn ions are flipped with respect to the ground state configuration, in spin DFT, one only has access to “impure” single-determinant states that are only eigenfunctions of \mathbf{S}_z . In principle one has to consider many such spin-flip configurations to extract properties of real spin excitations [316]. However, since we are only concerned with an investigation of principle, we consider just one such spin flip configuration in which the local moments on one of the Mn^{3+} and one of the Mn^{4+} ions are flipped with respect to the ground state. These two ions are shaded light-purple in the figure 7.5. Such a configuration results in a total spin of $M_S = 9$ for the $Mn_{12}TE$ molecule and is ~ 150 meV higher in energy than the ground state configuration with $M_S = 10$. The PDOS around the Fermi level for the $M_S = 9$ configuration is plotted in figure 7.6. In this case, two e_g derived peaks, one occupied and one empty, in the minority-spin PDOS are apparent. These arise from the spin on one of the Mn^{3+} ions being flipped.

7.5 Transport properties

In this section we present the results for both the zero bias and finite bias transport properties of the $Mn_{12}TE$ -Au setup of figure 7.5. The calculations are carried out using the NEGF transport code SMEAGOL [317]. Figure 7.5 shows the main device or scattering region and the infinite leads attached on either side of the device are described by effective self energies [317]. Bias voltages of up to 0.4 eV are considered. The basis sets, pseudopotentials and real space mesh parameters used are exactly the same as used with SIESTA for the DFT electronic structure calculations. For integration along the real energy axis [317], a uniform mesh of 1536 energy points is employed over a 0.4 V bias window which translates to an energy resolution of ~ 0.26 meV per energy point. Before we move on to the results, we discuss some of the implications that the GGA electronic structure holds, for a description of the electronic transport. Firstly, as the HOMO of the $Mn_{12}TE$ molecule is located at the Fermi level set by the gold surface, this system cannot exhibit a conductance gap close to zero bias even though the molecule is effectively very weakly coupled to the Au surface. One would expect that a method such as LSDA+ U where the HOMO-LUMO gap is bigger, might predict a mid-gap position for the Fermi-level of gold and therefore also a conductance gap. However, in experiments one is often interested in not just the two terminal transport properties of these magnetic molecules but more in the interplay between the magnetism and the transport properties. Therefore one might consider a three terminal device configuration in which the HOMO level of the molecule is gated up or down to be level with the chemical potential of the Au surface and then study the low bias transport properties. The GGA electronic structure is effectively equivalent to such a gated setup. A second issue one must consider at finite bias is the position of the unoccupied molecular states. Since the GGA gap at ~ 0.5 eV is underestimated with respect to the experimental gap, the empty LUMO states would enter the bias window at a much smaller value of the bias in the GGA description. Furthermore as local xc functionals are not capable of describing Coulomb blockade type behaviour [318] in weakly coupled systems, the LUMO states would also effect the total current as soon as they enter the bias window. These issues should be borne in mind while interpreting the GGA results.

7.5.1 Zero bias transmission

In figure 7.6(b) the zero bias transmission-coefficient is plotted as a function of the energy for both the $M_S = 10$ and $M_S = 9$ configurations. We focus on a narrow energy window

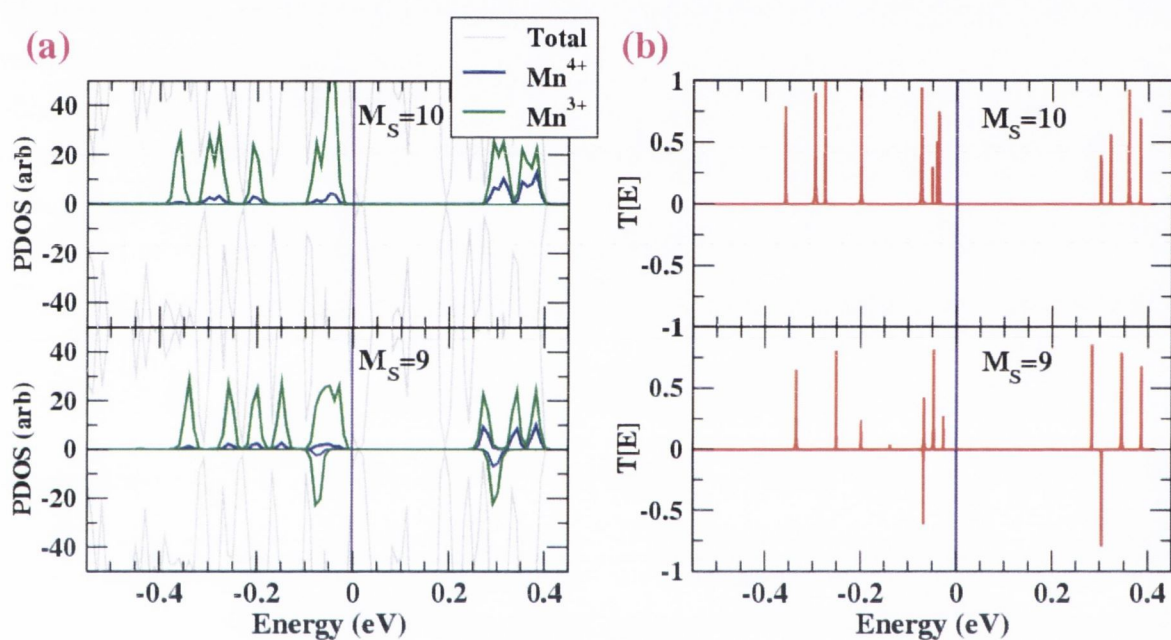


Figure 7.6: Panel (a) shows the PDOS of the device region for a narrow energy range around the Fermi level. Panel (b) plots the zero-bias transmission coefficients. The transmission peaks appear as sharp resonances with little broadening. Also the peaks correspond well to the Mn PDOS in panel (a).

of ~ 0.8 eV around the Fermi level as it is the only one relevant at low bias. In figure 7.6(a) the PDOS for the device region (figure 7.5) in the same energy range is presented. In the $M_S = 9$ configuration, two e_g type states one filled and one empty belonging to the flipped Mn^{3+} ion appear in the minority spin PDOS. The transmission peaks in figure 7.6(b) appear as very sharp resonances with very little broadening. This shows that the Mn_{12} core is effectively very weakly coupled to the electrodes and electron tunneling as opposed to ballistic conduction through a single molecular level is the main mechanism. Also transmission peaks map neatly onto the Mn-O derived molecular states in the PDOS of figure 7.6(a). As discussed earlier, the molecular orbitals of $Mn_{12}TE$ are either purely Mn-O derived or Carbon-Sulphur hybrids but there is no one molecular state that extends over the entire $Mn_{12}TE$ molecule. Therefore the system is essentially composed of individual impedances in series viz., the TE groups on one side, the Mn_{12} core and the TE groups on the other side through which electrons have to sequentially tunnel through. This tunneling behaviour is indeed observed experimentally [307] where currents of the order of tenths of nano-Amperes are recorded.

7.5.2 I-V Characteristics

In figure the 7.7 current-voltage characteristics of $Mn_{12}TE$ for both the spin-configurations studied are presented. The calculated current is of the order of a few nano-Amperes. Figure 7.7(a, b) plot the spin-resolved current and the total current against the voltage respectively. The following features emerge:

The current in the $M_S = 10$ configuration is completely spin-polarized with the minority-spin current being virtually zero. This is expected as one can see from the zero-bias transmission in figure 7.6(b) that there are no transmission peaks in the down-spin channel for $M_S = 10$.

The current for the $M_S = 9$ configuration is not perfectly spin polarized and the transmission peak in the minority-spin seen in figure 7.6(b) duly conducts.

However the total current (see figure 7.7(b)) is different for the $M_S = 10$ and $M_S = 9$ configurations and markedly so in some bias regions. In fact in the range between 100 meV and 200 meV positive bias, the current for the $M_S = 10$ case flattens out while the current for the $M_S = 9$ configuration actually decreases with bias. Also in both spin configurations, the current for negative bias is substantially smaller from that for positive bias and the device therefore exhibits rectification.

The differential conductance(DC) corresponding to the I-V curves in figure 7.7(b) is plot-

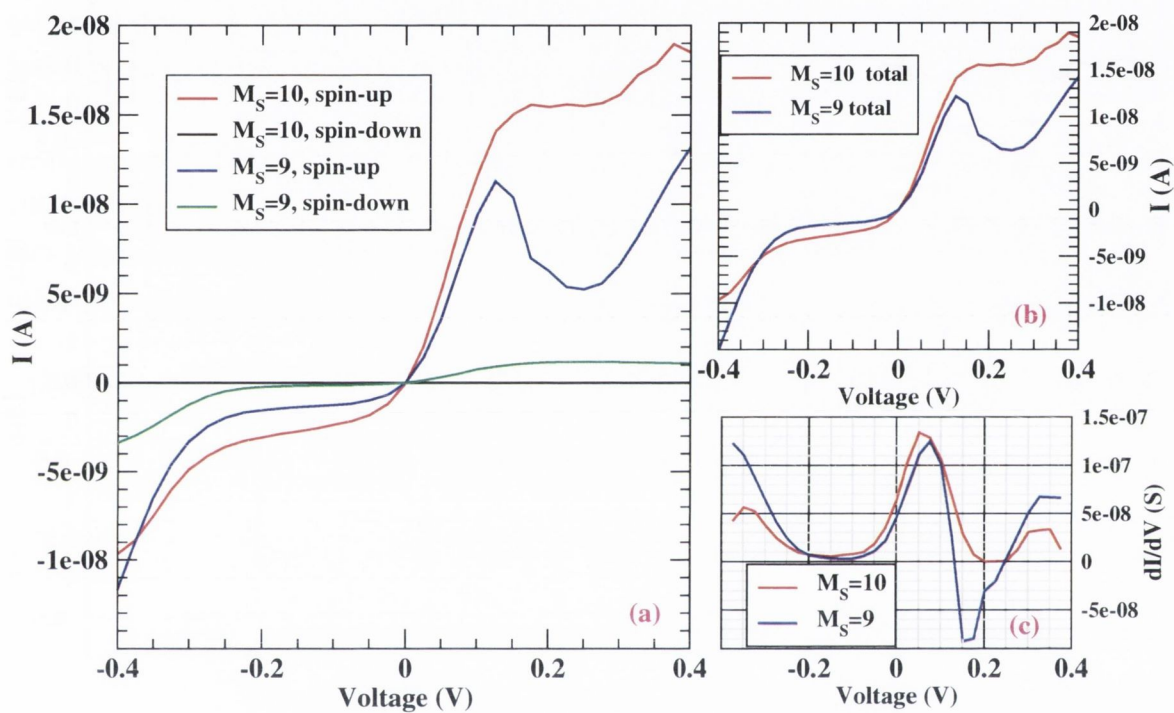


Figure 7.7: Panel (a) shows the spin-resolved I-V curves for the $Mn_{12}TE$ molecule between gold electrodes (see figure 7.5). The current for the $M_S = 10$ configuration is completely spin polarized while the current for the $M_S = 9$ is only partially spin-polarized. Panel (b) shows the total currents for both spin configurations and regions where the two differ substantially are obvious. Panel (c) plots the differential conductance corresponding to the currents in (b). The $M_S=9$ configuration shows NDC between $\sim 100 - 200$ meV.

ted in figure 7.7(c). Because of the flat regions observed in both the I-V curves, the DC is close to zero over a range of positive and negative bias for both spin configurations. In the 100-200 positive bias range, the DC is in fact negative for $M_S = 9$. In order to under-

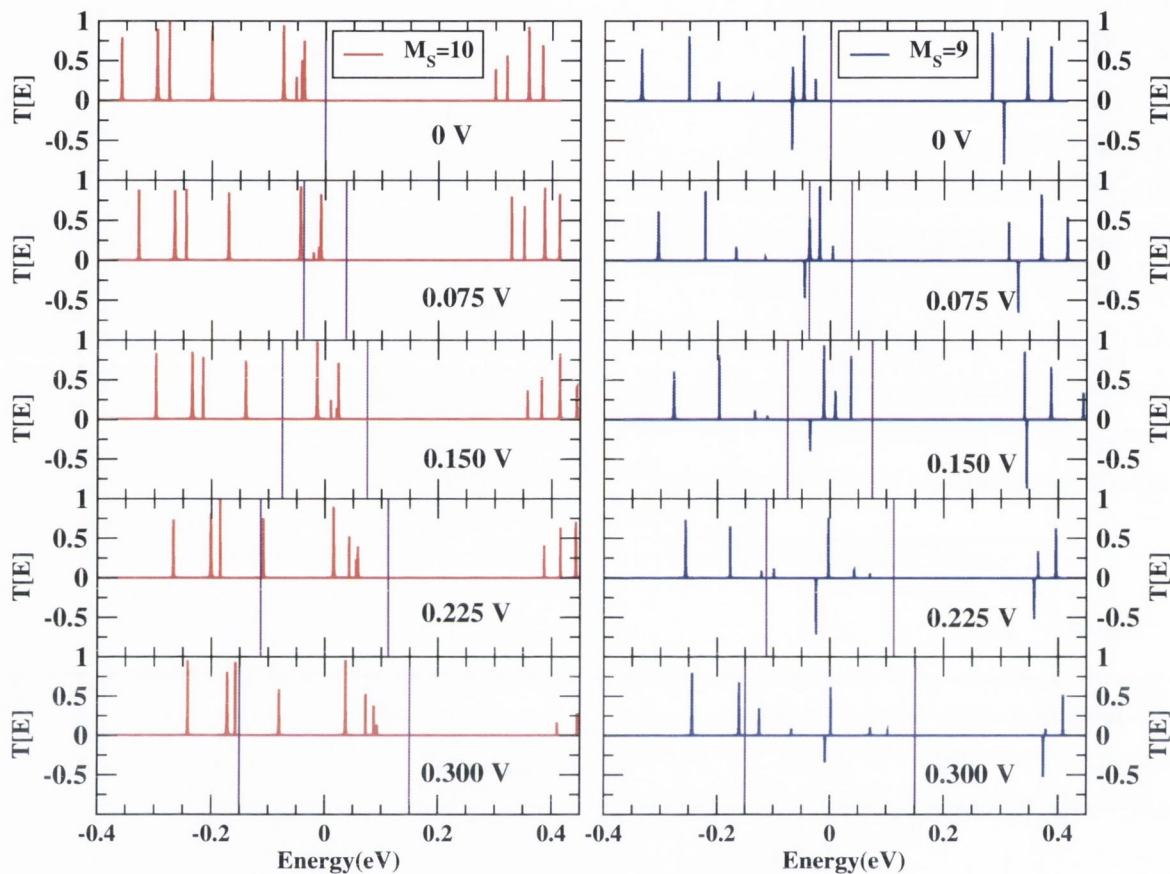


Figure 7.8: Evolution of the transmission coefficients with applied positive bias is shown for both the $M_S = 10$ (left) and $M_S = 9$ (right) spin configurations. The bias window is indicated by the two vertical indigo lines. The transmission peaks clearly show a rightward drift as the bias is increased. This originates for the fact that the $Mn_{12}TE$ states are coupled stronger to the left lead and follow its chemical potential μ_L . Also some transmission peaks inside the bias window are seen to get suppressed in the 150-225 meV bias range which explains the regions of low and negative DC seen in the I-V curves.

stand some of these observations, we look at the evolution of the transmission coefficients under bias. The transmissions for various positive bias voltages are plotted in figure 7.8 for both $M_S = 10$ (left panel) and $M_S = 9$ (right panel). What is immediately apparent is right-ward drift of all the transmission peaks towards higher energies as the bias is increased from 0 to 300 meV. This is a clear sign that the $Mn_{12}TE$ molecule is not only

weakly coupled but also asymmetrically coupled to the leads and in this particular case relatively more strongly to the left electrode than to the right. Therefore as the chemical potential of the left lead (μ_L) is increased with respect to the right lead, the molecular states just follow the left chemical potential as they try to equilibrate with it. Given the complicated geometry of the TE groups that anchor the $Mn_{12}TE$ molecule to the surface this kind of asymmetric coupling is indeed possible even in reality and often likely in typical experimental situations.. The decreasing DC and flattening out of the current between 100-250 meV seen for the $M_S = 10$ case is also relatively easily explained. Between 75 meV and 225 meV no new transmission peaks enter the bias window and the current therefore remains constant. However even when some new peaks enter the bias window at around 200-225 meV, the current does not immediately increase. This might be explained by the fact that some of the transmission peaks already inside the bias window are seen to shrink in amplitude and therefore their contribution is simultaneously decreasing. These features are even more pronounced in the case of the $M_S = 9$ configuration. Once the bias reaches 75-100 meV, the first set of transmission peaks are all inside the bias window and the DC starts to decrease towards zero. However between 150-225 meV, some of the right most peaks inside the bias window are seen to decay in amplitude substantially and although a new set of states start to conduct the current actually decreases resulting in the negative DC. Beyond 250 meV however, the size of the peaks remains constant in both the cases and the current once again rises as new states enter the bias window. Yet another subtle feature that comes out from comparing the motion of the transmission peaks for the $M_S = 10$ and $M_S = 9$ configurations is that in the $M_S = 9$ case, while all the states are dragged along by μ_L , they do so at different speeds and states that are farther away from μ_L tend to lag behind as the bias is increased. This does not seem to be case for the $M_S = 10$ configuration in which the states seem to move more as a group. The reason for this complicated behaviour of the states is not presently clear. One can however infer from the different rates of motion of the peaks and the decrease in amplitude of some of them that the coupling to the leads is changing dynamically under bias. The amplitude of the transmission scales as the product of the coupling strengths Γ_L and Γ_R to the left and right leads respectively as given by

$$T(E, V) = Tr[\Gamma_L G_M^\dagger \Gamma_R G_M] \quad (7.1)$$

where G_M is the retarded Green's function for the scattering region. Therefore a change in the effective coupling to either lead as a result of charge density redistribution under bias

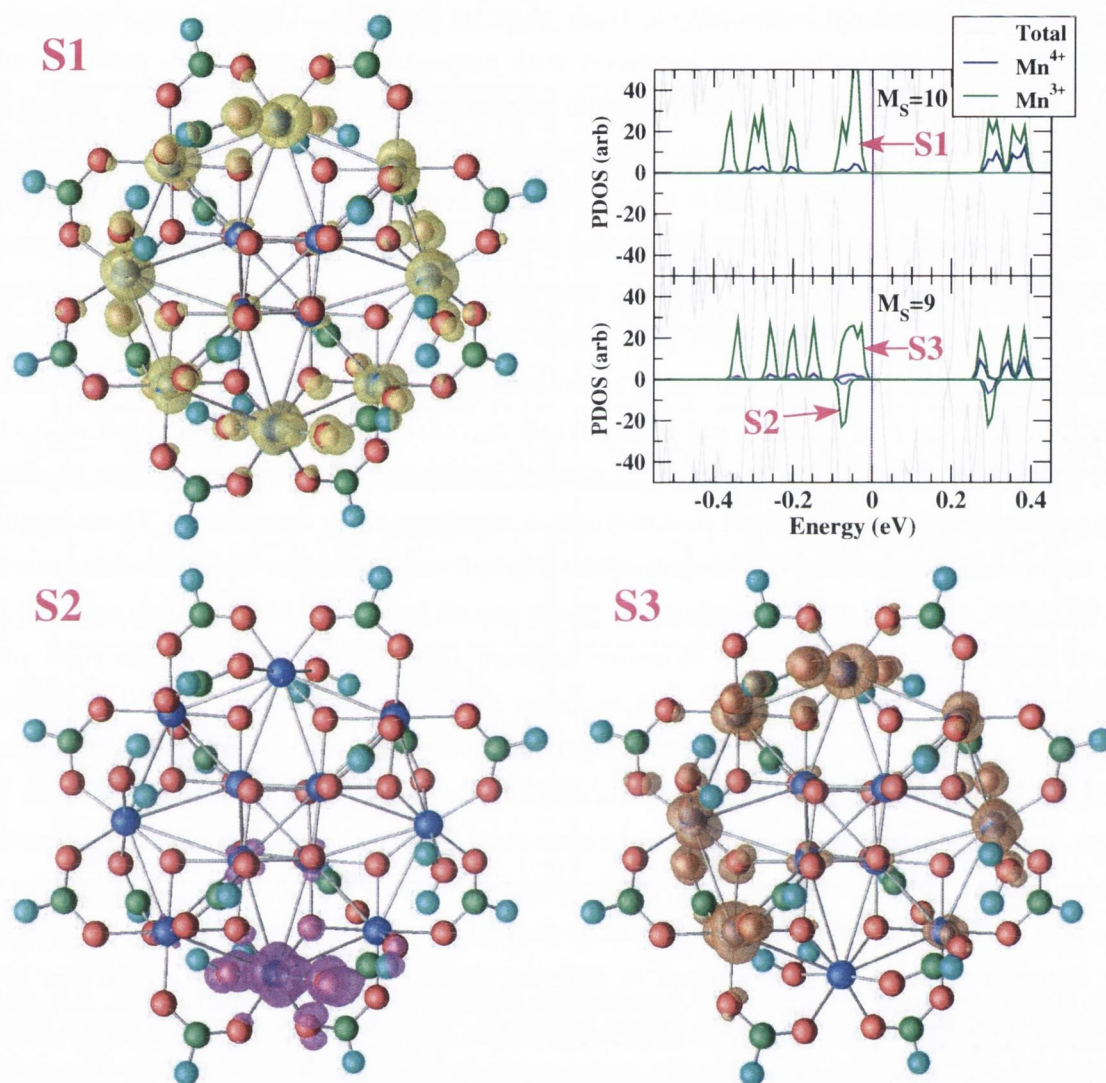


Figure 7.9: The spatial charge distribution of some representative $Mn_{12}TE$ molecular states close to the Fermi energy are plotted. The organic functional groups are not included for clarity. The S1 state is the HOMO for the $M_S = 10$ spin-configuration and is seen to be spread over the Mn^{3+} ring. The electron in the S2 state however is forced to localize. The HOMO for the $M_S = 9$ configuration is the S3 state and the e_g contribution from the spin-flipped ion is notably missing. The different spatial charge density distributions of the state might cause their effective coupling to the leads to be different. Furthermore the states states might also have different charging/discharging behaviour under bias.

can lead to a decay of the transmission amplitudes. Also a closer look at the distribution in space of the charge density of some of the Mn-O derived states in the static case might offer some clues towards understanding the mechanism. In figure 7.9 we plot the charge

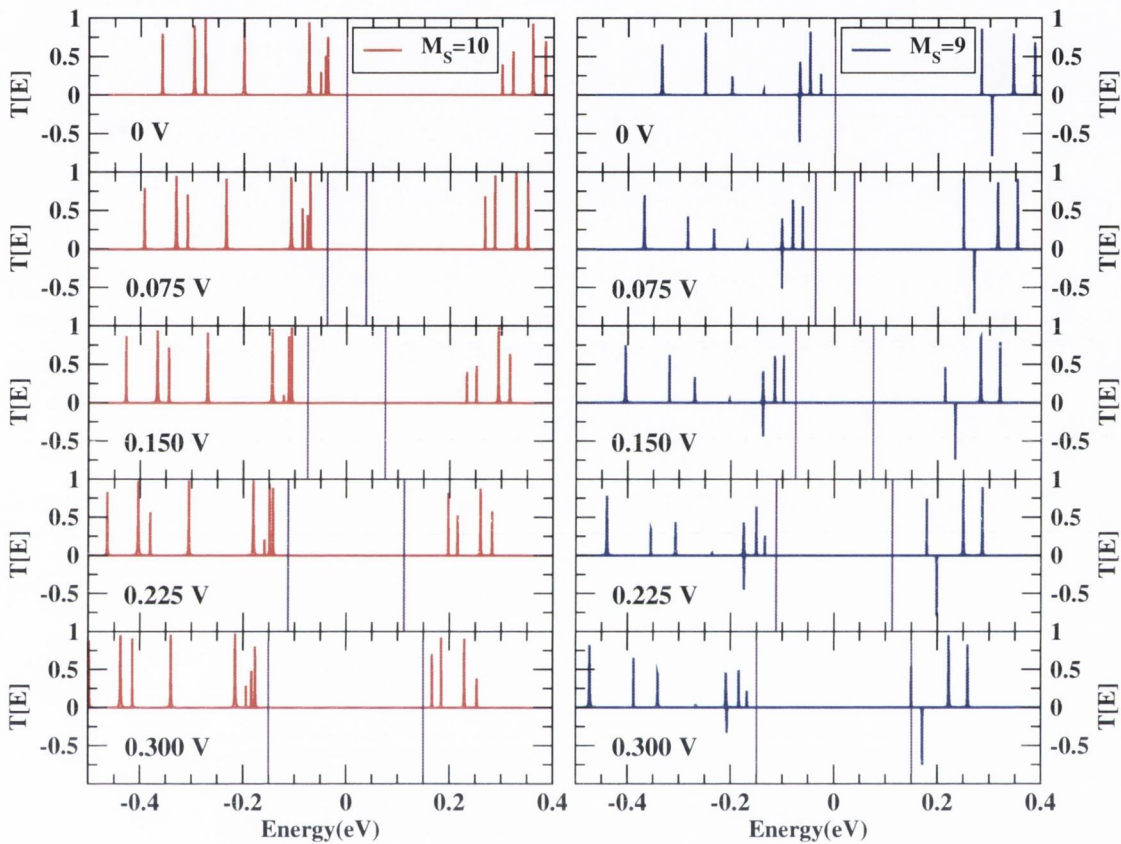


Figure 7.10: Evolution of the transmission coefficients with applied negative bias is shown for both the $M_S = 10$ (left) and $M_S = 9$ (right) spin configurations. The bias window is indicated by the two vertical indigo lines. The transmission peaks clearly show a leftward drift as the bias is increased and the chemical potential of the left lead is lowered. Since the states are coupled more strongly to the left they follow μ_L and in doing so avoid the bias window. Thus the current in the negative bias case is suppressed.

density distribution in space for some of the molecular states of $Mn_{12}TE$ around the Fermi level. The states plotted are indicated in the accompanying PDOS. The S1 state is the HOMO of the $M_S = 10$ configuration and it is apparent that the charge density is rather uniformly spread over the ring of eight Mn^{4+} ions. However, the S2 state which corresponds to one of the two peaks in the minority-spin channel for the $M_S = 9$ configuration is seen to be essentially localized on a single Mn^{3+} ion, viz., the one whose spin is reversed in

setting up the $M_S = 9$ configuration. Thus when the local moment on one of the Mn^{3+} ions is flipped, the electron in the e_g orbital of that ion is forced to localize as there are no other e_g states in the same energy range in the minority-spin channel between which the electron can hop. The state plotted as S3 is the majority-spin HOMO of the $M_S = 9$ configuration and the missing charge at the spin-flipped Mn^{3+} site is strikingly apparent. Therefore, given their different geometries, the couplings to the leads of the S1, S2 and S3 states are likely to be different. It is in general difficult to precisely quantify the effective coupling to the leads of individual molecular states but a newly developed method due to Rungger (*et. al.*)[319] valid in the weakly coupled limit is currently being used to currently investigate the problem. Finally we look at the evolution of the transmission peaks under negative applied bias. This is plotted in figure 7.10. As seen in the positive bias case the molecular states are coupled preferentially towards the left lead. Therefore as the chemical potential of the left lead μ_L is now lowered to apply a negative bias, the states once again try to equilibrate with the left lead and thus follow μ_L . In this case however, in doing so they effectively stay outside the bias window and the current as a result is much smaller. Note that effective bias window in the calculations is wider by about $\sim kT$ where k is the Boltzmann constant, because of the Fermi smearing applied to the distribution functions of the leads. The increase in current that one sees after the negative bias goes past -200 meV is essentially due to a set of originally un-occupied states entering the bias window from above.

Before we conclude, a few comments on the quantitative accuracy of the calculations are pertinent. One of the major issues for theoretical simulations of molecular transport experiments is the uncertainty involved in the device geometry. In the case of small molecules and devices with a limited parameter space, several different calculations in varying geometries can be carried out and the results compared to experimental data. However, such an approach is a lot more demanding in the case of systems such as $Mn_{12}TE$ on gold surfaces due to the large size of the system and more importantly the complexity of the geometry. The fact that these molecules are also tunnel devices only compounds the problem as small changes in geometry can lead to sizeable differences in the calculated current. On top of the uncertainties about device geometry, there are other issues such as the approximations made with regards to xc functionals or even limitations at the theoretical level. For instance, whether manybody effects such as Coulomb blockade and the Kondo effect observed in these SMMs can be described within the framework of the NEGF formalism combined with DFT is still an open question. Therefore, a fully quantitative theoretical

description of the transport properties of these SMMs presents itself as a very challenging problem in the field for the near future.

7.6 Conclusions

In conclusion, the electronic structure and transport properties of a functionalized Mn_{12} single molecule magnet $Mn_{12}TE$ are investigated in order to test whether a change in the magnetic environment within such a molecule can lead to detectable changes in its I-V characteristics. We ascertain that the GGA electronic structure of $Mn_{12}TE$ is qualitatively accurate both for the free standing molecule as well as the molecule in contact with a gold surface. Then, the I-V characteristics between 0 to 400 meV for two different spin configurations of the molecule $M_S = 10$ and $M_S = 9$ are calculated using the NEGF transport code SMEAGOL in a two terminal device setup. We find that the transport is mainly via sequential tunneling which leads to currents of the order of nano Amperes. Furthermore the device exhibits rectification properties because of weak asymmetric coupling to the leads. The total current in the two spin configurations studied is found to be different driven mainly by differences in wave function localization and charging effects. Regions of negative differential conductance are also observed for the $M_S = 9$ configuration. These results therefore suggest that information about the local spin state of such single molecule magnets can indeed be identified from a detailed knowledge of the I-V characteristics.

Chapter 8

Conclusions and future work

In summary, we have discussed the implementation of “beyond-LDA” density functional approaches viz., orbital dependent functionals [52] and the ASIC approximation [55], into the efficient numerical DFT framework of the SIESTA [54] program and presented their application to some topics of current interest.

We began in chapter 2 by providing an overview of the underlying theoretical framework upon which most of the work presented in this thesis is based. We summarized Kohn-Sham density functional theory [49] and introduced the SIESTA code which is a versatile and efficient platform well suited to DFT simulations of large electronic systems ranging in size from several hundred to thousands of atoms. We also presented some salient features of the SMEAGOL code [51] which implements a numerically efficient non-equilibrium Green’s functions (NEGF) [95] based algorithm for first principles electronic transport calculations.

In chapter 3, an overview of orbital dependent functionals and the optimized effective potential (OEP) method [52] was presented. Two different orbital dependent exchange-correlation functionals viz., the exact exchange (EXX) and self interaction corrected functionals (SIC) were discussed in the context of the Krieger-Li-Iafrate (KLI) approximation [119] to the OEP. Subsequently, their implementation in the SIESTA code was also outlined. As an application of these orbital dependent functionals, the long standing problem of overestimation of polymer polarizabilities in DFT was revisited and the performance of SIC functionals in this regard was analyzed. Using a test system consisting of chains of hydrogen molecules, we showed that at the level of the KLI approximation, SIC functionals afford major improvements over conventional LSDA/GGA approximations in predicting the polarizabilities of molecular chains. Interestingly, we find that SIC functionals also outperform the exact exchange functional at the KLI level, predicting polarizabilities accu-

rately to within 10-15% of quantum chemistry approaches such as MP4 [118]. Orbital dependent functionals are increasingly being used to address a variety of problems for which LSDA/GGA are inadequate. In particular, the importance of such functionals in electronic transport calculations has been recently discussed [320, 321, 322]. We are currently in the process of implementing these functionals into the SMEAGOL code firstly for calculating zero-bias transport properties and subsequently for calculations at low-bias in the weakly coupled regime.

Chapter 4 presented a detailed discussion on the atomic self interaction correction (ASIC) approximation. This method, based on the work of Filippetti and Spaldin [129], comes across as a computationally efficient way to rectify the shortcomings of conventional LSDA in predicting the electronic structure and spectra of strongly correlated solids as well as molecules. The implementation of the method within the SIESTA code was also described and its performance over a wide variety of molecular and solid state test systems was analyzed. In particular the scaling parameter α that accounts for screening effects was discussed. Because the ASIC method predicts molecular ionization potentials and removal energies accurately, it has immediate relevance in molecular electronic transport calculations where the correct placement of the eigenvalues of highest occupied molecular orbitals is crucial [321]. Thus, we have also implemented the ASIC method within the SMEAGOL code and electronic transport calculations using ASIC by Toher *et al*, are soon to be published [323]. In terms of future improvements to the ASIC method, we are currently investigating two main aspects. Firstly, in order to avoid the scaling parameter α , we are studying the possibility of employing semi-local quantities such as the Laplacian of the density $\nabla^2 n$, kinetic energy density τ (see equation 2.36 in chapter 2) etc to derive a more natural and self-consistent way to scale the ASIC potential in various systems. Secondly, although strictly speaking the ASIC total energy is not variational, one might want to calculate forces within ASIC assuming that the system is not too far away from the Born-Oppenheimer surface. We are currently testing forces and stress calculations within ASIC for various systems.

DFT calculations investigating the phenomenon of d^0 ferromagnetism in HfO_2 were presented in chapter 5. Since native defects in HfO_2 are the most likely cause behind the experimentally observed ferromagnetic signatures [27], we investigated the electronic structure of both oxygen vacancies (V_{O}) which are n-type dopants and Hf vacancies (V_{Hf}) which are p-type dopants in HfO_2 . We showed that V_{O} centers form doubly occupied deep donor states and are non-magnetic in their neutral ground state. Also, additional electron

doping or partial hole doping of the V_O defect states gives rise to local moments on the V_O centres but does not lead to long range ferromagnetism. We showed that Hf vacancies on the otherhand, spontaneously exhibit a spin-polarized ground state driven by strong exchange among the O-2p orbitals that form the defect molecular orbitals. Furthermore, individual V_{Hf} centers also couple ferromagnetically and can lead to ferromagnetism in highly defective samples. Since the initial reports of ferromagnetism in un-doped HfO_2 , similar experimental reports of high temperature ferromagnetism in un-doped thin-films of a variety of wide-gap oxides such as TiO_2 , In_2O_3 [324] and ZnO [325] have emerged. While some of these experimental findings have been received with scepticism in the community, there are also other reports of ferromagnetism in oxides that have been doped with non-magnetic impurities. For example Carbon and Copper doped ZnO thin-films have recently been reported as being ferromagnetic [326, 327] at room temperature. Theoretical calculations on these wide-gap oxide systems seem to suggest that hole states localized on O-2p orbitals at the top of the valence band generally lead to ferromagnetism if p-type defect or dopant concentrations are sufficiently high [326, 328]. However, the question of whether most of these wide-gap oxides can be doped p-type in the first place is widely debated in the experimental community. Ferromagnetic signatures in HfO_2 , TiO_2 and In_2O_3 are observed in oxygen deficient growth or treatment conditions [324] which must lead to the formation of n-type and not p-type defects. Oxides such as ZnO are also strongly n-type and reports of p-doping in ZnO are generally looked at with suspicion. On the other hand, there is also some experimental evidence suggesting that the magnetic signatures observed mostly arise from grain boundaries or thin-film interfaces and not from the bulk layers in these samples [11, 27, 324, 325]. Thus the current scenario in this field of d^0 ferromagnetism is one of confusion and detailed theoretical investigations of these systems, focussing on the electronic structure of native defects at interfaces and surfaces and their interactions with bulk defects, are necessary in order to resolve some of the conflicting issues.

In chapter 6 a detailed investigation of the magnetism in Co doped ZnO ($ZnO:Co$) was presented emphasizing in particular the role played by native n-type defects. We showed that substitutional Co ions only interact at first nearest neighbour (NN) separation and by themselves cannot lead to long range order in $ZnO:Co$. We also showed that a random and homogenous distribution of n-type donor defects such as oxygen vacancies (V_O), Zinc interstitials (Zn_I) and hydrogen (H_I) does not in any way enhance ferromagnetism in this system as defect and dopant interactions are short ranged. We identified instead, Co and V_O pair complexes as the most likely candidates that can lead to ferromagnetism in

ZnO:Co. Furthermore, we attributed the experimentally observed ferromagnetic signatures in ZnO:Co to blocked superparamagnetism and proposed a phase diagram for the material. While experimental research work on transition metal doped ZnO continues in an effort to realize high- T_c ferromagnetism in these materials, it is becoming increasingly apparent that these systems are unlikely to form ideal magnetic semiconductors [11]. Recently, it has even been suggested that the observed ferromagnetism in some transition metal doped oxides might not be related to the transition metal dopant at all but might instead be a phenomenon closely related to d^0 ferromagnetism [11]. This debate is therefore likely to continue into the near future. Nevertheless, the presence of local antiferromagnetic interactions and the major role played by native defects which are inherently difficult to control, is likely to severely diminish the utility of these materials to spintronics.

Finally, in chapter 7 we studied the electronic transport properties of a prototypical Mn_{12} based magnetic molecule functionalized by organic thio-ether functional groups [48] and attached to gold electrodes. We investigated the DFT electronic structure of the Mn_{12} single molecule magnet (SMM) using both the GGA exchange-correlation functional and the LDA+ U method. We showed that the GGA and LDA+ U description of the system was qualitatively similar. We then presented the transport properties of the SMM calculated using the non-equilibrium Green's functions formalism implemented in the SMEAGOL code [51]. In particular, the dependence of current-voltage (I-V) characteristics of the SMM on its local magnetic configuration was investigated. We found the transport properties of the molecule to be dominated by tunneling type behaviour across the organic functional groups and asymmetric coupling to the leads. We observed asymmetric I-V curves under positive and negative bias as well as localization driven changes in the current for different spin configurations of the Mn_{12} cluster on the molecule. Thus we show that information about the local spin-state of the molecule can be inferred from a detailed knowledge of the (I-V) characteristics. While the results of this work serve to illustrate the feasibility of first principles theoretical transport calculations on these relatively large molecular systems, a more quantitative description of the transport properties of these SMMs requires the use of more sophisticated theoretical tools. Firstly, advanced density functionals capable of accurately describing the strongly correlated electronic structure of the Mn_{12} core in these molecules need to be employed. Secondly, the spin-orbit (SO) [329] interaction needs to be included self-consistently into the calculations in order to investigate the interplay between charge transport and the magnetic anisotropy in these molecules. Thirdly, time dependence also needs to be explicitly incorporated into the calculations via

time dependent density functional theory (TD-DFT) [330], in order to model effects such as current induced local spin excitations or magnetic relaxation within the molecule. Some of these theoretical developments within *ab initio* electronic transport codes have only become available recently while others are still being developed. Thus, transport calculations on these Mn_{12} molecular magnets represent a very challenging and exciting problem in the field for the near future.

Bibliography

- [1] Y. Ohno *et al.*, Nature **402**, 790 (1999)
- [2] H. Ohno, Science, **291**, 840 (2001)
- [3] S. A. Wolf *et al.*, Science, **294**, 1488 (2001)
- [4] A. Aviram and M. A. Ratner, Chem. Phys. Lett., **29**, 277 (1974)
- [5] C. S. Lent, Science, **288**, 1597 (2000)
- [6] H. W. Postma *et al.*, Science **293**, 76 (2001)
- [7] P. Grünberg *et al.*, Phys. Rev. Lett. **57**, 2442 (1986)
- [8] M. Baibich *et al.*, Phys. Rev. Lett. **61**, 2472 (1988).
- [9] S. J. Pearton *et al.*, J. Appl. Phys. **93**, 1 (2003).
- [10] C. Liu *et al.*, J. Mater. Sci: Mater. Electr. **16** 555 (2005)
- [11] J. M. D. Coey, Current Opinion in Solid State and Materials Science **10**, 83 (2006)
- [12] K.Y. Wang *et al.*, in Proc. 27th Int. Conf. on Phys. of Semicon., Flagstaff, AZ, USA, July 2004, (New York 2005) p. 333.
- [13] T. Jungwirth *et al.*, Phys. Rev. B. **72**, 165204 (2005).
- [14] T. Dietl *et al.*, Science, **287**, 1019 (2000)
- [15] K. Ueda, H. Tabata and T. Kawai, Appl. Phys. Lett. **79**, 988-990 (2001).
- [16] J. B. Goodenough, *Magnetism and the Chemical Bond*, WileyInterscience, New York, 1962.

- [17] C. Zener, Phys. Rev. **82**, 403 (1951); J. B. Goodenough, Phys. Rev. **100**, 564 (1955)
- [18] M.A. Ruderman and C. Kittel, Phys. Rev. **96**, 99 (1954)
- [19] C. Zener, Phys. Rev. **81**, 440 (1950)
- [20] F. Holtzberg *et al.*, *Rare earth magnetic semiconductors*. In: Handbook on semiconductors. Amsterdam, North Holland, 1980.
- [21] H. Ohno, Science, **281**, 951 (1998).
- [22] J. M. D. Coey *et al.*, Nat. Mater. **4**, 173 (2005)
- [23] A. Kaminski and S. Das Sarma, Phys. Rev. Lett. **88**, 247202 (2002)
- [24] M. Venkatesan *et al.*, Phys. Rev. Lett. **93**, 177206 (2004).
- [25] D. A. Schwartz and D. R. Gamelin, Adv. Mat. **16**, 2115 (2004).
- [26] H.-J. Lee *et al.*, Appl. Phys. Lett. **88**, 062504 (2006).
- [27] J. M. D. Coey, Solid State Sciences **7**, 660 (2005)
- [28] M. Venkatesan *et al.*, Nature **430**, 630 (2004) ; J. M. D. Coey *et al.*, Phys. Rev. B. **72**, 024450 (2005)
- [29] R. M. Martin, *Electronic Structure*, Cambridge, UK (2004)
- [30] A. H. MacDonald *et al.*, Nature Materials **4**, 195 (2005).
- [31] V. I. Anisimov, J. Phys.: Condens. Matter **9** 767 (1997)
- [32] J.P. Perdew and A. Zunger, Phys. Rev. B **23**, 5048 (1981)
- [33] G. Binnig, H. Rohrer, C. Gerber, and E. Wihel, Phys. Rev. Lett. **50**, 120 (1983).
- [34] M. A. Reed, C. Zhou, J. Muller, T. P. Burgin, and J. M. Tour, Science **278**, 252 (1997).
- [35] J. Chen, M. A. Reed, A. M. Rawlett, and J. M. Tour, Science **286**, 1550 (1999).
- [36] Z. Yao, H. W. C. Postman, L. Balents, and C. Dekker, Nature (London) **402**, 273 (1999).

- [37] S. J. Tans, A. R. M. Verschueren, and C. Dekker, *Nature (London)* **393**, 49 (1998).
- [38] C. Collier, E. Wong, M. Belohradsky, F. Raymo, J. Stoddart, P. Kuekes, R. Williams, and J. Heath, *Science* **285**, 391 (1999).
- [39] Y. Huang, X. Duan, Y. Cui, L. Lauhon, K.-H. Kim, and C. Lieber, *Science* **294**, 1313 (2001).
- [40] P. Kuekes, J. Heath, and R. S. Williams (2000), US Patent (Hewlett-Packard) # 6128214.
- [41] N. Garcia, M. Munoz, and Y. W. Zhao, *Phys. Rev. Lett.* **82**, 2923 (1999).
- [42] J. J. Versluijs, M. A. Bari, and J. M. D. Coey, *Phys. Rev. Lett.* **87**, 26601 (2001).
- [43] J. R. Petta, S. K. Slater, and D. C. Ralph, *Phys. Rev. Lett.* **93**, 136601 (2004).
- [44] Z. H. Xiong, D. Wu, Z. V. Vardeny, and J. Shi, *Nature (London)* **427**, 821 (2004).
- [45] R. Sessoli, H. Tsai, A. Schake, S. Y. Wang et al. *J. Am. Chem. Soc.* **115**, 1804, (1993)
- [46] S. J. Blundell and F. L. Pratt, *J. Phys.: Condens. Matter* **16**, R771 (2004)
- [47] J. R. Friedman, M. P. Sarachik, J. Tejada and R. Ziolo *Phys. Rev. Lett.* **76**, 3830, (1996)
- [48] Sessoli et.al, *Chem. Commun.*, 2005, 1640
- [49] R. G. Parr and W. Yang, *Density-Functional Theory of Atoms and Molecules*, vol. 16 of The International Series of Monographs on Chemistry (Oxford University Press, Oxford (UK), 1989).
- [50] S. Datta. *Electronic Transport in Mesoscopic Systems*, Cambridge University Press, Cambridge, UK, 1995.
- [51] A.R. Rocha, V.M. Garcia-Suarez, S. Bailey, C. Lambert, J. Ferrer, and S. Sanvito. *Phys. Rev. B*, **73**, 085414, 2006.
- [52] E. Engel, (Springer, Berlin, 2003), vol. 620 of Lecture Notes in Physics.
- [53] J. B. Krieger, Y. Li, and G. J. Iafrate: *Phys. Lett. A* **146**, 256 (1990).

- [54] E. Artacho, D. Sanchez-Portal, P. Ordejón, A. García, and J.M. Soler. Phys. Stat. Sol., **215**:809, 1999.
- [55] C. D. Pemmaraju *et al.*, Phys. Rev. B **75**, 045101 (2007)
- [56] J. P. Perdew, K. Burke, and M. Ernzerhof, Phys. Rev. Lett. **77**, 3865 (1996).
- [57] E. Merzbacher, Quantum Mechanics (John Wiley & Sons Inc., New York, 1998).
- [58] R. G. Parr and W. Yang, *Density-Functional Theory of Atoms and Molecules*, vol. 16 of The International Series of Monographs on Chemistry (Oxford University Press, Oxford (UK), 1989).
- [59] J. P. Perdew and S. Kurth, (Springer, Berlin, 1998), vol. 500 of Lecture Notes in Physics.
- [60] A Szabo and N.S Ostlund, Modern Quantum Chemistry (Macmillan, New York, 1982)
- [61] P. Fulde, Electron Correlations in Molecules and Solids (Springer, Berlin, 1993).
- [62] P. Hohenberg and W. Kohn, Phys. Rev. **136**, B864 (1964).
- [63] W. Kohn and L. Sham, Phys. Rev. **140**, A1133 (1965).
- [64] U. von Barth and L. Hedin, J. Phys. C: Cond. Matt. **5**, 1629 (1972).
- [65] J. Perdew and A. Zunger, Phys. Rev. B **23**, 5048 (1981).
- [66] J. P. Perdew, K. Burke, and M. Ernzerhof, Phys. Rev. Lett. **77**, 3865 (1996).
- [67] J. P. Perdew and Y. Wang, Phys. Rev. B **33**, 8800 (1986)
- [68] A.D. Becke, Phys. Rev. A **38**, 3098 (1988)
- [69] C.Lee, W. Yang, and R. G. Parr, Phys. Rev. B **37**, 785 (1988)
- [70] T. Grabo, T. Kriebich and E.K.U. Gross, Molecular Engineering **7**; 27-50, (1997)
- [71] E. Engel, (Springer, Berlin, 2003), vol. 620 of Lecture Notes in Physics.
- [72] J. B. Krieger, Y. Li, and G. J. Iafrate: Phys. Lett. A **146**, 256 (1990).
- [73] A.D. Becke, J. Chem. Phys. **98**, 1372 (1993)

- [74] V. I. Anisimov, J. Zaanen, and O. K. Andersen, *Phys Rev B* **44**, 943 (1991).
- [75] M. Levy, *Proc. Natl. Acad. Sci.* **76**, 6062 (1979)
- [76] E. J. Baerends and O. V. Gritsenko, *J. Phys. Chem.* **101**, 5383 (1997).
- [77] J. F. Janak, *Phys. Rev. B* **18**, 7165 (1978).
- [78] J. P. Perdew and M. Levy, *Phys. Rev. B*, **56** , 16021 (1997)
- [79] L. J. Sham and M. Schlüter, *Phys. Rev. Lett* **51**, 1888 (1983)
- [80] X. Gonze, J. M. Beuken, R. Caracas, F. Detraux, M. Fuchs, G. M. Rignanese, L. Sindic, M. Verstraete, G. Zerah, F. Jollet, M. Torrent, A. Roy, et al., *Comp. Mat. Sci.* **25**, 478 (2002).
- [81] W. H. Press, B. P. Flannery, S. A. Teukolsky, and W. T. Vetterling, *Numerical Recipes in Fortran* (Cambridge University Press, Cambridge (UK), 1992), 2nd ed., URL <http://library.lanl.gov/numerical/bookfpdf.html>.
- [82] R.M. Martin. *Electronic Structure: Basic Theory and Practical Methods*. Cambridge University Press, Cambridge, UK, 1989.
- [83] N. Troullier and J.L. Martins. *Phys. Rev. B*, **43**,1993 (1991).
- [84] L. Kleinman and D. M. Bylander, *Phys. Rev. Lett*, **48**, 1425 (1982)
- [85] S. G. Louie, S. Froyen, and M. L. Cohen. *Phys. Rev. B*,**26** 1738, 1982.
- [86] E. Artacho, D. Sanchez-Portal, P. Ordejón, A. García, and J.M. Soler. *Phys. Stat. Sol.*, **215**:809, 1999.
- [87] J.M. Soler, E. Artacho, J.D. Gale, A. García, J. Junquera, P. Ordejón, and D. Sanchez-Portal. *J. Phys. Cond. Matter*, **14**:2745, 2002.
- [88] J.M. Soler, E. Artacho, J.D. Gale, A. García, J. Junquera, P. Ordejón, and D. Sanchez-Portal. *SIESTA: Spanish Initiative for Electronic Structure Calculations with Thousands of Atoms*, <http://www.uam.es/departamentos/ciencias/fismateriac/siesta>.
- [89] H. J. Monkhorst and J. D. Pack, *Phys. Rev. B* **13**, 5188 (1976).
- [90] R. Car and M. Parrinello, *Phys. Rev. Lett.* **55**, 2471 (1985).

- [91] W.M. Hoe, A. J. Cohen, and N. C. Handy, Chem. Phys. Lett. **341**, 319 (2001)
- [92] R. van Leeuwen and E. J. Baerends, Phys. Rev. A **49**, 2421 (1994).
- [93] A. Filippetti and N.A. Spaldin. Phys. Rev. B, **67**, 125109, 2003.
- [94] C.D. Pemmaraju, T. Archer, D. Sanchez-Portal, and S. Sanvito. Phys. Rev. B, **75**, 045101, 2007.
- [95] S. Datta. *Electronic Transport in Mesoscopic Systems*, Cambridge University Press, Cambridge, UK, 1995.
- [96] C. Caroli, R. Combescot, P. Nozieres, and D. Saint-James. J. Phys. C, **5**, 21, 1972.
- [97] J. Ferrer, A. Martin-Rodero, and F. Flores. Phys. Rev. B (Rapid Comm.), **38**, 10113, 1988.
- [98] A.R. Rocha, V.M. Garcia-Suarez, S. Bailey, C. Lambert, J. Ferrer, and S. Sanvito. Phys. Rev. B, **73**, 085414, 2006.
- [99] L.V. Keldysh. Sov. Phys. JETP, **20**, 1018, 1965.
- [100] A.R. Rocha, V.M. Garcia-Suarez, S.W. Bailey, C.J. Lambert, J. Ferrer, and S. Sanvito. Nature Materials, **4**, 335, 2005.
- [101] A.R. Rocha, V.M. Garcia-Suarez, S.W. Bailey, C.J. Lambert, J. Ferrer, and S. Sanvito. *SMEAGOL: Spin and Molecular Electronics in Atomically Generated Orbital Landscapes (non-equilibrium electronic transport)*, www.smeagol.tcd.ie, 2004.
- [102] S. Sanvito, C.J. Lambert, J.H. Jefferson, and A.M. Bratkovsky. Phys. Rev. B, **59**, 11936, 1999.
- [103] A.R. Rocha, *Theoretical and computational aspects of electronic transport at the nanoscale*, PhD Thesis, Trinity College Dublin (2007)
- [104] J. P. Perdew and S. Kurth, (Springer, Berlin, 1998), vol. 500 of Lecture Notes in Physics.
- [105] E. Engel, (Springer, Berlin, 2003), vol. 620 of Lecture Notes in Physics.
- [106] B. Champagne et al., J. Chem. Phys. 109, 10 489 (1998).

- [107] S. J. A. van Gisbergen et al., Phys. Rev. Lett. 83, 694(1999).
- [108] O.V. Gritsenko and E. J. Baerends, Phys. Rev. A 64, 042506 (2001).
- [109] H. Iikura et al., J. Chem. Phys. 115, 3540 (2001).
- [110] A. Abdurahman, A. Shukla, and G. Seifert, Phys. Rev. B 66, 155423 (2002).
- [111] M. Gruning, O.V. Gritsenko, and E. J. Baerends, J. Chem.Phys. 116, 6435 (2002).
- [112] P. Mori-Sanchez, Q.Wu, and W.Yang, J. Chem. Phys. 119,11001 (2003).
- [113] S.Kummel, J. Comput. Phys. 201, 333 (2004).
- [114] S.Kummel et al., Phys. Rev. Lett. 93, 213002 (2004)
- [115] J.P Perdew and Alex Zunger, Phys. Rev. B 23, 5048 (1981)
- [116] R.A. Heaton and C.C. Lin, J. Phys. B:At. Mol. Phys. 16, 2079 (1983).
- [117] M.R. Pederson, R.A. Heaton and C.C. Lin, J. Chem. Phys. 80, 1972 (1984).
- [118] S.Kummel and J.P Perdew, Phys. Rev. B 68, 035103 (2003)
- [119] J.B. Krieger, Y. Li and G.J. Iafrate, Phys. Rev. A 45, 101 (1992).
- [120] J. Garza, J.A. Nichols and D.A. Dixon, J. Chem. Phys. 112, 7880 (2000).
- [121] J. M. Soler, E. Artacho, J. D. Gale, A. Garca, J. Junquera, P. Ordejon and D. Sanchez-Portal, J. Phys. Cond. Matter 14, 2745 (2002).
- [122] J. Pipek and P. G. Mezey, J. Chem. Phys. 90, 4916, (1989)
- [123] J.P. Perdew, K. Burke, and M. Ernzerhof, Phys. Rev. Lett. 77 (1996) 3865-3868.
- [124] A.D. Becke, Phys. Rev. A 38, 3098 (1988)
- [125] C. Lee, W. Yang, R.G. Parr, Phys. Rev. B 37, 785 (1988)
- [126] W.M. Hoe, A. J. Cohen, and N. C. Handy, Chem. Phys. Lett. 341, 319 (2001)
- [127] Mol. Phys, Vol. 99, No. 5, 403 (2001)
- [128] R. van Leeuwen and E. J. Baerends, Phys. Rev. A 49, 2421 (1994).

- [129] A. Filippetti and N.A. Spaldin, Phys. Rev. B **67**, 125109 (2003).
- [130] P. Hohenberg and W. Kohn, Phys. Rev. **136**, B864 (1964).
- [131] E. Runge and E.K.U. Gross, Phys. Rev. Lett. **52**, 997 (1984).
- [132] J.P. Perdew, A. Ruzsinsky, J. Tao, V.N. Staroverov, G.E. Scuseria and G.I. Csonka, J. Chem. Phys. **123**, 062201 (2005).
- [133] W. Kohn and L.J. Sham, Phys. Rev. **140**, A1133 (1965).
- [134] S. Goedecker, Rev. Mod. Phys. **71**, 1085 (1999).
- [135] P. Ordejón, Comp. Mat. Sci. **12**, 157 (1998).
- [136] V.I. Anisimov, J. Zaanen and O.K. Andersen, Phys. Rev. B **44**, 943 (1991).
- [137] V.I. Anisimov, F. Aryasetiawan and A.I. Lichtenstein, J. Phys.: Condens. Matter **9**, 767 (1997).
- [138] M. Cococcioni and S. de Gironcoli, Phys. Rev. B **71**, 035105 (2005).
- [139] M. Wierzbowska, D. Sánchez-Portal and S. Sanvito, Phys. Rev. B **70**, 235209 (2004).
- [140] J.P. Perdew, Phys. Rev. Lett. **55**, 1665 (1985).
- [141] J.P. Perdew and K. Schmidt, in *Density Functional Theory and Its Applications to Materials*, edited by V. Van Doren, C. Van Alsenoy and P. Geerlings (AIP, Melville, NY, 2001).
- [142] J.P. Perdew, K. Burke and M. Ernzerhof, Phys. Rev. Lett. **77**, 3865 (1996).
- [143] J. Tao, J.P. Perdew, V.N. Staroverov and G.E. Scuseria, Phys. Rev. Lett. **91**, 146401 (2003).
- [144] J.P. Perdew and A. Zunger, Phys. Rev. B **23**, 5048 (1981).
- [145] H.B. Shore, J.H. Rose and E. Zaremba, Phys. Rev. B **15**, 2858 (1977).
- [146] K. Terakura, T. Oguchi, A.R. Williams and J. Kübler, Phys. Rev. B **30**, 4734 (1984).
- [147] J.F. Janak, Phys. Rev. B **18**, 7165 (1978).

- [148] J.P. Perdew, R.G. Parr, M. Levy and J.L. Balduz Jr., Phys. Rev. Lett. **49**, 1691 (1982); J.P. Perdew and M. Levy, Phys. Rev. Lett. **51**, 1884 (1983).
- [149] J.P. Perdew and M. Levy, Phys. Rev. B **56**, 16021 (1997).
- [150] J.P. Perdew, in *Density Functional Methods in Physics*, edited by R.M. Dreizler and J. da Providencia (Plenum, NY, 1985), p. 265.
- [151] C. Toher, A. Filippetti, S. Sanvito and K. Burke, Phys. Rev. Lett. **95**, 146402 (2005).
- [152] E. Fermi and E. Amaldi, Accad. Ital. Rome **6**, 119 (1934).
- [153] D. Vogel, P. Krüger and J. Pollmann, Phys. Rev. B **54**, 5495 (1996).
- [154] D. Vogel, P. Krüger and J. Pollmann, Phys. Rev. B **55**, 12836 (1996).
- [155] D. Vogel, P. Krüger and J. Pollmann, Phys. Rev. B **58**, 3865 (1998).
- [156] J. M. Soler, E. Artacho, J. D. Gale, A. García, J. Junquera, P. Ordejón and D. Sanchez-Portal, J. Phys. Cond. Matter **14**, 2745 (2002).
- [157] M. Levy, Proc. Natl. Acad. Sci. USA **76**, 6062 (1979).
- [158] J.G. Harrison, R.A. Heaton and C.C. Lin, J. Phys. B: At. Mol. Phys. **16**, 2079 (1983).
- [159] M.R. Pederson, R.A. Heaton and C.C. Lin, J. Chem. Phys. **80**, 1972 (1984).
- [160] M.R. Pederson, R.A. Heaton and C.C. Lin, J. Chem. Phys. **82**, 2688 (1985).
- [161] S. Goedecker and C.J. Umrigar, Phys. Rev. A **55**, 1765 (1997).
- [162] O.A. Vydrov and G.E. Scuseria, J. Chem. Phys. **121**, 8187 (2004).
- [163] O.A. Vydrov and G.E. Scuseria, J. Chem. Phys. **122**, 184107 (2005).
- [164] S. Kümmel and J.P. Perdew, Mol. Phys. **101**, 1363 (2003).
- [165] J.B. Krieger, Y. Li and G.J. Iafrate, Phys. Rev. A **45**, 101 (1992).
- [166] J. Garza, J.A. Nichols and D.A. Dixon, J. Chem. Phys. **112**, 7880 (2000).
- [167] S. Patchkovskii, J.A. Nichols and D.A. Dixon, J. Chem. Phys. **114**, 639 (2001).
- [168] Y.H. Kim, M. Stadele and R. M. Martin, Phys. Rev. A **60**, 3633 (1999).

- [169] R.A. Heaton, J.G. Harrison and C.C. Lin, *Phys. Rev. B* **28**, 5992 (1983).
- [170] A. Svane and O. Gunnarsson, *Phys. Rev. Lett.* **65**, 1148 (1990).
- [171] A. Svane, *Phys. Rev. Lett.* **68**, 1900 (1992).
- [172] M. Arai and T. Fujiwara, *Phys. Rev. B* **51**, 1477 (1995).
- [173] Z. Szotek, W.M. Temmerman and H. Winter, *Phys. Rev. B* **47**, 4029 (1993).
- [174] W.M. Temmerman, Z. Szotek and H. Winter, *Phys. Rev. B* **47**, 1184 (1993); Z. Szotek, W.M. Temmerman and H. Winter, *Phys. Rev. Lett.* **72**, 1244 (1994); A. Svane, *Phys. Rev. Lett.* **72**, 1248 (1994); A. Svane, *Phys. Rev. B* **53**, 4275 (1996); A. Svane, V. Kanchana, G. Vaitheeswaran, G. Santi, W.M. Temmerman, Z. Szotek, P. Strange and L. Petit, *Phys. Rev. B* **71**, 045119 (2005).
- [175] L. Petit, T.C. Schulthess, A. Svane, Z. Szotek, W.M. Temmerman and A. Janotti, *Phys. Rev. B* **73**, 045107 (2006).
- [176] Z. Szotek, W.M. Temmerman, A. Svane, L. Petit, G.M. Stocks and H. Winter, *Phys. Rev. B* **68**, 054415 (2003).
- [177] L. Petit, A. Svane, W.M. Temmerman and Z. Szotek, *Phys. Rev. Lett.* **88**, 216403 (2002); L. Petit, A. Svane, W.M. Temmerman and Z. Szotek, *Phys. Rev. B* **63**, 165107 (2001).
- [178] A. Zunger, *Phys. Rev. B* **22**, 649 (1980).
- [179] M.M. Rieger and P. Vogl, *Phys. Rev. B* **52**, 16567 (1995).
- [180] A. Filippetti and V. Fiorentini, *Phys. Rev. Lett.* **95**, 086405 (2005).
- [181] A. Filippetti and V. Fiorentini, *Phys. Rev. B* **73**, 035128 (2005).
- [182] A. Filippetti and N.A. Spaldin, *Phys. Rev. B* **68**, 045111 (2003).
- [183] B.B. Van Aken, T.T.M.A. Palstra, A. Filippetti and N.A. Spaldin, *Nature Mat.* **3**, 164 (2003).
- [184] P. Delugas, V. Fiorentini and A. Filippetti, *Phys. Rev. B* **71**, 134302 (2005).
- [185] A. Filippetti, N.A. Spaldin and S. Sanvito, *Chem. Phys.* **309**, 59 (2005).

- [186] A. Filippetti, N.A. Spaldin and S. Sanvito, *J. Magn. Magn. Mater.* **290**, 1391 (2005).
- [187] B. Baumeier, P. Krüger and J. Pollmann, *Phys. Rev. B* **73**, 195205 (2006).
- [188] N. Marzari and D. Vanderbilt, *Phys. Rev. B* **56**, 12847 (1997).
- [189] M.R. Norman, *Phys. Rev. B* **28**, 3585 (1983).
- [190] N. Troullier and J.L. Martins, *Phys. Rev. B* **43**, 1993 (1991).
- [191] S.G. Louie, S. Froyen and M. L. Cohen, *Phys. Rev. B* **26**, 1738 (1982).
- [192] L. Kleinman and D.M. Bylander, *Phys. Rev. Lett.* **48**, 1425 (1982).
- [193] O.F. Sankey and D.J. Niklewski, *Phys. Rev. B* **40**, 3979 (1989).
- [194] E. Artacho, D. Sanchez-Portal, P. Ordejón, A. García and J. M. Soler, *Phys. Status Solidi B* **215**, 809 (1999).
- [195] J. Junquera, O. Paz, D. Sanchez-Portal and E. Artacho, *Phys. Rev. B* **64**, 235111 (2001).
- [196] S.L. Dudarev, G.A. Botton, S.Y. Savrasov, C.J. Humphreys, and A.P. Sutton, *Phys. Rev. B* **57**, 1505 (1998).
- [197] L.J. Sham and M. Schlüter, *Phys. Rev. Lett.* **51**, 1888 (1983); L.J. Sham and M. Schlüter, *Phys. Rev. B* **32**, 3883 (1985).
- [198] W.G. Aulbur, M. Städele and A. Görling, *Phys. Rev. B* **62**, 7121 (2000).
- [199] R.J. Magyar, A. Fleszar and E.K.U. Gross, *Phys. Rev. B* **69**, 045111 (2004).
- [200] G. Baldini and B. Bosacchi, *Phys. Status Solidi* **38**, 325 (1970).
- [201] S. Nakai and T. Sagawa, *J. Phys. Soc. Japan* **26**, 1427 (1969).
- [202] J.C. Phillips, *Phys. Rev.* **136**, A1705 (1964).
- [203] R.C. Whited, C.J. Flaten and W.C. Walker, *Solid State Comm.* **13**, 1903 (1973).
- [204] Y. Kaneko and T. Koda, *J. Cryst. Growth* **86**, 72 (1988).
- [205] H. Yamashita, K. Fukui, S. Misawa and S. Yoshida, *J. Appl. Phys.* **50** 896 (1979).

- [206] V. Bougrov, M.E. Levinshtein, S.L. Rumyantsev, A. Zubrilov, in *Properties of Advanced Semiconductor Materials GaN, AlN, InN, BN, SiC, SiGe*, Eds. Levinshtein M.E., Rumyantsev S.L., Shur M.S., John Wiley & Sons, Inc., New York, 2001, 1-30.
- [207] B.R. Nag, Phys. Stat. Sol. (b) **237**, vol. 2 R1 (2003) and reference therein.
- [208] M. Oshikiri and F. Aryasetiawan, Phys. Rev. B **60**, 10754 (1999) and reference therein.
- [209] S.C. Erwin and C.C. Lin, J. Phys. C: Solid State Phys. **21**, 4285 (1988) and reference therein and reference therein.
- [210] M.L. Bortz, R.H. French, D.J. Jones, R.V. Kasowski and F.S. Ohuchi, Phys. Scr. **41**, 537 (1990).
- [211] E.A. Mikajloa, H.E. Dorsett and M.J. Fordb, J. Chem. Phys. **120**, 10799 (2004).
- [212] W.R.L. Lambrecht and B. Segall, in *Properties of Group II Nitrides* Ref. [1], p. 125. See this compilation, as well, for a comprehensive list of references up to 1994.
- [213] S.A. Ding, S.R. Barman, K. Horn and V.L. Alpherovich, in *Proceedings of ICPS-23*, edited by M. Scheffler and R. Zimmermann World Scientific, Singapore, 1996, p. 525.
- [214] L.F.J. Piper, T.D. Veal, P.H. Jefferson, C.F. McConville, F. Fuchs, J. Furthmüller, F. Bechstedt, H. Lu and W.J. Schaff, Phys. Rev. B **72**, 245319 (2005).
- [215] K. Ozawa, K. Sawada, Y. Shirotori and K. Edamoto and M. Nakatake, Phys. Rev. B **68**, 125417 (2003).
- [216] L. Ley, R.A. Pollak, F.R. McFeely, S.P. Kowalczyk and D.A. Shirley, Phys. Rev. B **9**, 600 (1974).
- [217] W.R.L. Lambrecht, B. Segall, S. Strite, G. Martin, A. Agarwal, H. Morkoc and A. Rockett, Phys. Rev. B **50**, 14155 (1994).
- [218] A. R. Rocha, V. M. Garcia-Suarez, S. Bailey, C. Lambert, J. Ferrer, S. Sanvito, Phys. Rev. B **73**, 085414 (2006); Nature Materials **4**, 335 (2005).
- [219] NIST Computational Chemistry Comparison and Benchmark DataBase, <http://srdata.nist.gov/cccbdb/default.htm>

- [220] O.A. Vydrov, G.E. Scuseria, J.P. Perdew, A. Ruzsinszky and G.I. Csonka, *J. Chem. Phys.* **124**, 094108 (2006).
- [221] O.A. Vydrov and G.E. Scuseria, *J. Chem. Phys.* **124**, 191101 (2006).
- [222] T. Koopmans, *Physica* **1**, 104 (1933).
- [223] L. Hedin and A. Johansson, *J. Phys. B* **2**, 1336 (1969).
- [224] A. Filippetti, *Phys. Rev. A* **57**, 914 (1998).
- [225] P. Baltzer, M. Larsson, L. Karlsson, B. Wannberg and M. Carlsson Göthe, *Phys. Rev. A* **46**, 5545 (1992).
- [226] D.P. Chong, O.V. Gritsenko and E.J. Baerends, *J. Chem. Phys.* **116**, 1760 (2002).
- [227] N.I. Medvedeva *et.al*, *Phys. stat. sol. (b)* **160**, 517 (1990).
- [228] X. Zhao and D. Vanderbilt, *Phys. Rev. B* **65** 233106 (2002).
- [229] A. S. Foster, F. Lopez Gejo, A. L. Shluger and R. M. Nieminen, *Phys. Rev. B* **65**, 174117.
- [230] W.L. Scopel, A.J.R. da Silva, W. Orellana and A. Fazzio, *Appl. Phys. Lett.* **84**, 1492 (2004).
- [231] M. Venkatesan, C. B. Fitzgerald, J. M. D. Coey, *Nature* **430**, 630 (2004) Brief Communications.
- [232] J. M. D. Coey, M. Venkatesan, P. Stamenov, C. B. Fitzgerald, and L. S. Dorneles, *Phys. Rev. B* **74**, 024450 (2005).
- [233] R. Monnier and B. Delley, *Phys. Rev. Lett.* **87** 157204 (2001).
- [234] I. S. Elfimov, S. Yunoki, and G. A. Sawatzky, *Phys. Rev. Lett.* **89**, 216403 (2002).
- [235] A. Zywietz, J. Furthmüller, and F. Bechstedt, *Phys. Rev. B* **62**, 6854 (2000).
- [236] J. M. Soler *et.al*, *J. Phys. Cond. Matter* **14**, 2745 (2002).
- [237] D.M. Ceperley and B.J. Alder, *Phys. Rev. Lett.* **45**, 566 (1980)
- [238] N. Troullier and J. L. Martins, *Phys. Rev. B* **43**, 1993 (1991).

- [239] J. Osorio-Guillèn, S. Lany, S. V. Barabash, and A. Zunger, *Phys. Rev. B* **75**, 184421 (2007)
- [240] C. D. Pemmaraju and S. Sanvito, *Phys. Rev. Lett.* **94**, 217205 (2005)
- [241] G. Bouzerar and T. Ziman, *Phys. Rev. Lett.* **96**, 207602 (2006)
- [242] V.E. Wood and A.E. Austin, *Magnetoelectric interaction phenomena in crystals*, [London: Gordon and Breach (1975)].
- [243] Special issue on Transparent Conducting Oxides, edited by D.S. Ginley and C. Bright [MRS Bull. **25** (2000)]
- [244] L.E. Halliburton, N.C. Giles, N.Y. Garces, M. Luo, C. Xu, L. Bai and L.A. Boatner, *Appl. Phys. Lett.* **87**, 172108 (2005).
- [245] S.A. Wolf, D.D. Awschalom, R.A. Buhrman, J.M. Daughton, S. von Molnár, M.L. Roukes, A.Y. Chtchelkanova and D.M. Treger, *Science* **294**, 1488-1495 (2001).
- [246] M.H. Huang, S. Mao, H. Feick, H. Yan, Y. Wu, H. Kind, E. Weber, R. Russo and P. Yang, *Science* **292**, 1897-1899 (2001).
- [247] M. Kroutvar, Y. Ducommun, D. Heiss, M. Bichler, D. Schuh, G. Abstreiter and J.J. Finley, *Nature (London)* **432**, 81-84 (2004).
- [248] A.H. MacDonald, P. Schiffer and N. Samarth, *Nature Materials* **4**, 195-202 (2005).
- [249] K. Ueda, H. Tabata and T. Kawai, *Appl. Phys. Lett.* **79**, 988-990 (2001).
- [250] D.A. Schwartz, N.S. Norberg, Q.P. Nguyen, J.M. Parker and D.R. Gamelin, *J. Am. Chem. Soc.* **125**, 13205-13218 (2003).
- [251] K. Rode, A. Anane, R. Mattana, J.-P. Contour, O. Durand and R. LeBourgeois, *J. Appl. Phys.* **93**, 7676-7678 (2003).
- [252] W. Prellier, A. Fouchet, B. Mercey, Ch. Simon and B. Raveau, *Appl. Phys. Lett.* **82**, 3490-3492 (2003).
- [253] M. Venkatesan, C.B. Fitzgerald, J.G. Lunney and J.M.D. Coey, *Phys. Rev. Lett.* **93**, 177206 (2004).

- [254] J. H. Kim, H. Kim, Y. E. Ihm, and W. K. Choo, *J. Appl. Phys.* **92** (2002) 6066.
- [255] M. H. Kane, K. Shalini, C. J. Summers, R. Varatharajan, J. Nause, C. R. Vestal, Z. J. Zhang, and I. T. Ferguson, *J. Appl. Phys.* **97** (2005) 023906.
- [256] H.-J. Lee, S.-Y. Jeong, C.R. Cho and C.H. Park, *Appl. Phys. Lett.* **81**, 4020-4022 (2002).
- [257] A.C. Tuan et al., *Phys. Rev. B* **70**, 054424 (2004).
- [258] M. Kobayashi et al., *Phys. Rev. B* **72**, 201201(R) (2005).
- [259] S.C. Wi et al., *Appl. Phys. Lett.* **84**, 4233-4235 (2004).
- [260] Y.Z. Peng, T. Liew, T.C. Chong, W.D. Song, H.L. Li and W. Liu, *J. Appl. Phys.* **98**, 114909 (2005).
- [261] K. Ando, *J. Appl. Phys.* **89**, 7284-7286 (2001).
- [262] A.S. Risbud, N.A. Spaldin, Z.Q. Chen, S. Stemmer and R. Seshadri, *Phys. Rev. B* **68**, 205202 (2003).
- [263] C.B. Fitzgerald, M. Venkatesan, J.G. Lunney, L.S. Dorneles and J.M.D. Coey, *Appl. Sur. Sci.* **247**, 493496 (2005).
- [264] C. Song et al., *Phys. Rev. B* **73**, 024405 (2006).
- [265] Sati et al., *Phys. Rev. Lett.* **96**, 017203 (2006).
- [266] G.L. Liu et al., *Appl. Phys. Lett.* **90**, 052504 (2007).
- [267] L.S. Dorneles et al., *J. Magn. Magn. Mater.* **310**, 2087-2088 (2007).
- [268] A. Dinia, G. Schmerber, C. Mény, V. Pierron-Bohnes and E. Beaurepaire, *J. Appl. Phys.* **97**, 123908 (2005).
- [269] J. Cui and U. Gibson, *Phys. Rev. B* **74**, 045416 (2006).
- [270] H.S. Hsu et al., *Appl. Phys. Lett.* **88**, 242507 (2006).
- [271] X. Han, G. Wang, J. Jie, X. Zhu and J.G. Hou, *Thin. Sol. Films* **491**, 249-252 (2005).
- [272] D.A. Schwartz and D.R. Gamelin, *Adv. Mat.* **16**, 2115-2119 (2004).

- [273] N. Khare, M.J. Kappers, M. Wei, M.G. Blamire and J.L. MacManus-Driscoll, *Adv. Mat.* **18**, 1449-1452 (2006).
- [274] H.-J. Lee et al., *Appl. Phys. Lett.* **88**, 062504 (2006).
- [275] F.A. Selim, M.H. Weber, D. Solodovnikov and K.G. Lynn, *Phys. Rev. Lett.* **99**, 085502 (2007).
- [276] S. Lany and A. Zunger, *Phys. Rev. Lett.* **98**, 045501 (2007).
- [277] A. Janotti and C.G. van de Walle, *Nature Materials* **6**, 44 (2007).
- [278] A. O. Ankiewicz, *J. Appl. Phys.* **101**, 024324 (2007).
- [279] T. Dietl, H. Ohno, F. Matsukura, J. Cibert and D. Ferrand, *Science* **287**, 1019 (2000).
- [280] J.B. Goodenough, *Magnetism and chemical bond* [Wiley-Interscience, New York-London, 1963].
- [281] J.M.D. Coey, M. Venkatesan and C.B. Fitzgerald, *Nature Materials* **4**, 173 (2005).
- [282] J. M. Soler et al., *J. Phys.: Condens. Matter* **14** (2002) 2745.
- [283] N. Troullier and J. L. Martins, *Phys. Rev. B* **43**, 1993 (1991).
- [284] D.M. Ceperley and B.J. Alder, *Phys. Rev. Lett.* **45**, 566 (1980)
- [285] C. D. Pemmaraju *et al.*, *Phys. Rev. B* **75**, 045101 (2007)
- [286] A. Akande and S. Sanvito, *J. Chem. Phys.* **127**, 034112, (2007).
- [287] O. Madelung, M. Schulz, and H. Weiss, *Numerical Data and Functional Relationships in Science and Technology* (Springer-Verlag, Berlin, 1982), Vol. 17. *Semiconductors Physics of Group IV elements and III-V Compounds*, edited by K. H. Hellwege and O. Madelung, Landolt-Bornstein, New Series, Group III, Vol.17, Pt.a (Springer, Berlin 1982); *Intrinsic Properties of Group IV Elements and III-V, II-VI, and I-VII Compounds*, edited by K. H. Hellwege and O. Madelung, Landolt-Bornstein, New Series, Group III, Vol.22, Pt.a (Springer, Berlin 1987).
- [288] A. F. Kohan, G. Ceder, D. Morgan and C. G. Van de Walle, *Phys. Rev. B.* **61**, 15019 (2000)

- [289] K. J. Kim *et al.*, Appl. Phys. Lett. 84, 4233 (2004).
- [290] N. A. Spaldin, Phys. Rev. B 69, 125201 (2004); E. C. Lee and K. J. Chang, Phys. Rev. B 69, 085205 (2004); C.H. Patterson cond-mat/0512101
- [291] S. Lany and A. Zunger, Phys. Rev. B 72, 035215 (2005)
- [292] V.Gavryushin, G. Raciukaitis, D.Juodzbališ, A.Kazlauskas, and V.Kubertavicius, J. Cryst. Growth 138, 924 (1994).
- [293] D. C. Look, G. C. Farlow, Pakpoom Reunchan, Sukit Limpijumnong, S. B. Zhang, and K. Nordlund, Phys. Rev. Lett. 95, 225502 (2005)
- [294] C.G. van de Walle Phys. Rev. Lett. 85, 1012 (2000)
- [295] D. Stauffer and A. Aharony, *Introduction to percolation theory*, [Taylor & Francis, London 1994].
- [296] J. Osorio-Guillén, S. Lany, S.V. Barbash and A. Zunger, Phys. Rev. B **75**, 184421 (2007).
- [297] P. Allia, M. Coisson, P. Tiberto, F. Vinai, M. Knobel, M.A. Novak and W.C. Nunes, Phys. Rev. B **64**, 144420 (2001).
- [298] J. Löffler, H.-B. Braun and W. Wagner, Phys. Rev. Lett. **85**, 1990 (2000).
- [299] K. Sato, T. Fukushima and H. Katayama-Toshida, Jpn. J. Appl. Phys. **46**, L682 (2007).
- [300] C.D. Pemmaraju, R. Hanafin, T. Archer, H.B. Braun and S. Sanvito (submitted to Nature Materials)
- [301] R. Sessoli, H. Tsai, A. Schake, S. Y. Wang et al. J. Am. Chem. Soc. **115**, 1804, (1993)
- [302] J. R. Friedman, M. P. Sarachik, J. Tejada and R. Ziolo Phys. Rev. Lett. **76**, 3830, (1996)
- [303] J. Park *et al.*, Nature (London) **417**, 722 (2002)
- [304] W.Liang *et al.*, Nature (London) **417**, 725 (2002)

- [305] *et al.*, Nature (London) **425**, 698 (2003)
- [306] H. B. Heersche *et al*, Phys. Rev. Lett, **96**, 206801 (2006)
- [307] Moon-Ho Jo *et al*, Nano Lett. **6**, 2014 (2006)
- [308] Sessoli *et.al*, Chem. Commun., 2005, 1640
- [309] J.M. Soler, E. Artacho, J.D. Gale, A. Garcóa, J. Junquera, P. Ordejón, and D. Sanchez-Portal. *SIESTA: Spanish Initiative for Electronic Structure Calculations with Thousands of Atoms*, <http://www.uam.es/departamentos/ciencias/fismateriac/siesta>
- [310] N. Troullier and J. L. Martins, Phys. Rev. B **43**, 1993 (1991).
- [311] J.P. Perdew, K. Burke, and M. Ernzerhof, Phys. Rev. Lett. **77**, 3865 (1996).
- [312] V. I. Anisimov, J. Zaanen, and O. K. Andersen, Phys Rev B **44**, 943 (1991).
- [313] J. Kortus, C. Massobrio and M. Drillon , J. Comput. Theor. Nanosci., **3**, 11 (2006)
- [314] U. del Pennino *et al*, Surf. Sci., **600** , 4185 (2006)
- [315] R.A. Robinson, P.J. Brown, D.N. Argyriou, D.N. Hendrickson, and S.M.J. Aubin, J. Phys. Condens. Matter **12**, 2805 (2000).
- [316] K. Park *et al* Phys. Rev. B **69**, 014416 (2004)
- [317] A.R. Rocha, V.M. Garcia-Suarez, S.W. Bailey, C.J. Lambert, J. Ferrer, and S. Sanvito. *SMEAGOL: Spin and Molecular Electronics in Atomically Generated Orbital Landscapes (non-equilibrium electronic transport)*, www.smeagol.tcd.ie, 2004.
- [318] Toher *et al*, Phys. Rev. Lett. **95**, 146402 (2005)
- [319] I. Rungger and S. Sanvito (*unpubsihed*)
- [320] C. Toher and S. Sanvito, Phys. Rev. Lett., **99**, 056801 (2007).
- [321] C. Toher, A. Filippetti, S. Sanvito, and Kieron Burke, Phys. Rev. Lett., **95**, 146402
- [322] San-Huang Ke *et al.*, J. Chem. Phys. **126**, 201102 (2007)
- [323] C. Toher and S. Sanvito (*in preparation*)

- [324] N. H. Hong *et al.*, Phys. Rev. B **73**, 132404 (2006)
- [325] N. H. Hong *et al.*, J. Phys.: Condens. Matter **19** 036219 (2007)
- [326] H. Pan *et al.*, Phys. Rev. Lett. **99**, 127201 (2007)
- [327] D. B. Buchholz *et al.*, Appl. Phys. Lett. **87**, 082504 (2005)
- [328] H. Weng *et al.*, Phys. Rev. B **73**, 132410 (2006)
- [329] E. Merzbacher, *Quantum Mechanics* (John Wiley & Sons Inc., New York, 1998).
- [330] E. Runge and E.K.U. Gross, Phys. Rev. Lett. **52**, 997 (1984)

Appendix A

Publications stemming from this work

- Ferromagnetism Driven by Intrinsic Point Defects in HfO₂, C. D. Pemmaraju and S. Sanvito, Phys. Rev. Lett. **94**, 217205 (2005)
- Atomic-orbital-based approximate self-interaction correction scheme for molecules and solids, C. D. Pemmaraju, T. Archer, D. Sanchez-Portal, and S. Sanvito, Phys. Rev. B **75**, 045101 (2007)
- Polarizability of molecular chains: does one need exact exchange? C. D. Pemmaraju, S. Sanvito, and K. Burke (submitted to Phys. Rev. B)
- Impurity-Ion pair induced high-temperature ferromagnetism in Co-doped ZnO. C. D. Pemmaraju, R. Hanafin, T. Archer, H.B. Braun and S. Sanvito, (in preparation)
- *Ab initio* simulations of the transport properties of Mn₁₂ based spin-devices. C. D. Pemmaraju, I. Rungger, and S. Sanvito, (in preparation)